Dipl.-Ing. Christof Weinländer BSc

Processing Biogas for the use in Solid Oxide Fuel Cells

Doctoral Thesis

In fulfilment of the requirements
for the degree
Doctor of Technical Sciences

submitted to
Graz University of Technology
Faculty of Mechanical Engineering and Economical Sciences

Supervisor
Univ.-Prof. Dipl.-Ing. Dr. techn. Christoph Hochenauer

Second Supervisor
Univ.-Prof. Dipl.-Ing. Dr. techn. Matthäus Siebenhofer

Bärnbach, March 2019

Affidavit

I hereby declare that I am the sole author or this thesis, that I have not used any sources other those cited, and that I have made explicit reference to the sources of all material that was quoted, whether directly or indirectly. The document uploaded to the TUGraz online platform is identical to this text.

Graz, _____ _____

Date Signature

Abstract

The use of efficient and low-emission technologies for the generation of electrical energy is of great importance. Modern power plants must enable sustainable operation based on renewable primary energy sources and at the same time have a high overall efficiency in order to counteract dependence on fossil fuels. In particular, the energy conversion by means of solid oxide fuel cells (SOFCs) is becoming increasingly interesting for the energy supply. In the fuel cell (FC), the chemical energy of the fuel is converted directly into electrical energy which manifests itself in a higher electrical efficiency than in conventional heat engines.

A unique feature of SOFCs is their fuel flexibility and the associated possibility to convert not only hydrogen (H_2), but also carbon monoxide (CO) and hydrocarbons. Among the different types of fuels, biogas is considered as an alternative and environmentally friendly fuel. Biogas is a renewable fuel that can be obtained by anaerobic digestion (AD) of biomass. Biogas, however, contains impurities in the form of hydrogen sulfide (H_2S) and hydrogen chloride (HCl) in different concentrations. These have a negative impact on the performance and durability of the SOFC and, in the case of H_2S, also on the catalyst of the reformer.

In order to avoid a performance loss of the SOFC, commonly referred to as degradation, the supplied biogas must be cleaned. The required purities are 2 parts per million by volume (*ppmv*) for H_2S and 10 *ppmv* for HCl. Depending on the biogas production, the impurities of H_2S vary in the range of 50 - 6800 *ppmv* and for HCl in the range of 0.1 - 25 *ppmv*. Conditioning the biogas to reduce the H_2S and HCl content is, therefore, essential for safe operation of an SOFC.

Different basic procedural operations are available for this task. The H_2S separation operations can be divided into two groups. The physicochemical and biotechnological processes. The physicochemical processes include, for example, adsorption and absorption. The most competitive desulfurisation technology in 1-10 kW_{el} power plants is adsorption as it is simple, effective and cost efficient. Activated carbons, metal oxides and zeolites are used in adsorption. However, the issues involved in the use of adsorption for safe operation of an biogas fuelled SOFC system are extensive. On the one hand, it is necessary to check the adsorbents regarding their separation performance under different boundary conditions. Additionally, possible cross-sensitivities to substances present in the biogas, such as ammonia (NH_3), must be investigated.

The focus of this work is the adsorptive separation of H_2S , HCl and NH_3 from biogas. For the characterization of the adsorbents, at first gas mixtures consisting of the pollutant to be adsorbed and inert gas were used. Subsequently, the inert gas was replaced by methane (CH_4)) and carbon dioxide (CO_2), which are the main components of biogas. It was shown that gas purification by means of adsorption sufficiently removes pollutants from biogas and, thus, safe operation of a SOFC can be ensured. The variation of different factors such as concentration of H_2S, $GHSV$, temperature and moisture content complete the experiments. The observed separation behavior of the different adsorbents allows an adsorber design tailored to biogas. To complete the overall concept of a biogas fuelled SOFC combined cooling heat and power (CCHP), a catalyst for steam reforming (SR) and a 10-cell SOFC stack were tested during operation.

The components required for the process of engineering the system structure are described in detail and options for system design are explained. The evaluation serves as a base for improvement potentials at the component and system level, which have to be taken into account in future product developments and are already partially considered in subsequent projects. The results underline that with the help of adsorptive cleaning steps it is possible to purify biogas in an extent that it can be used to operate a SOFC based CCHP system.

Kurzfassung

Dem Einsatz effizienter und schadstoffarmer Technologien zur Erzeugung elektrischer Energie kommt eine große Bedeutung zu. Moderne Kraftwerke müssen einen nachhaltigen Betrieb auf Basis regenerativer Primärenergiequellen ermöglichen und zugleich einen hohen Gesamtwirkungsgrad aufweisen, um der Abhängigkeit von fossilen begrenzten Brennstoffen entgegenzuwirken. Insbesondere die Energieumwandlung mittels Festoxidbrennstoffzellen (engl. Solid Oxide Fuel Cells) wird für die Energieversorgung zunehmend interessanter. In der Brennstoffzelle wird die chemische Energie des Brennstoffs direkt in elektrische Energie umgewandelt, was sich unter anderem in einem höheren elektrischen Wirkungsgrad bemerkbar macht als bei herkömmlichen Wärmekraftmaschinen.

Ein Alleinstellungsmerkmal von SOFCs ist ihre Brennstoffflexibilität und die damit einhergehende Möglichkeit neben Wasserstoff auch Kohlenmonoxid und Kohlenwasserstoffe umzusetzen. Unter den verschiedenen Arten von Brennstoffen wird Biogas als alternativer und umweltfreundlicher Brennstoff betrachtet. Biogas ist ein erneuerbarer Brennstoff, welcher durch anaerobe Vergärung von Biomasse gewonnen werden kann. Biogas enthält jedoch Verunreinigungen in Form von Schwefelwasserstoff H_2S und Chlorwasserstoff HCl in unterschiedlichen Konzentrationen, welche einen negativen Einfluss auf die Leistung und Haltbarkeit der SOFC und im Falle von H_2S auch auf den Katalysator des Reformers haben.

Um eine Leistungseinbuße, welche allgemein als Degradation bezeichnet wird, der SOFC zu vermeiden, muss das zugeführte Biogas gereinigt werden. Die dabei erforderlichen Reinheiten liegen für H_2S bei 2 *ppmv* und für HCl bei 10 *ppmv*. Je nach Ursprung des Biogases variieren die Verunreinigungen von H_2S im Bereich von 50 – 6800 *ppmv* und für HCl im Bereich von 0.1 – 25 *ppmv*. Eine Aufbereitung des Biogases zur Reduktion des H_2S und HCl Gehalts ist für den sicheren Betrieb einer SOFC somit unbedingt notwendig.

Für diese Aufgabe bieten sich unterschiedliche verfahrenstechnische Grundoperationen an. Die Operationen zur H_2S Abtrennung lassen sich in physikalisch-chemische Verfahren sowie biotechnologischen Verfahren unterteilen. Zu den physikalisch-chemischen Verfahren werden beispielsweise Adsorption und Absorption gezählt. Die wettbewerbsfähigste Technologie zur Entschwefelung in Anlagen der Leistungsklasse 1-10 kW_{el} ist die Adsorption, da sie einfach, effektiv und kostengünstig ist. Dabei kommen Aktivkohlen, Metalloxide und Zeolithe zum Einsatz. Die beim Einsatz der Adsorption auftretenden Fragen zum sicheren Betrieb eines mit Biogas betriebenen SOFC Systems sind jedoch umfangreich. Einerseits ist es notwendig

die Adsorbentien hinsichtlich ihrer Trennleistung bei unterschiedlichen Randbedingungen zu überprüfen, und zusätzlich müssen mögliche Querempfindlichkeiten gegenüber im Biogas vorhandenen Stoffen, wie beispielsweise NH_3, untersucht werden.

Der Fokus dieser Arbeit liegt auf der adsorptiven Abtrennung von H_2S , HCl und NH_3 aus Biogas. Für die Charakterisierung der Adsorbentien wurde zunächst auf Gasmischungen, bestehend aus dem zu adsorbierenden Schadstoff und Inertgas, zurückgegriffen. Anschließend wurde das Inertgas durch Methan CH_4 und Kohlendioxid CO_2 ersetzt, welche die Hauptbestandteile von Biogas darstellen. Dabei wurde gezeigt, dass die Gasreinigung mittels Adsorption die Schadstoffe aus dem Biogas ausreichend entfernt und somit ein sicherer Betrieb der SOFC gewährleistet werden kann. Die Variation unterschiedlicher Faktoren wie Konzentration an H_2S, Raumgeschwindigkeit, Temperatur und Feuchtegehalt runden die Experimente ab. Das dabei beobachtete Trennverhalten der unterschiedlichen Adsorbentien ermöglicht eine auf Biogas zugeschnittene Adsorberauslegung. Zur Vervollständigung des auf Biogas basierenden SOFC CCHP Gesamtkonzeptes wurden zusätzlich ein Katalysator zur Dampfreformierung und ein 10 Zellen SOFC Stack im Betrieb untersucht.

Die für den verfahrenstechnischen Systemaufbau erforderlichen Komponenten werden im Detail beschrieben und mögliche Optionen bei der Systemgestaltung werden erläutert. Die Auswertung dient zur Erarbeitung von Verbesserungspotenzialen auf Komponenten- und Systemebene, die in zukünftigen Produktentwicklungen zu berücksichtigen sind und in nachfolgenden Projekten zum Teil bereits aufgegriffen werden. Die gewonnenen Ergebnisse unterstreichen, dass mit Hilfe von adsorptiven Reinigungsschritten die Möglichkeit geschaffen wird Biogas soweit zu reinigen, dass es zum Betrieb eines SOFC basierten Kraft-Wärme-Kälte-Kopplung Systems genutzt werden kann.

Acknowledgments

The present thesis was made in the course of my work as a research assistant at the Institute of Thermal Engineering at the Graz University of Technology within the scope of the project "SOFCool" funded by the Austrian Research Promotion Agency FFG.

I would like to take this opportunity to thank Professor Christoph Hochenauer for his support. Especially, for the possibility to prepare this thesis and the optimal working environment provided to me within my work. With his broad knowledge in SOFCs and his motivational skills, he managed to push me forward even when I was dealing with slow progress or unsatisfactory results.

A cordial thank you is directed to Professor Matthäus Siebenhofer, Chair of Chemical Process Engineering at the Graz University of Technology for the critical examination of this work and the adoption of the second expert report.

I am also grateful to everyone in the Fuel Cell Department at AVL List GmbH in Graz, who brought their expert knowledge to numerous technical discussions. I want to express my special thanks to Dr. Martin Hauth, who played a decisive role in this research project. His expertise in SOFCs and biogas has greatly enriched and spurred this work. Thanks for the insightful discussions, the constructive comments and the warm encouragement.

Many colleagues contributed to the success of the project and, thus, to the prerequisites for this thesis. I would like to thank Raphael Neubauer, Moritz Husmann, Bernhard Stöckl, Michael Preininger and Christian Gaber for their cooperation.

Thanks to my colleague Christoph Schluckner for the numerous tips when dealing with LaTeX.

I would like to thank my parents and my family, whose motivation and financial support for my education allowed me do this thesis.

I am grateful to you, Simone. You have always supported me and tolerated my many absences. You have always cheered me up, brought me to other thoughts and again motivated me for my work.

Bärnbach, March 2019 Christof Weinländer

To my family.

Contents

List of Figures

List of Tables

Acronyms

ppmv	parts per million by volume
slpm	standard litre per minute
AC	absorption chiller
AD	anaerobic digestion
AFC	alkaline fuel cell
Al_2O_3	aluminium oxide
ATR	autothermal reforming
BET	Brunauer, Emmett and Teller
C	carbon
C_2H_4	ethylene
$C_2H_4O_2$	acetic acid
C_2H_6	ethane
C_2H_6O	ethanol
$C_3H_6O_2$	propionic acid
$C_3H_6O_3$	lactic acid
C_3H_7COOH	butyric acid
C_3H_7OH	propanol
$C_5H_{10}O_2$	valeric acid
$C_6H_{12}O_2$	capronic acid
C_6H_5Cl	chlorbenzene
CCHP	combined cooling heat and power
CFY	chromium iron yttrium
CH_3OH	methanol
CH_4	methane
$CHCl_3$	chloroform
CHO	carbon-hydrogen-oxygen
CHP	combined heat and power
Cl	chlorine
CO	carbon monoxide
Co	cobalt

CO_2	carbon dioxide
COD	chemical oxygen demand
COP	coefficient of performance
Cr_2O_3	chromia
Cr_2O_3	chromium oxide
Cu	copper
CuO	copper oxide
DR	dry-reforming
EDX	energy-dispersive X-ray spectroscopy
EU	European Union
F	fluorine
FC	fuel cell
Fe	iron
FE-SEM	field emission scanning electron microscope
FeO	iron oxide
GDC	gadolinium doped cerium
GHG	greenhouse gas
H_2	hydrogen
H_2CO_3	carbonic acid
H_2O	water
H_2S	hydrogen sulfide
HCl	hydrogen chloride
HF	hydrofluoric acid
HOB	heat only boiler house
HOR	hydrogen oxidation reaction
HPWS	high pressure water scrubbing
IKTS	Institute of Ceramic Technologies and Systems
IUPAC	International Union of Pure and Applied Chemistry
IWT	Institute of Thermal Engineering
K_2CO_3	potassium carbonate
K_2S	potassium sulfide
KCl	potassium chloride
$KHCO_3$	potassium bicarbonate
KHS	potassium hydrosulfide

KI	potassium iodide
KOH	potassium hydroxide
LaO	lanthanum oxide
LSM	lanthanum strontium manganite
LUB	length of unused bed
MCFC	molten carbonate fuel cell
MFC	mass flow controller
Mn	manganese
$MnCO_3$	manganese carbonate
MnO	manganese oxide
Mo	molybdenum
MTZ	mass transfer zone
N_2	nitrogen
NaCl	natrium chloride
NaOH	sodium hydroxide
NH_3	ammonia
NH_4Cl	ammonium chloride
Ni	nickel
Ni/GDC	nickel-gadolinium doped cerium oxide
Ni/YSZ	nickel-yttria stabilized zirconia
$NiCl_2$	nickel chloride
NiO	nickel oxide
NiO/YSZ	nickel oxide-yttria stabilized zirconia
NO_x	nitrogen oxides
O/C	oxygen to carbon
O_2	oxygen
OCV	open circuit voltage
ORR	oxygen reduction reaction
PAFC	phosphoric acid fuel cell
PID	proportional-integral-derivative
POX	partial oxidation
Pt	platinum
PTFE	polytetrafluoroethylene
Rh	rhodium
Ru	ruthenium

S/C	steam to carbon
SEM	scanning electron microscope
Si	silicia
SiO_2	silicon dioxide
Sn	tin
SO_2	sulfur dioxide
SO_x	sulfur oxides
SOFC	solid oxide fuel cell
SR	steam reforming
SRB	sulfate-reducing bacteria
TiO_2	titanium dioxide
TPB	triple phase boundary
WGSR	water-gas shift reaction
XRD	X-ray diffraction
YSZ	yttrium-stabilized zirconia
Zn	zinc
ZnO	zinc oxide

Symbols

Symbol	Description	Unit
BT	breakthrough time	h
b	parameter of the Langmuir equation	$1/bar$
Cl_{cap}	chloride capture capacity	mg/g
c_{HCl}	HCl concentration	mol/L
$c_{i,0}$	solute concentration of the feed	ppmv
c_i	inlet concentration	ppmv
c_o	outlet concentration	ppmv
η_{FU}	fuel utilization	%
ε	efficiency	%
F_A	solute feed rate	$g/(cm^2s)$
FR	gas flow rate	L/h
$\Delta_R G$	Gibbs enthalpy	J
$GHSV$	gas hourly space velocity	h^{-1}
k_H	parameter of the Henry equation	$1/bar$
k	parameter of the Freundlich equation	$1/bar^n$
LUB	length of unused bed	m
L	bed length	m
M	molar mass	g/mol
m_{sample}	sorbent weight	g
n	exponent of the Freundlich equation	–
ϕ_{H_2O}	relative humidity	%
p_0	vapor pressure	N/m^2
p_A	partial pressure adsorptive	N/m^2

Symbol	Description	Unit
p	total pressure	N/m^2
$P_{el_{SOFC}}$	electric power generated by the SOFC	W
$\dot{Q}_0$	rate of heat flow cooling capacity	W
$\dot{Q}_{eg}$	rate of heat flow exhaust gas	W
$\dot{Q}_{fg}$	rate of heat flow flue gas	W
$\dot{Q}_f$	rate of heat flow fuel	W
$\dot{Q}_{heat}$	rate of heat flow heat sink	W
$\dot{Q}_l$	rate of heat flow loss	W
$q_{i,b}$	adsorbent phase concentration of solute i at breaktpoint time	mg/g
$q_{i,sat}$	adsorbent phase concentration of solute i	mg/g
ρ_b	bulk density of the adsorbent	kg/m^3
S_{cap}	sulfur capture capacity	mg/g
$S_{removal}$	sulfur removal efficiency	%
t	time	h
t^*	ideal breakpoint time	h
t_b	breakpoint time	h
U_N	Nernst Voltage	V
U_{th}	theoretical cell voltage	V
V_{mol}	gas molar volume at standard conditions	L/mol
v	superficial velocity	m/s
X_E	equilibrium loading	kg/kg
X_{mon}	monomolecular loading	kg/kg

1

Introduction

This chapter is intended to provide a basic understanding of SOFC based CCHP systems operated with biogas and why upgrading biogas is essential. In the introduction, an overview of the alternatives for energy conversion and the associated effects on the climate will be given. Afterwards, the opportunities of the SOFC will be explained. The conclusion of this chapter provides the section which explains the motivation behind this work. In the process, the guiding ideas and the resulting scientific questions are derived from the sections described above. The scientific questions are answered in the respective chapter as well as in summary in the conclusion. This thesis focuses on upgrading biogas for the use in an SOFC CCHP with a power output of 7 kW_{el}. Different researchers indicated SOFCs as feasible core elements of CCHP systems [1–5]. The use of biogas as a fuel for the SOFC CCHP system provides an attractive solution to save CO_2 and simultaneously convert biogas into electricity, heat and cooling in a highly efficient manner. Figure 1.1 shows a flowsheet of a biogas operated SOFC CCHP system.

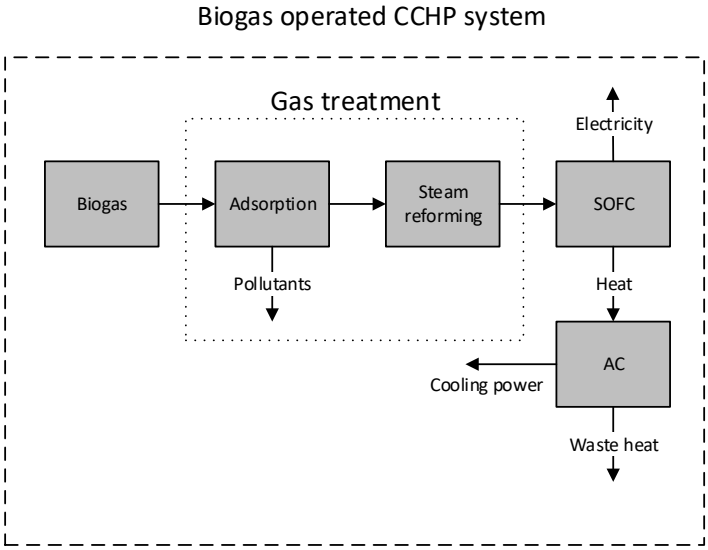

Figure 1.1: Flowsheet of a biogas operated SOFC CCHP system.

First, the biogas enters the gas treatment unit. Thereby, pollutants such as H_2S are separated by means of adsorption. Synthesis gas is produced in a SR from the purified gas. The synthesis gas is then fed to the SOFC where it is converted into electricity and heat. The resulting waste heat is used to operate the AC. Depending on the nature and origin of the biogas, sometimes very different compositions and accompanying substances result. This poses a challenge for the gas purification concept since ultimately it should be possible to operate a SOFC CCHP plant with a variety of different biogases. The adsorptive gas upgrading approach investigated in this work is a basic unit operation and is feasible with respect to the required biogas purities. In addition, the biogas upgrading through SR and the construction of a 10-cell SOFC stack is presented in this work. The AC shown in Figure 1.1 is not part of this work.

1.1 Energy transformation

In the last 50 years, global energy consumption has rapidly increased and is expected to continue to grow over the next 50 years [6, 7]. The use of energy is carried out in a chain of technical processes. On a large scale, primary energy is first converted into final energy (electricity, steam, hot water) in energy conversion plants. Subsequently, the energy is transported to the consumers via transport and distribution networks and finally transferred to useful energy (light, mechanical energy, room heat, process heat) at the point of use. For public and industrial power supply, the following three groups of energy conversion plants are generally distinguished:

- A heat only boiler house (HOB) is an energy conversion plant in which the primary energy used is exclusively converted into heat. The heat transfer medium is usually steam at various pressure levels, and for heating purposes, hot or warm water in industrial applications. District heating is typically supplied from a dedicated heating plant [8].
- A power station is an energy conversion plant in which the primary energy used is exclusively converted into electricity. A coal power station for example, burns coal in air and captures the heat released to generate steam for operating a steam turbine. The rotation of this steam turbine in turn drives a generator; the net result is electricity [9].
- A combined heat and power (CHP) plant is an energy conversion plant in which the primary energy used is being transformed into power (mechanical or electrical energy) and heat (cogeneration of heat and power) in a combined process. Heat from a CHP system can be provided in any number of useful forms. For example, from high pressure steam to low pressure hot water; as hot gas or heated air; and through the use of absorption or adsorption refrigeration processes as chilled water for low temperature refrigeration applications. CHP generation traditionally allows for higher energy performances than separate production of heat and electricity [10–12]

In addition to these known groups of energy conversion plants used in large and small scale, there is also the technology of CCHP systems which derived from CHP systems. CCHP

systems, including various technologies, provide an alternative to meet and solve energy-related problems, such as energy shortages, energy supply security, emission control, and the economy and conservation of energy. Supplementary to providing energy, heating and cooling power, the high efficiency is a great advantage of CCHP technology [13, 14].

The comparison in Figure 1.2 illustrates the high efficiency of CCHP systems. The overall efficiency of a power plant, transmission and distribution grid is assumed to be 30%. Heating is provided by a boiler with the effectiveness ε of 80%, and cooling is provided by an absorption chiller with a coefficient of performance (COP) of 0.7. In the CCHP unit, however, electricity is provided by the prime mover. Heating is prepared by recovering the waste heat, and cooling is produced by using the recovered heat in the AC. Figure 1.2 shows that to provide the same demands, the CCHP overall efficiency can be as much as 30% higher than the efficiency of the combination of power plant, boiler and AC. In addition, the CCHP consumes 37.76% less fuel ((131.75+56.25+45 units of prime energy) : 145 units of prime energy). This higher efficiency means considerable fuel savings and pollution reduction, leading to a more economically efficient system [14].

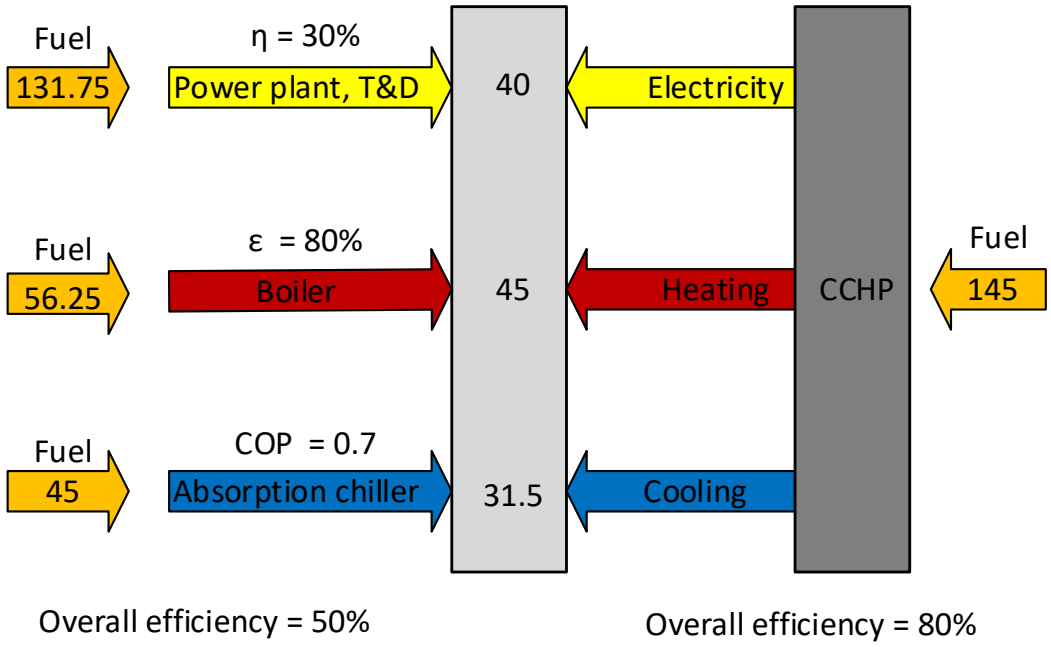

Figure 1.2: Comparison between power plant, boiler and AC versus CCHP system [14].

A typical CCHP system is shown in Figure 1.3. It consists of a turbine, a generator and an AC. The turbine is operated with natural gas and the mechanical energy is further converted into electricity power by the generator. Furthermore the AC utilizes exhaust gas and jacket water from the turbine to generate heating power in winter and cooling power in summer. If

waste heat from the turbine is insufficient, a combustor in the AC can burn natural gas as a supplement. Thus, the energy demands of cooling, heating and electrical power in a building or a district can be met by this system simultaneously [13].

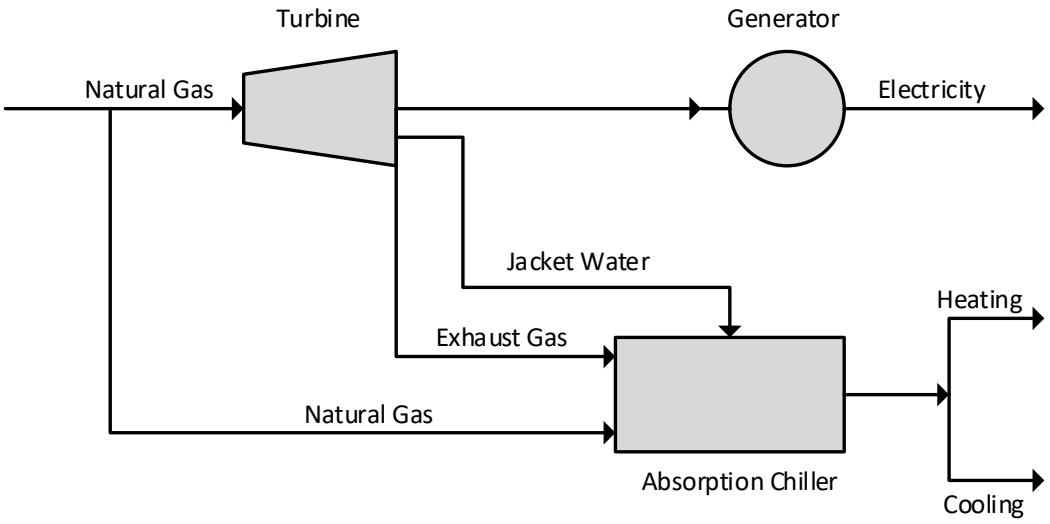

Figure 1.3: Typical CCHP process [13].

Following the successful development of the CCHP systems, the research on SOFC based CCHP has been attractively increasing. SOFC CCHP can be used optimally anywhere in industry and commerce, when in addition to the power requirement process, energy for heating heat and cooling is required. The system is able to generate electricity, and energy for heating and cooling within certain limits. In addition, the high electrical (>50%) and overall efficiency (>90%) allows to save operating costs while reducing greenhouse gas (GHG) emissions. Together with the local power grid, this solution provides additional security of supply for companies with critical processes. Furthermore, significantly less pollutants than in comparable applications (for example, combustion engines) are emitted. An important factor in this context is the almost noiseless generation of useful energy. This minimizes the environmental impact of industrial residential areas [1].

1.2 Climate issues

When burning fuels pollutant, emissions arise mainly in the form of particulate matter, sulfur dioxide (SO_2), nitrogen oxides (NO_x) and CO. In addition, combustion of carbon contained in fuels forms CO_2. While this is not a pollutant, it does have a negative impact on the climate. The worldwide increase of CO_2 in the atmosphere has increasingly attracted attention in connection with the greenhouse effect. The current atmosphere contains a volume fraction of

approximately 380 *ppmv* CO_2. In 1900, this concentration was only 290 *ppmv*. The increase in average CO_2 concentration in the atmosphere is said to have been caused by the industrial revolution, e.g. the burning of fossil fuels. CO_2 in the atmosphere is similar to the glazing of a greenhouse: the CO_2 lets the short-wave solar radiation pass through, but reflects the long-wave heat radiated from the earth and, thereby, increases the average temperature in the lower atmosphere [15]. On 12 December 2015, the international community passed the Paris Climate Agreement, which came into force on 4 October 2016. The goal is to get the man-made climate change under control to keep the future increase in average global temperature well below 2 °C. Climate change is driven by the emission of GHGs. The most important source of GHG emissions is, both globally and in Europe, the use of fossil fuels. The objectieves of the Paris Agreement can be achieved by a major exit of the use of fossil fuels by the middle of the century [16]. Figure 1.4 displays the temperature deviation from average for land and ocean between January and December 2017. In summary, it can be said that the 2017 average global temperature across land and ocean surface areas was 0.84 °C above the 20th century average of 13.9 °C. 2017 also marks the 41st consecutive year since 1977 with global land and ocean temperatures at least nominally above the 20th century average, with the six warmest years on record occurring since 2010. The annual global land and ocean temperature has increased at an average rate of 0.07 °C per decade since 1880, however, the average rate of increase is twice as great since 1980. From 1900 to 1980 a new temperature record was set on average every 13.5 years, however, since 1981 the rate has increased to every 3 years [17].

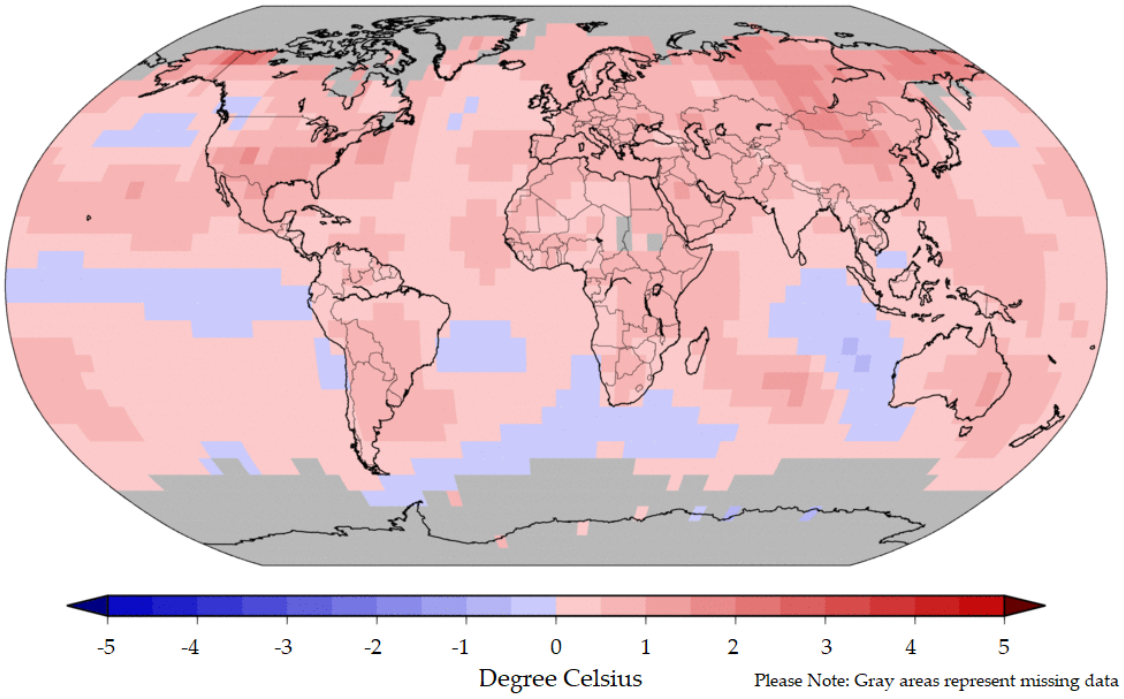

Figure 1.4: Land and ocean temperature deviation from average in 2017 [17].

In Austria, the temperature increase in the past has more than doubled compared to the global average. After three years of extremely mild winters, the winter 2016/2017, despite a very cold

January, was still around 0.5 °C warmer than the annual mean temperature. Climate models predict that the temperature in Austria or the Alpine region will continue to rise stronger than the global average in future. Climate change leads to economic consequences for tourism, agriculture, forestry, energy and the health service. Furthermore, migratory pressure from southern countries, which are particularly affected by climate change (e.g. Africa), will increase [16].

1.3 Opportunities of the SOFC

Due to its fuel flexibility, the SOFC tends to become a short-term usable and highly efficient technology for energy conversion. Not restricted by the Carnot cycle, SOFC has a high energy conversion efficiency up to 60%, and it is very suitable for distributed generation systems and has a broad application prospect. A SOFC makes it possible to produce electricity with high efficiency from natural gas, biogas, methanol (CH_3OH), NH_3 and gases from the reforming of all current fossil fuels. With advances in technology development, the SOFC could become the next generation of decentralized technology of the future because these FCs provide many advantages over traditional energy conversion systems including high efficiency, reliability, modularity, fuel adaptability, and very low levels of sulfur oxides (SO_x) and NO_x emissions. The quiet, vibration-free operation of SOFCs also eliminates noise, usually associated with conventional power generation systems. Due to their high operation temperatures, some hydrocarbon fuels (e.g. natural gas) can be reformed within narrow limits inside the cell stack without the requirement for an expensive, external reformer [18, 19]. In addition to all these advantages, it is essential to optimize the investment cost and long-term stability of SOFC systems in order to enable market entry [20–23].

Over the past few years about 40,000 SOFC-based CHP systems have been installed in Japanese homes under the Ene-Farm programme to provide electricity and hot water. These systems operate on natural gas and provide an electric conversion efficiency of about 45-50% [24]. The Australian company Ceramic Fuel Cells, Ltd. produced CHP systems called BlueGEN and tested them in Australia, New Zealand and Europe [25]. In 2015, Ceramic Fuel Cells, Ltd. was taken over by SOLIDpower. At the beginning of 2016, the first systems were delivered to end customers in Europe. The manufacturer advertises the system with an electrical efficiency of 60%, a thermal efficiency of 25% and an annual electricity production of up to 13,000 *kWh* [26]. Another important player in the fuel cell market is Bloom Energy Corporation. Bloom Energy is manufacturing and installing large scale stationary power units in the 100-200 *kW* range and is the largest manufacturer of SOFC units with over 75 *MW* of generation capacity [27].

1.4 Motivation and objectives of the work

The advantages of a SOFC CCHP system in terms of efficiency and CO_2 savings have already been explained in the previous sections. Modern power plants for generating electricity and heat are subject to two basic requirements in the long term. On the one hand, the primary energy source must be largely renewable in terms of sustainability and, on the other hand, the overall efficiency of such systems must be as high as possible over the year. Only a high overall efficiency at nominal load is no longer sufficient nowadays. If these two requirements are met, the efficiency of the plant can be significantly increased and, as a result, CO_2 emissions can be reduced. This, in turn, offers an economic potential for low energy costs, especially if, in a fair comparison with conventional power plants, the costs incurred there would be included due to environmental pollution. Explained in numbers, SOFCs can reach electrical efficiencies above 60% and SOFC CCHP systems can obtain overall efficiencies over 80% [20, 28].

A flow chart of the SOFC CCHP system discussed in this thesis is shown in Figure 1.5. $\dot{Q}_f$, the heat rate flow fuel, or in other words the upgraded biogas is passed into the SOFC and transformed into $P_{el_{SOFC}}$ (electrical power). The rate of heat flows $\dot{Q}_{fg}$, flow flue gas and $\dot{Q}_l$, flow loss leave the SOFC. The temperature level of $\dot{Q}_{fg}$, which is fed into the AC, is around 300 °C, which is a very favorable range for thermally driven ACs. In the AC, $\dot{Q}_{fg}$ is transformed into $\dot{Q}_{eg}$, $\dot{Q}_0$ and $\dot{Q}_{heat}$ - the rates of heat flow exhaust gas, cooling capacity and heat sink.

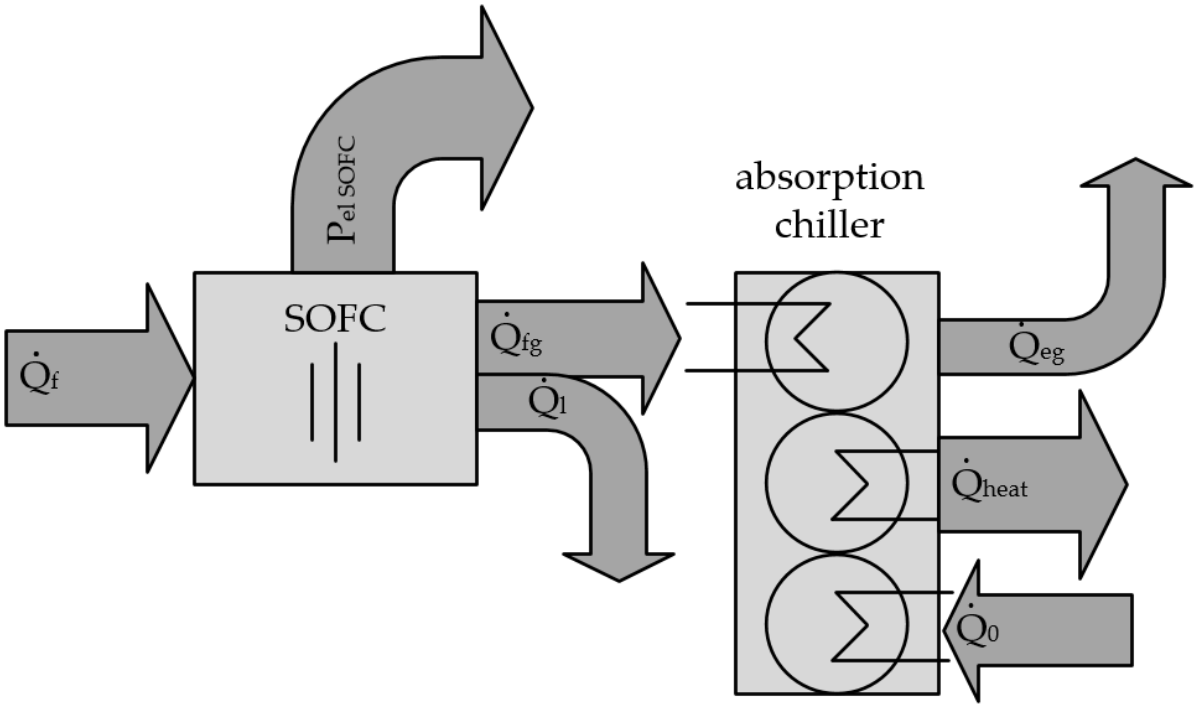

Figure 1.5: SOFCool SOFC CCHP flowsheet.

The basis of this work results from the requirements of the SOFC when operating with biogas. It has been repeatedly reported that even a few *ppmv* of H_2S is adsorbed on the nickel (Ni) of the SOFC anode, covering the active sites, inhibiting the fuel adsorption and leading to the reduction of fuel oxidation and cell performance. Blesznowski et al. recently studied anode Ni/YSZ supported SOFCs and claimed that H_2S up to 1 *ppmv* has negligible effect while 2 *ppmv* at the same conditions exhibited significant voltage decline in 200 *h* operation [29–32]. Another critical component in biogas with respect to SOFCs is HCl. As regard to the influence of HCl on SOFC, it may attack the Ni of the anode resulting in cell degradation. Trembly et al. studied electrolyte supported SOFCs at 800 °C with Ni/YSZ as current collection layer and nickel-gadolinium doped cerium oxide (Ni/GDC) anode interlayer. They found 17% and 26% performance loss in 100 *h* due to the presence of 20 *ppmv* and 160 *ppmv* HCl respectively in the feed [32, 33]. The choice of a suitable gas purification concept is hampered by the strong variation of biogas in terms of composition and proportion of pollutants. For example, H_2S concentrations vary from 50 to 6800 *ppmv* depending on the source of the biogas. A similar situation arises for HCl, in which case the content varies from 0.1 to 25 *ppmv* [34].

From this point of view, the following research questions arose in the context of this work:

1. What are the limits of SOFCs with respect to H_2S and HCl load in the feed gas? What is the cause of carbon deposits and how can they be prevented? How much does the concentration of H_2S and HCl vary in biogases?

2. Which gas upgrading operation is suitable for the specific requirements of a small scale (7 kW_{el}) SOFC CCHP system?

3. How is the operation of H_2S and HCl removal influenced by different parameters like temperature, $GHSV$, pollutant inlet concentration and biogas composition?

4. Is a successful commissioning of the subsystems (gas purification, steam reforming and 10-cell stack) possible? This forms the basis for future work and a possible coupling of the systems.

5. What is the service interval of this biogas upgrade approach?

This thesis is basically structured according to the order of questions given above. Chapter 2 provides more information to characterize the questions given above in more details. This includes the characterization of SOFC operating limits with respect to H_2S and HCl concentration as well as the characterization of biogases and the cause of carbon depositions, which answers question 1. Chapter 2 also provides an answer to research question 2 about suitable H_2S and HCl removing processes. Suitable means operations which comply with the strict tolerances for SOFC operation with respect to H_2S and HCl. In addition Chapter 2 provides

the theoretical fundamentals for answering research question 3.

Chapter 3 focuses on the experimental part. It describes the structure of the individual test rigs and discusses the results obtained. The focus is on extensive experiments which are necessary to answer research question 3. This includes investigations in terms of the influence of operating temperature, $GHSV$, pollutant inlet concentration and biogas composition. In addition, the commissioning of the SR test rig and the 10-cell SOFC stack will be described and the results obtained will be discussed. Thus, research question 4 is answered.

This thesis further includes Chapter 4 where the new findings and results were used for a basic design of a gas purification unit for a 7 kW_{el} SOFC CCHP. This chapter should outline the suitability for biogas purification of the identified concept and answer research question 5.

Chapter 5 gives a summary and conclusion of all findings and provides the possible answers to the research questions in a condensed form. Due to the extensive subject matter and the divergent topics, this project was edited by two PhD students. The AC shown on the right-hand side in Figure 1.5, including all the necessary peripherals, was investigated by Johannes Albert in a separate thesis. The research concerning the FC, the gas purification and the reforming was subject of this doctoral thesis.

2

Fundamentals

This chapter is intended to provide more fundamental information about SOFCs and their operating limits with respect to H_2S and HCl load of the feed gas. Furthermore, the fundamentals regarding SR and the effect of carbon formations are explained. In addition, this chapter gives an overview about suitable gas cleaning options and, thus, provides answers to the following research questions, which are stated in section 1.4:

- What are the limits of SOFCs with respect to H_2S and HCl load in the feed gas? What is the cause of carbon deposits and how can they be prevented? How much does the concentration of H_2S and HCl vary in biogases?

- Which gas upgrading operation is suitable for the specific requirements of a small scale ($7\ kW_{el}$) SOFC CCHP system?

2.1 SOFC

2.1.1 Operating principle

The operating principle of a SOFC is shown in Figure 2.1. The description of the basics is done with the help of [35–37]. The SOFC is an electrochemical energy converter that converts the chemical energy of fuels directly into electricity at operating temperatures between 750 and 900 °C. In comparison to the heat engine, the conversion takes place at a higher theoretical efficiency according to the Carnot cycle. Due to the absence of temperature cycling, FCs do not follow the Carnot cycle, and therefore not limited by the Carnot efficiency. It is a galvanic element and its basic structure consists of an anode and a cathode separated by a gas-tight, electrically non-conductive, ion-permeable electrolyte layer. The anode and the cathode are continuously fed with the reactants to be converted into electrical energy. The resulting reaction products are discharged at the same rate.

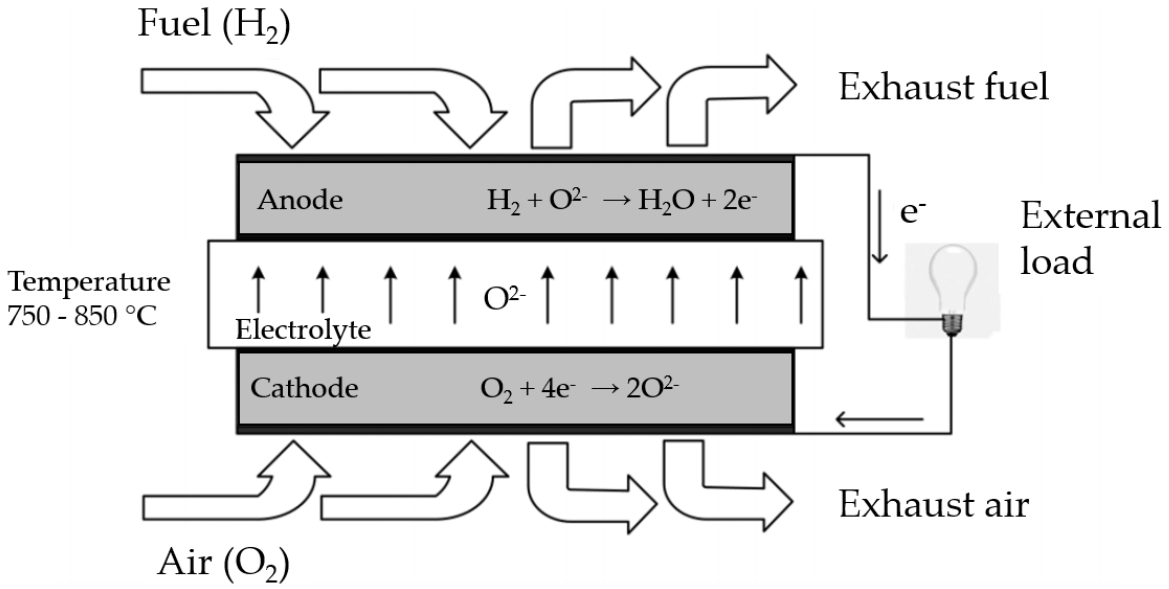

Figure 2.1: Schematic of a SOFC operating with H_2 as fuel [36].

The electrolyte is made from a ceramic such as yttrium-stabilized zirconia (YSZ) which acts as a conductor of oxide ions at temperatures from 650 to 750 °C. This ceramic material allows oxygen atoms to be reduced on its porous cathode surface by electrons, thus, being converted into oxide ions, which are then transported through the ceramic body to a fuel-rich porous anode zone where the oxide ions can react, e.g. with H_2, giving up electrons to an external circuit.

At the cathode, oxygen (O_2) molecules from the air are reduced by receiving four electrons from the external electrical circuit, leading to the formation of two oxygen ions. This reaction is called the ORR, (Equation 2.1), and is the rate limiting step in the cell electrochemistry [38].

$$O_2 + 4e^- \rightharpoonup 2O^{2-} \tag{2.1}$$

The ORR contains three steps: First, the O_2 molecule is adsorbed onto the surface, where it then dissociates. Secondly, the dissociated O_2 molecule then diffuses from the surface to the triple phase boundary (TPB). Finally, the oxygen ion is formed from the electron transfer and diffuses into the electrolyte. The process is shown in Figure 2.2.

The electrons in the external circuit stem from the oxidation reaction of H_2, CO_2 or CH_4 and other hydrogen rich hydrocarbon gases at the anode. This reaction is called the hydrogen oxidation reaction (HOR) which is shown in Equation 2.2.

$$2H_2 + 2O^{2-} \rightharpoonup 2H_2O + 4e^- \tag{2.2}$$

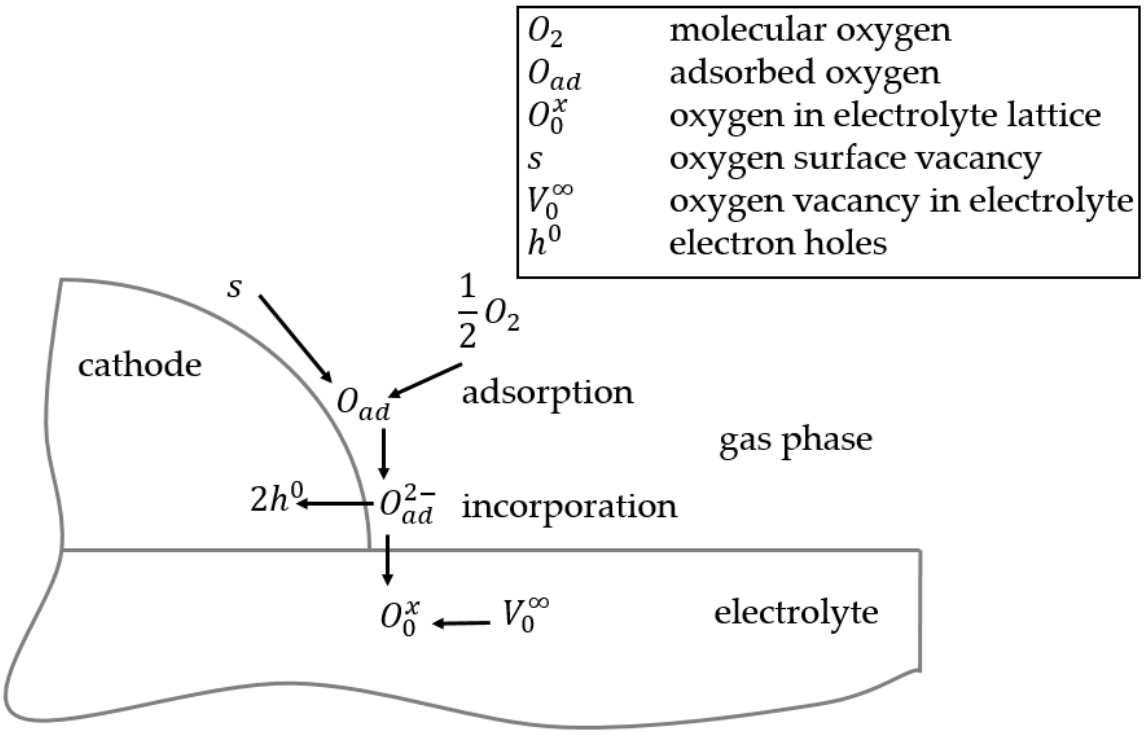

Figure 2.2: The ORR reaction [35].

Combining the previous two half-cell reactions (ORR and HOR) into an overall reaction for the SOFCs results in the electrochemical reaction given by Equation 2.3. At the boundary between the electrolyte and the anode, when H_2 is utilized as fuel, the H_2 atoms react with the O^{2-} which have passed through the electrolyte, forming water (H_2O), and releasing electrons which are gathered into the external circuit.

$$2H_2 + O_2 \rightharpoonup 2H_2O \tag{2.3}$$

An overview of the advantages and disadvantages of SOFCs is shown in Table 2.1.

Fuel flexibility is one of the key aspects that may allow SOFCs to penetrate the market of small and medium sized electricity generators and / or CCHP systems. SOFCs compared to other FC technologies have the great potential of fuel flexibility especially with regard to fuels derived from biomass [39, 40]. Since SOFCs are operated at high temperature, expensive catalysts such as platinum (Pt) or ruthenium (Ru) can be avoided completely [41, 42]. Another advantage of SOFCs is the solid electrolyte compared to other FCs that use a liquid electrolyte like thealkaline fuel cell (AFC), the phosphoric acid fuel cell (PAFC) or the molten carbonate fuel cell (MCFC). The solid electrolyte has the advantage, as opposed to those of a liquid type, that the FC is able to operate in any spatial position [43, 44]. Another advantage of SOFCs is the high temperature of the waste heat. The integration of the SOFC into a CHP or CCHP system enables total efficiencies >90% [45–47].

Table 2.1: SOFC advantages and disadvantages [37].

Advantages	**Disadvantages**
Fuel flexibility	Significant high-temperature materials issues
Non-precious metal catalyst	Sealing issues
Solid electrolyte	Relatively expensive components/fabrication
High-quality waste heat for cogeneration applications	

On the other hand, there are obviously also disadvantages which should be mentioned at this point. A critical cost factor arises from the very high temperature at which present SOFCs must operate. This results in material issues such as thermal stress and limited material flexibility. Much of the current research is focused on developing SOFC materials for use at 700 °C, which aims at making alternative materials available to significantly reduce cost [48, 49]. Another major challenge is the development of suitable sealants for SOFCs. Such sealants must withstand harsh conditions. They must be inert at the high operating temperatures that SOFCs require for operation (i.e., resistant to environments composed of oxidative and reducing gases) as well as thermo-chemically and thermo-mechanically compatible with the materials with which they are in contact [50, 51]. Another issue that remains to be solved relates to the application-related prices of SOFCs. Applications in CHP demand lower prices. Kendall suggests around $5,000 per kW as a barrier for market entry [52].

2.1.2 Designs

Generally, there are four different types of cell designs in operation:

- cathode supported,
- electrolyte supported,
- anode supported and
- externally supported designs shown in Figure 2.3

In each of the designs, one cell component is usually thicker by about 1–5 mm than other components in order to provide mechanical support to the cell. In order to increase the mechanical strength and the cell performance, the thickness of the different components of the cell other than the support materials is in the range of 5–50 μm. The mechanical strength of the cell can be increased by reducing the cracks or the porosity and the thermo-mechanical stress

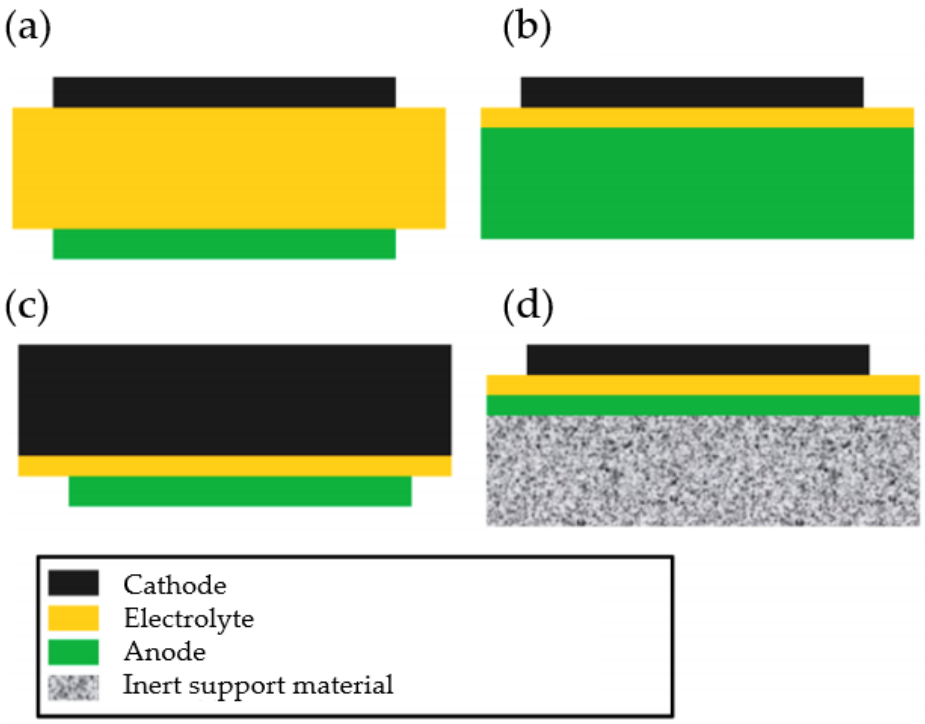

Figure 2.3: Different types of fuel cell design: (a) electrolyte; (b) anode; (c) cathode and (d) metal or ceramic supported [25].

that develops due to mismatched thermal expansion coefficient of the different components of the cell [53–56].

The most commonly used design, as well as the design of the cells used in this work, is the electrolyte supported fuel cell. The advantages over the other designs lie in mechanical strength and fabrication simplicity. The thickness of the non-porous electrolyte is in the range of 50–500 μm. The electrodes are deposited on either side by wet methods like dip coating or screen printing. The disadvantage of this type of design is the reduced overall performance due to thicker electrolyte layer required for mechanical strength of the cell [25, 53].

Comparatively, there has been little attention paid to the cathode-supported SOFC. The reason behind this are the high costs which incur through the use of rare earths, i.e. lanthanum oxide (LaO). Furthermore, cost of support structures developed with lanthanum strontium manganite (LSM), due to its low mechanical strength and high density, resulted in extremely high manufacturing cost. Another disadvantage is that LaO reacts with zirconia at the temperatures that are required for ceramic processing [25, 35]. In order to avoid high temperature processing routes, temperature processing techniques like vapor deposition is used, but it increases the manufacturing cost [57]. This design was abandoned in early 2000 due to high cost of support materials and high manufacturing cost [58].

FC designs based on anode support, especially nickel oxide-yttria stabilized zirconia (NiO/YSZ) cermets, are extremely popular because of their high strength, ease in fabrication and their high electrical conductivity with small ohmic losses. However, high thermal expansion of nickel

oxide (NiO) as compared to zirconia and large change in volume due to reduction of the anode material during cell operation makes it prone to electrolyte cracking. The problem of electrolyte cracking can be sorted out by controlling the thickness of the electrolyte, the microstructure support and by carefully selecting the content of NiO in the composition of NiO/YSZ [35, 55, 59, 60].

The supported cell designs are further split into two sub categories, namely ceramic and metal supported designs. Ceramic support materials are usually preferred for the ceramic based fuel cell due to their inertness and low thermal expansion coefficient. The cathode degradation is limited due to reduced use of high chromium concent in high temperature alloys [61]. These cells are generally considered not to be suitable for systems that undergo fast and continuous thermal cycles due to their high stiffness and lower toughness [25, 35, 55].

Cell designs based on metal support are difficult to manufacture since metal cannot be heated to the high temperature which is normally required for processing of ceramic components. Besides that, high temperature metal alloys are chemically unstable in the cathode's oxidizing environment, which results in the reduction of the cell's lifetime. Apart from these problems, it is a very attractive design due to its very high electrical conductivity, high strength and excellent resistance to thermal shock [35, 55, 59].

2.1.3 Electrolyte

The electrolyte for a SOFC must meet a very exacting combination of electrical, chemical and mechanical requirements in order to be suitable for practical application. It has to be stable in both reducing (fuel side) and oxidizing (air side) environments, and must have sufficiently high ionic conductivity with low electronic conductivity at the cell operating temperature. At 650-750 °C, the electrolyte becomes conductive for oxygen ions. Furthermore, it must be able to form the material into a thin, strong gas-tight layer [52].

Electrode porosity is required for gaseous diffusion between the electrode's outer surface and the electrode/electrolyte interface. The electrolyte is a thin, fully dense oxygen ion conductor, but not an electronic conductor. The electrolyte needs to be fully dense to prevent gaseous fuel from contacting air and burning. Typical electrolyte materials for SOFCs are oxides with low valence element substitutions, which create oxygen vacancies through charge compensation. There are various materials that have been explored as possible electrolytes for SOFC applications. YSZ and gadolinium doped cerium (GDC) are the most common materials used for the oxide conducting electrolyte [62]. A more detailed description of the materials used for electrolytes can be found in the literature [35, 37]. Currently, YSZ (3, 8, or 10% yttria, abbreviated to YSZ) is the most commonly used electrolyte for SOFCs. It provides high conductivity at temperatures above 700 °C, while exhibiting negligible electronic conductivity at these temperatures [63].

2.1.4 Anode

The basic requirement of an anode (i.e. fuel oxidation electrode) is to provide sufficient active sites for the oxidation of the fuel under operating conditions. The simplest oxidation reaction at an anode is:

$$H_{2(g)} \rightharpoonup 2H^{+}_{(i)} + 2e^{-} \tag{2.4}$$

Equation 2.4 illustrates that three phases are required to meet in one place to produce a working anode. The gas-phase H_2, a phase to carry the H^+ ions from the electrolyte and a phase to carry electrons to the circuit. For a SOFC, this means a porous anode is made of ionic and electronic conductors. The ionic and electronic conductivity can be from a single phase or from a composite of an ionic conducting phase and an electronic conducting phase. This intersection of three phases is called TPB. It is the critical part of the anode and needs careful microstructural engineering to give good performance [52, 62, 64, 65].

The most important feature of an anode material is to have adequate electronic conductivity to produce a low enough resistance to get the electrons out of the cell. Usually, for good performance, the total sheet resistance of a component in a SOFC is less than 0.15 $\Omega\ cm^{-2}$ [66]. This value includes electronic, ionic and chemical resistances. The anode must also be physically and chemically compatible with the other components of the cell, especially the electrolyte. The thermal expansion of the anode must match that of the other cell components, with no phase changes of significant volume difference, which would otherwise cause cracking of the cell on thermal cycling [52, 67, 68].

The catalytic properties of the anode in a SOFC are very important in determining the overall cell performance. Usually, the catalyst is part of the anode, and the high temperature provides sufficient kinetics. If one of the more commonly available hydrocarbon fuels, i.e. CH_4, is to be used in a fuel cell, then the catalyst requirements are more complicated. To use a hydrocarbon directly in a fuel cell, the anode catalyst must be able to oxidise the hydrocarbons, sometimes without the need of water or reforming (Equation 2.5) [52, 69].

$$CH_{4(g)} + 4O^{2-}_{(i)} \rightharpoonup CO_{2(g)} + 2H_2O_{(g)} + 8e^{-} \tag{2.5}$$

This reaction is kinetically slow and, therefore, the hydrocarbons are typically reformed to form smaller molecules, ideally CO and H_2 and the anode only needs to oxidise these species. The reforming can be done externally or via internal reforming in the cells themselves. The hydrocarbons are typically not only reformed with steam (Equation 2.6), but can also be reformed with small amounts of O_2/air.

$$CH_{4(g)} + H_2O_{(g)} \rightharpoonup CO_{(g)} + 3H_{2(g)} \tag{2.6}$$

Equation 2.6 is endothermic and forms a good synergy to use the waste heat from the FC to drive the gas reforming. Both the CO and H_2 produced from reforming can be used in a SOFC (unlike low-temperature fuel cells), but the anode needs to catalyse the oxidation of both, H_2 to H_2O (Equation 2.7) and CO to CO_2 (Equation 2.8) [52].

$$H_{2(g)} + O^{2-}_{(i)} \rightharpoonup H_2O_{(g)} + 2e^- \tag{2.7}$$

$$CO_{(g)} + O^{2-}_{(i)} \rightharpoonup CO_{2(g)} + 2e^- \tag{2.8}$$

The kinetics according to Equation 2.8 are typically more sluggish than the hydrogen oxidation reaction (Equation 2.7). In a lot of cases this reaction is bypassed by the faster gas-phase water-gas shift reaction (WGSR) (Equation 2.9), reacting the CO with water, from feed or hydrogen oxidation, to form more H_2 which is then utilised by the faster hydrogen oxidation reaction [52, 70].

$$CO_{(g)} + H_2O_{(g)} \rightharpoonup CO_{2(g)} + H_{2(g)} \tag{2.9}$$

In practice, hydrocarbon fuels are normally introduced with extra water, usually with a minimum S/C ratio of 2, over a SR catalyst where reactions according to Equations 2.6 and 2.9 take place [52, 71].The reforming reactions compete with the cracking and Boudouard reactions, according to Equations 2.10 and 2.11, respectively.

$$CH_{4(g)} \rightharpoonup C_{(s)} + 2H_{2(g)} \tag{2.10}$$

$$2CO_{(g)} \rightharpoonup CO_{(g)} + C_{(s)} \tag{2.11}$$

This formation of solid carbon (C) can quickly block pipes and destroy an anode by filling up the pores and breaking up the structure of the anode. This is a particular problem for Ni-based anodes. External reforming (e.g. SR), in a dedicated external unit, can allow better control of the reforming process. These external reformers also allow the careful management of the S/C ratio in order to ensure no carbon formation anywhere in the system [72]. Sulfur compounds, mainly H_2S, are present in biogas at significant levels. H_2S will react with the electrode surface even at *ppmv* levels and result in blocked reactions required for both SR and fuel oxidation, thus, severely degrading Ni-catalyst performance [73]. Besides H_2S, HCl which is also present in biogas at significant concentrations, is a problematic component that has a negative influence on the SOFC performance [32]. The influence of H_2S and HCl is investigated in detail in Section 2.3. Furthermore, the concentration range of these substances in biogas is discussed in Section 2.4.

2.1.5 Cathode

In FCs, the O_2 dissociation reaction generally requires a large overpotential and causes the major loss in efficiency. The high operating temperature of the SOFC helps the electrode reaction to proceed without precious metal catalysis. This, however, does not mean that any material can be used as the cathode. Properties required for cathode materials are:

- High electronic conductivity,
- high catalytic activity,
- mechanical stability and compatibility with different cell components, and
- chemical stability and compatibility with different cell components [52].

Understanding of mechanical behavior of the cathode materials has developed strongly in the last decade [74]. The most commonly used cathode material is $(La_{0.84}Sr_{0.16})\ MnO_3$ [75–77]. Generally, the SOFC cathode plays a crucial role and determines the overall cell output performance. Corrosion and poisoning effects caused by external contaminants should be taken into account for the cathodes because ambient air is continuously supplied directly to the cathodes during operations. For example, the cathode is always subject to corrosion caused by CO_2 and humidity in air during cell storage and working condition which can lead to the delamination of the cathode from the electrolyte [78–81]. Furthermore, silicia (Si) is one of the typical contaminants from the sealing materials. The presence of Si has been reported to poison the cathode through the Si species reacting with the cathode and, thus, reducing the surface exchange reactions [82–84].

Another issue regarding SOFC cathodes is chromium oxide (Cr_2O_3) poisoning. The cathode needs to be compatible with the electrolyte and interconnect the layer arranged between each individual cell in a stack. The interconnects' purpose is to connect each cell in series, so that the electricity each cell generates can be combined. There are many alloys that have been investigated as metallic interconnects, but almost all of them contain Cr_2O_3 as a protective oxide scale [85].

To minimize Cr_2O_3 poisoning, several approaches have been tried. One approach to mitigate the effect of Cr_2O_3 poisoning, is coating the surface of the interconnects for less Cr_2O_3 vaporization. Wang et al. performed experiments with $CuMn_{1.8}O_4$ spinel coating and observed improvement in cell performance and significantly less Cr_2O_3 depositions near the cathode/electrolyte interface [86].

2.1.6 Cell losses

During operation of SOFCs (under electrical load), the cell voltage depends on the operating conditions. Figure 2.4 shows the qualitative relationship between cell voltage and current as a current-voltage characteristic (UI characteristic curve).

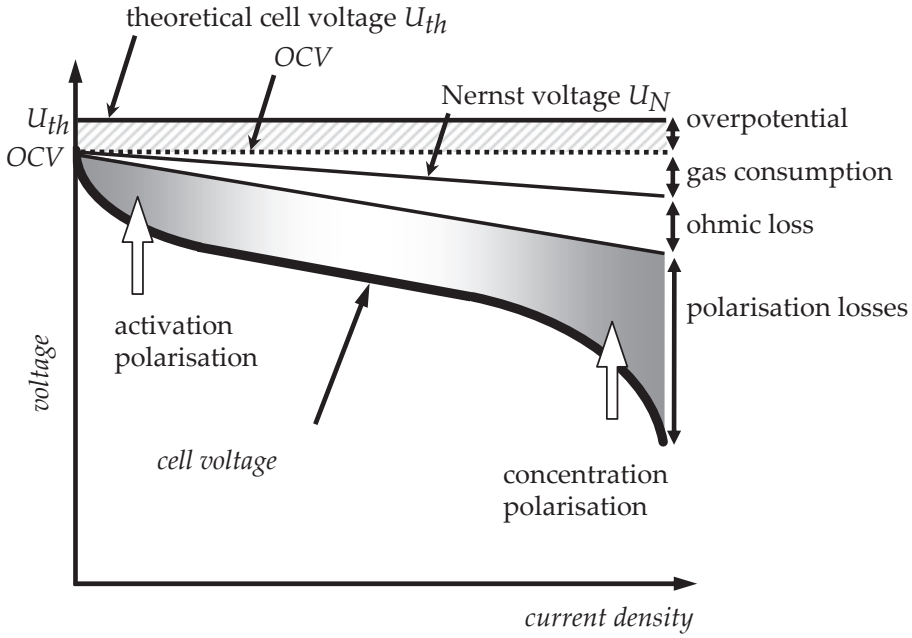

Figure 2.4: Principle course of the cell voltage at electrical stress. The current-voltage (UI) characteristic shows the dependence of the working voltage on the current density [52].

It can be seen from the diagram that the open circuit voltage (OCV) is already below U_{th} (theoretical cell voltage) in real operation. This is due to effects such as weakness, or problems in the measurement setup or in the electrolyte. As a result, small amounts of fuel gas can be converted directly. But even a small electronic residual conductivity of the electrolyte can lead to a high-impedance internal short circuit. This can already load the cell electrically, without an externally measurable current flow. The difference between OCV and U_{th} is called overpotential. If the cell is electrically charged so that electrons flow over the external circuit, further losses occur [35, 52]:

- Gas consumption: The charge transport, coupled with the partial reactions, causes a further increase in the H_2O partial pressure at the anode and a lowering of the O_2 partial pressure at the cathode. This effect, referred to as gas consumption, reduces the U_N (Nernst voltage) at the respective operating point of the cell as the current density increases [52].
- Ohmic losses: With the outer charge transport, an internal O_2^- diffusion current passes through the electrolytes and an electron current through the electrodes. The current causes a voltage drop as a function of the conductivity of the material flowed through and an ohmic resistance results [35].
- Polarisation losses: The charge transport occurs through O_2^- diffusion and causes further losses, which reduce the voltage at the operating point. The nonlinear losses are due to the diffusion in the porous electrodes and the electrochemical reaction in the active regions of the electrode. These non-linear and current-density-dependent losses are referred to as

polarization losses [35].

- Activation polarization: The installation and removal of O_2^- ions as well as the associated electrochemical partial reactions are lossy. The losses caused by the electrochemical processes are summarized under activation polarization.
- Concentration polarisation: With increasing current density and thus increasing demand of educts (O_2 respectively H_2), they must migrate from the gas space through the porous electrode to the TPB. On the anode side, the removal of the product (H_2O) is also required. Since the mass transfer (gas diffusion) by the porous electrodes does not proceed infinitely fast and lossless, the partial pressure at the TPB decreases and leads to the depletion of the educts or the enrichment of the products.

2.2 Mk 351 stack

The 10 cell SOFC-stacks type Mk 351 used in this thesis were provided by the Fraunhofer Institute of Ceramic Technologies and Systems (IKTS). Their assembly is presented in Figure 2.5. The cells were electrolyte supported planar cells with 127 cm^2 active area (110 * 115 mm^2). The electrolyte is made of 10Sc1CeSZ. This substrate has a high ionic conductivity and has a thickness of 165 μm. The interconnects, made by Plansee, are made of chromium iron yttrium (CFY). The bipolar plates have 130 * 150 * 3.2 mm^3 dimensions and a utilization of 65% interconnect area for electrochemical conversion [87].

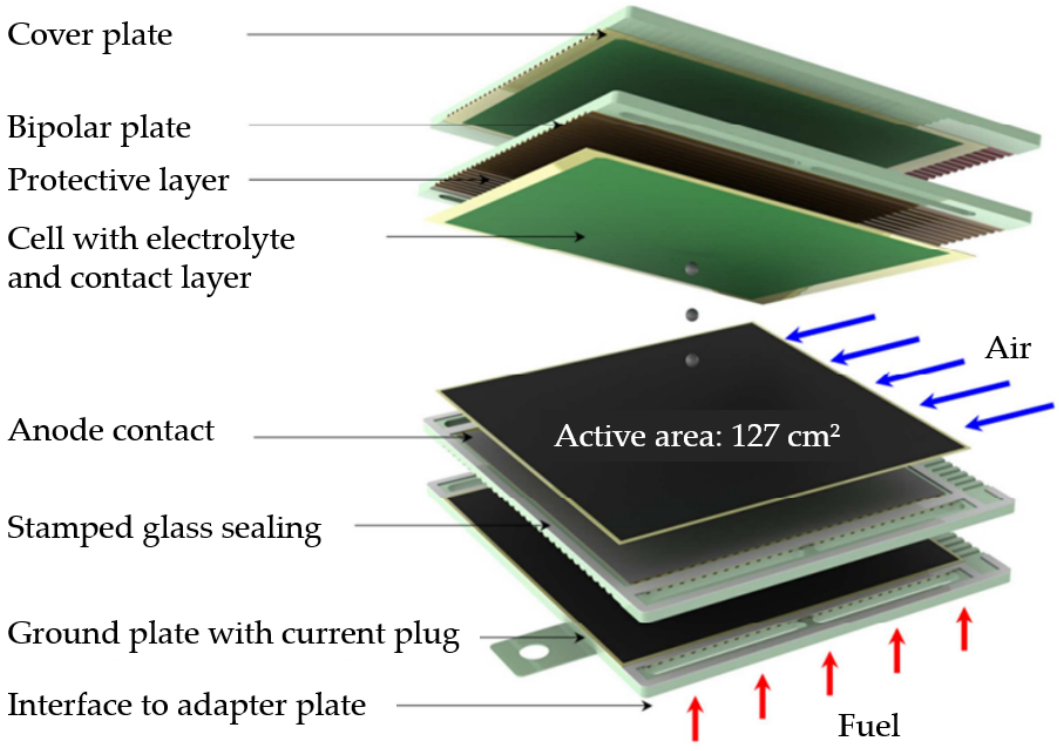

Figure 2.5: Mk 351 assembly [88].

2.3 The effect of biogas impurities on SOFC

This section provides answers to the scientific question 1 of this thesis. For this purpose, the reason for formation of carbon deposits is explained. Further, the effect of H_2S and HCl on the SOFC will be explained. The question of H_2S and HCl in biogas are discussed in Section 2.4. Feeding biogas directly into an SOFC may result in two problems:

- Carbon depositions: With respect to its catalytic performance and electrical conductivity, Ni is the commonly used material on the anode [89]. Feeding dry hydrocarbon fuels includes the risk of carbon formation. Deposited carbon can block the pores on the fuel electrode or cover the Ni-catalyst. This may lead to less fuel utilization and anode deactivation [90, 91].
- Biogas contains several pollutants like H_2S and HCl that can affect the SOFC performance and the electrode stability. H_2S is present in the range from 50 - 6800 of *ppmv* while HCl varys from 0.1 - 25 *ppmv* [92–94]. Sulfur compounds are generally the most abundant in biogas and decompose to H_2S at the SOFC operating temperature. H_2S is a well-known poison for nickel based ceramic cells [95]. H_2S adsorbs on the Ni active sites preventing H_2 and CO oxidation as well as also CH_4 reforming [96]. The effect of chlorine compounds, generally decomposed to HCl in the H_2 rich anode environment, is less understood than sulfur compounds. However, a deactivation mechanism similar to that of sulfur (dissociative chemisorption on the Ni surface) but less severe was generally observed [97, 98].

2.3.1 Carbon depositions

Ni/YSZ cermet is the most commonly used SOFC anode material due to its catalytic effect on the electrochemical oxidation of fuel. A crucial disadvantage of Ni/YSZ cermet anodes is the propensity of carbon depositions due to Ni, which is also an excellent catalyst for carbon deposition reactions such as CH_4 cracking, reduction of CO and disproportionation of CO (see chemical reactions according to Equation 2.10, 2.11 and 2.12).

$$CO_{(g)} + H_{2(g)} \rightharpoonup C_{(s)} + H_2O_{(g)} \tag{2.12}$$

Factors which thermodynamically favor carbon depositions include lower temperatures, higher carbon:oxygen ratios and low oxygen fluxes. In addition to this, carbon deposition is strongly influenced by kinetic factors, especially the relative rates of the forward and reverse Boudouard reaction (Equation 2.11) and CH_4 decomposition (Equation 2.10) reactions. The mechanism of carbon formation depends on the material (e.g. if it is a metal or metal oxide). This is important because the effect of the structure and location of carbon on deactivation can be more relevant than the total quantity of carbon deposited on the catalyst. In the case of metals, the rate of

carbon deposition is a function of the type of metal, the crystal size, the promoters, and the interaction between the metal and the support [99–102]. According to [103], three different mechanisms leading to carbonaceous deposits (coke) can be distinguished:

1. Hydrocarbons are adsorbed on the Ni surface and form a non-reactive film that can encapsulate the Ni particles at temperatures lower than 500 °C. The catalytic Ni surface is, thus, deactivated by this process.
2. At temperatures higher than 600 °C, pyrolysis of hydrocarbons can occur on the Ni surface, which also leads to the deactivation of the catalytic Ni surface.
3. At temperatures higher than 450 °C, diffusion of adsorbed carbon from the surface into the Ni particle takes place, followed by a nucleation process. Carbon then starts to grow in a fibrous (whisker-like) structure out of the Ni particle, thereby, lifting parts of the Ni particles and, thus, irreversibly breaking apart the anode microstructure. In extreme cases, this process may ultimately lead to a complete destruction of the anode.

Formation of solid carbon is favoured thermodynamically in a large proportion of the potential operating space of SOFCs. Figure 2.6 shows the region in which carbon deposition is favoured at different temperatures, showing that all common carbon containing fuels (ethylene (C_2H_4), ethane (C_2H_6), H_2O, ethanol (C_2H_6O) and propanol (C_3H_7OH)) are in the carbon deposition region below 1000 °C [104].

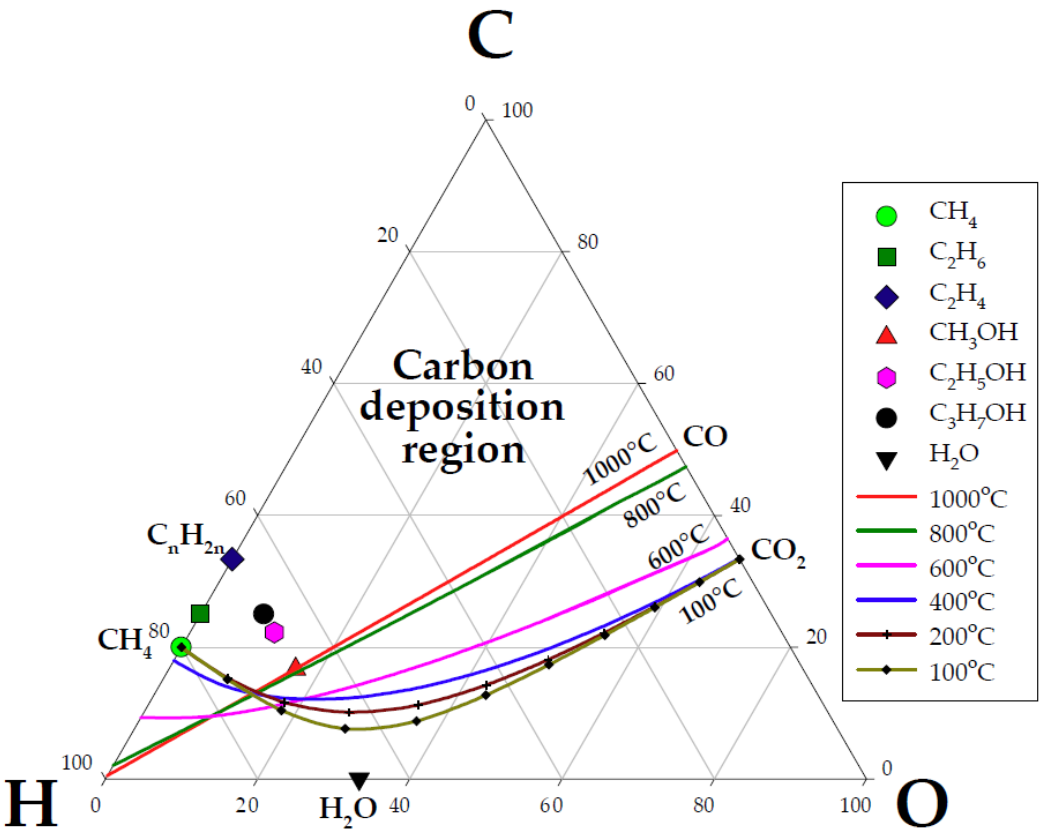

Figure 2.6: Carbon deposition limit lines at various temperatures in the C-H-O diagram [104].

Different strategies have been proposed to avoid or suppress carbon deposition in SOFCs. One attempt suggested that the carbon deposition on a Ni/YSZ anode could be avoided by lowering the operation temperature below 700 °C and increasing the operation current density. These operation parameters, however, are difficult to attain in real SOFC systems [105–107]. Another approach is the use of a high S/C ratio to avoid carbon deposition, but it reduces the cell electrical efficiency by diluting the fuel. Moreover, the strongly endothermic reforming reaction introduces excessively large temperature gradients in the stack [108, 109]. Schluckner et al. [110] strongly recommended efficient S/C ratios to avoid formation of graphite or carbon nanofibers on Ni catalysts. Therefore, the real SOFC system usually uses an external reformer to supply syngas derived from the steam reforming of CH_4. The syngas derived from steam reforming consists of CO_2, CO, H_2, vapor and residual CH_4. Biogas naturally contains the reforming agent CO_2. However, for typical biogas, the content of CO_2 is insufficient to conduct the reforming process safely. Biogas contains about 3-5% H_2O and 35-50% CO_2, depending on the source (Table 2.2). For those cases, steam is added to prevent carbon deposition [111]. However, the catalyst used for external SR faces the same problems as the SOFC anode namely, carbon depositions. These issues will be discussed in Section 2.7.

2.3.2 H_2S

A disadvantage of using biogases as a fuel is their naturally occurring contaminant content such as H_2S [112]. It is widely recognized that sulfur compounds, especially H_2S, are the major poisons for FC systems [113, 114]. Biogas can contain 50 to 6800 *ppmv* of H_2S, which is known to have detrimental effects on SOFC performance. Several studies have investigated the influence of H_2S on SOFC anodes as a function of current density, temperature and partial pressure in the anode stream [95, 115]. Sulfur poisoning on the anode can essentially influence the FC performance in two degradation ways, which are generally referred to as short-term and long-term effects. The fast physisorption and chemisorption of sulfur with a deactivation of the TPB are among the short-term-effects. Structural modifications and Ni-migration phenomena can be considered as long-term sulfur effects: the main effects on long-term sulfur exposure are related to micro-structural changes, such as Ni-particle coarsening or Ni-migration, in addition to the formation of bulk nickel sulfide [116, 117].

Rasmussen and Hagen [115] as well as Hauch et al. [31] concluded that sulfur poisoning can be represented as a two-step process: an initial voltage drop followed by a constant voltage or a voltage degradation/decrease depending on the test parameters. The initial cell voltage degradation is very significant in terms of instantaneous voltage reduction, i.e. a sudden short-term effect, which is potentially much more critical than the subsequent long-term degradation [116]. The first voltage drop can be described through the chemisorption mechanism of sulfur compounds on Ni active sites. Critical conditions for a biogas fed SOFC arise when the H_2S concentration is greater than 2 *ppmv*. This condition can be representative for a partial failure

of the gas cleaning section, where the sulfur breakthrough is above the threshold concentration for a SOFC [118].

The aforementioned two-stage degradation process with an instantaneous drop followed by a slower, longer-term continuous degradation is shown in Figure 2.7. A representative sulfur poisoning and recovering processes of a single SOFC with Ni/YSZ cermet anode upon exposure to a fuel containing 50 *ppmv* H_2S under constant cell voltage can be seen in this figure. The two stages of the poisoning process can be spotted easily: a dramatic drop (-16.67%) in cell current occurred in the first several minutes followed by a slow but continuous performance drop (up to -3.96%) in the next 120 *h*. Upon removal of H_2S from the fuel, the cell performance first had a quick rebound then recovered gradually. The downward spike at 145 *h* was due to the fluctuation in flow rate upon the gas switch. The recovery was not complete and the cell performance stabilized at 96% of the initial value after 50 *h*. The used fuel composition was 50 *ppmv* H_2S, 1.5% H_2O, 48.5% N_2, balance H_2. The test runs were performed at 800 °C and ambient pressure [119].

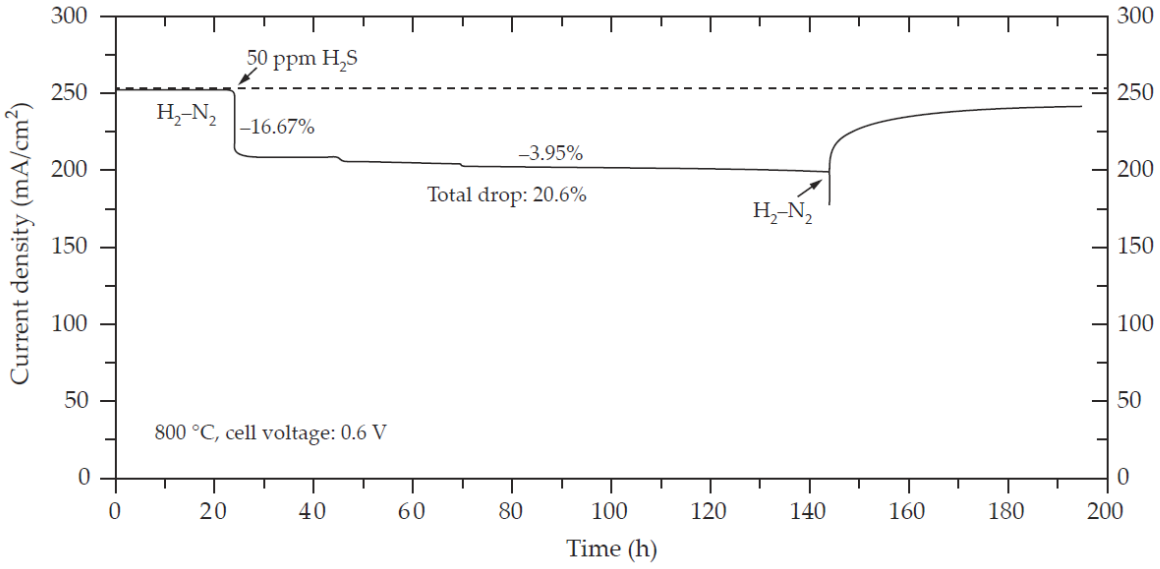

Figure 2.7: Effect of 50 *ppmv* H_2S in fuel on cell performance at 800 °C showing two-stage degradation [119].

Blesznowski et al. [29] recently studied Ni/YSZ based anodes at 800 °C under 250 mA/cm^2 with H_2S in the feed (47.5% H_2, 47.5% N_2, 3% H_2O) and claimed that H_2S up to 1 *ppmv* has negligible effect while 2 *ppmv* at the same conditions exhibited significant voltage decline in 200 *h* operation. The voltage drop can also be considered serious even at 1 *ppmv* H_2S in the feed, however, only at 750 °C. Li et al. [120] investigated long-term durability of a cell with Ni/YSZ anode in the syngas feed (48% H_2, 5% CO, 13% CO_2, 4% CH_4 and 30% H_2O) containing 2 *ppmv* H_2S. No noticeable power loss was shown through impedance spectra, and the cell was stable for almost 500 *h* at SOFC operating temperature of 800 °C and current density 625 mA/cm^2. Scanning electron microscope (SEM) investigations showed that the cell remained invulnerable. Analysis of fuel using mass spectrometer indicated that H_2 oxidation and WGSRs take advantage over CH_4 reforming. They predicted that 30% H_2O in the feed may

have inhibited the sulfur poisoning impact. Hauch et al.[31] studied long term effects (500 *h*) of 2 *ppmv* H_2S to SOFCs with Ni/YSZ anode in gas mixture (30% CH_4, 60% H_2O and 10% H_2) at 850 °C under low (1 A/cm^2) and high (1.38 A/cm^2) current densities. At low current density, performance loss was reversible and the anode was found intact in post investigations. While at high current density, the performance was also reversible, but long-term degradation was irreversible and post investigations showed lack of percolating Ni near the anode-electrolyte boundary. Literature [95], suggests that the maximum H_2S concentration has to be 8 *ppmv* to avoid any damage to the anode [32].

This section illustrates that there is a span from 1 to 8 *ppmv* for a recommended H_2S tolerance of SOFC anodes. Based on these results, a H_2S limit of 2 *ppmv* was chosen for the experiments and design calculations in this thesis.

Sulfur chemisorption mechanism on an Ni surface

It is well known that sulfur compounds interact with Ni catalysts and reversibly or irreversibly decrease the cell performance. This interaction depends on the temperature, current density, H_2S concentration, fuel mixture and duration of the sulfur exposure [115, 118, 121, 122].

At least two different types of reactions can take place on Ni catalyst particles:

1. Chemisorption:

$$H_2S_{(g)} \leftrightarrow HS_{(ads)} + H_{(g/ads)} \leftrightarrow S_{(ads)} + H_{2(g/ads)} \tag{2.13}$$

2. Sulfidation:

$$Ni + H_2S \rightharpoonup NiS + H_2 \tag{2.14}$$

$$3Ni + xH_2S \rightharpoonup Ni_3S_x + xH_2 \tag{2.15}$$

According to [121, 123, 124], the chemical reaction as shown in Equation 2.13 is the dominating one at 700–800 °C for H_2S concentrations below 50 *ppmv*. At higher H_2S concentrations, the FC performance through Ni sulfide formation, following Equations 2.14 and 2.15 becomes relevant. It should be mentioned that the situation of a high H_2S concentration in the anode feed is of limited practical interest as a H_2S removal step should always be foreseen in SOFC plants.

Another important point is to understand how electrochemical behavior influences sulfur adsorption on Ni. According to [125], electrochemical poisoning by sulfur is described as:

$$H_2S_{(g)} + O^{2-} \rightharpoonup H_2O_{(g)} + S_{(on\ Ni-TPB)} + 2e^-_{(on\ Ni)} \tag{2.16}$$

This reaction is different from the chemisorption of sulfur at any other Ni point:

$$H_2S_{(g)} \rightharpoonup H_{2(g)} + S_{(on\ Ni)} \tag{2.17}$$

When operating a FC, it is important to understand whether the sulfur will be more prone to adsorbing at the TPB than on the Ni in the anode support. A large amount of the Ni catalyst area is available, but only a relatively small portion is in the TPB zone. If sulfur adsorbs selectively on the TPB, a very rapid degradation would result. Otherwise, Ni in the support could act as a sulfur trap, thus, delaying the time necessary to yield equilibrium coverage [116].

2.3.3 HCl

Besides H_2S, HCl is a biogas pollutant that can affect SOFC performance in a negative way. There is scarce literature found on the influence of HCl on SOFC operation. The concentration of HCl in biogas varies from 0.1 to 25 *ppmv*, depending on the source of the biogas. HCl has several negative effects: corroding the metal parts of the equipment as well as reacting with other species in the biogas to form ammonium chloride (NH_4Cl) and natrium chloride (NaCl), which creates deposits and causes fouling after condensing in cooler parts of the equipment. As regard to the influence of HCl on SOFC, it may attack the Ni of anode resulting in cell degradation [32].

According to the elementary reactions in the Ni/YSZ anode, $H_{2(g)}$ adsorbs dissociatively on Ni surfaces and then $H_{(ad)}$ will react with oxygen ions at the TPB to form $H_2O_{(g)}$ (Equation 2.18).

$$2H_{(ad)} + O^{2-} \rightharpoonup H_2O_{(g)} + 2e^- \tag{2.18}$$

If chlorine (Cl) compounds are contained in the biogas feed, the adsorption of HCl on Ni surfaces occurs (Equation 2.19) [126].

$$HCl_{(g)} \rightharpoonup Cl_{(ad)} + 0.5H_{2(g)} \tag{2.19}$$

It has been reported that the presence of electronegative species such as $Cl_{(ad)}$ may hinder the adsorption of H_2 on Ni surfaces, or in other words reduce the electrochemical reaction rate. The adsorption of Cl on Ni surfaces blocks possible reaction sites at the TPB, may prevent the electrochemical reaction according to Equation 2.18 and may lead to an increase in anode overpotential [33].

An investigation of the microstructural changes of Ni/YSZ anode, following exposure to adsorbed Cl, observed significant effects both near the anode surface and in the middle of the anode layer. Haga et al. [127] concluded the change to be due to the formation of nickel

chloride ($NiCl_2$) (Equation 2.20) under the prevailing experimental conditions. Furthermore, they concluded that this adsorption-desorption mechanism is a partially reversible poisoning process. The fact that recovery is only partial is due to gaseous $NiCl_{2(g)}$ transported out of the FC, which decreases the amount of Ni electrode catalyst and active sites [126, 127].

$$Ni_{(s)} + 2HCl_{(g)} \rightharpoonup NiCl_{2(g)} + H_{2(g)} \tag{2.20}$$

Marina et al. [128] investigated the influence of HCl on a Ni/YSZ anode-supported SOFC at operating temperature of 700 °C. The synthetic fuel gas they used consisted of 30% H_2, 23% CO, 21% CO_2 and 26% H_2O. They observed a modest, but rapid decrease in cell performance upon introduction of 50 *ppmv* concentrations of HCl to synthetic fuel gas, with rapid recovery observed when HCl exposure ceased. The results which correspond to a cell operating at a constant potential of 0.8 *V* in synthetic fuel gas with 50 *ppmv* HCl at 700 °C are shown in Figure 2.8. Within a few hours of HCl exposure, the output of this cell decreased by ~3%, and essentially completely recovered within a few hours when exposure ceased. No long-term loss in performance due to HCl exposure could be discerned. Current density had no effect on the poisoning and no microstructural changes of the anode were observed in post investigations [32, 128].

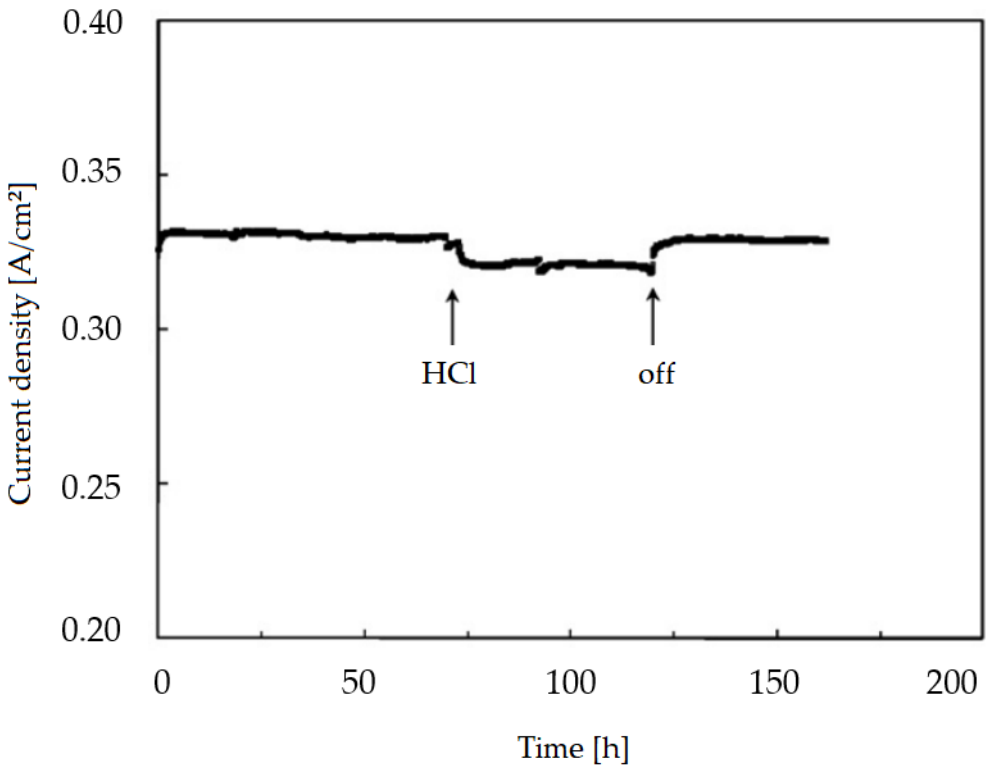

Figure 2.8: Current density generated by the Ni/YSZ anode-supported cell at a cell potential of 0.8 *V* in the presence of 50 *ppmv* HCl in fuel gas at 700 °C [128].

Trembly et al. [33] investigated an electrolyte supported SOFC at 800 °C with Ni/YSZ as a current collection layer and Ni/GDC as an anode interlayer. They reported 17% and 26%

performance loss in 100 *h* due to the presence of 20 *ppmv* and 160 *ppmv* HCl respectively in the feed (29.1% H_2, 28.6% CO, 12% CO_2, 3.2% N_2 and 27.1% H_2O). The cell exhibited rather steady operation after 100 *h* operating time and loss was reversible when HCl had been removed from the feed [32]. The degradation rate reported by Trembly et al. [33] seems higher than the degradation rate reported by other authors who tested anode supported cells instead. Xu et al. [129] suggested that an anode supported cell seems to be more tolerant to HCl as compared to an electrolyte supported cell. Aravind et al. [130] investigated SOFC degradation at 850 °C with 9 *ppmv* HCl in H_2 feed and found no significant degradation in 90 *min*. Based on this literature research, a HCl tolerance of SOFC anodes as high as 10 *ppmv* seems satisfying. As a result, a criterion of 10 *ppmv* HCl was selected for gas purification, for the experiments and for the design calculations in this work.

2.4 Biogas

In the previous section, the advantages of SOFCs have been described. As a summary, SOFCs provide low emissions, clean condensates and exhaust gas, low noise and vibration free operation, and a high electrical efficiency [131]. The high efficiency results from the direct conversion of chemical energy into electrical energy. The theoretically achievable useful work is limited solely by the free enthalpy of the chemical reaction and can, thus, be higher than in the coupling of a heat engine (Carnot efficiency) with a generator for power generation. Especially for small SOFC systems (<30 kW), the comparison of the efficiency with the system performance results in a clear benefit over conventional converter technologies [35]. In extending these benefits by the factor of sustainability, biogas comes into play.

Biogas is the name popularly used to denote the flammable mixture of gases that are generated when organic material undergoes anaerobic decomposition. The mixture contains 35–70% CH_4, 25-45% CO_2, and traces of other gases such as N_2, O_2, H_2S, HCl and NH_3. Considering biogas as a clean and renewable form of energy carrier that could well substitute the conventional energy sources such as fossil fuels, the optimization of this type of energy becomes crucial [132]. In the industrialized countries, the production of waste and residues increases linearly with increasing prosperity resulting in a great untapped potential for biogas plants [133].

Biogas is a versatile renewable energy source which can be used for replacement of fossil fuels and is mainly utilized in the applications shown in Figure 2.9. A part of the biogas is used in boilers to produce merely heat [134]. This heat can be converted into useful thermal energy, such as steam or hot water. Although boilers do not need a high-quality biogas, a desulfurization is a prerequisite to increase the lifetime of the equipment used. In the literature, a maximum H_2S input concentration of 1000 *ppmv* is recommended for boilers which are operated with biogas [34, 135].

In biogas operated CHP plants, electricity is generated by burning biogas. Then a heat recovery unit is used to capture heat from the combustion system's exhaust stream. This heat can be

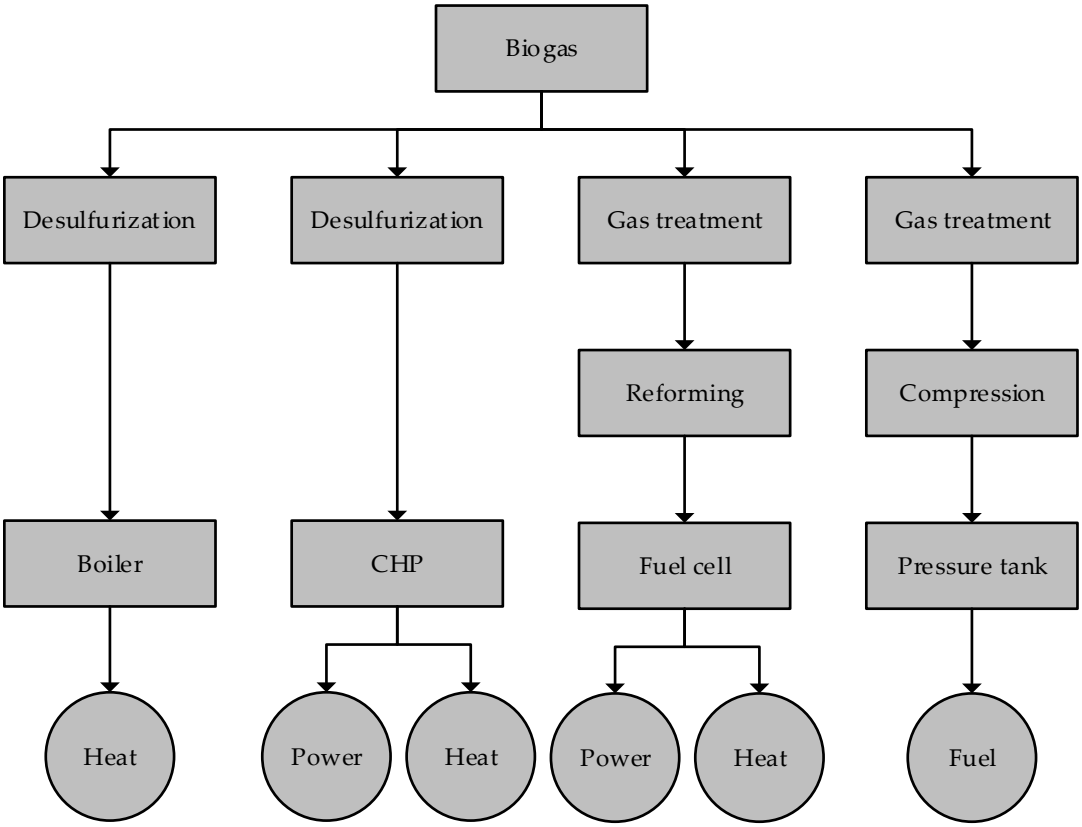

Figure 2.9: Possible uses of biogas [136].

converted into useful thermal energy, generally in the form of hot water or steam. These CHP systems are normally provided with a four-stroke spark ignition engine. Stirling engines, gas turbines or micro gas turbines, alternatives to the four stroke engine, are not applied [137]. The maintenance costs for reciprocating engines (four-stroke spark ignition) increases with increasing H_2S concentration in the biogas. H_2S removal is a must if concentrations are higher than 1000 *ppmv* and should not exceed 100 *ppmv* in order to keep the maintenance costs low [92]. Biogas powered CHP systems based on gas turbines seem to be less sensitive to H_2S. H_2S concentrations up to 70,000 *ppmv* are considered to be uncritical [135].

An extensive gas treatment is required for the use of biogas in FCs. When using biogas in a SOFC, the following steps are required: The biogas has to be purified, especially by removing H_2S and HCl, before feeding the FC (see Section 2.3.2 and 2.3.3). The H_2S concentration should be less than 2 *ppmv* when used in SOFCs to avoid damage to the anode. The comparison with the previously described applications boiler and gas engine as well as the associated H_2S concentration of 1000 or 100 *ppmv* already provides a clue to the significantly increased gas quality required. In addition, the biogas must be reformed to avoid carbon deposits at the anode and, thus, ensure safe operation of the SOFC (see Section 2.3.1). SOFC-based CHPs are considered as small-scale power plants of the future for the production of power and heat with overall efficiency exceeding 60% and low emissions [92].

Another interesting option is the use of biogas as fuel for vehicles. A simple desulfurization is not sufficient to meet the required standards. In order to convert biogas into biomethane, a gas treatment consisting of two major steps is performed: Firstly, a cleaning process to remove the trace components and secondly an upgrading process to adjust the calorific value. Besides the presence of H_2S, the presence of CO_2 in biogas is a major problem and its removal is required to improve the calorific value. The removal of CO_2 from biogas, to obtain biomethane with purities between 97 - 99%, is the most expensive step in biogas upgrading. Biogas that has been upgraded by removing H_2S, CO_2 and moisture, and that meets national requirements is specified as biomethane. In Austria, biomethane needs to fulfill at least the following requirements: $CH_4 \geq 96$ vol%, $CO_2 \leq 3$ vol%, $O_2 \leq 0.5$ vol%, $H_2 \leq 4$ vol% and $H_2S \leq 5$ *ppmv* [138]. Biomethane is a flexible and easily storable fuel that can be used wherever natural gas is used without the requirement to change any settings on equipment designed to use natural gas. The steps compression and pressure tank depend on the grid pressure of the natural gas grid and the gas upgrading system (inlet pressure). If the biogas is fed into a high-pressure transport network, a two-stage compression is usually necessary. In this case, the combination of a screw compressor (first stage) and a piston compressor (second stage) is recommended [139, 140].

Currently, the vast majority of the produced biogas is used in CHP plants for electricity and heat production. The use of biogas in FCs and its use as a fuel or natural gas substitute is still in the development stage. For economic reasons, the deployment of biogas in CHPs is of particular interest as it is now mainly utilized in Europe. With low demand for heat during the summer months, feeding electricity into the grid must ensure that the resulting biogas is

used continuously. This kind of electrical energy is nowadays increasingly provided as "green electricity" [140].

A biogas based CCHP system is a green energy system with biogas as fuel. The CCHP distributed generation pathway is particularly attractive due to its high overall conversion efficiency and on site integration options. On site cogeneration offers a reduction in the use of fossil fuels for heat generation and the grid electricity demand. Among the available decentralized cogeneration technologies, FCs offer the highest electrical efficiency and the lowest pollutant emissions [141]. This technology is especially attractive for instance for buildings and hospitals where a seasonal (winter/summer) or spatial (surgery room/patient room) distribution for heating and cooling is desired [142].

2.4.1 Anaerobic digestion

Biogas refers to a combustible gas mixture of CH_4 and CO_2, which is usually produced by AD of biomass. In anaerobic CH_4 fermentation, bacteria degrade the substrate in an O_2-free atmosphere. Such processes take place, e.g. in bogs, landfills and manure pits [34]. In biogas plants, these processes are achieved through targeted use of anaerobic bacteria and precise regulation of temperature, pH and of the chemical oxygen demand (COD) content used for the production of biogas. The biodegradation of the substrate, which is divided into four stages is shown in Figure 2.10. It is carried out in series by different bacterial strains.

In the first step called hydrolysis, the biomass is formed from polymeric organic compounds (e.g. carbohydrates, fats, proteins) by hydrolytic and fermentative bacteria in a whole range of low molecular weight compounds (initially in monomers such as amino acids and sugars followed by lower fatty acids, lactic acid, alcohols, etc.). The percentage of composition of these intermediates is influenced by the hydrogen partial pressure. At low H_2 concentrations, a substantial amount of acetic acid ($C_2H_4O_2$) is formed while a higher partial pressure causes the formation of propionic acid ($C_3H_6O_2$), butyric acid (C_3H_7COOH) and lactic acid ($C_3H_6O_3$) as well as C_2H_6O. The hydrolysis of carbohydrates takes place within a few hours, while the hydrolysis of proteins and lipids occurs within few days. Lignocellulose and lignin are degraded only slowly and incompletely [143, 144].

In the second and third step, called acid and acetate formation respectively, the reaction products of the hydrolysis are converted into precursors of biogas such as $C_2H_4O_2$, CO_2 and H_2. By-products of these reactions are ammonium compounds, H_2S, alcohols and thiols, the so-called mercaptans. When the H_2 partial pressure is low, H_2, CO_2 and acetate are predominantly formed by the acetogenic bacteria. When the H_2 pressure is high, predominantly C_3H_7COOH, capronic acid ($C_6H_{12}O_2$), $C_3H_6O_2$ and valeric acid ($C_5H_{10}O_2$), and C_2H_6O are formed. From these products, the methanogenic microorganisms can process only acetate, H_2 and CO_2. The acetogenic phase limits the rate of degradation in the final stage. From the quantity and the

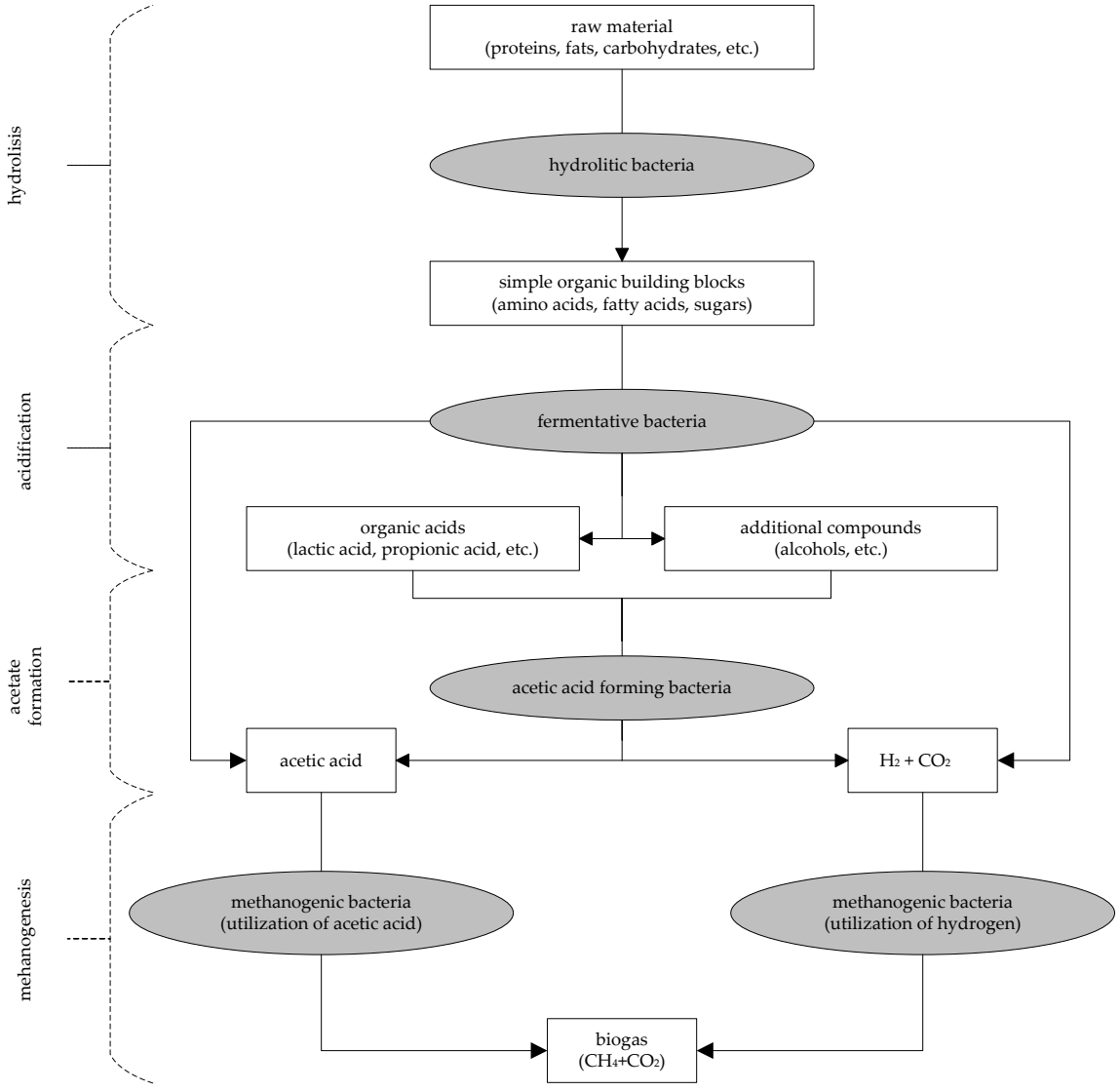

Figure 2.10: Anaerobic degradation of organic substrates to biogas [143].

composition of the biogas a conclusion can be drawn about the activity of the acetogenic bacteria [143, 144].

In the fourth stage, the CH_4 formation takes place under strictly anaerobic conditions. This reaction is categorically exergonic. About 70% of the biogas is formed by splitting $C_2H_4O_2$ into CO_2 and CH_4, while the remaining about 30% is formed by combining H_2 and CO_2 to CH_4 and H_2O. CH_4 formation is very closely linked to the degradation of $C_3H_6O_2$ since the methanogens must ensure that the H_2 partial pressure does not become too high by continuously converting the H_2 into CH_4. All CH_4 generators can produce biogas from H_2 and CO_2. The formation of biogas from $C_2H_4O_2$ is energetically less favorable. It can, therefore, only be accomplished by a part of the methanogenic bacteria. Nevertheless, most of the biogas is made from $C_2H_4O_2$. The partial steps usually take place simultaneously in a biogas plant, but not at the same rate. The rate-determining step in most fermentation processes is hydrolysis. Especially, cellulose and hemicellulose are only slowly hydrolyzed by the bacteria. When large quantities of readily degradable compounds are provided, CH_4 formation becomes the rate limiting step [143, 144].

AD has been developed mainly to process agricultural wastes in order to provide renewable sources of energy. However, other benefits such as environmental, agronomic, hygienic and social benefits can be obtained by using this technology as well [145]. For example, in the European Union (EU), 1500 million tons of biomass could be digested anaerobically each year. Half of this amount can be attributed to energy crops [146].

AD is a complex biological process that converts organic materials into CH_4. Biogas contains mainly CH_4 (35–70% vol.) and CO_2 (25–45% vol.). Additionally, trace amounts of other components such as H_2O, H_2S, CO, N_2, O_2, H_2, NH_3, halogenated hydrocarbons and siloxanes can be present [147].

The theoretical or stoichiometric production of CH_4 in AD can be calculated with the following equations [148]:

$$C_\alpha H_\beta O_\delta N_\gamma S_\varepsilon + yH_2O \rightharpoonup xCH_4 + \gamma NH_3 + \varepsilon H_2S + (\alpha - xCO_2) \tag{2.21}$$

$$x = \frac{(4\alpha + \beta - 2\delta - 3\gamma - 2\varepsilon)}{8} \tag{2.22}$$

$$y = \frac{(4\alpha - \beta - 2\delta + 3\gamma + 2\varepsilon)}{4} \tag{2.23}$$

Taking into account the stoichiometry of the above equations, the levels of CH_4 and CO_2 produced from the decomposition of different substrates can be estimated as follows: 35–70% for CH_4 and 25–45% for CO_2 [149].

All types of biomass can be used as substrates for biogas production as long as they contain carbohydrates, proteins, fats, cellulose and hemicelluloses as main components. The composition of biogas and the CH_4 yield depend on the feedstock type, the digestion system and the retention time [150].

2.4.2 Biogas composition

The composition of biogas depends on the type of raw materials used and can only be slightly influenced by the process management [151]. A selection of average biogas compositions with respect to the substrates used are reported in Table 2.2.

Table 2.2: Different biogas compositions compared to natural gas [92–94].

Composition	Farm scale AD plant	Centralised AD plant	Landfill	Sewage treatment plant	Natural gas
CH_4 [*vol%*]	55-60	60-70	35-65	60-65	81-89
H_2 [*vol%*]	0	0	0-3	0	0
CO_2 [*vol%*]	35-40	30-40	25-45	35-40	0.67-1
N_2 [*vol%*]	<1-2	2-6	<1-17	<1-2	0.28-14
O_2 [*vol%*]	<1	0.5-1.6	<1-3	<0.05-0.7	0
H_2S [*ppmv*]	25-30	0-2000	30-500	<0.5-6800	0-2.9
NH_3 [*ppmv*]	100	100	5	<1-7	0
HCl [*ppmv*]	<0.1	<0.2	<25	0-1.5	-
Siloxanes [mg/m^3]	<0.03-<0.2	<0.08-<0.5	<0.3-36	<1-400	-
Moisture [%]	≈3	≈3	≈3	≈3	<0.02

The following section describes the main components of biogas and their influence on the SOFC CCHP system.

2.4.3 Methane

CH_4 is a colorless and odorless gas that is readily soluble in organic solvents such as alcohol and ether. CH_4 is a very stable compound. It represents the first member of the homologous series of alkanes. CH_4 ignites at about 600 °C. The calorific value is 55.55 [*MJ/kg*]. CH_4-air mixtures containing 4.4-16.5 vol% of CH_4 are explosive. The relative molecular weight is 16.043 [*g/mol*] and the density under normal conditions is 0.72 [*g/L*]. The critical temperature for the liquefaction of methane is -82.5 °C. Above this temperature, no liquefaction takes place even at very high pressures. This is disadvantageous since the long-term storage in a small space for later use would only be possible at uneconomically low temperatures [34]. Amongst

hydrocarbon fuels, CH_4 has attracted much attention for direct operation of SOFCs. Studies have shown that various chemical and electrochemical reactions may take place simultaneously on the SOFC anode when fuelled with CH_4 resulting in carbon depositions (see Section 2.3.1) [106, 152]. Carbon deposition is a significant problem arising from the direct feed of hydrocarbons and leads to faster cell degradation. Surface carbon can deactivate the SOFC anode by blocking the access of reactants to reaction sites [153].

2.4.4 Carbon dioxide

Apart from CH_4, CO_2 is the main component in biogas. CO_2 is an inert biogas component and a colorless, non-combustible, odorless gas. For thermal utilization of the gas, CO_2 elimination is not mandatory. CO_2 will decrease the volumetric energy content in biogas. If high volumetric energy content is important (e.g. the gas is used as a vehicle fuel or injected into the gas grid), the CO_2 should be removed [34].

CO_2 is formed during the decomposition of the different types of substrates used for biogas production. Its solubility in the condensate and the resulting formation of carbonic acid (H_2CO_3) contributes to the acidification and, thus, to the corrosiveness of the condensate. It is well known that CO_2 can act as an oxidant for hydrocarbons in the presence of a suitable catalyst. This process is the so-called dry-reforming (DR) as shown in Equations 2.24 and 2.25 for CH_4 and a general higher hydrocarbon, respectively [154, 155]:

$$CH_4 + CO_2 \rightharpoonup 2CO + 2H_2 \tag{2.24}$$

$$C_nH_m + nCO_2 \rightharpoonup 2nCO + \frac{m}{2}H_2 \tag{2.25}$$

Carbon deposition, described by Equation 2.10, is a particular problem with DR, especially with Ni-based catalysts [156]. Pt- and rhodium (Rh)-based catalysts show greater tolerance to carbon deposition [157]. Therefore, in addition to steam, CO_2 can also reform the CH_4, though it also represents a possible source of carbon deposition. Like SR, DR is also a strongly endothermic reaction [155].

In terms of SR Navadol et al. [158] concluded that the presence of CO_2 in the feed inhibited the production of H_2 from CH_4 SR, which is mainly due to the inhibition of CH_4 and steam adsorption by CO_2. Consequently, the removal of CO_2 might be required in order to maximize the yield of H_2 production from CH_4 SR. In terms of H_2S adsorption, Sitthikhankaew et al. [159] concluded that the presence of CO_2 inhibited the H_2S adsorption performance due to the competitive adsorption and reaction between CO_2 and H_2S on the surface of activated carbon. In addition potassium hydroxide (KOH) could react with CO_2 to produce potassium bicarbonate ($KHCO_3$), K_2CO_3, and potassium hydrosulfide (KHS) (Equations 2.26, 2.27 and 2.28). Hence,

the content of KOH could decrease and affect the chemical reaction between H_2S and KOH [159].

$$CO_2 + KOH \rightharpoonup KHCO_3 \tag{2.26}$$

$$CO_2 + 2KOH \rightharpoonup K_2CO_3 + H_2O \tag{2.27}$$

$$K_2CO_3 + H_2S \rightharpoonup KHCO_3 + KHS \tag{2.28}$$

2.4.5 Water

H_2O is a quantitatively important component of biogas. The condensate is produced during cooling, and the amount of condensate increases with increasing gas pressure. The more the pressure increases, the more aggressive the condensates are since the solubility equilibria then shift to the products dissociated in H_2O. Since H_2O is always present during AD, some of it will evaporate in the digester and, thus, be present in the produced biogas. Biogas leaving the digester is, therefore, always saturated with H_2O. The amount of H_2O in the biogas depends on how much water can be present before the gas becomes saturated with water. The H_2O concentration corresponding to the saturation in biogas depends on the pressure and the temperature inside the digester. H_2O can cause corrosion in pipelines in the presence of other compounds such as CO_2 due to formation of H_2CO_3. Besides that, H_2O lowers the energy content of the gas and can, thus, affect energy utilization from the gas [34].

In SR, the concentration of H_2O plays a key role. A carbonaceous fuel reacts with water vapor resulting in synthesis gas. A detailed description of this procedure can be found in section 2.7. Huang et al. [160] concluded that the H_2S breakthrough capacity of activated carbon decreased with increasing the relative humidity of gas stream. The reason is attributed to a competitive adsorption between moisture and H_2S, and the rate of chemical reaction is restrained by moisture. In terms of SOFC the presence of H_2O limits the deposition of carbon but at the same time reduces the power delivered. A negative effect could derive from its excessive presence. A high amount of H_2O increases the risk of sintering of the Ni anode [161].

2.4.6 Nitrogen and oxygen

The presence of O_2 and N_2 in biogas can lower the heating value of the gas. Normally, O_2 and N_2 are only present in traces in biogas from sewage and dedicated AD plants (see Table 2.2) as CH_4 is formed under anaerobic conditions. On the other hand, landfill gas contains 1–3 vol% O_2 and 1–17 vol% N_2 as some air may be sucked in together with the landfill

gas through the underpressure collection system. If present in large quantities, the removal of O_2 and N_2 can be costly and impede the use of biogas for vehicle fuel or grid injection [34, 93].

O_2 can cause corrosion in gas pipelines and other equipment and can lead to flammable mixtures being formed with the CH_4 in the biogas. Therefore, the content of O_2 has to be carefully controlled. When operating a SOFC, O_2 on the fuel side (anode) is undesirable. The oxygen ions diffuse through the electrolyte due to the high O_2^- activity on the cathode side and low O_2^- activity on the anode side. The fuel simply prevents a buildup of O_2^-on the anode side by consuming the O_2^- [162]. A well known drawback of SOFCs is their susceptibility to thermomechanical failure when the anode side is exposed to oxidising conditions at high temperatures. The basic mechanism behind this instability is the oxidation of Ni into NiO (Equation 2.29). The oxidation of Ni into NiO entails a substantial volumetric expansion and thus exerts significant stress when the internal porosity is not sufficient to accommodate the expansion of the oxidising Ni/NiO phase. From a thermodynamic point of view, the metal is oxidised if and only if the partial pressure of O_2 is larger than the oxidation threshold at a given temperature [163].

$$Ni + \frac{1}{2}O_2 \rightharpoonup NiO \tag{2.29}$$

Subotic et al. [164] performed carbon removal experiments on SOFCs using O_2 enriched gasification mixtures. They concluded that feeding the anode with a very low amount of O_2 in a wide temperature range showed high carbon removal rates but resulted in further deterioration of the cell performance, and eventually led to mechanical degradation.

To achieve conversion of H_2S to elemental sulfur using potassium iodide (KI) impregnated activated carbon, a two-fold stoichiometric O_2 concentration in the gas is required [137]. Except for this, no evidence was found in the literature for a negative or positive effect of O_2 or N_2 on the adsorption of H_2S and HCl.

It is generally known that N_2 is stable. In terms of SR there is a serious risk that NH_3 can be formed from the N_2 impurity contained in biogas by the reaction with reformed H_2 during the SR process [165].

2.4.7 Hydrogen sulfide

Biogas often contains a variety of sulfur compounds such as sulfides and disulfides. H_2S is toxic and strongly corrosive to many kinds of steel [166]. H_2S is formed in anaerobic degradation processes from organically bound sulfur and from sulfate (see Figure 2.11). During anaerobic treatment of sulfate-containing material, the presence of sulfate will increase the intricacy of the biodegradation pathways involved. Acidogens and methanogens will compete with sulfate-reducing bacteria (SRB) for the available organic compounds and H_2. The outcome of

this competitive reaction is important as it will determine to which extent sulfide and CH_4 will be produced (see Figure 2.11). In general, interspecies H_2 will be oxidised by SRB rather than by hydrogenotrophic methanogens. The competition between SRB and methanogens for acetate appears to be much more complex, influenced by a large variety of factors [167, 168]. Biogas has to be purified, especially by removing H_2S, before feeding the SOFC. H_2S is adsorbed on the Ni active sites preventing H_2 and CO oxidation as well as CH_4 reforming [96]. The effect of H_2S on SOFC anode poisoning is described in detail in Section 2.3.2. It is also important to note that H_2S is highly toxic and can cause serious health risks.

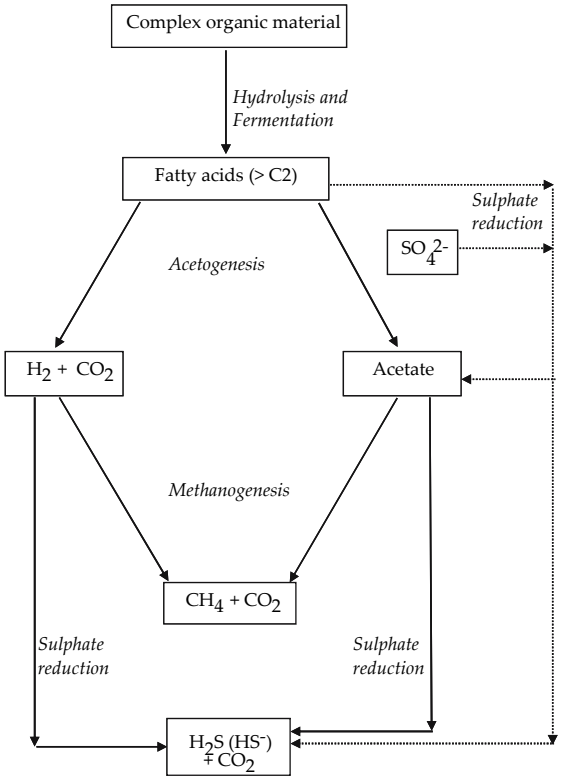

Figure 2.11: Scheme of the anaerobic degradation pathway of organic material and possible interactions of organic substrate and H_2 with sulfate [168].

2.4.8 Ammonia

NH_3 is formed during the anaerobic degradation of feedstocks rich in protein. NH_3 concentration in biogas is generally very low, not exceeding 100 *ppmv* [94]. High NH_3 concentrations in biogas are a problem because the combustion of NH_3 in gas engines leads to formation of NO_x. NH_3 formation can be avoided by controlling the biogas process as NH_3 is formed at high pH values and elevated temperatures. High levels of NH_3 in the digester can cause inhibition of CH_4 production in the digester [34, 144].

An innovative and very promising application is the direct use of NH_3 in SOFCs. In recent years, NH_3 has emerged as a promising fuel for electricity generation in SOFCs because it is relatively cheap, carbon-free, easy to store and transport, less flammable than other fuels and relatively safe because any leakage is easily detectable from the odour [169]. In commercial SOFCs, the anode is based on Ni which is an excellent catalyst for the NH_3 cracking reaction. Consequently, NH_3 is directly cracked in the cell into H_2 and N_2 resulting in a suitable mixture for the operation of the cell [170]. The research activity in this field is focused on the optimization of anodic composition to reduce the operating temperature [171, 172]. However, there is no long term experience with SOFCs operating with NH_3.

2.4.9 Halogenated compounds

Halogenated compounds are often found in landfill gases and only rarely in biogases produced from organic wastes. Halogenated compounds are substances containing one or more halogen atoms (fluorine (F), Cl). Halogenated compounds in landfill gas can largely be explained as originating directly from the substrate by means of vaporisation of these substances. In this case, different gas composition is due to different composition of the landfill sites. Some examples of such compounds in biogas are chloroform ($CHCl_3$), chlorobenzene chlorbenzene (C_6H_5Cl) and HCl. The source of halogen compounds in the biogas may be contaminants in the wastewater (e.g. chemicals used for water treatment and effluent treatment) and solid wastes. Halogenated compounds lead to corrosion in downstream pipes and applications and measures have to be taken into account to keep the concentrations low [147, 173].

In order to protect the SOFC from degradation, the HCl content of the feed biogas has to be limited to levels as low as 10 *ppmv* because chlorine does cause SOFCs degradation. Cl hydrocarbons decompose to HCl quickly at SOFC operating temperatures [174]. Depending on the operating temperature, adsorbed halogens disrupt cell operation in a variety of ways. At 650 °C, adsorbed halogens reversibly occupy available active sites on the Ni, preventing dissociation of the fuel [175]. According to [176], this effect is less pronounced for H_2 than for carbon containing fuels. At operating temperatures >700 °C Cl reacts more readily with the Ni-catalyst and the non-zero vapor pressure of $NiCl_2$ results in sublimation. The effect of HCl on SOFC anodes is described in detail in Section 2.3.3. In the case of adsorptive desulfurisation by means of ZnO, care must be taken to separate HCl in a preliminary stage, since HCl has a negative effect on the adsorption performance of H_2S by ZnO [177]. In terms of SR it is reported that HCl poisons CH_4 reforming and water-gas shift activity of Ni catalysts [178].

2.4.10 Siloxanes

Siloxanes are volatile silicones bonded by organic radicals and are generally present in sewage gas and landfill gas (see Table 2.2). Siloxanes mainly originate from silicon-containing com-

pounds used in industrial materials or consumer products such as cosmetics, pharmaceuticals and shampoo. [92, 179].

During biogas combustion, siloxanes are converted to microcrystalline silicon dioxide (SiO_2). The chemical and physical properties of SiO_2 are similar to glass. Due to the deposition of these crystalline deposits extensive engine erosion or blockage can occur. In gas engines, siloxane deposits usually form on nozzles and blades, causing erosion and lowering the operating efficiency [92, 180].

The SOFC performance can be impaired by the poisoning effect of siloxanes. Porous cermet anodes, SR catalysts and FC anodes can be silicated and ultimately deactivated by deposits of segregated silica [181]. Generally speaking, a distinction can be made between degradation mechanisms being intrinsically or extrinsically sourced. The reason behind intrinsically sourced degradation could be impurities in raw materials and microstructure coarsening. Due to the grain growth of Ni particles, it was assumed that the initial degradation is of intrinsic nature. If impurities or unexpected material is being introduced into the cell in order to induce degradation, the process is then usually called an extrinsically sourced degradation. Degradations of the extrinsic type are in general all conditions that induce Ni redox cycles, carbon formation or secondary phase formation [182].

2.5 Gas treatment

Gas treatment includes the purification step to achieve the required concentrations of H_2S and HCl, and the reforming step which the gas undergoes after purification (see Figure 1.1). After discussing the H_2S and HCl limits of SOFC anodes in the last section, suitable technologies for gas treatment are now to be revealed. In addition to the required gas purities, the technologies should also be discussed regarding their suitability in a system of the 7 kW_{el} performance class. Suitable technologies for gas purification can be divided into the following groups [183]:

- Absorption/scrubbing
- Membrane purification
- Adsorption

Absorption depends on the solubility of various gas components in a liquid solvent. In this process, biogas meets a counter-flow of liquid in a column that is filled with packing material to increase the contact area between gas and liquid [136]. The crucial disadvantage of absorption is that it usually eliminates a problem with a contaminated gas stream only to create a contaminated liquid stream. Besides, high investment cost as well as high consumption of water and/or chemicals has to be mentioned. Among the advantages are the high efficiency of removal (up to 99%) and the ability to handle a wide range of pollutants [184, 185].

One of the most common technologies used to remove CO_2 and H_2S from biogas since these gases are more soluble in H_2O, is high pressure water scrubbing (HPWS). The operating pressure of the HPWS is 10 *bar*. Biogas is fed at the bottom of a packed column while water is fed counter-currently on top [186]. The water solubility of H_2S is enhanced by making the water alkaline or by oxidation to more water-soluble compounds. According to [187], the location of the cleaning steps should be carefully considered because the presence of HCl may affect the H_2S removal. HCl has a great affinity for H_2O and the absorption can be easily accomplished as long as a suitable method is found to bring the gas and the water into contact. The absorption of HCl into H_2O generates heat which has to be removed from the system. The theoretical maximum concentration achievable is dependent on the temperature and the partial pressure of HCl in the exhaust gas [188]. Another process based on chemical absorption is the catalytic oxidation with chelated iron salt solutions. Apart from the advantage of removal efficiencies as high as 99.99% or even higher, H_2S gets converted into elemental sulfur in this process. On the other hand, reports about plugging and foaming problems refer to a complex process control [184].

Although a separation of H_2S and HCl to achieve the desired purities would be possible with these absorption/scrubbing methods, it is not considerable due to the high investment cost as well as the chemicals or water requirements. An economical operation of these absorption systems is only possible with larger systems. Systems such as those described here in the 7 kW_{el} power class can be operated more economically by means of other cleaning methods.

The membrane technology is a competitive alternative to the conventional absorption based biogas cleaning system. The membrane acts as a permeable barrier that allows specific compounds to pass. It controls the permeability based on the applied driving forces such as the difference in concentration, pressure, temperature, and electric charges of different species [189]. Usually, hollow fiber membrane is used in acid gas removal and the separation driving force is the concentration gradient. This is different from microfiltration, ultrafiltration, and reverse osmosis where the driving force is typically the pressure difference. In the acid gas removal, the gas flows inside the tube while the liquid solvent flows in the shell side of the module or vice versa and in co-current or counter-current configuration [183]. During the last 40 years, the membrane-based gas separation process has become a part of market share [190, 191]. Commercial membranes were studied at ambient temperature with H_2S concentrations between 100 and 5000 *ppmv* in CH_4 and achieved promising results [192].

Major disadvantages of this technology are the high cost of the membranes and their fragility. It is estimated that the lifetime of the membranes for biogas purification is around 5 years [189, 193].

Adsorption can be achieved using metal oxides, activated carbon or zeolites. The adsorption process involves the transfer of a solute in the gas stream to the surface of an absorbent material due to physical or van der Waals forces. By properly choosing the adsorbent, the

process can remove H_2S, HCl, moisture and other impurities from biogas either selectively or simultaneously [136].

A commonly used adsorbent for the adsorption of gases and vapors is activated carbon. Activated carbon has a high specific surface area of more than 1000 m^2/g. The surface area, the pore volume, and the surface chemistry promote many catalytic reactions. Carbonaceous materials are usually obtained from different organic precursors such as wood and coconut shells. The carbon materials are activated physically and chemically [183].

Adsorption is advantageous due to equipment compactness, low energy requirement, low capital investment cost and, finally, due to its safety and simplicity of operation [194]. Due to the advantages mentioned above, adsorption is the most suitable option for small systems $<$30 kW [62]. A detailed description of the adsorption process is given in Section 2.6.

After cleaning the biogas, or in other words removing H_2S and HCl, the gas needs to be upgraded to a H_2 rich gas. As described in Section 2.3.1, this step is necessary in order to avoid the major problem encountered in the CH_4 reforming progress. By operating SOFC anodes with hydrocarbons, two types of damage can arise. Firstly reversible aging of the catalyst surface can be caused by various deposits, e.g. coke molecules. Secondly irreversible damage to the catalyst as a result of carbon whisker growth maybe observed [124]. In order to operate SOFCs with hydrocarbon fuels, it is essential to take two important factors into consideration [103]:

1. Stability: Preventing permanent blocking of the electrochemically active surface of the catalyst by adsorption of sulfurous components or higher hydrocarbons, carbon formation and deposition, as well as chemical reactions with the Ni catalyst which might otherwise result in Ni3C or NiS formation [103].
2. Efficiency: Developing a system that is less complex and directly utilizes hydrocarbons in a stable operating point [103].

Typically, there are three main catalytic processing routes for converting CH_4 or higher hydrocarbons to syngas, a H_2-rich gas, or a CO- and H_2-rich gas mixture [195]:

- partial oxidation (POX)
- SR
- autothermal reforming (ATR)

POX, in which CH_4, natural gas or a hydrocarbon is heated in the presence of a stoichiometric amount of pure O_2 has attracted a lot of attention in recent years. POX of CH_4 is a highly exothermic reaction [196]. The chemical reaction for methane is shown below [52].

$$CH_4 + \frac{1}{2}CO_2 \rightharpoonup CO + 2H_2 \tag{2.30}$$

Among the advantages of POX of CH_4 are good response time, its compactness as well as less sensitivity for fuel variation. However several disadvantages, which include the lowest H_2 yields as well as the highest pollutant emissions when being compared to SR and ATR have to be considered. Additionally, high operating temperatures might result in catalyst degradation. In terms of system configuration, convenience, and cost, it may be simpler to use O_2 or air instead of steam. However, using air as the source of O_2 might result in a product gas which is diluted with residual N_2. When used in a SOFC CCHP system, this leads to reduced cell voltage and electrical efficiency. One of the main problems is the development of a catalyst as well as an operating regime which ensures high selectivity to POX at sufficiently high activity and at the same time avoiding carbon deposition on the catalyst. Supported Ni catalysts are generally preferred due to cost reasons although highly dispersed Pt and Rh catalysts are also commonly used because of their greater activity and resistance to carbon deposition [197, 198]. It is obvious that carbon deposition is rather undesirable in internally reforming SOFCs as well as in heterogeneously catalysed hydrocarbon conversion processes.

SR is an endothermic reaction that combines a hydrocarbon fuel with steam over a catalyst at high temperatures (500 - 900 °C). The SR of CH_4 involves two endothermic reactions (SR) and the exothermic reaction (WGSR) as follows [196]:

$$CH_4 + H_2O \rightharpoonup CO + 3H_2 \tag{2.31}$$

$$CO + H_2O \rightharpoonup CO_2 + H_2 \tag{2.32}$$

Reactions (2.31) and (2.32) are reversible and are normally at equilibrium as the reaction rates are very fast. Therefore, the composition of the product gas from a conventionally used reformer reactor is controlled by thermodynamics. Usually, steam is added well above the stoichiometric requirement of reaction (2.31) which means that the equilibrium of reaction (2.32) moves towards producing more CO_2 compare to CO. The reason behind is the attempt to avoid carbon deposition through the Boudouard reaction (2.11) which is catalysed by Ni as well [199]. Among the advantages of SR is the fact that it is a well-established process for the production of H_2 or synthesis gas from natural gas or other hydrocarbons. Additionally, it has the highest H_2 yield when being compared to the other methods discussed above. Furthermore, conventional SR catalysts are relatively low in cost. The only disadvantage is the required thermal management of the reactor [37]. As a result of these characteristics, and since it is easy to avoid the possible carbon deposits by adjusting the S/C ratio, this process has been chosen for biogas refurbishment for the SOFC CCHP plant. A detailed description of the method is given in Section 2.7.

ATR presents a flexible choice, providing reasonable H_2 and CO yields. The process is catalyzed and involves input streams of both air and water that will react with the fuel stream to produce syngas. Effectively, an ATR combines the exothermic nature of a POX reaction (hydrocarbon

fuel reacting with air) with the endothermic SR reaction to balance the heat requirements. The ATR reaction is [37]:

$$C_xH_y + zH_2O + (x - \frac{1}{2}z)O_2 \rightharpoonup xCO_2 + (x + \frac{1}{2}y)H_2 \tag{2.33}$$

The value for the S/C ratio, here shown as z/x, should be chosen such that the reaction is energy neutral, i.e. neither exothermic nor endothermic. Consequently, the ability to influence the carbon deposits by means of the S/C ratio no longer exists, which precludes the combination with an SOFC. The advantage is a thermally neutral system component, moderate in cost, size and weight requirements. On the downside, a more extensive control system is needed for ATRs to ensure robust operation of the fuel processing system [37].

2.6 Adsorption

It has been known for more than a century that some solids are able to remove colour from solutions which contain dyes. Similarly, air contaminated with unpleasant odours can be made odourless by passing the air though a vessel that contains charcoal. Despite the fact that such phenomena were not well understood before the early twentieth century, they still show the potentials of adsorption technology yet to come [200].

The future significance of the adsorption technology increases through the current development of process engineering towards more selective separations. This has led to a steadily growing number of industrial applications and the development of very specific adsorbents [201]. Adsorption is generally carried out the following ways:

- Discontinuous adsorption in a fixed-bed adsorber. The use of two adsorbent vessels allows a nearly continuous operation (changeover operation of at least two fixed-bed adsorbers, continuous operation with regard to the feed phase, discontinuous operation with respect to the adsorbent).
- Continuous adsorption (moving bed, single or multi-stage fluidized bed, rotary adsorber) [202].

2.6.1 Definitions

Countless chemical, physical, and biological processes usually take place at the boundary between two phases, however, others are being initiated at the interface. The type of phases in contact determine the underlying process which can be attributed to one of the following systems: liquid-liquid, liquid-gas, solid-liquid and solid-gas [203].

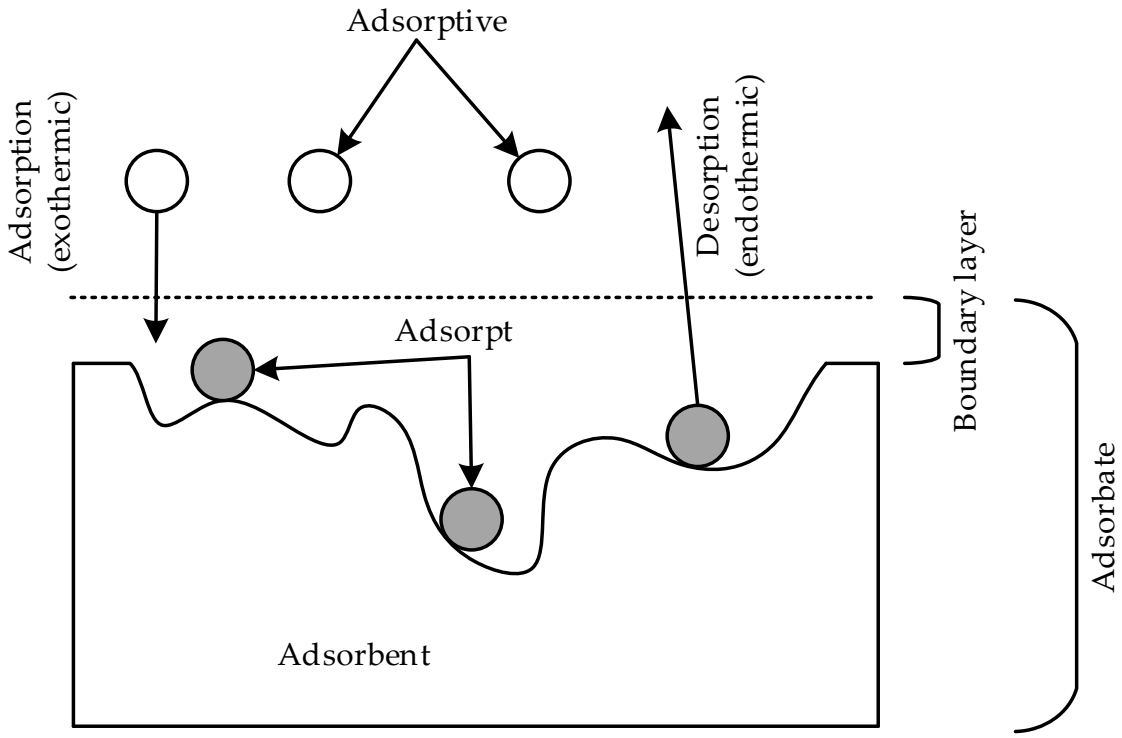

Figure 2.12: Definitions and terms used in adsorption [201].

On a large industrial scale adsorption processes deal mainly with the solid-gas [204] and solid-liquid [205] interfaces, however, in different laboratory separation techniques all of the abovementioned types of interfaces are being used [206].

In adsorption, one or more components (adsorptive) from a fluid (liquid or gas) are attached to solids (adsorbent). The reverse process (removal) is called desorption. So these are mass transfer mechanisms in the two-phase system solid-fluid [207].

$$Adsorbent + Adsorptive \underset{\text{Desorption}}{\overset{\text{Adsorption}}{\Longleftrightarrow}} Adsorbate \tag{2.34}$$

The definitions and terms used are shown in Figure 2.12 and described in Table 2.3.

Adsorption can either be a result from the universal van der Waals interactions (physisorption, physical adsorption) or it can have the characteristics of a chemical process (chemisorption or chemical adsorption). Chemisorption occurs only as a monolayer contrary to physisorption [206]. The physical adsorption process is comparable to the condensation process of the adsorptive. Physical adsorption is a reversible process. At a temperature close to the critical temperature of a given gas, physical adsorption is particularly effective. Chemisorption is a rather specific process that can only take place on some solid surfaces for a given gas. Favourable conditions allow both processes to occur simultaneously or alternatively. Physical

Table 2.3: Definitions and terms used in adsorption [201].

Term	Definition
Adsorption	Addition of a molecule from a gaseous or liquid phase to a solid
Desorption	Removal of an adsorbed molecule from a solid and transfer to fluid phase
Adsorbent	Solid that binds the molecule to be adsorbed
Adsorptive	Molecule to be adsorbed which is in the fluid phase
Adsorpt	Molecule bound to the adsorbent
Adsorbate	Complex of adsorbent and adsorbent

Table 2.4: Differences between physisorption and chemisorption [200].

Parameter	Physisorption	Chemisorption
Temperature	Low	Often high
Adsorption enthalpy	Low	High
Occupancy	Multilayer	Monolayer
Regeneration	Almost completely	Often disabled after use

adsorption results in a decrease in free energy and entropy of the adsorption system. Therefore this process is exothermic [203]. A comparison of the properties between physisorption and chemisorption can be found in Table 2.4.

As with all thermal separation processes, the driving force for adsorption is external imbalance. The system tries in the course of the process to achieve a new state of equilibrium from this imbalance. While the state of this equilibrium is described by thermodynamics, the rate at which the new equilibrium is obtained is determined by the kinetics [201].

2.6.2 Description of the physical process

Adsorption-desorption processes consist of several sub-steps. It is a complex interplay of different convective and diffusive mass transport processes which are coupled with the actual adsorption / desorption, and various heat transfer and heat conduction processes. Usually they consist of seven sub-steps which are shown in Figure 2.13. The description of these processes has been taken from [201].

1. Mass transport to the outer boundary layer ($1 \rightarrow 2$)
   The adsorptive molecule first passes through convective and diffusive transport mecha-

nisms to the boundary layer around the granular adsorbing material.

2. Mass transport through the boundary layer (2 → 3)
   The mass transport through the boundary layer takes place by diffusion. In this case, a linear concentration gradient in the boundary film is usually assumed.

3. Mass transport in the pores of the adsorbent (3 → 4)
   In the pores of the adsorbent, various diffusion mechanisms take place partially parallel, partially in succession. Since sub-steps 2 and 3 are diffusion controlled, they are often grouped together in a simplified model.

4. Adsorption (4)
   The actual adsorption is an exothermic addition of the adsorptive molecule to the adsorbent. If one considers this process as an equilibrium reaction, then this following "reaction equation" obeys:

$$Adsorptive + Adsorbent \rightleftharpoons Adsorbate + Adsorption\ heat \tag{2.35}$$

   Since the actual adsorption is generally not the rate-limiting step, their kinetics are often neglected. It is assumed that it is infinitely fast. The limitation of adsorption processes usually results from slow diffusion processes.

5. Energy transport within the adsorbent (4 → 5)
   The released heat of adsorption is transported mainly by heat conduction to the surface of the adsorbent particle. This sub-step in particular is not very effective in gas-phase processes because the adsorbent materials have (almost) the properties of thermal insulators due to their pore structure.

6. Energy transport through the boundary layer (5 → 6)
   For the heat transport through the boundary layer, the same statements apply as for the mass transport through the boundary layer (2 → 3). Most model approaches attempt to describe material and energy transport in an analogous way.

7. Energy Transport in the bulk Fluid Phase (6 → 7)
   The evacuation of the released energy takes place in the free fluid via convection and heat conduction (analogous to mass transfer).

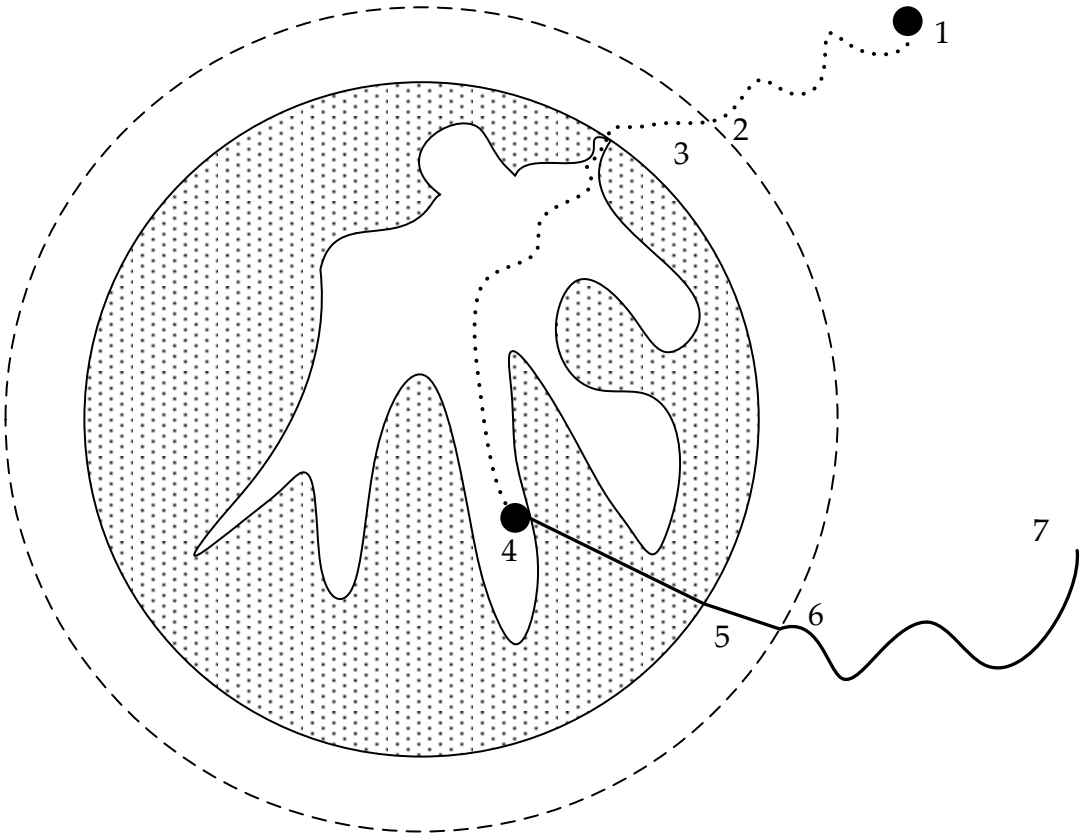

Figure 2.13: Sub-steps of adsorption [201].

2.6.3 Factors affecting adsorption

The following Section gives an overview of the influencing factors which are experimentally investigated in Chapter 3. The investigated effects should be enumerated and their possible effects addressed. The results and the corresponding explanations can be found in Chapter 3. In principle, the factors affecting adsorption can be split into:

- those affecting the rate of adsorption, and
- those affecting the loading capacity of the sorbent [208].

Temperature has a negative effect on adsorption capability, and adsorption capability decreases when adsorption temperature increases, as shown in Figure 2.14. Adsorption reactions are exothermic. Small variation in temperature does not tend to alter the adsorption process to a significant extent. In a thermal separation process, under constant process conditions (pressure, temperature, concentration), a state occurs in which all driving forces for mass transfer come to a standstill. The involved phases are then in equilibrium. The adsorption equilibrium is usually given for a constant temperature (isotherm). The adsorption isotherm describes, depending on the adsorption concentration in the fluid phase, the adsorbed amount of substance or the loading of the adsorbent. In general, the equilibrium load decreases with increasing temperature [38, 201].

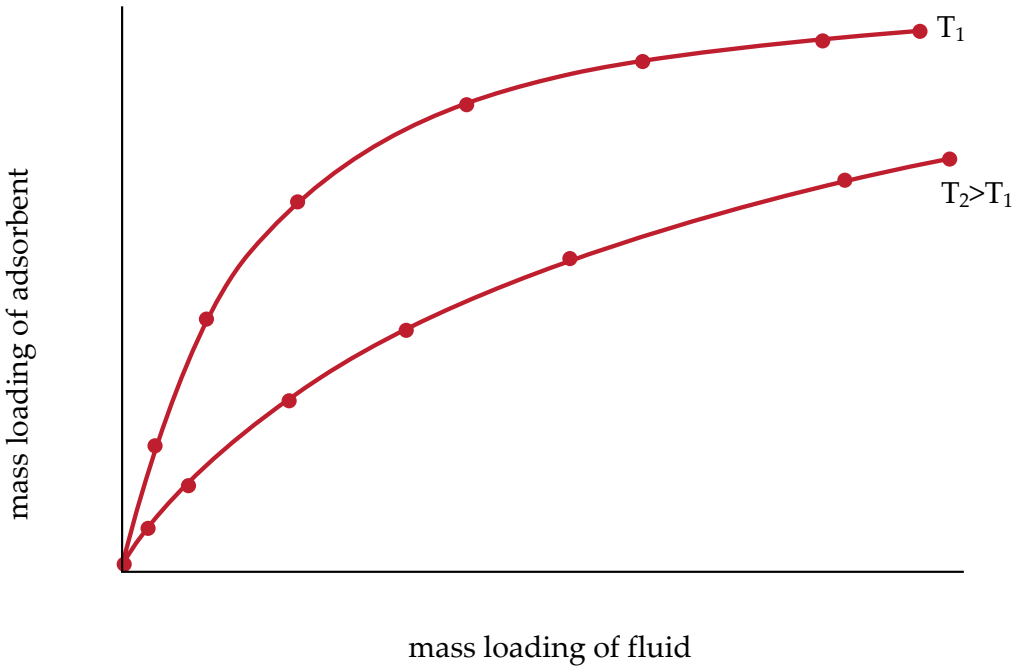

Figure 2.14: Influence of temperature on the loading of the adsorbent [209].

The gas hourly space velocity makes it easier to compare one catalyst to another. $GHSV$ is defined as follows [209]:

$$GHSV = \frac{gas\ flow\ [\frac{m^3}{h}]}{adsorber\ volume\ [m^3]} \tag{2.36}$$

$GHSV$ and performance have an inverse relationship: as the space velocity increases, the performance of the adsorber decreases. This makes sense for a given adsorber volume because as the space velocity increases, the gas flow rate has to increase. Increasing the flow rate results in steeper breakthrough curves and decreasing breakthrough times. This is because of the residence time of the solute in the column, which is not long enough for adsorption equilibrium to be reached at high flow rate. So at high flow rate the adsorbate solution leaves the column before equilibrium is achieved. Furthermore, a fixed saturation capacity of bed based on the same driving force gives rise to a shorter time for saturation at higher flow rate. [209]. Depending on the adsorbent used and the other boundary conditions, this effect may be strong or weak and must be investigated experimentally.

The effect of inlet adsorbate concentration on effluent concentration is shown in Figure 2.15. Four different adsorbate concentrations are shown. All other parameters such as bed height and flow rate are kept constant. For larger feed concentration, steeper breakthrough curves are found, because of the lower mass-transfer flux from the bulk solution to the particle surface due to the weaker driving force. In addition, at high concentration, the isotherm gradient is lower, yielding a higher driving force along the pores. Thus the equilibrium is attained faster for values of higher adsorbate concentration [210].

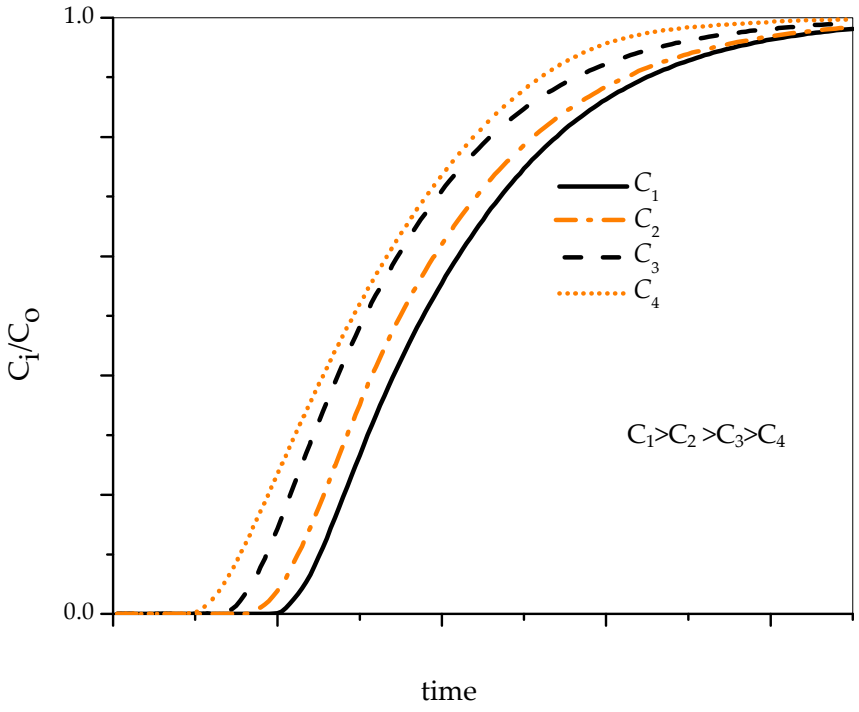

Figure 2.15: Effect of inlet adsorbate concentration on breakthrough curve [210].

The majority of fixed-bed adsorbers are cylindrical, vertical vessels. However, when large volumes of fluid are being treated by small inventories of adsorbent, the pressure drop may become excessive unless the bed height (or depth) is very small. If cylindrical vessels are needed for pressure or ease of fabrication, they have been installed horizontally in such cases with vertical flows. Because of the low pressure drop and the low ratio of bed height to the horizontal dimension, flow distribution is much more critical than in vertical vessels. The flow direction for adsorption in a vertical fixed bed is determined by the potential for lifting or fluidizing the bed. For gas and vapour phase applications velocities which cause crushing of an adsorbent tend to be much higher than those required to lift a bed and therefore it is convenient to arrange to have the highest flowrate in the downwards direction through a vertical bed [200, 211].

There are two major considerations to be made when selecting the particle size of the adsorbent. They are the effects of size on the mass transfer characteristics and on the pressure drop. Pressure drop through packed beds of adsorbent particles is usually predicted by the Ergun equation [212]. Generally, the pressure drop per unit length of packed bed is inversely proportional to the particle size to a power not less then unity. Thus, pressure drop can be reduced by selecting the larger particle size. The mass transfer rate for adsorption is also inversely proportional to the particle size to a power not less than unity. High mass transfer rates are desirable. Therefore, the size of the packed bed can be reduced by selecting the smaller particle size. Since these two criteria are not compatible, trade-offs must be made in the design [211].

2.6.4 Types of adsorbers

The design of an adsorber is essentially determined by its mode of operation, i.e. by the discontinuous or continuous operation. The following description is only an overview of the possibilities and is based on [200, 213].

Discontinuous adsorption operation

The advantages are the simple adsorber design, the proven technology, and the low mechanical and thermal wear of the adsorbent. The disadvantages are the large amounts of adsorbent and desorption aids, the limited dimensions of the adsorber or desorber (possibly forced to operate in parallel), the sensitivity of the adsorbent against dust deposition as well as poisoning and thermal stress. The discontinuous adsorption is usually carried out in containers with fixed bed, honeycomb bodies, annular layer or with a single-stage fluidized bed. The flow should be as even as possible and the fluid phase should be distributed as even as possible in the adsorbent bed to. In this work, only fixed bed adsorbers were used. A fixed bed adsorber is displayed in Figure 2.16.

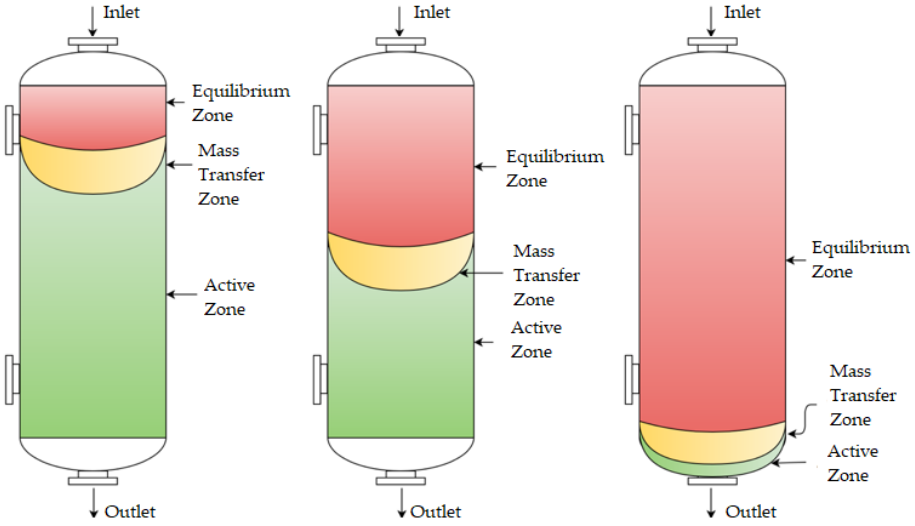

Figure 2.16: Fixed bed adsorber with equilibrium (saturation) zone, MTZ and active zone [214].

The transfer of adsorbate molecules from the feed to the solid initially occurs at the bed entrance as soon as the fluid is passed through a fixed bed of the adsorbent. The zone in which the mass transfer takes places moves progressively through the bed towards the exit, as shown schematically in Figure 2.16, as soon as the adsorbent in this region becomes saturated with the adsorbate molecules. Once the breakthrough of the adsorbate is obtained, it is essential to take the bed off-line in order to regenerate the adsorbent. The pressure drop correlates with the flow rate [200]. A description of the influence of particle size, $GHSV$ and inlet concentration can be found in Section 2.6.3.

Continuous adsorption operation

The advantages (in comparison to discontinuous adsorption operation) are among other things the shorter desorption phase at higher temperatures, the smaller dimensions of the adsorber and the desorber, the lower amounts of desorption and adsorbent auxiliaries as well as the relative insensitivity of the adsorbent against poisoning and dust separation. Among the disadvantages are the higher mechanical wear of the adsorbent as well as the high cost of conveyor technology. Figure 2.17 shows a continuously operated rotating adsorber with eight segments.

Adsorption takes place in six of those segments, whereas the bed in the seventh segment is regenerated by a hot gas while the adsorbent in the bed number eight is cooled by a cold gas. The described adsorption units are often used for the cleaning of waste gases or polluted air. The unique characteristic of a rotating adsorber is that many compact fixed beds can be arranged, and in a distinct bed different process steps such as adsorption, desorption, purging and cooling can be carried out in succession [207].

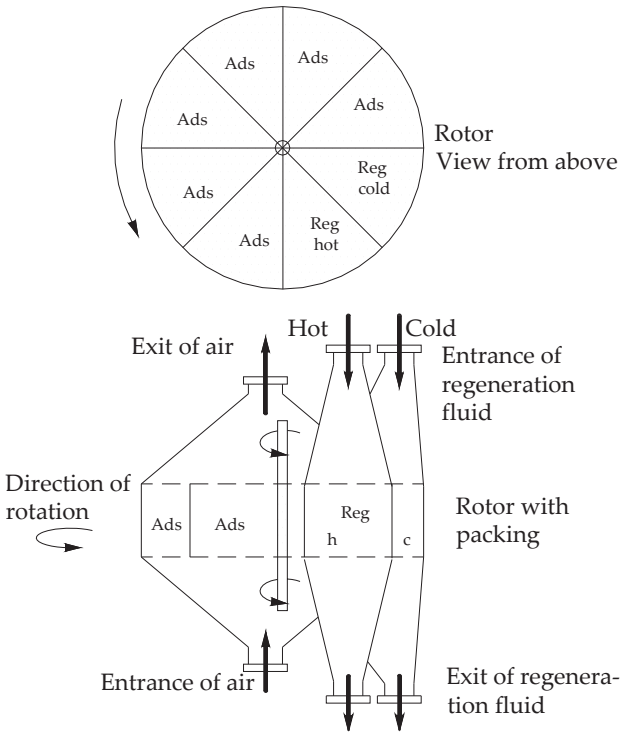

Figure 2.17: Continuously operated rotating absorber for cleaning of waste gas [207].

2.6.5 Adsorbents

In order to prevent the negative effects which H_2S and HCl have on the CCHP system (see Section 2.3), it is essential to clean the biogas. As described in Section 2.5, small-scale systems ($<30\ kW$) are suitable for adsorption-based processes. The suitability is based on the fact that the investment costs are low and the operating costs remain within a moderate range.

To be effective, adsorbents, in addition to their chemical properties, must above all have a high surface area in terms of their volume. The technical adsorbents used are essentially silica gel, activated carbon, molecular sieves and mixed metal oxides. Common among them is the more or less regular, with pores interspersed structure in which the pores are interconnected. The size of the pores is decisive for the adsorption or for the adsorbable components. The pores are subdivided into [200]:

- micropores ($<2\ nm$),
- macropores (2 - 50 nm) and
- mesopores ($>50\ nm$).

The actual adsorptive effect and, thus, the active surface are largely based on the micropores. The adsorptive is transported through the macropores. They can be considered as accesses to the actual active surface. To withstand the process environment, adsorbents are usually

produced in granular, spherical or extruded forms with various sizes ranging mostly between 0.5-8 *mm*. Additional special shapes, e.g. tri-lobe extrudates are also available so that pressure drops can be kept at a low level when the adsorbent is packed into a vessel. Other forms are available for special purposes, such as powders and monoliths. Some adsorbents, particularly zeolites, require a material that acts as a binder in order to provide mechanical strength as well as a suitable macropore structure which enables the adsorbate molecules to gain ready access to the internal microporous structure [200].

In the following, adsorbents used in the experimental part of this work will be discussed. For a detailed examination of the production processes and modes of action of adsorbents, reference should be made to the relevant literature [200, 202, 207].

Activated carbon

The ability to provide adsorptive properties has been attributed to carbonaceous materials for a long time. One of the earliest applications may be the discovery that charred materials could be used to remove tastes, colours and odours from water centuries ago [200]. Depending on the application, activated carbon is supplied in powdered form as so-called powdered coal, in granular form or as cylindrically pressed carbon. In the case of powdery activated carbons, the equilibrium states are reached faster, whereas granulates and cylindrically pressed carbon are technically easier to handle. Compared to inorganic sorbents, activated carbon is an inexpensive sorbent. The surface of carbon is essentially non-polar although a slight polarity may arise from surface oxidation. As a result, carbon adsorbents tend to be hydrophobic and organophilic. They are, therefore, widely used for the adsorption of organics in decolorizing sugar, water purification, and solvent recovery systems as well as for the adsorption of gasoline vapors in automobiles and other air purification systems [215].

The adsorption capacity of activated carbons depends on their physical (porous) structure as well as on their chemical structure. The H_2S adsorption performance of activated carbon improves significantly by impregnating it with basic compounds like K_2CO_3 or sodium hydroxide (NaOH) [216, 217]. The reaction pathways of H_2S on the surface of alkaline materials that may occur are shown below:

H_2S is a diproton acid that reacts with a hydroxyl group like NaOH as follows [216–219]:

$$H_2S + NaOH \rightharpoonup NaHS + H_2O \tag{2.37}$$

or

$$H_2S + 2NaOH \rightharpoonup Na_2S + 2H_2O \tag{2.38}$$

For activated carbons impregnated with K_2CO_3, the following reactions may occur in the presence of H_2S [216–219]:

$$H_2S + K_2CO_3 \rightharpoonup KHS + KHCO_3 \tag{2.39}$$

or

$$H_2S + K_2CO_3 \rightharpoonup K_2S + H_2CO_3 \tag{2.40}$$

Zeolite

Zeolites are minerals that can either be produced synthetically or occur in many different compositions in nature. Zeolites differ distinctly from other sorbents regarding the pore size distribution and the crystal lattice into which the adsorbate molecules can either enter or not. Pore size is completly uniform. Since internal porosity is high, the majority of adsorption takes place internally. This is the reason why zeolites are capable of separating effectively on the basis of size. This is also the reason why they have been assigned the commonly used description of molecular sieves. Differences in molecular size, shape and other properties such as polarity are the basis for processes of adsorption and desorption of molecules in zeolites. Cavities fill and empty reversibly in physical adsorption. This mechanism is generally considered to be one of pore filling. Therefore, the surface area concepts used for other types of adsorbent strictly do not apply. The empirical formula of a zeolite framework is

$$M_{(n/2)} \cdot Al_2O_3 \cdot xSiO_2 \cdot yH_2O \tag{2.41}$$

where x is larger than or equal to 2, n is the cation valency and y represents the water contained in the cavities [200]. By heating the water can be reversibly removed which leaves a microporous structure that may account for up to 50% of the crystals by volume. The oxygen atoms to combined silicon and aluminium atoms ratio is always equal to two and, therefore, a negative charge is introduced by each aluminium atom on the zeolite framework which is balanced by an exchangeable cation. By changing the type and position of the cation the channel size and properties of the zeolite are being changed as well, including its selectivity in a given chemical system. The number of cations per unit cell determine the positions occupied by cations in a framework [200]. So far, about 40 naturally occurring zeolites have been discovered and a further 200-300 synthetic zeolites have been produced [201].

Adsorption technologiy and catalysis are the main field of application of synthetic zeolites. Zeolites facilitate desulfurization at ambient temperature and moderate pressures [94]. Zeolites are crystalline, hydrated aluminosilicates with a defined lattice structure that contains exchangeable alkali metal or alkaline earth metal cations. The lattice structure is composed

of $[SiO_4]^{4-}$- and $[AlO_4]^{5-}$- tetrahedrons as primary building blocks, each having an oxygen atom with each neighbouring tetrahedron. The tertiary structure of the zeolites is formed by a secondary structure. The resulting cavities are connected by windows, which cause the molecular sieving effect of the zeolites due to their size. Because of the steric selectivity, only molecules with a sufficiently small kinetic diameter can penetrate the windows and adsorb in the cages. The various basic frameworks result from the so-called module which is determined by the ratio of SiO_2 to aluminium oxide (Al_2O_3) [200].

Metal oxide

Desulfurization performed over metal oxide based sorbents seems to be an effective way for gas purification. The desulfurization reaction can be written as

$$Me_xO_y + yH_2S \rightharpoonup Me_xS_y + yH_2O \tag{2.42}$$

where *MeO* and *MS* are the metal oxide and metal sulfide, respectively [183, 220, 221]. The desulfurization on the metal oxide can occur with the formation of a solid or liquid phase that contains the sorbent metal and sulfur. Several metal oxides are suitable for desulfurization of fuel gas. Elseviers and Verelst [221] reported that the cleaning capabilities of metal oxides in a temperature spectrum from 80 to 650 °C are as follows: tin (Sn) <Ni <iron (Fe) <manganese (Mn) <molybdenum (Mo) <cobalt (Co) <zinc (Zn) <copper (Cu). ZnO and CuO are the two most favored sorbents. ZnO has been widely used to remove H_2S at temperatures between 300 and 400 °C because of its high equilibrium constant and high sulfur capacity in this temperature spectrum. CuO has an extremely high equilibrium sulfidation constant that allows an extremely low equilibrium constant even at high temperatures [222]. It is reported that iron oxide (FeO) is being used to adsorb H_2S (100 *ppmv*) in syngas and at temperature below 500 °C.

Carbide formation reduces the adsorption performance above the reduction temperature [223]. FeO is cost effective, but non-regenerable. Therefore, substantial volumes of sulfide might be wasted [224]. Other studies have shown that for desulfurization Fe is only appropriate in a moderate temperature range. Therefore, it is commonly used in combination with MnO and Zn in order to enhance the sorbent stability at higher temperature [225].

Apart from Fe, ZnO is also used as H_2S adsorbent at high temperature of about 400 °C leading to an almost complete removal of 10,000 *ppmv* H_2S. Due to sintering, reduction of the active metal into metallic elements, and sulfate formation, which is similar to the other metal-based sorbents, the activity of ZnO-based sorbents is reduced during the regeneration [226, 227]. High volatility and strength, which is necessary for making granular sorbents, are characteristic for ZnO. It is reported that titanite and zinc ferrite are used to decrease Zn volatilization losses in order to obtain a better regenerability of Zn [228]. Nevertheless, zinc titanate sorbents

show a steady decline in the sulfur capacity with further cycling [229]. It is reported that by using mixed oxide of Zn, Co, Ni, and titanium dioxide (TiO_2) with an inorganic binder bentonite to make Zn-Ti based sorbents, H_2S is removed from a gas mixture containing 1.5% H_2S, 11.7% H_2, 9.6% CO, and 5.2% CO_2 balanced with N_2. These sorbents display good sulfur removal capacities at 480 °C, without any indication of deactivation even after 15 cycles of the desulfurization and regeneration processes [230]. Ni and Co are being used as active sites in the sorbents throughout the desulfurization process. Additionally, to avoid any change in the sorbents physical properties, the sorbent structure is stabilized.

By adding Ni, which prevents SO_2 slippage, the regeneration ability of the Zn-based sorbents is increased [230]. Despite its propensity to reduce to the metallic form in the syngas environment and agglomerate, Cu-based sorbents have been increasingly used to adsorb H_2S [231]. In a temperature range of about 550–650 °C, the Cu-based sorbents are developed to adsorb H_2S down to 5 *ppmv*. Solely from a thermodynamic standpoint, chromia (Cr_2O_3) is preferred for the stabilization of CuO contrary to a total reduction to the elemental Cu when it comes into contact with the fuel gas in the designated temperature range [232]. When CuO is doped with Mn-based sorbents, the reactivity and stability is increased, however under thermal stress is observed [233].

Activated alumina

Activated aluminas are granular with particle diameters between 2 *mm* and 10 *mm* in the trade. They are often used for gas and liquid drying. These adsorbents are acid sensitive, but well resistant to weak alkalis. In the gas-phase, activated alumina is widely used for desiccation since it has higher capacity for water than zeolites. However, they compete heavily with molecular sieves, which have high capacities at low vapor pressures. A further application is to remove acidic gases such as HCl and hydrofluoric acid (HF) (Hydrofluoric acid) from air [207, 234].

Activated alumina is widely used as substrate for catalysts and adsorbents. The choice of researchers and refinery operators for this adsorbent was based on the following two reasons:

- Primarily, activated alumina is a highly porous material with large surface area. Simultaneously, the mechanism of HCl adsorption on activated alumina relies on chemisorption as well. Upon consideration of the synergetic effects of chemisorption and physisorption, alumina's surface area and morphology seems to be an integral part in boosting the adsorbent's capacity for HCl removal. Due to the interactions between the polar HCl molecule and polar sites on alumina surface, the process of physical adsorption takes place. However, evidence of HCl chemisorption on alumina surface was found, which may occur through two different paths: firstly, the dissociation of HCl onto Al-O pairs with the formation of Al-Cl species and a new hydroxyl group and, secondly, the dissociation of HCl on the Al-OH pairs with the formation of Al-Cl species and H_2O [235, 236].

- The second reason is that activated alumina was found to remove HCl from both gas and liquid contaminated streams. However, some authors [111] claim that in liquid phase applications this adsorbent is relatively ineffective. They reported that this behavior is a main characteristic of liquid systems with rather low HCl levels, where the diffusion of the contaminant through the liquid film of adsorbed hydrocarbon compounds is hindered [237].

H_2O has a strong influence on HCl adsorption on activated alumina, unlike the sorption on metal oxides. The simple explanation for this is the fact that the H_2O molecule is polar, meaning that it has a dipole moment even higher than HCl. This means that H_2O has to compete with HCl for adsorption on the active hydroxyl groups of the activated alumina surface [238].

2.6.6 Thermodynamics

The basic approach to adsorptive equilibria (loading versus partial pressure) must provide a suitable description of both the equation of state for the fluid phase and the adsorption energy levels due to the various adsorption sites involved. The knowledge of the distribution of the molecules in the fluid phase and on the adsorption sites is the key issue in understanding and describing adsorptive equilibria. Statistical considerations lead to an occupation index for each individual site, dependent on the chemical potential of the gas phase, i.e. its pressure and temperature. However, the statistical approach is different for surface adsorption with only one molecule per energy level, with a restricted number of adsorbed molecules per energy level and with pore condensation. Each approach exhibits a characteristic picture for adsorption isotherms as is apparent in the International Union of Pure and Applied Chemistry (IUPAC) classification of types (Figure 2.18) [234].

Type I is the simplest isotherm and corresponds to unimolecular adsorption as characterized by a maximum limit in the amount adsorbed. Type I describes gases at temperatures above their critical temperature. The more complex Type II isotherm is associated with multimolecular Brunauer, Emmett and Teller (BET) adsorption and is observed for gases at temperatures below their critical temperature and for pressures below, but approaching, the saturation pressure. Type I and II isotherms are desirable, exhibiting strong adsorption [234].

The Type III isotherm displayed in Figure 2.18 is undesirable because the extent of adsorption is low except at high pressures. It corresponds to multimolecular adsorption where heat of adsorption of the first layer is less than that of succeeding layers. In the limit, as heat of adsorption of the first layer approaches zero, adsorption is delayed until the saturation pressure is approached. Types IV and V are the capillary- condensation versions of Types II and III, respectively [234, 239].

The simplest case of adsorption are one-component processes. In the following, the Henry, Freundlich and Langmuir isotherms are discussed. Information on other adsorption isotherms, such as BET isotherm or Toth isotherm can be found in the literature [234, 239, 240].

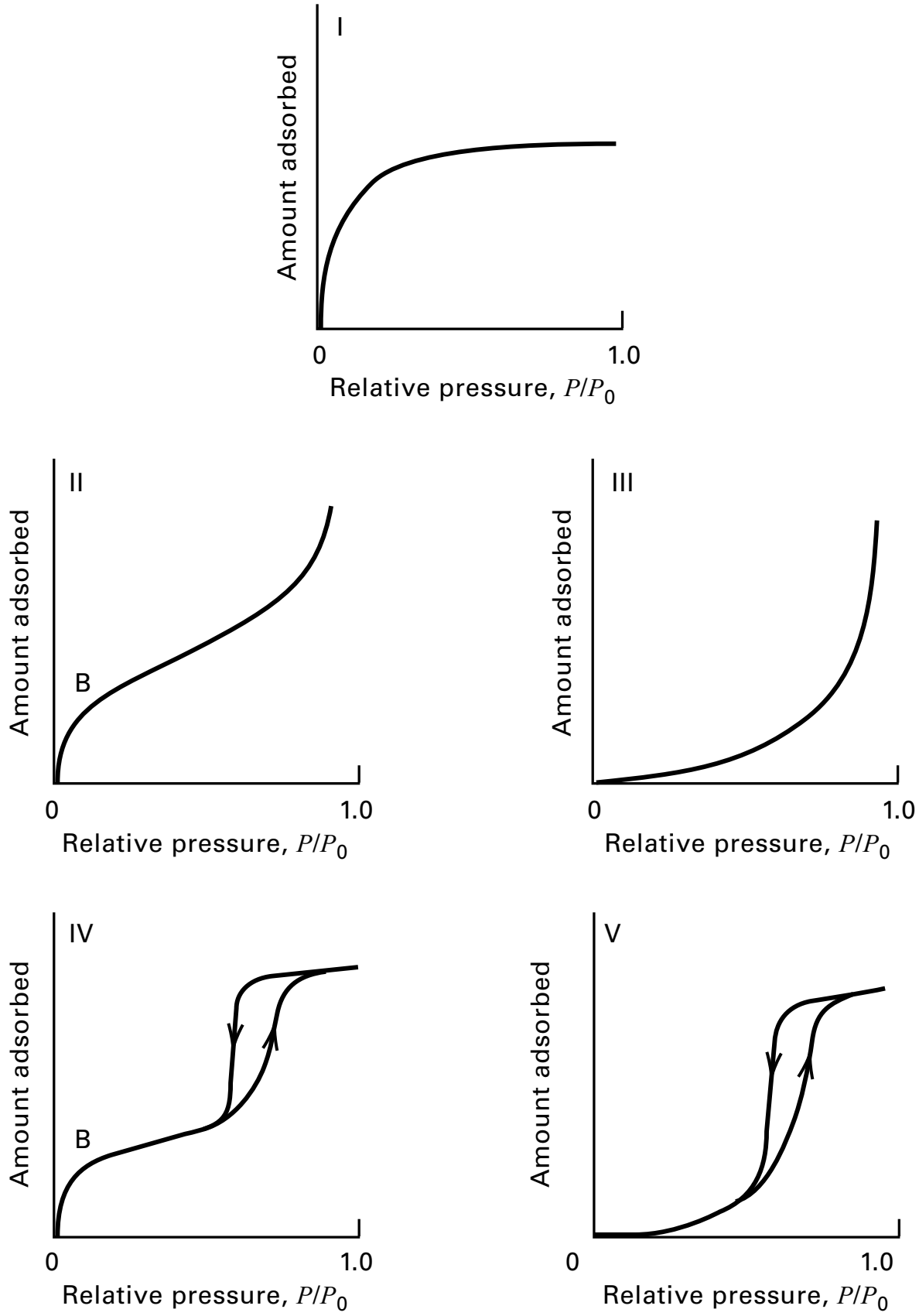

Figure 2.18: Brunauer's five types of adsorption isotherms (p/p_0 = total pressure/vapor pressure) [239].

Henry's adsorption isotherm

The structurally simplest isotherm equation is the one-parameter Henry equation (Equation 2.43):

$$X_E = k_H \cdot p_A \tag{2.43}$$

where X_E is equilibrium loading; k_H is an empirical temperature dependent constant for the component; and p_A is the partial pressure of the species. The amount of the surface adsorbate is represented to be proportional to the partial pressure of the adsorptive gas. As the temperature increases, the amount adsorbed decreases because of Le Chatelier's principle for an exothermic process [234, 239, 240].

Freundlich adsorption isotherm

The equation attributed to Freundlich is empirical and nonlinear in pressure (Equation 2.44):

$$X_E = k \cdot {p_A}^n \tag{2.44}$$

where X_E is equilibrium loading; k and n are temperature-dependent constants for a particular component and adsorbent; and p_A is the partial pressure of the species. Since the exponent must be adapted to the measured data, there is no typical form of the isotherms, but all potential functions are summarized under the collective term "Freundlich-Isotherm". The Freundlich isotherm is generally used to describe the adsorption of gas solid systems having a heterogeneous surface. This is the case provided that the range of adsorbate concentration is not too wide as the isotherm equation does not have a proper Henry's law behavior at low concentration, and it does not have a finite limit when adsorbate concentration is sufficiently high [234, 239, 240].

Langmuir adsorption isotherm

The Langmuir isotherm describes monolayer adsorption on homogeneous flat surface and is restricted to Type I isotherms. It is derived from mass-action kinetics, assuming that chemisorption is the reaction. Langmuirs's isotherm takes the form of (Equation 2.45):

$$X_E = X_{mon} \cdot \frac{b \cdot p_A}{1 + b \cdot p_A} \tag{2.45}$$

where X_E is equilibrium loading; X_{mon} is monomolecular loading; b is the temperature-dependent constant for the component; and p_A is the partial pressure of the species. The basic assumptions for Langmuir isotherm include:

- The adsorbed molecule or atom is held at definite, localized sites;
- Each site can accommodate one and only one molecule or atom;
- The adsorption energy is constant over all sites (homogeneous surface) and there is no interaction between neighboring adsorbate [234, 239, 240].

2.6.7 Capture-capacity

The S_{cap} and Cl_{cap} values of the sorbent samples were calculated using Equations 2.46 and 2.47, which had been used by Novochinskii et al. and Kim et al. [241, 242]. The corresponding nomenclature is given in Table 2.5.

$$S_{cap} = \frac{FR \cdot \int_0^t (c_{in} - c_{out}) \cdot d_t \cdot 32 \cdot 10^{-4}}{V_{mol} \cdot m_{sample}} \tag{2.46}$$

$$Cl_{cap} = \frac{FR \cdot \int_0^t (c_{in} - c_{out}) \cdot d_t \cdot 35.45 \cdot 10^{-4}}{V_{mol} \cdot m_{sample}} \tag{2.47}$$

Table 2.5: Nomenclature for S_{cap} and Cl_{cap} calculation.

Symbol	Description
BT	Breakthrough time in h
t	Time that elapsed after the start-up of sorbent sulfidation
FR	Gas flow rate in L/h
V_{mol}	Gas molar volume in L/mol at standard conditions
c_i	Inlet H_2S/HCl concentration in $ppmv$
c_o	Outlet H_2S/HCl concentration in $ppmv$
32	Molar weight of sulfur in g/l
35.45	Molar weight of chloride in g/l
$1x10^4$	A coefficient necessary for adjusting the units invovled
m_{sample}	Sorbent weight in g
S_{cap}	Sulfur capture capacity in (*g of sulfur)/(per 100 g of sorbent*)
Cl_{cap}	Chloride capture capacity in (*g of chloride)/(per 100 g of sorbent*)

2.6.8 Scale-Up

The scale-up of adsorption processes usually involves changes in flow rates and in the dimensions of the column. A safe way to scale up is to keep the column length constant, however, this is sometimes not feasible. The scale-up of a fixed-bed adsorption focuses on the breakthrough curve for a single column. A fixed bed process represents a cyclic batch system in which the adsorbent bed is saturated and refreshed or regenerated in a periodic manner. Separations in fixed bed processes are conventionally carried out with the gaseous phase moving through a stationary bed of adsorbent particles. An alternative is the moving bed process in which both the gaseous phase and the adsorbent move in a counter current process [202, 239, 243].

Vessels and columns, which hold the adsorbent in a fixed position, provide distinct advantages over their counterparts in which the adsorbent is allowed to move. Firstly, such equipment is simple and relatively inexpensive to fabricate. Secondly, minimal attrition of adsorbent occurs when it remains fixed in a position. Despite the apparent simplicity of fixed beds, they are difficult to design accurately because the progress of the MTZ introduces time into the design equations which brings complications in the design. Although several short-cut design techniques exist, they can vary considerably in their accuracy [239, 243].

Several approaches can be used to scale up fixed-bed adsorption processes [200]. The method described here and used in this work is the length of unused bed (LUB) concept. It allows scale-up based on data from laboratory columns, keeping the particle size and superficial velocity constant. The experiments in Section 3.1 describe a gas feed continuously flowing through a fixed bed packed with the adsorbent. The influence of different parameters is monitored by continuously measuring the concentration of the solute out of the column with time. These experiments normally aim at the determination of the breakthrough point at which the concentration of the solute in the eluent becomes equal to the initial concentration or a specified maximum value and the adsorbent bed becomes saturated with the solute [243].

At first, the adsorbent in the column is fresh with all its adsorption sites. As time passes, some of the adsorption sites are used up and concentration in the effluent rises with time (see Figure 2.19). The efficiency of the column can be explained by means of the breakthrough curves. A breakthrough curve is obtained by plotting column effluent concentration versus time of treatment. The shape of the graphs may vary considerably for different situations. However, in general an S-shaped breakthrough curve is obtained [239, 243].

In discussing the LUB method of scale-up, it is necessary to define t_b (breakthrough time) and t^* (ideal breakthrough time) on a breakthrough curve, which are indicated in Figure 2.19. The break-point time is usually taken at the relative concentration, ($c_i/c_{i,o}$, where $c_{i,0}$ is the feed concentration) of 0.05 or 0.10 [239]. Since only the fluid last exiting the column has this concentration, the average fraction of the solute removed from the start of feeding to the break-point time is usually 0.99 or higher. The ideal adsorption time is the time for breakthrough that would occur if the solute were in perfect equilibrium with the bed of adsorbent, which would

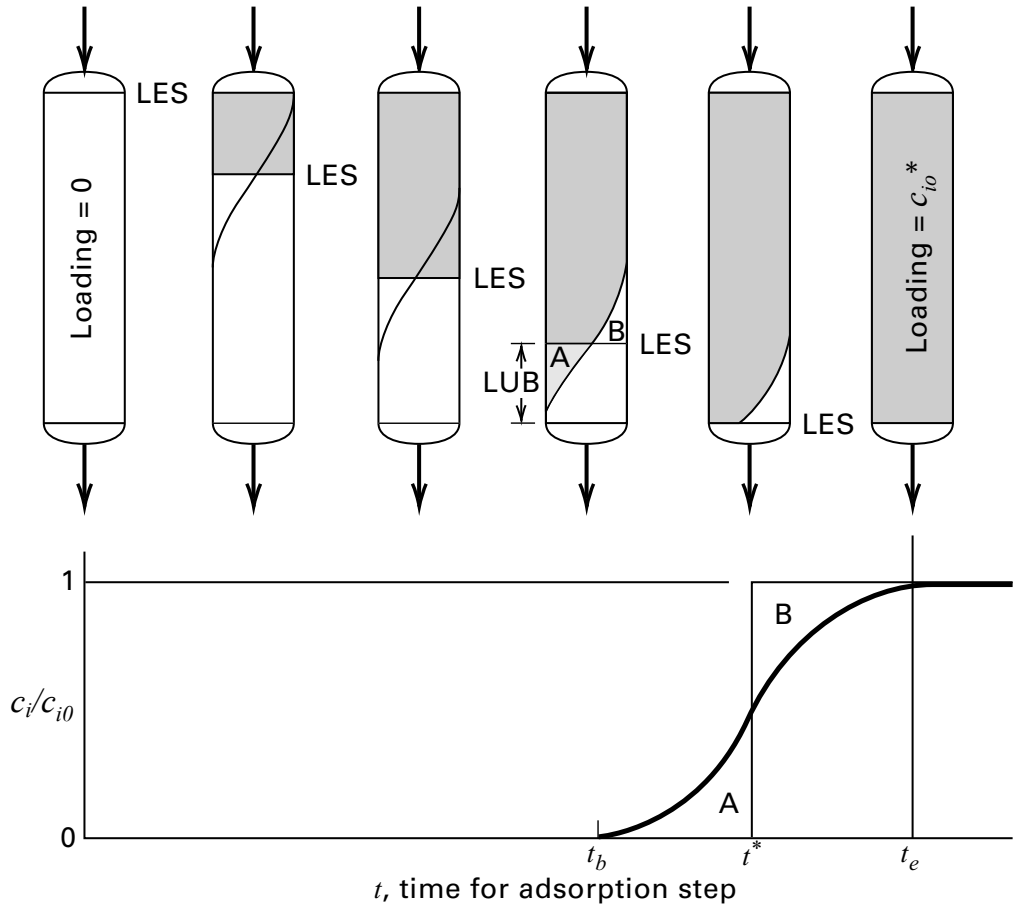

Figure 2.19: Breakthrough curve for a fixed-bed adsorber, showing the break-point time t_b and the ideal adsorption time t*. The ratio of mobile phase concentration of solute to solute concentration in feed to the adsorber is $c_i/c_{i,o}$ [239].

give a vertical breakthrough curve. For a symmetrical breakthrough curve, the ideal adsorption time is the time at which $c_i/c_{i,o} = 0.5$. At the ideal adsorption time for a bed initially free of the solute to be adsorbed, based on a unit area of bed cross section [243]:

$$v * c_{i,0} * t^* = L * \rho_b * q_{i,sat} \tag{2.48}$$

The nomenclature corresponding to Equation 2.48 is given in Table 2.6.

Table 2.6: Nomenclature for adsorber scale-up.

Symbol	Description
L	bed lenght
$q_{i,sat}$	adsorbent phase concentration of solute i
v	superficial velocity
$c_{i,0}$	concentration of solute i in the feed
ρ_b	bulk density of the adsorbent

The ideal adsorption time is, therefore, given by:

$$t^* = \frac{L * \rho_b * q_{i,sat}}{v * c_{i,0}} \tag{2.49}$$

The amount of the solute adsorbed at the break point can be determined by integrating the breakthrough curve up to time t_b as indicated in Figure 2.20. The width of the breakthrough curve defines the width of the MTZ in the bed. For adsorption, where the equilibrium isotherm is favorable, the concentration profile in the mass transfer zone takes on a characteristic shape that does not change as the zone propagates through the bed [243].

At the break-point time, the adsorbent between the inlet of the bed and the beginning of the MTZ is completely saturated (in equilibrium with the solute in the feed). The adsorbent in the MTZ goes from being completely saturated to being almost free of solute, and the adsorbent could be assumed to be on the average about half-saturated. This would be equivalent to half the adsorbent in MTZ being saturated and the other half being unused. The scale-up principle is that the length of the unused bed in the MTZ does not change as the bed length is changed [243]. The LUB can be determined directly from the breakthrough curve obtained experimentally. If $q_{i,b}$ is the average adsorbent phase concentration of solute i at the breakpoint time, then the fraction of bed capacity utilized at the breakpoint time is $q_{i,b}/q_{i,sat}$. Therefore, the unused fraction of the bed is $1 - q_{i,b}/q_{i,sat}$ [243]. From Equation 2.48,

$$\frac{q_{i,b}}{q_{i,sat}} = \frac{t_b}{t^*} \tag{2.50}$$

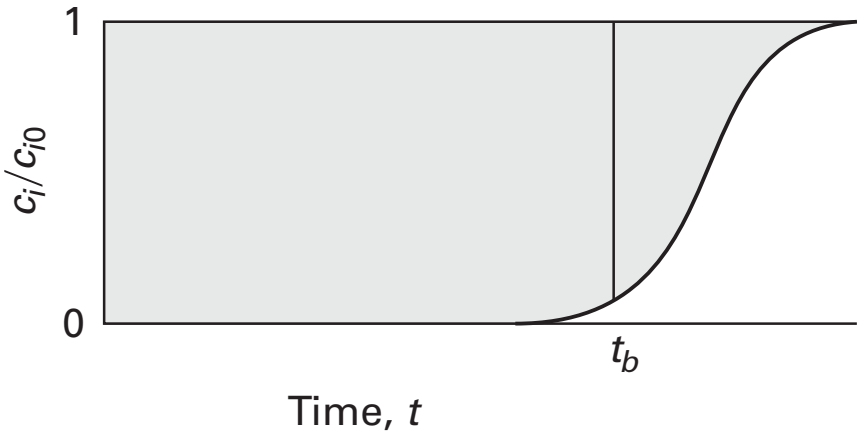

Figure 2.20: Integration of the breakthrough curve for a fixed-bed adsorber. The area of integration to the left of a vertical line at time t is proportional to the amount of solute adsorbed up to that time. The ratio of mobile phase concentration of solute to solute concentration in feed to the adsorber is $c_i/c_{i,o}$ [243].

so that LUB can be written as[239]:

$$LUB = (1 - \frac{q_{i,b}}{q_{i,sat}}) * L = (1 - \frac{t_b}{t^*}) * L \tag{2.51}$$

where t_b and t^* are stoichiometric times determined by integration of the breakthrough curve [239]:

$$t^* = \int_0^\infty (1 - \frac{c_i}{c_{i,0}}) * dt \tag{2.52}$$

$$t_b = \int_0^{t_b} (1 - \frac{c_i}{c_{i,0}}) * dt \tag{2.53}$$

In scale-up calculations, the length of the column required can easily be found by adding the LUB to the length calculated by assuming local equilibrium, with a shock wave concentration front [239].

2.7 Steam reforming

The overall goal of fuel reforming is to convert a hydrocarbon fuel into a H_2 rich gas. SR has to be designed in a way that the capture of heat to sustain its endothermic reaction is possible.

A commonly used SR design is a tubular reformer which consists of a furnace that contains tubes filled with catalysts through which the SR reactants pass. As already described in Section 2.3.1, SOFCs are able to reform CH_4 internally, but as a consequence, carbon deposits, that permanently damage or destroy the cell are observed. Section 2.5 discusses various reforming processes of which SR, when coupled with a SOFC, is the most promising solution. SR catalysts can be gradually poisoned by sulfur compounds in the fuel when they are operated on biogas fuel and other sulfur-containing fuels. In order to solve this problem, many fuel processor subsystem designs include a sulfur removal bed upstream of the fuel reformer to clean the fuel to low sulfur levels (10-15 *ppmv*) [37]. Since the biogas of the SOFC CCHP plant is already purified by adsorption before reforming, this process step is eliminated.

2.7.1 Reactions

The SR process is a key technology for the production of synthesis gas and H_2. SR is the reaction between steam and hydrocarbons resulting in a mixture of H_2, CO, CO_2, CH_4 and unconverted steam. The latter may be replaced by CO_2 as a reactant. The reforming reactions are accompanied by the WGSR. In addition, the potential for carbon-forming reactions on the catalyst and thermal cracking of higher hydrocarbons must be considerated [244]. Hydrocarbon SR is described by Equation 2.54 [155].

$$C_nH_m + nH_2O \rightharpoonup nCO + (n + \frac{m}{2})H_2 \tag{2.54}$$

The thermodynamic equilibrium of this reaction is favored by high temperatures (>400 °C) and low pressure (1 *bar*). This effect can also be seen in Figure 2.21. The CH_4 conversion is plotted on the y-axis, and the associated temperature on the x-axis. In the upper part of the figure, the CH_4 conversions are shown at different S/C ratios at 1 *bar*. In the lower part of the figure, the pressure is increased to 20 *bar*, the remaining parameters stay the same. For all considered S/C ratios, a negative influence of the pressure increase on the CH_4 conversion is shown. At the same time, it can be seen in both cases that an increase of the S/C ratio has a positive influence on the CH_4 conversion [244].

The WGSR reaction (Equation 2.9) can occur, whereby some of the CO is converted to CO_2, with production of one mole of H_2 for every mole of CO converted. Undesirable reactions during SR are as the following [245]:

$$CO + H_2 \rightharpoonup C + H_2O \tag{2.55}$$

$$2CO \rightharpoonup C + CO_2 \tag{2.56}$$

$$CH_4 \rightharpoonup C + 2H_2 \tag{2.57}$$

$$C_nH_m \rightharpoonup nC + \frac{m}{2}H_2 \tag{2.58}$$

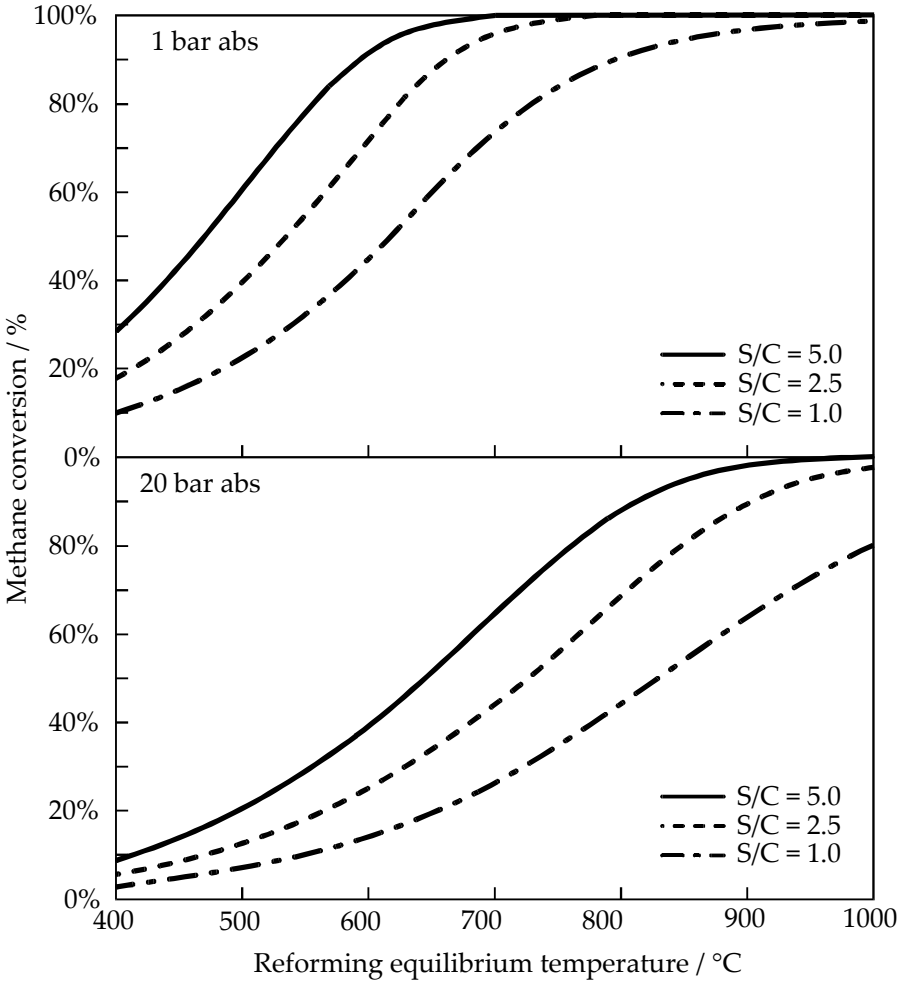

Figure 2.21: SR and CH_4 conversion at 1 and 30 *bar* for different S/C ratios [244].

When used for internal reforming in SOFCs, the above shown and undesirable reactions cause carbon depositions as a result from hydrocarbon pyrolysis (Equations 2.57 and 2.58). This depositions occur especially on the Ni cermet anode [246] as well as on other active components within the system. The thermodynamic minimum S/C ratio for all hydrocarbons is 1.0. However, more practical minimum S/C ratios which are usually required for avoiding the undesirable carbon-forming reactions generally tend to be upward of 1.7 for natural gas and higher for the higher hydrocarbons, e.g. 2.2 for naphtha. Steam is used in industrial practice with S/C ratios ranging from 2.5 for the lighter hydrocarbons to 7 for the hydrocarbons [155].

Common catalysts for SR are group 8 metals, in which Ni is the most widely used. The catalyst

used in the experimental part in this work is a Clariant Reformax 100, which is Ni based [247]. Co and Fe are also active, but Co will be oxidized under normal reforming conditions and Fe requires a strongly reducing atmosphere [155].

2.7.2 Catalyst

Group 8 metals of the periodic system of elements are active for the SR reactions. The preferred choice is Ni. SR catalysts made of Ni have proven industrial performance over many decades regarding their ease of manufacture, activation, stabilization and chemical reactivity [248]. Fe and Co are active as well, but Co will usually be oxidized under normal reforming conditions while Fe requires strongly reducing atmosphere. All these metals are subject to oxidation above a certain H_2O/H_2 ratio, being lower than that predicted by bulk thermodynamics and depending on the specific catalyst (metal particle size, support, etc.) [249]. The main challenges for reforming catalysts are sulfur poisoning, sintering and carbon formation. To some extent, the latter may be related to the first two. To prevent sulfur poisoning, the gas should be purified to a sulfur content of 10-15 *ppmv* before entering the catalyst [37]. Due to the requirement of the SOFC that the H_2S concentration after adsorption should not exceed 2 *ppmv*, the SR catalyst is not endangered by sulfur poisoning. For this reason, the sulfur poisoning of the catalyst will not be discussed further and a referrence to literature is made [250]. Most reformers are operating above the Tammann temperature of Ni ($T_T = \frac{1}{2}T_{melt} = 581°C$) and the catalyst is then being exposed to sintering. This results in growth of the Ni particles and a decrease in Ni surface area and activity. However, the sintering phenomenon is more complex and may take place below the Tammann temperature as well [73, 244].

2.7.3 Carbon formation

Carbon formation is an important factor to be considered in the conversion of hydrocarbon feedstocks either in the fuel processing reactor or in the anode chamber of the SOFC. The three different mechanisms leading to carbonaceous deposits on SOFC anodes have already been discussed in Section 2.3.1. The two main routes of carbon formation during SR, POX and ATR are:

- Hydrocarbon cracking or thermal decomposition (Equations 2.57 and 2.58),
- the Boudouard reaction (Equation 2.11) [155].

Large deposits of carbon on catalysts and metal surfaces can occur since both reactions are catalysed by transition metals. The Boudouard reaction, which dissociates CO to carbon and CO_2, is favoured thermodynamically at temperatures below 700 °C, however it is not kinetically favoured at temperatures below 300 °C. While CH_4 decomposition is favoured at high temperatures (>650 °C), decomposition of higher hydrocarbons usually occurs at much

lower temperatures: a higher carbon number corresponds to a lower activation temperature and, therefore, a higher propensity for carbon formation [246].

A critical problem to be avoided, or at least minimized, is the build-up of carbon on either the reforming catalyst or on the anode, or indeed anywhere else in the fuel supply inlet manifold, since over time this may result in a loss of reforming activity and blocking of active sites on the reforming catalyst and the anode as well as a loss of cell performance and poor durability. In some extreme cases, the growing carbon filaments or whiskers may restrict the flow of gas in the fuel supply system resulting in actual physical blockages and at the same time also push the anode particles apart and reduce conductivity [246].

Carbon deposition through hydrocarbon decomposition mostly occur at the inlet of the reforming catalyst or directly at reforming anode where almost no H_2 is present, and the carbon-forming reactions take place at a faster rate than the carbon-removal reactions. To get the problem caused by carbon deposition from higher hydrocarbons under control, a low temperature pre-reforming stage, which takes place at 250–500 °C, is often used to remove the higher hydrocarbons without carbon deposition. Pre-reforming of higher hydrocarbons can be carried out without resulting carbon deposition at these temperatures [246]. Assuming that thermodynamically graphitic carbon is the only possible condensed phase, carbon deposit propensity decreases with the increase of S/C and oxygen to carbon (O/C). This also enables ways for the carbon removal from the catalyst bed of the fuel processing reactor or the SOFC anode chamber [155].

2.8 Summary

At the end of this Chapter, the research questions submitted at the beginning will be repeated and the corresponding answers will be provided. Detailed answers to the questions are given in Chapter 2 and in the conclusion in Chapter 5. Based on the research questions provided in the Section "Motivation and Purpose of the Work" (Section 1.4) the following answers were found by means of literature research:

- What are the limits of SOFCs with respect to H_2S and HCl? What is the cause of carbon deposits and how can they be prevented? How much does the concentration of H_2S and HCl in biogases vary?

  A H_2S limit in the feed gas of 2 *ppmv* is necessary for SOFCs to prevent degradation of the cell. The limits for the HCl concentration of SOFCs are mentioned in the literature. Based on available data, a limit of 10 *ppmv* HCl was chosen for this work. Carbon deposits in the SOFC are caused by the catalyst Ni, that is used in the anode. Ni is an excellent catalyst for carbon deposition reactions. The use of an external reformer is recommended to supply syngas derived from the SR of CH_4. In order to avoid carbon deposits in the

Ni based reformer, an S/C ratio >2.2 must be selected. According to the literature, the values for H_2S concentration in biogas vary between 50 and 6800 *ppmv*. The concentration of HCl in biogas varies from 0.1 to 25 *ppmv*, depending on the source of biogas.

- Which gas upgrading operation is suitable for the specific requirements of a small scale (7 kW_{el}) SOFC CCHP system?

  Especially for small systems, adsorption opens up a variety of possibilities. If the system is supplied with a different fuel, the adsorbers can easily be adapted to any new pollutants in the biogas. Adsorption is advantageous due to equipment compactness, low energy requirement, low capital investment cost and due to its safety and simplicity of operation.

3
Experimental

This chapter represents the experimental part of this thesis. After discussing the effects of biogas on the catalyst as well as on the SOFC anode in the previous chapter, the focus will be on experiments on the separation of H_2S and HCl by means of adsorption. Various gas mixtures, including synthetic biogas, are used to determine the adsorption behaviour as well as the adsorption capacity of different adsorbents.

The main applications for small systems ($<30\ kW_{el}$) are auxiliary power units, electric utility and decentralized generation. Suitable application areas for SOFC CCHPs, for example, hospitals or server rooms. All parameters of the experiments were set in a way to represent reasonable values for real applications. The obtained results are discussed in a comprehensive manner and provide deeper insights into the adsorption behaviour of the sorbents. This is important and forms the basis for the scale-up of gas purification in Chapter 4. Hence, this chapter is intended to answer research question 3 stated on page 8:

- How is the operation of H_2S and HCl removal influenced by different parameters like temperature, $GHSV$, pollutant inlet concentration and biogas composition?

In addition to gas purification, a functioning SOFC CCHP system requires a reforming step to protect the SOFC anode from carbon deposits. For this purpose, the CH_4 contained in the biogas is converted by SR into a H_2-rich synthesis gas. The commissioning of the SR subsystem and the SOFC stack form the answer to question 4 of page 8:

- Is a successful commissioning of the subsystems (gas purification, steam reforming and 10-cell stack) possible?

The individual systems are integrated in the existing infrastructure and functional tests are carried out.

3.1 Adsorption

Adsorption is the trapping of pollutants on a solid with a high-surface area. The solid is typically an activated carbon, a metal oxide or a crystalline material with high internal porosity (zeolite, activated alumina) whose surface holds the pollutant through intermolecular forces. There are two types of adsorption: In physical adsorption the pollutant molecules are held in place in the pores by relatively weak physical attraction forces. In chemical adsorption strong chemical bonding forces act between adsorpt and adsorbent. The conventional adsorber vessel is a fairly long cylinder that can be installed in either a vertical or a horizontal position. Regeneration steam is frequently introduced from the bottom of the vessel. For continuous processes in which regenerative adsorption is used, two or more adsorbers are installed [184]. A detailed description of adsorption can be found in Section 2.6.

Use of adsorption as separation process in plants in the $<30\ kW_{el}$ power range is given by the following advantages:

- Low investment costs and average operating costs (see Section 2.5 for comparison with other separation methods);
- Adaptation to biogas of different origin or composition (see Table 2.2 for a comparison of different biogas compositions);
- Series connection in a kind of modular system to address different pollutants;
- High separation performance to meet the requirements of SOFCs, more precisely maximum inlet concentration of 2 *ppmv* for H_2S (Section 2.3.2) and 10 ppmv for HCl (Section 2.3.3).

The experimental part on adsorption investigates the effects of different parameters on the separation efficiency. As mentioned in Section 2.4.2 biogas contains H_2S in the range of 50 - 6800 *ppmv* and HCl in the range of 0.1 - 25 *ppmv*. The influence of temperature, gas composition, $GHSV$, humidity, grain size as well as the interaction with the pollutants H_2S, HCl and NH_3 are investigated. This is necessary to investigate the influence of the parameters and, consequently, to design a gas purification unit to protect the SR catalyst and the SOFC. H_2S and HCl pose a threat to the anode of the SOFC, which consists of Ni/YSZ Uncontrolled initiation would result from initial degradation to complete deactivation of the SOFC. A detailed explanation can be found in Sections 2.3.2 and 2.3.3. Similarly, H_2S is also a catalyst poison for the SR because the catalyst used is Ni based. The design of this gas purification unit based on the experimental results, the so-called scale-up, is dealt with in Chapter 4.

At the beginning an overview of the used adsorbents is given. Subsequently, the experiments for determining the influence of the above mentioned parameters are shown in subchapters. The following adsorbents were used for the separation of H_2S from the gas stream:

- Metal oxide based sorbents
  A standard adsorbent for desulfurisation is ZnO. According to the literature a ZnO bed

for H_2S removal should be operated at or over 300 °C [251]. The second metal oxide based sorbent is a mixture of CuO and MnO. According to literature, MnO-based sorbents achieve very good results at high, and CuO-based sorbents at low temperatures [252, 253].

- Impregnated activated carbon
  Impregnated activated carbons are not only characterized by their low price, but can also be adapted to different conditions through targeted impregnation. The used activated carbon is impregnated with K_2CO_3, which allows simultaneous adsorption sour gas components (HCl and H_2S) [34].
- Zeolites
  Zeolites are widely used as adsorbents for removing different chemicals in a variety of processes, as shape-selective catalysts or supports for active metals in the petrochemical industry and as ion exchangers. Zeolites used to capture the molecules are known as molecular sieves which are highly porous. Zeolites are effective for removal of some compounds such as H_2O and H_2S. There are 194 unique zeolites and over 40 naturally occurring zeolites mentioned in literature [254].

Activated carbon and two activated aluminas are used for the separation of HCl:

- Impregnated activated carbon
  The activated carbon used is the same as that used to separate H_2S. The impregnation with K_2CO_3 allows simultaneous adsorption of sour gas components (HCl and H_2S) [34].
- Activated alumina
  Activated alumina sorbent is widely used for HCl removal. The extensive surface structure of an activated alumina exhibits a very high affinity for chlorides. According to literature, it works well in removing HCl so that effluent chloride levels of less than 1 *ppmv* are achievable in properly designed adsorbers [255].

For the separation of NH_3, expected in traces in biogas according to Table 2.2, a sorbent was investigated. The background to this lies in a protection of the other sorbents which are required for H_2S and HCl separation and may be negatively affected by NH_3.

- Activated alumina
  Activated alumina is made from calcined granules of hydrated alumina. The sorbent used is a smooth, spherical adsorbent, custom formulated to provide optimum adsorption capacity for polar organic compounds. The NH_3 molecule is basic and polar in nature. According to the literature activated alumina is a suitable choice for adsorptive NH_3 removal [256].

3.1.1 Effect of temperature, GHSV and inlet concentration on H_2S adsorption [1]

In this test series, two commercially avialable sorbents were investigated for H_2S removal under various conditions, namely extrudates of ZnO and extrudates of a mixture of CuO and MnO. The sulfur capture capacity of the two sorbents was evaluated by varying the reaction temperature and space velocity. The sulfur capture capacity describes the maximum amount of sulfur that an adsorbent can adsorb under given conditions. This value is important in the design of a gas purification unit and also when comparing different sorbents. In addition, two H_2S inlet concentrations (200 and 1000 *ppmv*) were used to simulate different biogas feedstocks and cover the average and maximum H_2S load of biogas from conventional biogas plants. The goal of this test series is to determine the influence of H_2S inlet concentration, reaction temperature and *GHSV* of the ZnO and CuO-MnO sorbents on sulfur uptake. The physical characteristics of the ZnO sorbent and CuO-MnO mixture sorbent are listed in Table 3.1.

Table 3.1: Physical characteristics of ZnO sorbent and CuO-MnO sorbent [258, 259].

Sorbent	ZnO	CuO-MnO
Bulk density [kg/m^3]	1090	650
Pellet size [*mm*]	4.5	1.6
ZnO content [*mass%*]	87-93	0
CuO content [*mass%*]	0	>25
MnO content [*mass%*]	0	>25

The custom-made lab-scale unit to perform desulfurisation experiments included the following parts: a mixed and certified test gas with 200 and 1000 *ppmv* H_2S in N_2, a MFC, a reactor, a programmable heating unit and a gas analyser. A flowsheet of the test rig is represented by Figure 3.1. The feed gas is dosed with a MFC (Vögtlin red-y series). The reactor consists of two stainless steel pipes made of 1.4401 stainless steel in the following dimensions: 26.9 *mm* outer diameter; 21.6 *mm* inner diameter; each *400* mm long and connected with a union connection. The upper part of the reactor is used as a gas preheating zone. Two electric heating tapes coupled to proportional-integral-derivative (PID) controllers and type K thermocouples (mounted on the outer surface of the upper and lower reactor part) ensure gas preheating. The lower reactor part contains the test cell (material: 1.4401, 21.6 *mm* outer diameter; *18* mm inner diameter and *150* mm length) which is suitable for taking up different sorbents. The H_2S concentration in the reactor exhaust stream was continuously monitored with an ABB AO 2000 gas analyser (accuracy 0.05 *ppmv*). The test rig is represented by Figure 3.2.

The built-in calibration cell of the gas analyser allows calibration without the use of reference gases. The control of the MFC and the two programmable heating tapes is achieved with the aid of LabVIEW software. Furthermore, the LabVIEW program was used for recording relevant process data such as temperatures and outlet H_2S concentration. Different types of experiments

[1] Segments of Section 3.1.1 have already been published in Adsorption Science and Technology [257].

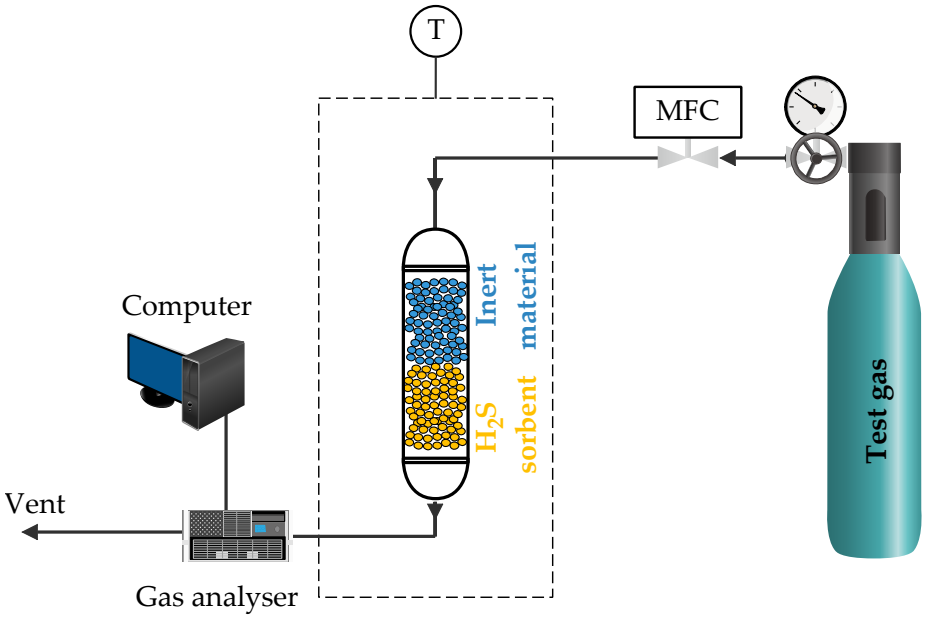

Figure 3.1: Flow chart of adsorption test rig consisting of a test gas, a reactor, a programmable heating unit and a gas analyser.

have been performed using the ZnO sorbent and the MnO–CuO mixture sorbent. At different temperatures and different *GHSV*, 200 and 1000 *ppmv* H_2S in N_2 test gas was passed through the sorbent bed and the outlet H_2S concentration was measured for a 30 minutes period. This investigation was carried out to find out the maximum sulfur capture capacity from the sorbents under different conditions. During typical test runs, sorbent pellets were loaded into the test cell and reactor temperature was varied. A layer of inert material was placed on top of the sorbent to ensure a homogeneous plug flow profile of the gas flow (see blue pellets in Figure 3.1). The *GHSV* was varied through the amount of sorbent pellets, or in other words, through the height of the reactor. While the reactor was heated up to the desired temperature, the reactor was purged with N_2. After reaching the operating temperature, the gas was fed into the reactor and data logging started. Before entering the gas analyser, the gas stream passed a sample gas cooler consisting of a temperature controller, a heat exchanger and a peristaltic pump. The test duration in this series of measurements was 30 minutes per sorbent. It should be noted that in the charts engraved in this series of measurements, the y-axes have different scales. However, direct comparisons with charts placed next to each other always have the same axis limits.

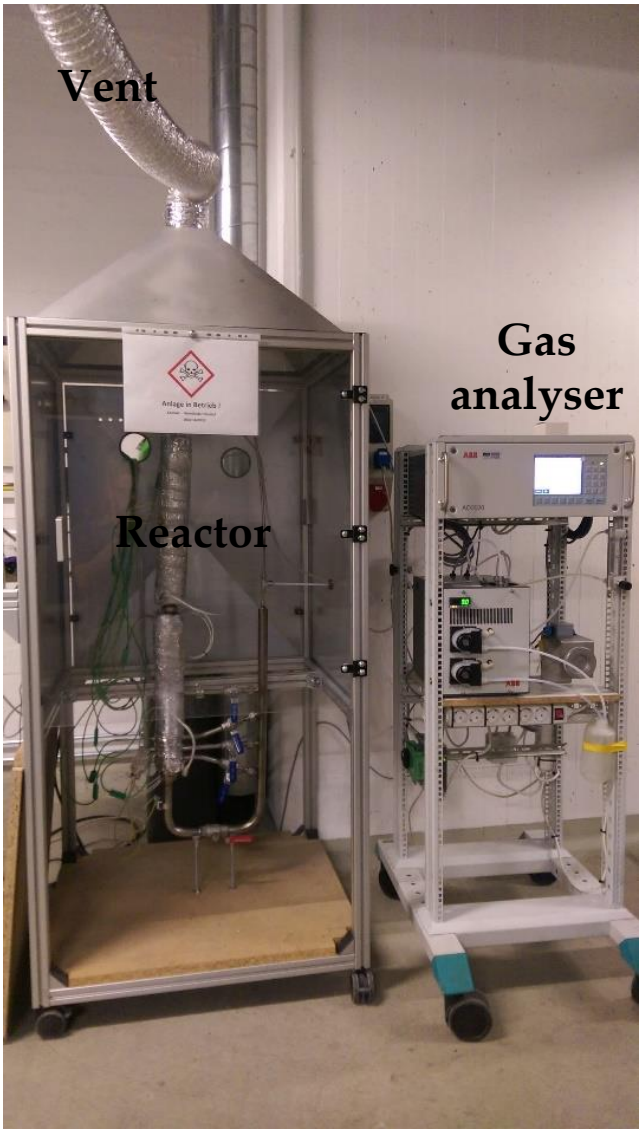

Figure 3.2: Test rig for adsorption experiments.

Effect of the reaction temperature

Experiments were conducted at different temperatures to determine the optimum temperature providing the highest sulfur removal efficiency. The sulfur removal efficiency ($S_{removal}$) of the sorbent used is defined as the amount of H_2S adsorbed at the sorbents surface related to the amount of H_2S passed through the reactor during the test run. Inlet H_2S concentration as low as 200 *ppmv* was selected to simulate a biogas feedstock with average sulfur content. The results of adsorption experiments showing the effect of temperature are shown in Figure 3.3. The horizontal dashed black line at 2 ppmv H2S marks the limit concentration for the SOFC. The effect of reaction temperature on H_2S outlet concentration of ZnO sorbent (left) and CuO-MnO sorbent (right) can be seen. The H_2S outlet concentration for both sorbents decreases when the temperature is increased.

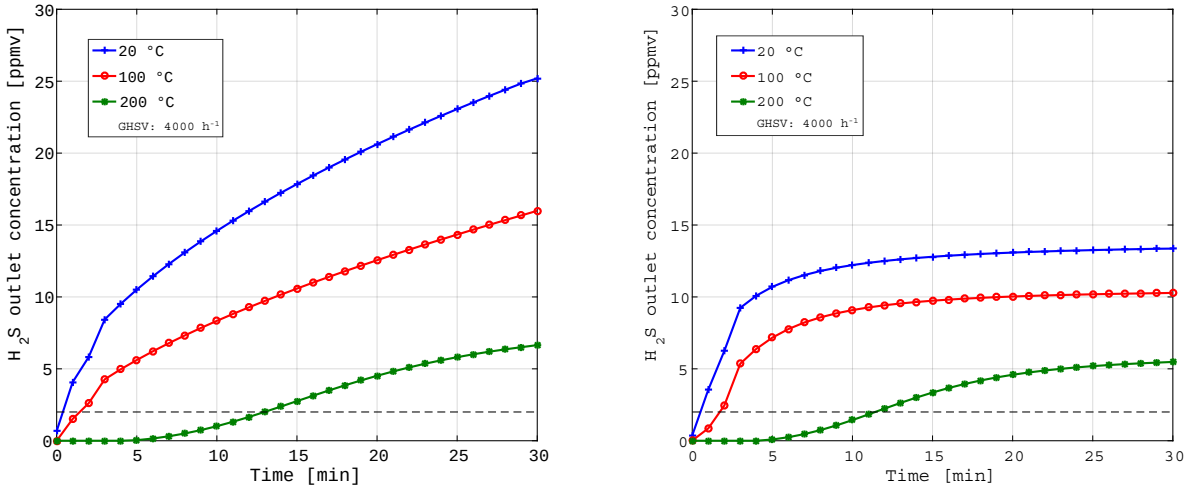

(a) ZnO sorbent

(b) CuO-MnO sorbent

Figure 3.3: Effect of reaction temperature on H_2S outlet concentration; $GHSV$ 4000 h^{-1}; H_2S inlet concentration 200 *ppmv* in N_2.

An increase of the reaction temperature from 20 °C to 200 °C led to a decreased H_2S concentration at the reactor outlet. In numbers, the removal efficiency increased from 91.93% to 98.72% for ZnO and from 94.26% to 98.71% for the CuO-MnO sorbent. The sulfur removal efficiency for ZnO extrudates observed in this study is in line with the literature [241]. The fact that the sulfur removal efficiency is not as high as in the cited literature might be result of the following reason: The reaction of ZnO with H_2S is favoured kinetically as the temperature increases. Kim et al. [241] achieved a sulphur removal efficiency of 99.99% at 363 °C. An attempt to reproduce this result failed due to the reactor material used (1.4401). This alloy contains 10-13% Ni, which reacts with the H_2S at elevated temperatures [260]. A preliminary test at 250 °C already resulted in a sulfur imbalance. For the sorbent consisting of CuO-MnO no comparative data was found in the literature. Wang et al studied various CuO adsorbents at room temperature for their ability to separate H_2S [253]. They concluded that overloading a sorbent with CuO (>50%) could not further increase the sulfur uptake. This means that an appropriate CuO content is required for the sorbent to achieve optimal performance. MnO is well known to achieve good results in adsorptive H_2S separation up to temperatures of 600 °C [252]. Another fact that must be considered in the influence of temperature is: The efficiency of sulfur removal is kinetically favoured at higher temperatures, while the equilibrium is restricted to lower temperatures. The operating temperature influences both the diffusion rate and the thermodynamic equilibrium [260].

Effect of GHSV

Figure 3.4 shows the effect of $GHSV$ upon H_2S outlet concentration on ZnO sorbent and CuO-MnO sorbent. All test runs were carried out with a test gas with 200 *ppmv* H_2S concentration

(balanced with N_2) and at a reaction temperature of 20 °C. Increasing space velocity from 4000 h^{-1} to 8000 h^{-1} elevated the H_2S outlet concentration dramatically from 25 *ppmv* to 70 *ppmv* for the ZnO sorbent after the monitored 30 minutes. Increasing the space velocity from 8000 h^{-1} to 12,000 h^{-1} had little impact and only slightly increased the H_2S outlet concentration from 70 *ppmv* to 84 *ppmv* after the monitored time span of 30 minutes. These results propose that S_{cap} of ZnO is restricted by the contact between gas and sorbent in the fixed bed reactor at higher *GHSV*s. A comparison with the literature [241] confirms the sensitivity of ZnO against increasing *GHSV*s.

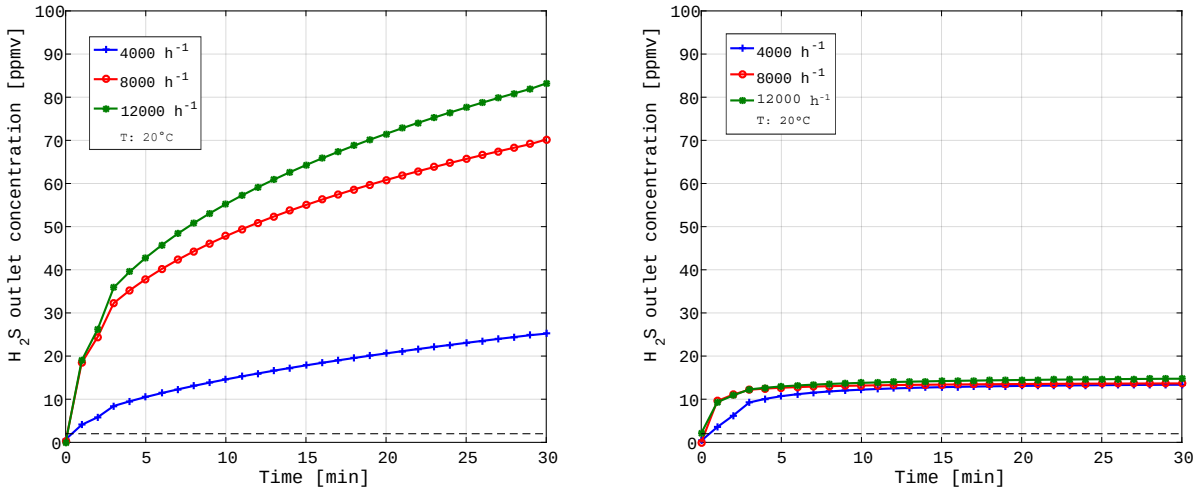

(a) ZnO sorbent

(b) CuO-MnO sorbent

Figure 3.4: Effect of *GHSV* on H_2S outlet concentration; reaction temperature 20 °C ; H_2S inlet concentration 200 *ppmv* in N_2.

On the right side of Figure 3.4 the obtained test results for the CuO-MnO sorbent are shown. It was found that the impact of the space velocity is minor, compared to the experimental runs with ZnO extrudates. Doubling the space velocity from 4000 h^{-1} to 8000 h^{-1} elevated the H_2S outlet concentration from 12.5 *ppmv* to 13 *ppmv* after 30 minutes. Increasing the space velocity up to 12,000 h^{-1} only slightly increased the outlet concentration by about 1 *ppmv*. Comparing the curves on the right side, indicates that the gas solid contact has no limiting effect at the tested *GHSV*s. An increase of the space velocity from 4000 h^{-1} to 12,000 h^{-1} led to a decreased sulfur removal efficiency from 91.93% to 70.77% for ZnO sorbent. Increasing the space velocity from 4000 h^{-1} to 12,000 h^{-1} for the CuO-MnO sorbent slightly decreased the sulphur removal efficiency from 94.26% to 93.28%. The effect of *GHSV* on H_2S adsorption performance at constant temperature and H_2S concentration led to the following conclusion: The adsorption efficiency is highly *GHSV* dependent for ZnO sorbent admitting that kinetic factors are crucial for this type of sorbent. A lower *GHSV* had beneficial effects on the ZnO sorbent performance. The conversion of H_2S with ZnO are strongly dependent on operational conditions. Increased conversion can be achieved using lower *GHSV*s, and higher temperatures. On the other hand, in the case of the CuO-MnO sorbent, there is no significant influence on

the *GHSV*s investigated. From this it can be concluded that the kinetics of ZnO are slower than those of CuO-MnO, or that ZnO requires a longer contact time between the gas and the adsorption zone [261].

Effect of H_2S inlet concentration

Figure 3.5 shows the effect on H_2S outlet concentration for test gases with 200 and 1000 *ppmv* H_2S inlet concentration. Increasing the inlet concentration from 200 to 1000 *ppmv* H_2S in N_2 on the ZnO extrudates had major impact on the H_2S outlet concentration. In numbers, the H_2S outlet concentration increased from 22 *ppmv* to 270 *ppmv* after 30 minutes. The graph on the right side shows the impact of increasing the inlet concentration on the CuO-MnO sorbent. The increase of the H_2S inlet concentration resulted in an increase of the outlet concentration from 12 *ppmv* to 68 *ppmv*. The horizontal dashed black line at 2 *ppmv* H_2S marks the limit concentration for the SOFC (see Section 2.3.2).

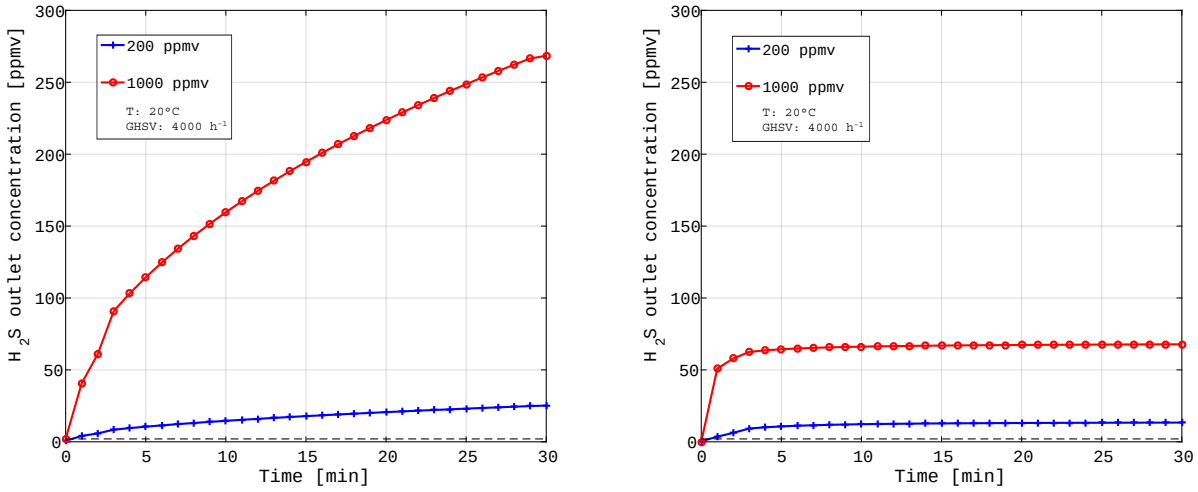

(a) ZnO sorbent **(b)** CuO-MnO sorbent

Figure 3.5: Effect of 200 and 1000 *ppmv* H_2S in N_2 inlet concentration on H_2S outlet concentration; reaction temperature 20 °C ; *GHSV* 4000 h^{-1}.

It can be seen that CuO-MnO sorbent reaches a kind of steady state after 5–6 minutes while ZnO still shows an increase after 30 minutes. For CuO-MnO sorbent the removal efficiency decreases from 94.3% to 93.5%. The H_2S removal study done by Xiao et al. [262] showed that at low concentration, lower mass-transfer flux from the bulk to the surface of sorbent takes place. On the other hand, higher inlet concentration increases the driving force along the pores, hence resulting in higher adsorption capacity. According to [261], besides the effect of driving force and mass transfer flux the adsorption could be limited by the rate of molecular diffusion into deeper pores.

Maximum sulfur capacity

All the tests carried out under different operating conditions for 30 minutes give an idea how the modification of one parameter affects the H_2S outlet concentration. Long time experiments at 20 °C, a $GHSV$ of 4000 h^{-1} and a H_2S inlet concentration of 1000 *ppmv* were performed to characterize the maximum S_{cap} of the sorbents. According to literature, such experiments were never actually carried out until complete saturation of the sorbent. Often, experiments are stopped when the initial concentration is 10-50% of the input concentration. The missing data is then extrapolated. After 22 hours, a H_2S outlet concentration of about 970 *ppmv* was measured in both sorbents (see Figure 3.6). Since these values changed only slightly or not at all, the experiments were stopped. The results can be seen in Figure 3.6 and Table 3.2. The CuO-MnO sorbent showed the best S_{cap} with 180.1 (*mg sulfur/g adsorbent*). The ZnO was measured and calculated at 46.3 (*mg sulfur/g adsorbent*). This difference between the S_{cap} values can be explained as follows. Already in the previous experiments it turned out that CuO-MnO sorbent shows a better performance for H_2S separation than the ZnO sorbent. The chosen conditions regarding temperature and $GHSV$ do not seem to be optimal for ZnO. The value determined for ZnO agrees with results in the literature [241, 242], for CuO-MnO no comparative values could be found in the literature. The S_{cap} value of the sorbent samples was calculated using Equation 2.46 (see Section 2.6.7).

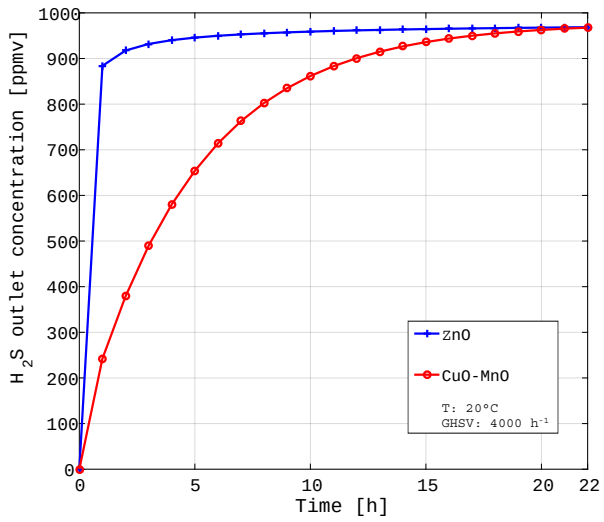

Figure 3.6: S_{cap}; Reaction temperature 20 °C; $GHSV$ of 4000 h^{-1}; H_2S inlet concentration 1000 *ppmv*.

Table 3.2: Calculated S_{cap} values for ZnO sorbent and CuO-MnO sorbent. Reaction temperature 20 °C; $GHSV$ of 4000 h^{-1}; H_2S inlet concentration 1000 *ppmv*.

Sorbent	ZnO	CuO-MnO
S_{cap} $[mg/g]$	46.3	180.1

3.1.2 Influence of gas composition and moisture on H_2S adsorption [2]

Three commercially obtainable sorbents were evaluated for H_2S removal: A K_2CO_3 impregnated activated carbon, a mixture of CuO-MnO and a CuOdoped zeolite. As explained in Section 3.1.1, the ZnO sorbent was not further investigated since the focus of this PhD thesis is on low temperature adsorption processes. ZnO shows its adsorption potential at elevated temperature. The S_{cap} was evaluated considering different gas mixtures at 60 °C and a $GHSV$ of 8000 h^{-1}. The test runs focus on the desulfurisation performance which was monitored by concentrating on the influence of CH_4, CO_2, N_2, and H_2O. Therefore, all test runs were carried out with a relative humidity ϕ_{H_2O} = 20% and humid. As stated in Section 2.4.5, the amount of H_2O in the biogas depends on how much H_2O can be present before the gas becomes saturated with H_2O. There are reports in the literature that moisture has a negative influence on the adsorption and reduces the adsorption capacity of the sorbents [241, 242, 263]. Furthermore, studies on breakthrough behavior and S_{cap} of the adsorbents were carried out leading to an optimized adsorption process. The physical characteristics of the commercially available sorbents are listed in Table 3.3.

Table 3.3: Physical characteristics of K_2CO_3 impregnated activated carbon, CuO-MnO sorbent and CuO doped zeolite [259, 264, 265].

Sorbent	K_2CO_3 impr. AC	CuO-MnO	Cuo doped zeolite
Bulk density [kg/m^3]	570	650	500
Pellet size [*mm*]	4	1.6	1.6
C content [*mass%*]	>50	0	0
CuO content [*mass%*]	0	>25	<25
MnO content [*mass%*]	0	>25	0
Al_2O_3 content [*mass%*]	0	0	>75

In order to investigate the influence of various biogas components, different test gases were used. The gas mixtures were mixed and bottled by a commercial supplier. A test gas consisting of 200 *ppmv* H_2S in N_2 was used as reference since this fraction of H_2S describes the average H_2S contamination of a biogas (see Table 2.2) .The other gas mixtures contain the same amount of H_2S beside CO_2 and CH_4, the main components of biogas. The accuracy of the certified mixtures was $\pm 3 ppmv$ H_2S. Barcia et al. [266] studied the adsorption and separation of CO_2, CH_4, and N_2 on a metal-organic framework. It was found that the intracrystalline diffusivity for CO_2 is one order of magnitude faster than for CH_4 and N_2. On the other hand, Yang et al. [267] examined different zeolites for their CO_2, CH_4, and N_2 adsorption properties. They found that zeolites show good selectivities for CO_2 and CH_4 because they have narrow pores or more balanced metal ions. Due to the observation that CH_4 and CO_2 seem to have an impact on H_2S adsorption and the circumstance that few to no data regarding their influence on activated

[2] Segments of Section 3.1.2 have already been published in Chemie Ingenieur Technik [222].

carbon or CuO-MnO sorbent is available, the influence of those compounds had to be analysed. Therefore, the influences of five different gas mixtures were examined. Mixture 1, consisting of N_2 and H_2S, represents the reference mixture. Mixtures 2 and 3 were used to investigate the influence of CO_2 or CH_4. The 19.98 vol% N_2 in these two mixtures are the result of mixing these gases in a ratio of 4:1 (pure CO_2 or CH_4/1000 *ppmv* H_2S in N_2). Mixtures 4 and 5 represent synthetic biogases whereby mixture 4 does not contain H_2 and O_2. According to Table 2.2, the CH_4 content of biogas varies from 35-65 vol% and the CO_2 content from 25-45 vol%. A large part of this concentration range is covered by gas mixtures 2 to 5. Gas mixtures 2 and 3, which contain 80 vol% of CH_4 or CO_2, serve to facilitate the identification of the impact of the respective component. The composition of the different gas mixtures are listed in Table 3.4. To investigate the impact of humidity, experiments were carried out with a relative humidity ϕ_{H_2O} = 20% and dry (ϕ_{H_2O} = 0%). In order to achieve these ϕ_{H_2O} = 20%, the gas mixtures were passed through a water-filled bubbler placed inside a heating thermostat.

Table 3.4: Composition of the gas mixtures.

Gas mixture	Mix 1	Mix 2	Mix 3	Mix 4	Mix 5
H_2S [*ppmv*]	200	200	200	200	200
N_2 [*vol%*]	99.98	19.98	19.98	0	0
CO_2 [*vol%*]	0	80	0	40	40
CH_4 [*vol%*]	0	0	80	59.98	57.98
H_2 [*vol%*]	0	0	0	0	0
O_2 [*vol%*]	0	0	0	0	0

The lab-scale test setup unit, constructed to perform desulfurisation experiments, included the following parts: mixed and certified test gases, MFCs, a bubbler, an adsorber, a programmable heating thermostat unit, and a gas analyser. A flow chart of the test rig is shown in Figure 3.7. The bubbler and adsorber are placed in the heating thermostat (Lauda type ECO) which is filled with water. Thermocouples connected to PID controllers ensure that the water and, therefore, the bubbler and the adsorber are at a steady-state temperature. The feed gases are dosed with MFCs (Vögtlin red-y series). The adsorber is made of a glass reactor which is 100 *mm* long and has an inner diameter of 17 *mm*, which is suitable for taking up different sorbents. The switch to an adsorber made of glass was done to exclude interactions of the H_2S with the Ni contained in the steel reactor. In order to achieve uniform gas distribution, a layer of inert material is placed on top of the sorbent. All pipes following the mass flow controller are made of polytetrafluoroethylene (PTFE) to avoid undesired reactions between sulfur and potential alloyings. To prevent a possible falsification of measurements, the H_2O in the bubbler was saturated with CO_2 before starting experiments with CO_2. The H_2S concentration in the gas stream at the reactor outlet was continuously measured with an ABB AO 2000 gas analyser. The control of the MFC and the heating thermostat as well as the recording of process data is achieved with LabVIEW.

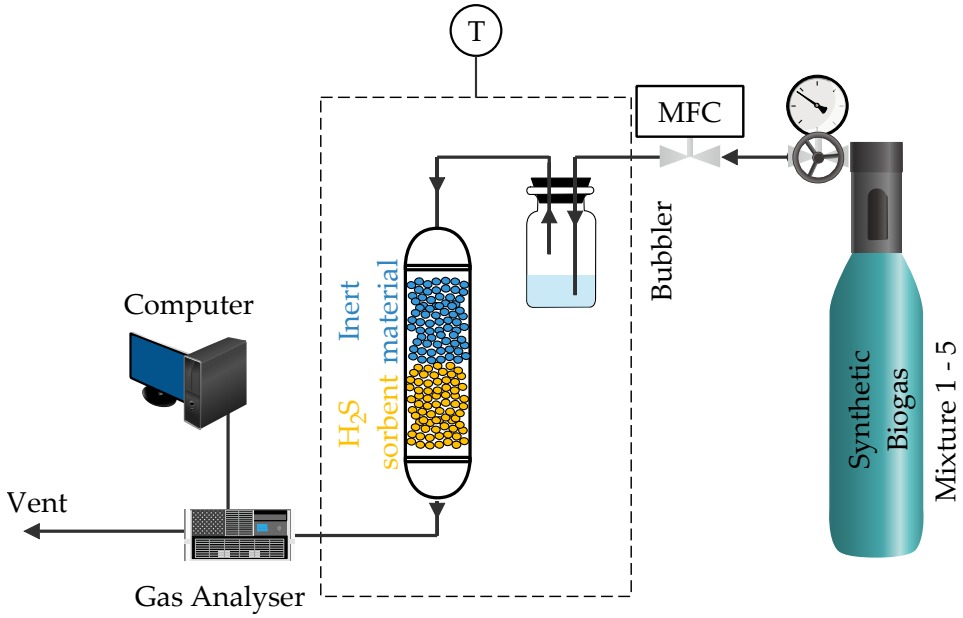

Figure 3.7: Flow chart of adsorption test rig consisting of a synthetic biogas, a bubbler, a reactor, a programmable heating thermostat and a gas analyser.

During typical test runs, sorbents were loaded into the adsorber, and the adsorber was mounted into the heating thermostat. In order to obtain comparable results, the adsorber was loaded with sorbents to achieve a $GHSV$ of 8000 h^{-1}. While heating up the reactor to the desired temperature of 60 °C, the adsorber was purged with N_2. After reaching the operating temperature, the gas mixtures were fed into the adsorber and data logging started. The flue gas from the adsorber was cooled in a sample gas cooler and was then passed through a moisture-trapping filter before passing the gas analyser. To eliminate differences and measurement errors, all measurements were carried out twice. All results were very well reproducible. The S_{cap} values were calculated according to Equation 2.46.

K_2CO_3 impregnated activated carbon

Breakthrough experiments usually take a substantial amount of time. In order to accelerate test runs, the breakthrough point was defined as 10% of the H_2S inlet concentration of 200 *ppmv*, i.e., after reaching 20 *ppmv* H_2S outlet concentration, experiments were stopped. According to literature, this procedure is often used in adsorption experiments [200]. In the following diagrams, this limit is represented by a horizontal line at 20 *ppmv* H_2S. In addition, the horizontal line at a H_2S concentration of 20 *ppmv* is used to calculate the breakthrough time. The line at 2 *ppmv* H_2S marks the limit for the SOFC. In Section 2.3.2, the H_2S tolerance of the SOFC was set at 2 *ppmv* based on literature data. The results of desulfurisation experiments showing the effect of gas composition on activated carbon are shown in Figure 33. All test runs were performed at a reaction temperature of 60 °C and a space velocity of $GHSV$ of 8000 h^{-1}.

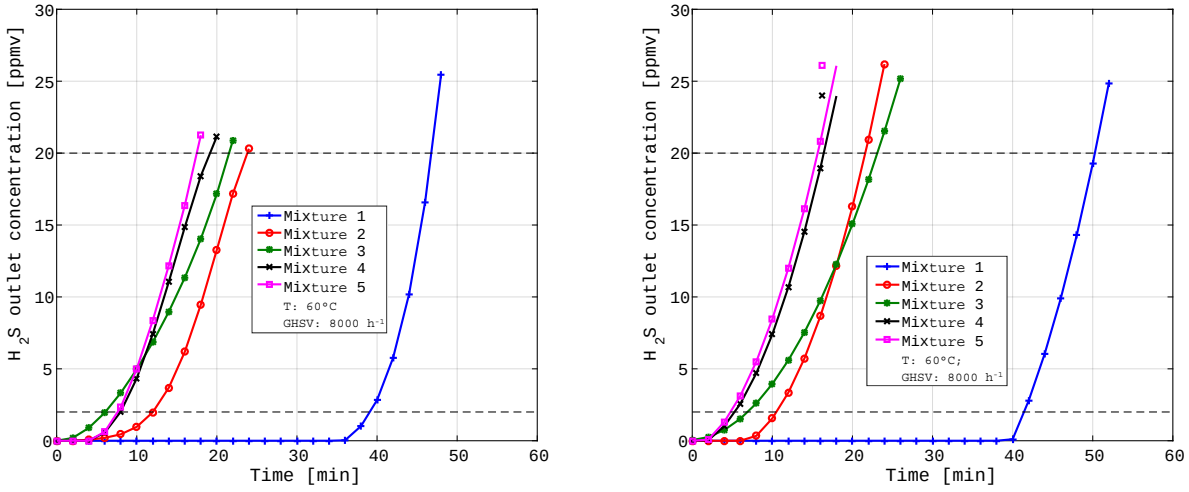

(a) Dry gas (ϕ_{H_2O} = 0%) **(b)** ϕ_{H_2O} = 20%

Figure 3.8: Effect of gas composition on H_2S outlet concentration of impregnated activated carbon. Temperature 60 °C; $GHSV$ of 8000 h^{-1}; H_2S inlet concentration 200 *ppmv*.

For the experiments without moisture, the following results were obtained: The best desulfurisation performance was achieved with gas mixture 1, containing 200 *ppmv* H_2S in N_2. The breakthrough was achieved after 46.5 *min*. Gas mixture 2, which contained 80 vol% CO_2 plus N_2 and 200 *ppmv* H_2S, did show the breakthrough after 23.7 *min*. The other gas mixtures broke through in the following order having a gap of about 2 *min* between each other. The third mixture to break through was gas mixture 3, followed by gas mixture 4 while gas mixture 5 had the last breakthrough. Comparing Figure 3.8 left and right leads to the following conclusion: The 20 vol% steam content has no negative influence on the adsorption performance of activated carbon. Upon comparison of gas mixtures 2 and 3, it seems that CH_4 has a slightly higher negative impact on H_2S adsorption performance than CO_2. Comparing gas mixtures 4 and 5 leads to the conclusion that 1 vol% H_2 and O_2 have a rather small negative influence on H_2S adsorption performance. According to the literature the presence of CO_2 and/or CH_4 may weaken the catalytic activity of the impregnated activated carbon [263]. Huang et al. [160] concluded that a ϕ_{H_2O} >50% in the gas stream significantly affects H_2S adsorption capability of impregnated activated carbon. The reasons could be attributed by both physic-sorption and chemi-sorption view points. The concurrent adsorption between H_2S and H_2O onto impregnated activated carbon might occur when the feed gas stream is humid. According to the Le Chatelier's principle, the binding reactions are unfavourable to proceed whenever water exists on the impregnated activated carbon [160].

Table 3.4 compares the results between dry and humid gas mixtures. While using gas mixture 1, S_{cap} decreased from 2.92 *mgS / gAds* for dry gas to 2.91 *mgS / gAds* for humid gas. The usage of gas mixture 5 resulted in a S_{cap} of 1.07 *mgS / gAds* for dry gas and 0.98 *mgS / gAds* for humid gas. In addition, the measured breakthrough times are given. Although the same breakthrough times are shown for mixtures 1 and 2, there are slight differences in S_{cap} and $S_{removal}$.It can

be seen that there is almost no difference between the results with and without steam. These results are in line with literature data [268, 269].

Table 3.5: Results for impregnated activated carbon. Temperature 60 °C; $GHSV$ of 8000 h^{-1}; H_2S inlet concentration 200 *ppmv*.

	Dry (ϕ_{H_2O} = 0%)					ϕ_{H_2O} = 20%				
Gas mixture	1	2	3	4	5	1	2	3	4	5
$S_{removal}$ [%]	99.33	97.53	96.55	96.93	97.20	98.95	97.77	96.68	96.69	96.77
S_{cap} [mg/g]	2.92	1.46	1.32	1.17	1.07	2.91	1.43	1.27	1.08	0.98
BT [min]	46	23	21	19	17	46	23	20	17	16

CuO-MnO sorbent

Figure 3.9 shows the results of desulfurisation experiment investigating the effect of gas composition on CuO-MnO sorbent. Comparing the results with the experiments carried out with impregnated activated carbon or zeolite, the breakthrough time after 22-27 h for the dry experiments and 5-12 h for the experiments with ϕ_{H_2O} = 20%, indicates the great performance of this sorbent. All test runs were performed at a reaction temperature of 60 °C and a space velocity of $GHSV$ of 8000 h^{-1}. Gas mixture 1 with 200 *ppmv* H_2S concentration, balanced with N_2, achieved the best desulfurisation performance, breaking through after 27.2 h for the dry run and 12 h for the run with ϕ_{H_2O} = 20%.

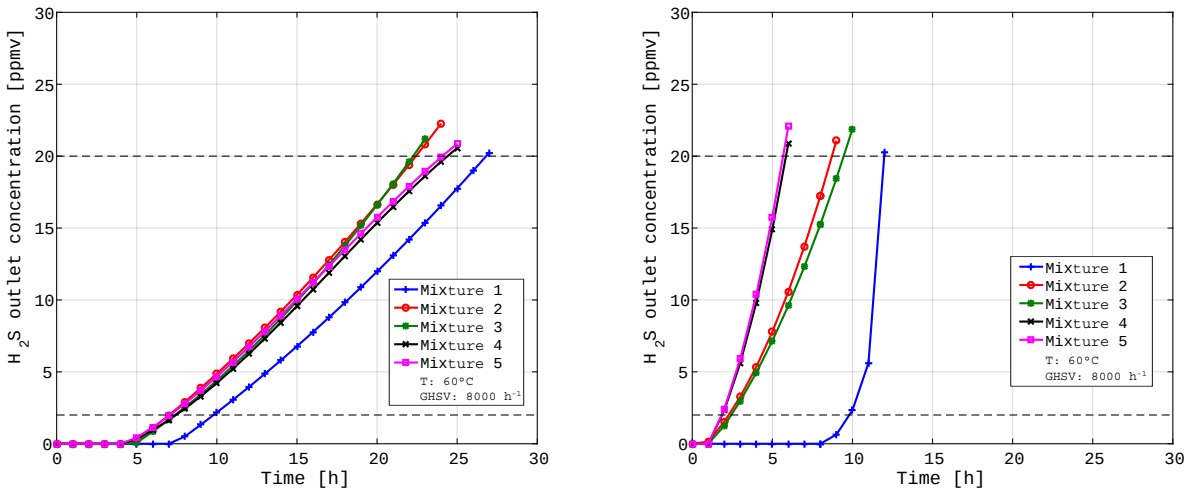

(a) Dry gas (ϕ_{H_2O} = 0%)

(b) ϕ_{H_2O} = 20%

Figure 3.9: Effect of gas composition on H_2S outlet concentration of CuO-MnO sorbent. Temperature 60 °C; $GHSV$ of 8000 h^{-1}; H_2S inlet concentration 200 *ppmv*.

When using dry gas mixture 1, the CuO-MnO sorbent achieved a breakthrough time of 27.2 h. Breakthrough times of 22.1 to 24.3 h were measured for the dry gas mixtures 2-4. Comparing

Figure 3.9 left and right side exhibits the fact that there is a major influence of steam content on the CuO-MnO sorbent. The breakthrough time dropped from 27.2 to 12 h for gas mixture 1 and from 24.1 to 5.9 h for gas mixture 5. Comparing the experiments with and without steam, S_{cap} decreased from 76.66 to 40.84 $mgS\ /\ gAds$ for gas mixture 1 and from 71.00 to 18.96 $mgS\ /\ gAds$ for gas mixture 5. Comparing the values for the breakthrough time, S_{cap}, and $S_{removal}$ (Table 3.6), it is evident that steam has a substantial influence on the desulfurisation performance of CuO-MnO sorbent. In addition, the significant difference to the previously investigated activated carbon should be pointed out. For the activated carbon, breakthrough times between 16 and 43 minutes were measured (see Table 3.5). Breakthrough times between 5.9 and 27.2 hours were measured under the same conditions for the CuO-MnO sorbent (see Table 3.6).
The addition of steam to the test gas mixtures resulted in a significant decrease of the parameters (S_{cap}, breakthrough time) in each gas mixture. Due to the fact that there was no data available, the results could only be compared with results from other metal oxide based sorbents. Novochinskii et al. [242] investigated the influence of steam on the H_2S separation efficiency of ZnO and came to the following conclusion: An increase in steam (H_2O) concentration decreases the H_2S capture and can cause the release of previously captured H_2S, because of a shift in the equilibrium of the reaction. Yazdanbakhsh et al. [270] investigated the influence of steam on H_2S adsorption performance of CuO based sorbent. They concluded that the presence of water vapor in an inert gas stream containing 500 $ppmv$ H_2S promotes the reduction of copper on the surface. Experiments performed at 700 °C led to the conclusion that the presence of moisture virtually eliminates the H_2S capacity for the adsorbent. X-ray diffraction (XRD) patterns for the reacted sample confirmed the presence of elemental copper on the surface.

Table 3.6: Results for CuO-MnO sorbent. Temperature 60 °C; $GHSV$ of 8000 h^{-1}; H_2S inlet concentration 200 $ppmv$.

	Dry (ϕ_{H_2O} = 0%)					ϕ_{H_2O} = 20%				
Gas mixture	1	2	3	4	5	1	2	3	4	5
$S_{removal}$ [%]	96.64	96.41	96.56	96.29	96.22	98.63	96.26	96.16	97.05	97.10
S_{cap} [mg/g]	79.66	67.35	67.18	72.04	71.00	40.84	29.79	32.32	19.51	18.96
BT [h]	27.2	22.2	22.1	24.3	24.1	12.0	8.7	9.5	5.9	5.9

CuO doped zeolite

Figure 3.10 shows the effect of different gas mixtures on the H_2S outlet concentration using a CuO doped zeolite for desulfurisation. As already observed with impregnated activated carbon and CuO-MnO sorbent gas mixture 1 achieved the best desulfurisation performance. CH_4 has only minor influence on the adsorption performance compared to N_2 whereas CO_2 seems to have a major impact in case of the zeolite. Compared to gas mixtures 1 and 2, CO_2 drops the breakthrough time from 117.4 and 108.5 to 76.5 minutes. Comparison of gas mixtures 4 and 5 shows that the influence of 1 vol% H_2 and 1 vol% O_2 seems to be negligible. Furthermore, it

can be seen that there is no influence of steam on the adsorption capacity of zeolite for gas mixetures 4 and 5.

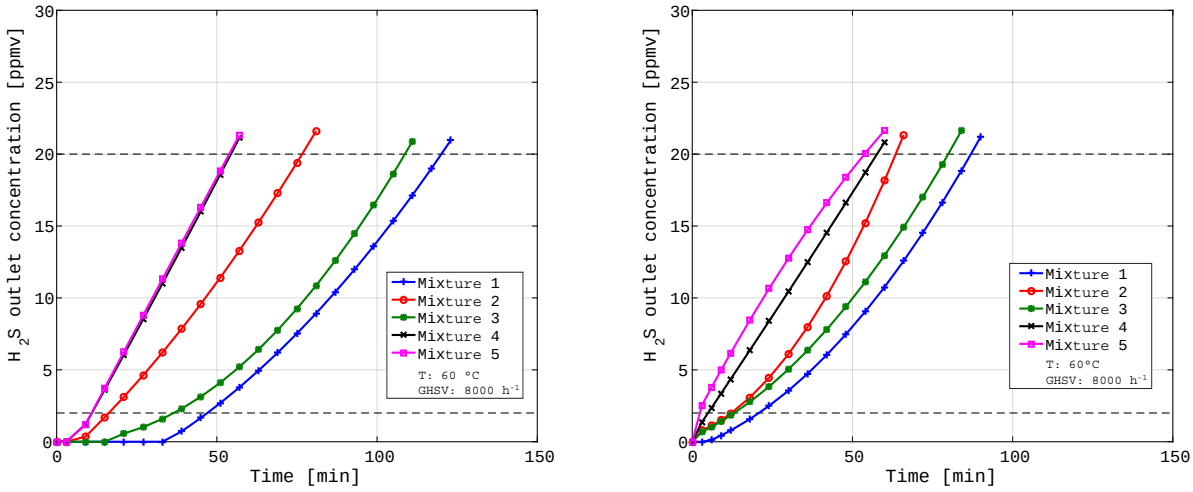

(a) Dry gas (ϕ_{H_2O} = 0%)

(b) ϕ_{H_2O} = 20%

Figure 3.10: Effect of gas composition on H_2S outlet concentration of CuO doped zeolite. Temperature 60 °C; $GHSV$ of 8000 h^{-1}; H_2S inlet concentration 200 *ppmv*.

Table 3.7: Results for CuO doped zeolite. Temperature 60 °C; $GHSV$ of 8000 h^{-1}; H_2S inlet concentration 200 *ppmv*.

	Dry (ϕ_{H_2O} = 0%)					ϕ_{H_2O} = 20%				
Gas mixture	1	2	3	4	5	1	2	3	4	5
$S_{removal}$ [%]	96.30	95.28	96.28	94.97	94.94	95.67	95.26	95.25	94.33	93.67
S_{cap} [*mg/g*]	7.15	4.61	6.61	3.31	3.323	5.15	3.53	4.88	3.49	3.26
BT [*min*]	117	76	108	55	53	85	58	81	58	55

Comparing the values for the breakthrough time, S_{cap}, and $S_{removal}$ (see Table 3.7), the influence of steam on the desulfurisation performance of CuO doped zeolite for gas mixes 1 - 3 can be seen. On the other hand, there is little to no influence for gas mixes 4 and 5. S_{cap} of CuO zeolite decreased from 7.15 to 5.15 *mgS / gAds* by moisturising gas mix 1. Passing dry and moisturised gas mix 5 through the reactor resulted in S_{cap} of 3.23 *mgS / gAds* for the dry gas and 3.26 *mgS / gAds* for the moisturised gas, respectively. The CuO doped zeolite shows a significant difference in breakthough time to the investigated CuO-MnO sorbent. Breakthrough times between 5.9 and 27.2 hours were measured for the CuO-MnO sorbent (see Table 3.6). Under the same conditions, breakthrough times between 53 and 117 minutes were measured for the CuO doped zeolite (see Table 3.7).

Steuten et al. [268] showed that the adsorption of H_2S is influenced by CO_2 and CH_4 contained in the gas mixture. When comparing adsorption of binary and ternary gas mixtures, a significant reduction of H_2S adsorption capacity was observed in latter one. This illustrates the strong

influence of competing compounds on H_2S adsorption. The zeolites MS4A and MS5A are able to adsorb CO_2 as well as H_2S [271]. Due to the increased H_2S outlet concentration which was observed by using gas mixes with CO_2, it seems obvious that a coadsorption of CO_2 was carried out besides H_2S.

Summary

The experiments carried out in Section 3.1.2 with K_2CO_3 impregnated activated carbon, CuO doped zeolite and CuO-MnO sorbent led to the following conclusions. The highest breakthrough time and S_{cap} results were obtained for both dry and humidified gas with the CuO-MnO sorbent. In the best case (gas mixture 1, dry), a breakthrough time of 27.2 hours and a S_{cap} of 79.66 mg/g was achieved. Switching to a humidified gas (ϕ_{H_2O} = 20%) reduced the breakthrough time to 12 hours and the S_{cap} to 40.84 mg/g (see Table 3.6). Even if there is a desulfurization performance gap between the gas mixtures for the dry case, it seems that the presence of CO_2, CH_4, O_2 and H_2 only has a minor influence. On the other hand, the experimental runs with humidified gas resulted in a major difference for the desulfurization performance between the gas mixtures.
Although the K_2CO_3 impregnated activated carbon has achieved lower breakthrough times and associated lower S_{cap} values, one advantage must be emphasized. The activated carbon was insensitive to the moisture in the gas. In comparison (gas mixture 1, dry and ϕ_{H_2O} = 20%) the breakthrough time of 41 minutes remained unchanged and S_{cap} reduced from 2.92 to 2.91 mg/g. The presence of CO_2 and/or CH_4 seems to inhibit the H_2S adsorption performance of activated carbon. On the other hand, comparing the adsorption performance between gas mixture 4 and 5 leads to the conclusion that the presence of O_2 and H_2 has a negligible influence on H_2S adsorption performance.
The desulfurization performance of CuO doped zeolite for the gas mixtures 1-3 dropped by around 20% after adding steam. On the other hand, there is little to no influence for the gas mixtures 4 and 5. A significant reduction in capacity of H_2S adsorption can be found in the literature when comparing a binary mixture to a ternary gas mixture [268]. It seems that a gas mixture containing 40 vol% CO_2 and around 58 vol% CH_4 are more steam tolerant than a mixture with 80 vol% CO_2 or CH_4 and 19 vol% N_2 (see Table 3.7). For the CuO-MnO sorbent and the CuO doped zeolite, breakthrough time and S_{cap} deteriorated due to the presence of moisture in the gas (see Tables 3.5, 3.6 and 3.7). Although the CuO doped zeolite showed better breakthrough times than the activated carbon, the gas mixtures 1-3 showed a negative influence of the gas moisture.

3.1.3 Influence of NH_3 on H_2S adsorption [3]

Besides H_2S and HCl, NH_3 is another impurity present in biogas (Table 2.2). The cited sources assume an NH_3 content up to 100 *ppmv*. The anaerobic degradation of proteins leads to the formation of NH_3 in biogas (see Section 2.4.8). The following experiments investigate the influence of NH_3 on H_2S adsorption and, thus, provide useful data for designing the SOFC CCHP systems gas cleaning unit. NH_3 can be considered as fuel for SOFCs. Due to the high operating temperature of the FC, the NH_3 is reformed directly in the cell. NH_3 decomposes into N_2 and H_2 over Ni-based cermet anode, and subsequently the generated H_2 is electrochemically oxidized to produce steam and electron [273]. Ni et al. [274] performed experiments with NH_3-powered SOFCs and came to the following conclusion: NH_3 is a technically feasible fuel for direct use in SOFCs. The influence of NH_3 on sorbents used for H_2S separation is unclear. No data was found in the literature either for activated carbons or for the other sorbents examined in this thesis. However, the influence of NH_3 on the adsorbents for H_2S separation must be investigated when operating the SOFC with biogas.

The physical properties and composition of the examined sorbents is given in Table 3.8. The K_2CO_3 impregnated activated carbon, CuO-MnO sorbent, CuO-doped zeolite and the MnO-doped zeolite (consisting of Al_2O_3, SiO_2, MnO and manganese carbonate (MnCO3)) were used to purge H_2S from the synthetic biogas feed. These adsorbents have already demonstrated their ability to separate H_2S in previous experiments. The activated alumina sorbent was used in a series of experiments to remove NH_3 from the gas stream in a pre-connected stage. The described sorbent is made up of spheres of promoted activated alumina derived from Al_2O_3 with large surface areas and specifically engineered pores. Activated alumina will preferentially adsorb highly polar molecules such as NH_3 [34].

Table 3.8: Physical properties of the used sorbents.

Sorbent	K_2CO_3 impr. AC	CuO-MnO sorbent	CuO doped zeolite	MnO doped zeolite	Activated alumina
Bulk density [kg/m^3]	570	650	500	560	620
Pellet size [*mm*]	4	1.6	1.6	1.6	3
C content [*mass%*]	>50	0	0	0	0
K_2CO_3 content [*mass%*]	2.5-10	0	0	0	0
Al_2O_3 content [*mass%*]	0	0	>75	<40	>95
SiO_2 content [*mass%*]	0	0	0	>45	0
CuO content [*mass%*]	0	>25	<25	0	0
MnO content [*mass%*]	0	>25	0	<40	0
$MnCO_3$ content [*mass%*]	0	0	0	<40	0

[3] Segments of Section 3.1.3 have already been published in Chemie Ingenieur Technik [272].

The custom-made test rig unit, used for the experiments presented in this research, is shown in Figure 3.11. The gas supply is ensured by means of a gas bottle which contains a certified test gas consisting of 200 *ppmv* H_2S in N_2. This corresponds to the average H_2S loading of a biogas (see Table 2.2). A test report issued by the supplier certifies a maximum deviation of ± 3 ppmv for the 200 *ppmv* H_2S. A pressure reducer connected to the gas bottle guarantees a gas pressure of 2.4 *bar* to supply the following installed MFC (Vögtlin red-y smart series). The MFC operates at an inlet pressure of 2.4 *bar* and reduces the outlet pressure down to 1.013 *bar* operating pressure. The connections between the gas bottle and the MFC are made of stainless steel. All the pipes, tubes, connections and other elements installed after the MFC are made of glass or PTFE. Unwanted side reactions of H_2S with alloying elements, which can occur in metal components, can now be excluded (see Section 3.1.1) . The NH_3 loading was attained by using a gas saturator (bubbling system). After passing the bubbling system, the gas flows through the adsorber which is a glass cylinder with an inner diameter of 16 *mm* and a length of 80 *mm*.

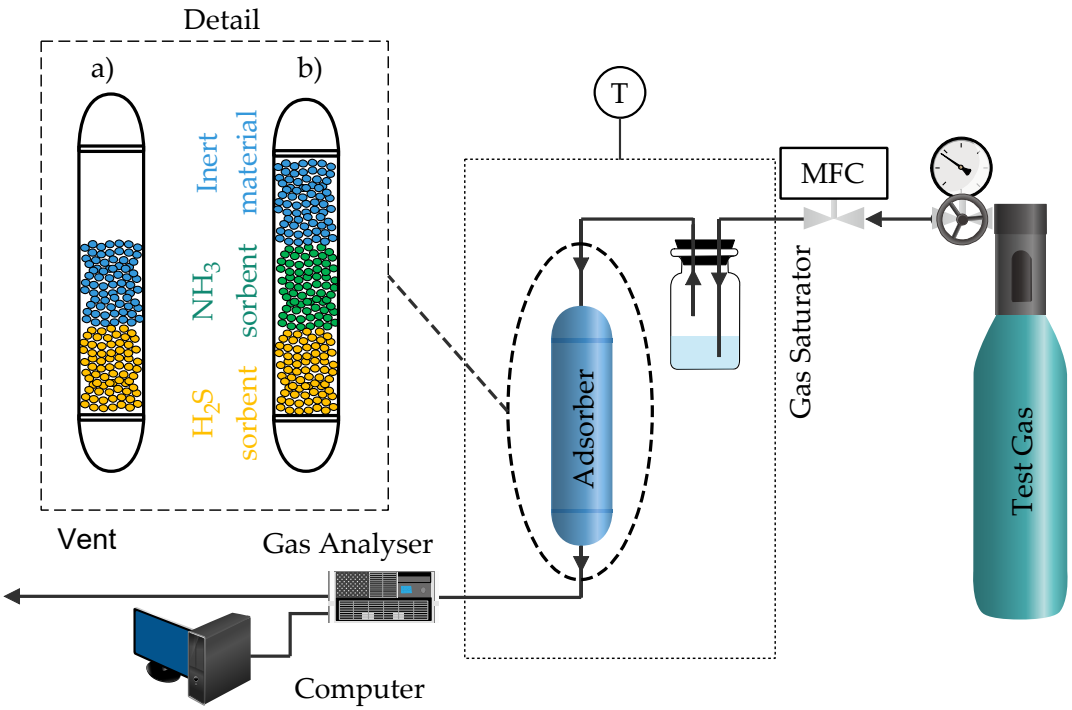

Figure 3.11: Flow chart of adsorption test rig consisting of a test gas, a MFC, a reactor, a programmable heating thermostat, a bubbler and a gas analyser.

The adsorber is placed in a heating thermostat (Lauda type ECO) which is filled with water to ensure a constant operating temperature of 20 °C. Depending on the experiment carried out, the reactor is filled differently. Reactor loadings for the experiments investigating the influence of NH_3 on the H_2S sorbent are displayed in detail a) in Figure 3.11. The yellow coloured pellets at the bottom symbolize the H_2S sorbent. The blue coloured pellets at the top symbolize inert

glass packings, which have the task of homogenizing the gas flow in the adsorber. The reactor filling, as shown in detail b), contains an additional sorbent for NH_3 removal (green) between the glass packings (blue) and the sorbent for H_2S removal (yellow). After passing the reactor, the gas enters a gas analyser for H_2S measurement. The ABB AO2020 gas analyser allows a continuous measurement of the H_2S concentration with an accuracy of 0.05 *ppmv*. After the measurement in the gas analyser, the gas is passed into a vent. The control of the MFC, the control heating thermostat such as the recording of process data is achieved with the aid of a computer running LabVIEW software.

Before starting the experiments, the composition of the test gas mixture was validated. For this purpose, the gas bottle was connected to the system and a continuous gas stream was set by means of the MFC. After flowing through the MFC, the gas was passed directly into the calibrated gas analyser. A stable measured value of 200 ppmv H_2S at the output was already achieved in less than one minute. Furthermore, the NH_3 loading of the gas was checked by means of a separate measuring setup. For this purpose, a defined gas stream was passed through the gas wash bottle which was filled with 1 or 5 vol% NH_3 in H_2O. Subsequently, the gas was passed into an additional gas wash bottle equipped with a frit. In this second wash bottle the change of the pH value was monitored by means of a pH meter for a certain period of time. Both gas wash bottles were placed in a thermostat at a defined temperature of 20 °C. The pH value shift over time with a defined gas flow as well as defined liquid volumes in the wash flasks allowed to calculate the NH_3 concentration in the gas (assuming that the use of a frit in the second wash bottle dissolves all the NH_3 in the H_2O).

After completion of this preliminary work, the test rig was ready for the experimental runs. The first step of each test run was the drying of the sorbents. For this purpose, the required amount of the sample was dried in an oven at 110 °C for 60 minutes. Subsequently, the reactor was loaded with a certain amount of sorbent. In order to be able to compare the different sorbents with each other, a constant $GHSV$ 8000 h^{-1} was maintained. Thereafter the reactor was mounted onto the test rig and connected to the gas supply and to the gas analyser. The operating temperature of the reactor and the gas wash bottle of 20 °C was ensured with the aid of the thermostat. After connecting all tubes, all seals were checked by passing N_2 through the apparatus. The next step consisted of activating the measurement data logging and feeding the test gas through the adsorber. A H_2S outlet concentration of 100 *ppmv* was used as termination criterion for the experiment. For further studies, the values were extrapolated to an outlet concentration of 200 *ppmv*. An overview of the boundary conditions used in the tests can be found in Table 3.9.

After completion of the test run, all parts were disassembled, cleaned and dried. To minimize differences and eliminate measurement errors, all measurements were done twice. All measurements were highly reproducible. The S_{cap} value was calculated according to equation 2.46. In order to investigate the microscopic topologies of the used sorbents, a SEM method was performed. The field emission scanning electron microscope (FE-SEM) used was a Zeiss Ultra 55. Energy-dispersive X-ray spectroscopy was used to figure out several chemical elements on

Table 3.9: Overview of the performed tests.

Test	Gas feed			Sorbent loading
	H2S [*ppmv*]	NH3 [*ppmv*]	Balance	
1	200	-	N_2	H_2S removal
2	200	540	N_2	H_2S + NH_3 removal
3	200	540	N_2	H_2S removal
4	200	2700	N_2	H_2S + NH_3 removal
5	200	2700	N_2	H_2S removal

the samples. The results of the microscopic investigations compare fresh adsorbent, adsorbent after contact with H_2S and adsorbent after contact with H_2S and NH_3. The FE-SEM results are presented at the end of each adsorbent test series.

CuO doped zeolite

The following boundary conditions were chosen for the experiments: a $GHSV$ of 8000 h^{-1} achieved by a constant gas stream of 0.5 standard litre per minute (*slpm*) and a constant bed height of the adsorbent in the reactor. Furthermore, all experiments were carried out at 20 °C. Figure 3.12 shows the results of the test runs performed with the CuO doped zeolite. The results were split into two diagrams for a better overview, because different scales were chosen on the x-axis.

The blue graph (Test 1) represents the breakthrough curve of the CuO doped zeolite when fed with 200 *ppmv* H_2S in N_2. The breakthrough was reached after 7.5 *h*. By using Equation 2.46 a Scap of 15.304 *mgS / gAds* was calculated. Bubbling the feed stream through a gas saturator loaded with 1% NH_3 is represented by the red (Test 2) and green (Test 3) breakthrough curves. Bubbling the 200 *ppmv* H_2S in N_2 feed through a gas saturator loaded with 1% NH_3 in H_2O leads to a NH_3 loading of 540 *ppmv*. It can be seen that supporting the H_2S sorbent with a sorbent for NH_3 removal, the time till complete breakthrough (c_i=c_o) increased by around 1 *h*.

The purple (Test 4) and lime (Test 5) breakthrough curves on the right side show the influence of a higher NH_3 concentration. Bubbling the 200 *ppmv* H_2S in N_2 feed through a gas saturator loaded with 5% NH_3 in H_2O leads to a NH_3 loading of 2700 *ppmv*. This results in a significant reduction of the breakthrough time and, consequently, of S_{cap}. A positive influence of the NH_3 removal stage can be seen by comparing the breakthrough time of the lime graph (Test 5) with the purple (Test 4). The time till complete breakthrough (c_i=c_o) for H_2S increased from 0.5 to 0.87 *h* due to the upstream NH_3 separation. The values for S_{cap} are given in Table 3.10. The presence of NH_3 has a negative effect on H_2S adsorption. In the literature, there are no

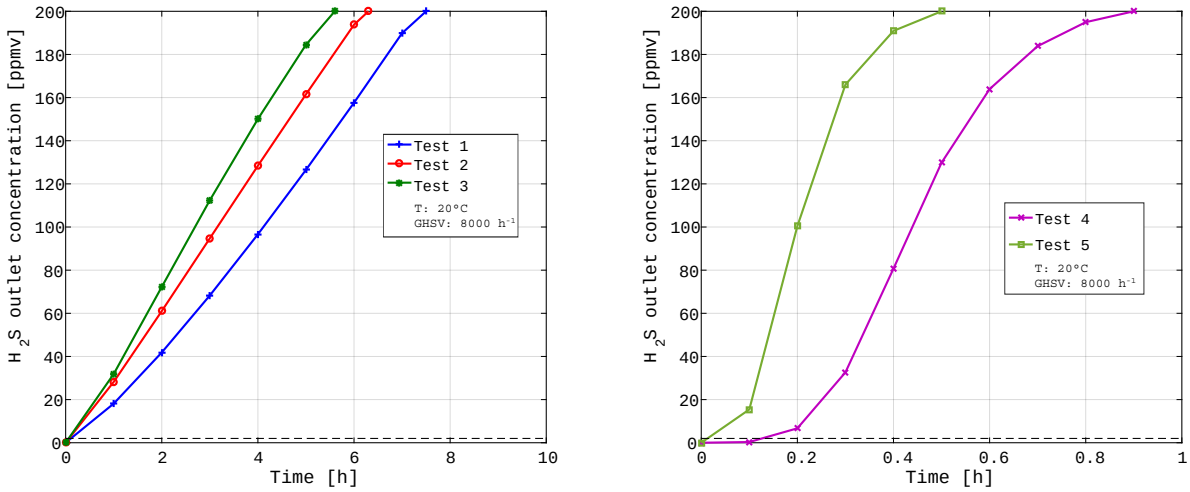

(a) Test 1,2,3 **(b)** Test 4,5

Figure 3.12: Effect of NH_3 on H_2S outlet concentration of CuO doped zeolite. $GHSV$ = 8000 h^{-1}; Temperature 20 °C.

indications of interactions between NH_3 and the zeolite, therefore, a microscopic examination was carried out.

Table 3.10: S_{cap} and BT values for CuO doped zeolite. $GHSV$ = 8000 h^{-1}; Temperature 20 °C.

Test	S_{cap} $[mg/g]$	BT $[h]$
1	15.304	7.6
2	11.791	6.3
3	9.968	5.7
4	2.163	0.9
5	1.083	0.5

The results of the microscopic examination are shown in Figure 3.13. The left picture shows the fresh sorbent, the middle picture the sorbent after contact with H_2S (Test 1) and the right picture after contact with H_2S and NH_3 (Test 5). There is no visual difference between the middle and right picture. An additionally performed energy-dispersive X-ray spectroscopy (EDX) confirms a higher sulphur content after Test 1 than after Test 5, but gave no further information. According to Table 3.10, this means that the sample which was used for desulfurization without NH_3 loading in the feed has taken up a higher amount of sulfur (15.304 mg/g) than the sample which was charged with NH_3 and H_2S in N_2 in the feed (1.083 mg/g). In terms of efficiency and also in the economic context, this means for a SOFC CCHP plant that a separation of the NH_3 in advance is necessary. This greatly improves the separation of the H_2S by the downstream adsorber and, thus, leads to a longer service life of the adsorber.

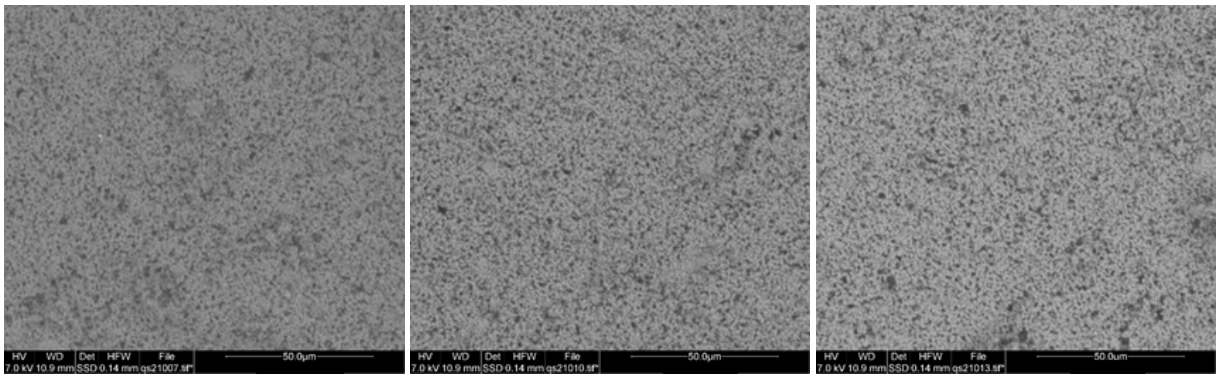

(a) Fresh zeolite **(b)** After contact with H_2S (Test 1) **(c)** After contact with H_2S and NH_3 (Test 5)

Figure 3.13: Microscopic examinations of the CuO doped zeolite.

MnO doped zeolite

The results for the test runs carried out with the MnO doped zeolite are shown in Figure 3.14. The dashed horizontal black line marks the 2 *ppmv* H_2S concentration for the SOFC. A description of the associated test parameters is given in Table 3.9. The best result in terms of S_{cap} and breakthrough time was obtained in the reference experiment with 200 *ppmv* H_2S in N_2 and MnO doped zeolite (Test 1). Until complete breakthrough (c_i=c_o), a time of 28.2 *h* elapsed and a S_{cap} of 67.51 *mgS / gAds* was achieved. Test 2 and 3 with 540 *ppmv* NH_3 and 200 *ppmv* H_2S in the feed (N_2) achieved breakthrough times (c_i=c_o) of 9.1 and 7.4 *h*, respectively. The difference in breakthrough time and S_{cap} resulted from the different reactor loadings. Test 2, the NH_3 pre-separation test, resulted in a breakthrough time of 9.1 *h* and a S_{cap} of 16.90 *mgS / gAds*. Analogous test conditions with the exception of NH_3 pre-separation reduced the breakthrough time to 7.4 *h* and the S_{cap} to 11.12 *mgS / gAds*. The effect of increasing the NH_3 concentration in the feed to 2700 *ppmv* is shown by Tests 4 and 5. A significant influence on the breakthrough time as well as on the S_{cap} was the consequence of this increase in the NH_3 content (see Figure 3.14 right). With upstream NH_3 adsorption, a breakthrough time of 0.7 *h* and a S_{cap} of 2.224 *mgS / gAds* were measured (Test 4). However, the same conditions without NH_3 separation resulted in a breakthrough time of 0.5 *h* and a S_{cap} of 1.490 *mgS / gAds*. The calculated values regarding S_{cap} can be found in Table 3.11.

Table 3.11: S_{cap} and BT values for MnO doped zeolite. $GHSV$ = 8000 h^{-1}; Temperature 20 °C.

Test	S_{cap} [*mg/g*]	BT [*h*]
1	67.51	28.2
2	16.90	9.1
3	11.12	7.4
4	2.224	0.7
5	1.490	0.5

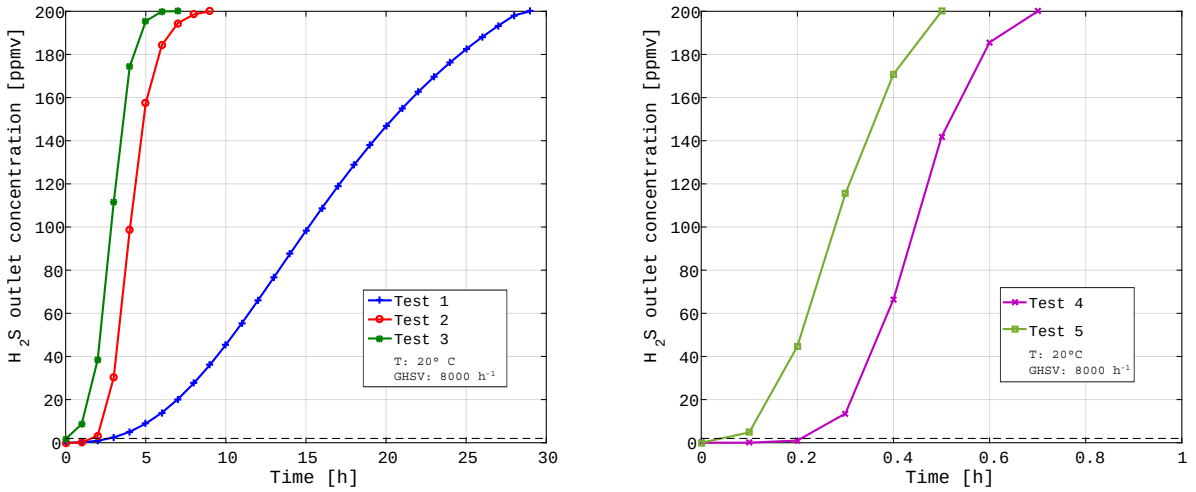

(a) Test 1,2,3 **(b)** Test 4,5

Figure 3.14: Effect of NH_3 on H_2S outlet concentration of MnO doped zeolite. $GHSV = 8000\ h^{-1}$; Temperature 20 °C.

A comparison of the results of Test 1 (reference experiment) with Test 2 and 3 leads to the following conclusion: The upstream NH_3 adsorber was dimensioned too small. Already at the beginning, a high proportion of NH_3 would have passed the adsorber as the large difference in the breakthrough time between Tests 1 and 2 shows. A larger NH_3 precursor would have prevented damage to the H_2S sorbent. Ideally (complete removal of NH_3) the BT and S_{cap} values should be analogous to those of Test 1. The remaining comparably small difference between Tests 2 and 3 shows that a certain amount of NH_3 was adsorbed because the breakthrough time was increased from 7.4 to 9.1 h. This confirms a positive effect of NH_3 separation before the desulfurization step. In comparison with the CuO doped zeolite (see results in Table 3.10) MnO doped zeolite shows higher values for S_{cap} and BT in Tests 1, 2 and 3 (see Table 3.11). In Tests 4 and 5, nearly identical results were achieved.

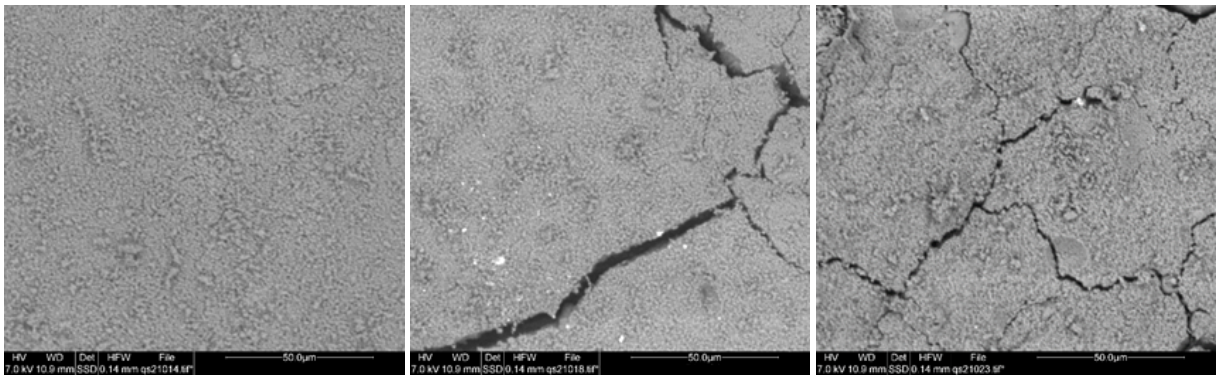

(a) Fresh zeolite **(b)** After contact with H_2S (Test 1) **(c)** After contact with H_2S and NH_3 (Test 5)

Figure 3.15: Microscopic examinations of the MnO doped zeolite.

A set of FE-SEM images from the MnO doped zeolite at different process steps is shown

in Figure 3.15. The image on the left side shows the raw material. The image in the middle displays the surface of the MnO-doped zeolite after contamination with H_2S (Test 1). The image on the right shows a zeolite sample after contamination with H_2S and NH_3 (Test 5). An additional EDX examination showed a higher sulfur peak in the middle sample than in the right one. This supports the suggestion that NH_3 has a negative impact on H_2S adsorption of the zeolite. In the literature no data was found on the influence of NH_3 on H_2S adsorption.

Impregnated activated carbon

The great advantage of the K_2CO_3 impregnated activated carbon is that it is capable of adsorbing different acidic gas components like H_2S and HCl. According to the literature small amounts of NH_3 may be present in the biogas (see Table 2.2), so the test for NH_3 stability is important. The experiments (3.9) performed with activated carbon show the same sequence of breakthrough times as in the experiments with CuO doped zeolite and MnO doped zeolite. The breakthrough curves are shown in Figure 3.16, the corresponding calculated values for S_{cap} are given in Table 3.12. The shape of the breakthrough curves for all 5 test runs look identical. The highest time till breakthrough (c_i=c_o) and associated highest S_{cap} was achieved in the reference experiment (Test 1) with 200 *ppmv* H_2S in N_2. The time till breakthrough was 19.1 *h*. It could be recorded 12.301 *mgS / gAds* (mg of sulfur per g of activated carbon). The addition of 540 *ppmv* NH_3 to the 200 *ppmv* H_2S loaded and N_2 balanced feed is evident in Tests 2 and 3. The breakthrough time of 14.2 *h* or a S_{cap} of 11.702 *mgS / gAds* was achieved with NH_3 pre-separation (Test 2). Without preliminary NH_3 separation, these values were reduced to 13.8 *h* and 11,269 *mgS / gAds*. Increasing the NH_3 concentration from 540 to 2700 *ppmv* resulted in the breakthrough curves of Test 4 and 5. Test 4, which was carried out with an upstream NH_3 separation step, resulted in a breakthrough time of 11.3 *h* and a S_{cap} of 10.484 *mgS / gAds*. The removal of NH_3 pre-separation at an NH_3 concentration of 2700 *ppmv* resulted in a breakthrough time of 10.2 *h* and a S_{cap} of 9.998 *mgS / gAds*.

Comparing the breakthrough curves with the S_{cap} given in Table 3.12, leads to the following conclusion: Impregnated activated carbon does not react as sensitively to the presence of NH_3 as the other sorbents investigated in this thesis. This is confirmed by comparing Tests 2 and 3 for the different adsorbents. For the CuO doped zeolite, the breakthrough time between test 2 and 3 (with and without NH_3 pre-separation) decreased from 6.3 to 5.7 hours (see Table 3.10). This corresponds to a decrease in the breakthrough time of 9.5%. For the MnO doped zeolite, the breakthrough time between Test 2 and 3 decreased from 9.1 to 7.4 hours (see Table 3.11). This corresponds to a reduction of 18.6%. For the activated carbon, the breakthrough time from Test 2 to 3 only decreased from 14.2 to 13.8 hours. This corresponds to 2.8% and confirms the tolerance to NH_3. According to literature [275], activated carbon impregnated with K_2CO_3 is insensitive to NH_3. Chemisorption is more selective than physical adsorption, where the size of molecules is crucial for effective trapping. In case of chemisorption, chemical bonds have to be formed between the surface of activated carbon and the adsorbed substance. Although a

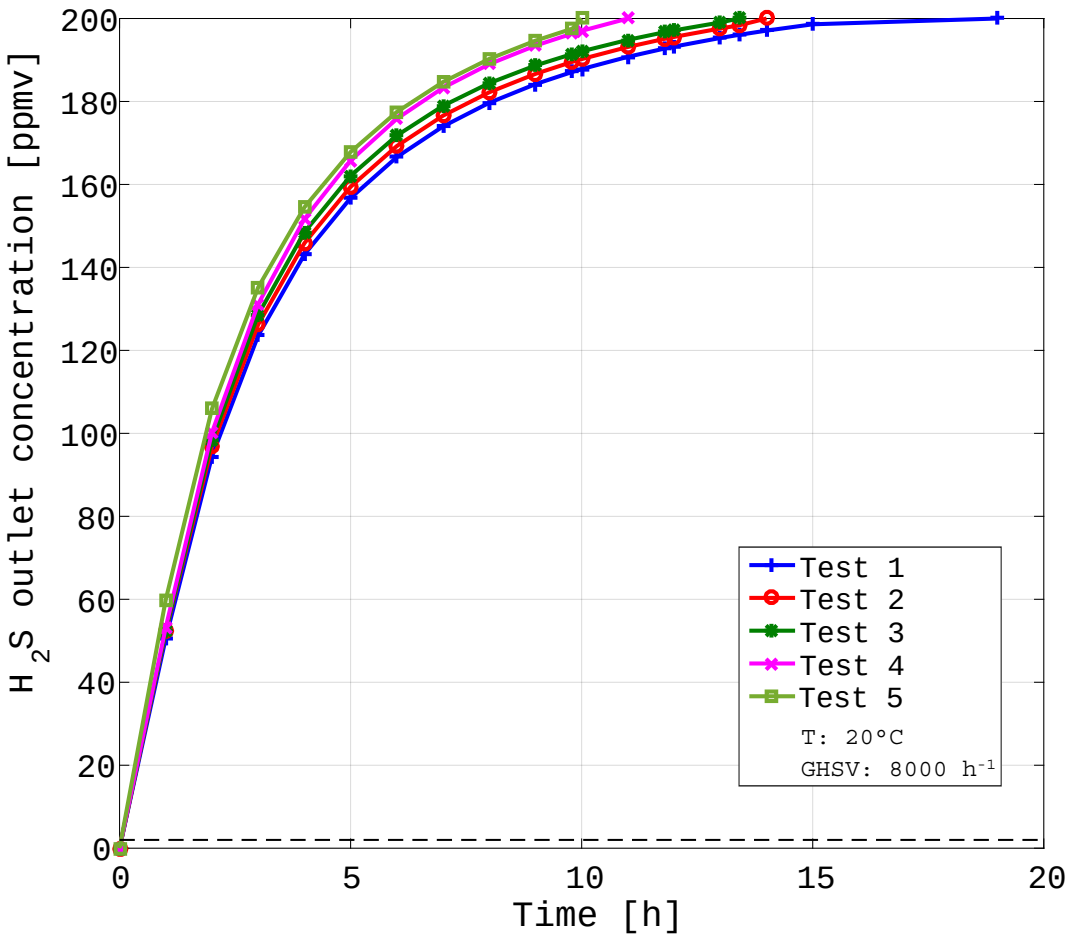

Figure 3.16: Effect of NH_3 on H_2S adsorption of K_2CO_3 impregnated activated carbon. $GHSV$ = 8000 h^{-1}; Temperature 20 °C.

positive influence of the NH_3 pre-removal is shown here as well, only a slight increase in S_{cap} results from upstream NH_3 removal. In numbers, S_{cap} rose from 9.998 $mgS\,/\,gAds$ (Test 5) to 10.484 $mgS\,/\,gAds$ (Test 4) and from 11.269 $mgS\,/\,gAds$ (Test 3) to 11.702 $mgS\,/\,gAds$ (Test 2).

Table 3.12: S_{cap} and BT values for K_2CO_3 impregnated activated carbon. $GHSV$ = 8000 h^{-1}; Temperature 20 °C.

Test	S_{cap} $[mg/g]$	BT $[h]$
1	12.301	19.1
2	11.702	14.2
3	11.269	13.8
4	10.484	11.3
5	9.998	10.2

The sample preparation for FE-SEM analyses requires that the samples are vapor deposited

with carbon to be registered in the detector. Activated carbon, with the exception of the impregnation, is made entirely of carbon and therefore could not be investigated by this method.

CuO-MnO sorbent

The test results for the experiments (3.9) carried out with the adsorbent based on CuO-MnO are shown in Figure 3.17. Even when looking at the x-axis, this adsorbent shows the highest S_{cap} and also the highest breakthrough time of the desulfurisation materials investigated. Analogous to the experiments already carried out with NH_3 with the other sorbents, the same sequence with respect to breakthrough curves was determined in the experiments with CuO-MnO sorbent.

For the reference experiment with 200 *ppmv* H_2S in N_2, a breakthrough time of 91 *h* was measured. The experiments with 540 *ppmv* NH_3 and 200 *ppmv* in the feed (N_2) achieved breakthrough times (c_i=c_o) of 78 *h* (Test 2) and 61 *h* (Test 3), respectively. Increasing the NH_3 concentration from 540 to 2700 *ppmv* results in the breakthrough curves of Test 4 and 5. Test 4, which was carried out with an upstream NH_3 separation step, resulted in a breakthrough time of 33 *h*. Test 5, which was carried out without preliminary NH_3 separation, was completed after a breakthrough time of 39 *h*.

Table 3.13: S_{cap} and BT values for CuO-MnO sorbent. $GHSV$ = 8000 h^{-1}; Temperature 20 °C.

Test	S_{cap} [mg/g]	BT [h]
1	150.85	91
2	137.58	78
3	98.010	61
4	70.274	39
5	63.642	33

Comparing the breakthrough curves of Test 1 and Test 2 , leads to the conclusion that the amount of sorbent of the upstream NH_3 removal may dimensioned too small. A larger NH_3 precursor would have prevented damage to the H_2S sorbent. If the NH_3 is completely separated, S_{cap} and BT should be the same values as in Test 1 (no NH_3 in the feed, see Table 3.9). If no NH_3 reaches the H_2S separation, there can be no interaction between NH_3 and the H_2S sorbent. In conclusion NH_3, after breaking through the upstream removal, penetrated the CuO-MnO sorbent and possibly blocked the sulfur uptake.

The above assumption also results from the comparison of Test 2 and Test 3. It can be seen easily that the upstream NH_3 removal (Test 2) expanded the time until breakthrough to 78 *h* compared to the test run without upstream NH_3 removal (Test 3, BT=61 *h*). On the other hand, increasing the amount of NH_3 in the feed up to 2700 *ppmv* had a major impact on S_{cap} and

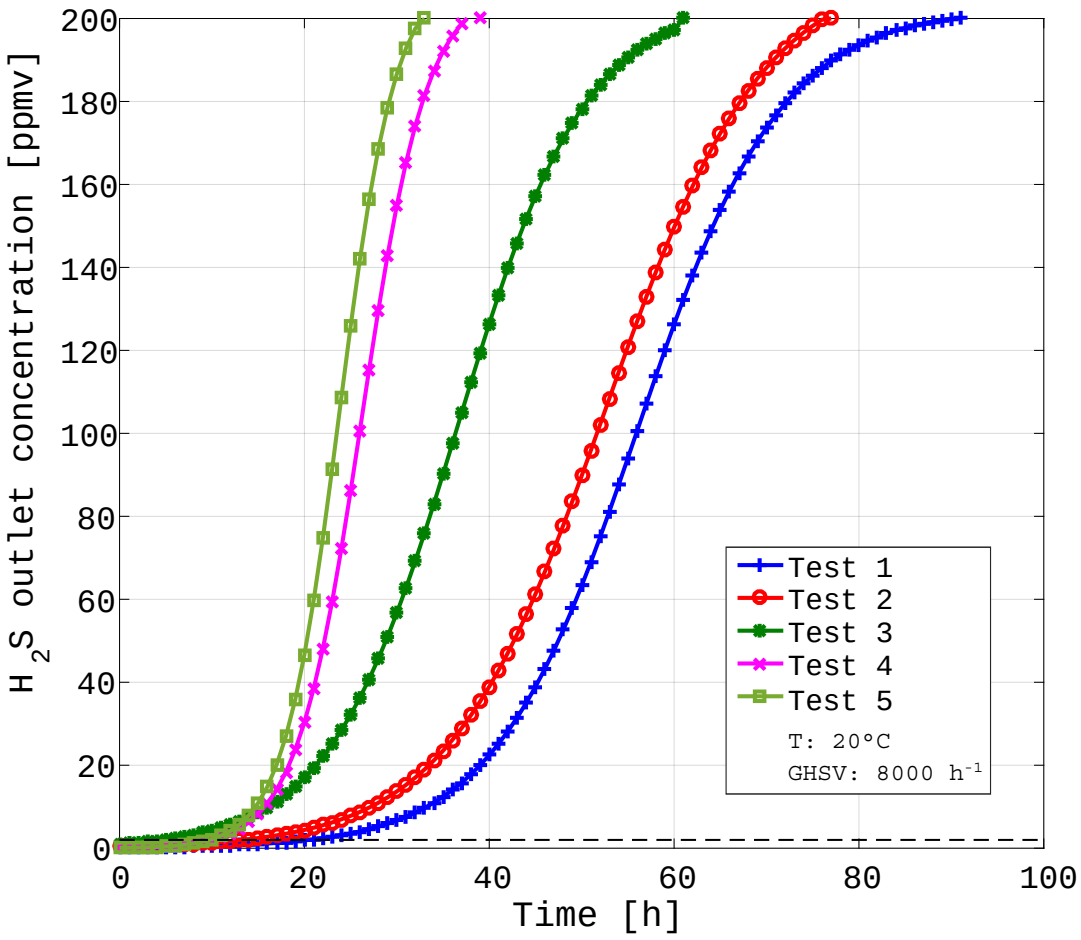

Figure 3.17: Effect of NH_3 on H_2S adsorption of CuO-MnO sorbent. $GHSV$ = 8000 h^{-1}; Temperature 20 °C.

breakthrough time (Test 5 and Test 4). In that case, the upstream NH_3 separator increased the time until breakthrough up to 36 h. The calculated S_{cap} for all cases are given in Table 3.13.

The results of the FE-SEM from the CuO-MnO based sorbent at different process steps is shown in Figure 3.18. The first image on the left side is a record of the raw material. The image in the middle shows the sorbent after the impurity with H_2S (Test 1). EDX evaluation confirms a major sulfur uptake. The image on the right side shows the CuO-MnO sorbent after contamination with H_2S and NH_3 (Test 5). A rugged surface and a crater are visible in the picture. In turn, these indications point to a harmful influence of NH_3. The corresponding EDX evaluation showed a very low sulfur peak compared to the evaluation of the middle image. In the literature [276], there is a general consensus that Cu forms complexes with NH_3, where the predominant oxidation state for Cu is +2. The exact formula of these compounds is being debated [275]. Changing the oxidation state of Cu is associated with loss of adsorptive properties. For interactions of NH_3 with MnO, no suitable information was found in the literature.

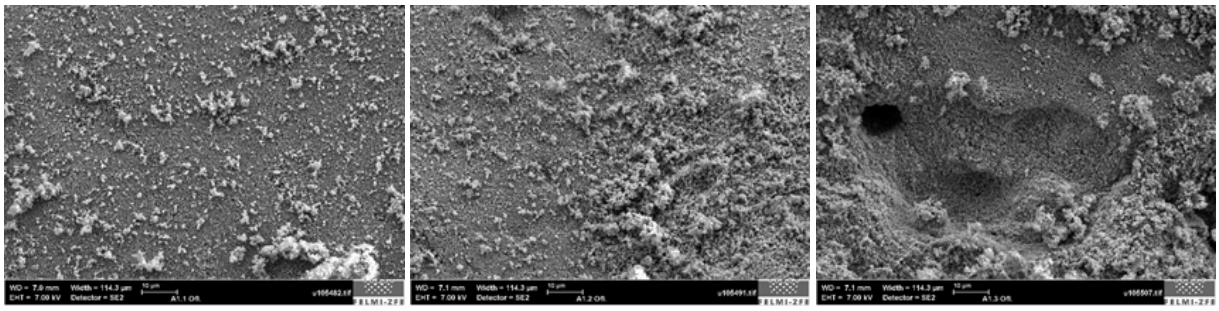

(a) Fresh zeolite **(b)** After contact with H_2S (Test 1) **(c)** After contact with H_2S and NH_3 (Test 5)

Figure 3.18: Microscopic examinations of the CuO-MnO sorbent.

Summary

In summary, the following conclusion can be made from this test series. The influence of NH_3 on the H_2S adsorption capacity is considerable and should not be disregarded when sizing an adsorber for H_2S separation. With the exception of the impregnated activated carbon investigated, there were major effects in terms of breakthrough time and S_{cap} on all other examined adsorbents. The effect of 540 *ppmv* NH_3 on the adsorption of H_2S (Test 3) should be summarized here with the case without NH_3 in the feed (Test 1). For the CuO-MnO adsorbent, the breakthrough time decreased from 91 to 61 h. At the same time, S_{cap} decreased from 150.85 $mgS\,/\,gAds$ to 98.010 $mgS\,/\,gAds$. For the MnO doped zeolite, the breakthrough time decreased from 28.2 to 7.4 h. At the same time, S_{cap} decreased from 67.51 $mgS\,/\,gAds$ to 11.12 $mgS\,/\,gAds$. For the CuO doped zeolite, the breakthrough time decreased from 7.6 to 5.7 h. At the same time, S_{cap} decreased from 15.30 $mgS\,/\,gAds$ to 9.96 $mgS\,/\,gAds$. Activated carbon impregnated with K_2CO_3 showed the least impact by adding NH_3 to the feed. In the following, the results of Tests 1 and 3 of K_2CO_3 impregnated activated carbon will be compared. In Test 1, a BT of 19.1 h and a S_{cap} of 12.30 $mgS\,/\,gAds$ were achieved. In Test 3 (without NH_3 separation), these values reduced to a breakthrough time of 13.8 and a S_{cap} of 11.27 $mgS\,/\,gAds$. From this the following conclusions can be drawn:

- A minor influence of NH_3 on the adsorption of H_2S was measurable for all investigated adsorbents for H_2S separation.
- With the exception of K_2CO_3 impregnated activated carbon, removal of NH_3 in a precursor is recommended for all H_2S separation adsorbents.
- The CuO doped zeolite and the MnO doped zeolite showed a significant influence of NH_3 on the H_2S separation and the lowest values for BT and S_{cap}. Expressed in numbers, S_{cap} decreased from 11.791 to 9.968 $mgS\,/\,gAds$ and BT from 6.3 to 5.7 h for the CuO doped zeolite between Test 2 and 3. Between Test 4 and 5, S_{cap} decreased from 2.163 to 1.083 $mgS\,/\,gAds$ and BT decreased from 0.9 to 0.5 h. For MnO doped zeolite, S_{cap} decreased from 16.90 to 11.12 $mgS\,/\,gAds$ and BT decreased from 9.1 to 7.4 h between Test 2 and 3. Between Test 4 and 5, S_{cap} decreased from 2.224 to 1.490 $mgS\,/\,gAds$ and

BT decreased from 0.7 to 0.5 h. An exception is Test 1 for the MnO doped zeolite. High values for S_{cap} (67.51 $mgS\,/\,gAds$) and BT (28.2 h) were achieved in comparison with the other adsorbents.

- As in the previous invenstigations (see 3.1.1 and 3.1.2), the CuO-MnO sorbent reached very high S_{cap} and BT values. In the worst case (Test 5), a BT of 33 h and a S_{cap} of 63.64 $mgS\,/\,gAds$ were measured. For comparison, in Test 5 with the CuO doped zeolite, a BT of 0.5 h and a S_{cap} of 1.083 $mgS\,/\,gAds$ were achieved (see Tables 3.13 and 3.10).
- The examination of the breakthrough curves of Tests 1-5 with K_2CO_3 impregnated activated carbon (Figure 3.16) clearly shows the tolerance of this adsorbent to NH_3. Although the breakthrough time between Test 1 and 5 decreased from 19.1 to 10.2 h, a satisfactory H_2S separation was achieved. The S_{cap} value only decreased from 12.30 to 9.99 $mgS\,/\,gAds$.

3.1.4 HCl adsorption and simultaneous H_2S and HCl adsorption [4]

As described in Section 2.4.9, HCl is one of the primary pollutants in biogas which has, in addition to H_2S, a negative impact on the life cycle of the SOFC. The concentration of HCl in biogas varies from 0.1 to 25 *ppmv*, depending on the source of the biogas (see Table 2.2). According to Section 2.3.3, the presence of Cl may hinder the adsorption of H_2 on Ni surfaces of the SOFC anode, or in other words reduce the electrochemical reaction rate. Based on the literature research in Section 2.3.3, a HCl tolerance of SOFC anodes as high as 10 *ppmv* seems satisfying. Therefore, the HCl content in the gas feed needs to be reduced and must not exceed 10 *ppmv*.

Experimental runs in a laboratory glass downflow fixed-bed reactor were carried out to analyse the HCl adsorption capacity of a K_2CO_3 impregnated activated carbon and two sorbents based on a mixture of Al_2O_3 and SiO_2. HCl removal was accomplished with the impregnated activated carbon and metal oxide based sorbents. HCl adsorption capacity was analysed under $GHSV$s 8000 h^{-1} and 16000 h^{-1}. These values represent common adsorber $GHSV$s [55] and provide a basis of comparison with the other experiments performed in this work.

In order to analyse the influence of HCl on the adsorption capacity, test gases with 100 and 1000 *ppmv* HCl content balanced with N_2 were used. To investigate the simultaneous adsorption of HCl and H_2S, a certified gas mixture with 100 *ppmv* HCl and 200 *ppmv* H_2S was used. Furthermore, pellets the size of 3 to 4 *mm* in diameter were crushed into a fraction between 500 and 1000 μm to investigate the influence of particle size on HCl adsorption performance. Additionally, the combined adsorption of HCl and H_2S was realized using the activated impregnated carbon. The physical characteristics of the K_2CO_3 impregnated activated carbon and the two sorbents based on a mixture of Al_2O_3 and SiO_2 are listed in Table 3.14. As described in Section 2.6.5, an activated alumina sorbent is widely used for HCl removal

[4] Segments of Section 3.1.4 have already been published in Adsorption Science and Technology [277].

because the extensive surface structure of activated alumina exhibits a very high affinity for chlorides.

Table 3.14: Physical properties of the investigated sorbents.

Sorbent	K_2CO_3 impregnated activated carbon	Activated alumina 1	Activated alumina 2
Bulk density $[kg/m^3]$	570	760	800
Pellet size [*mm*]	4	3	3
C content [*mass%*]	>50	0	0
K_2CO_3 content [mass%]	2.5-10	0	0
Al_2O_3 content [*mass%*]	0	>95.5	>94.5
SiO_2 content [*mass%*]	0	0.015	0.0.15

The experimental setup is schematically described in Figure 3.19. The custom built lab scale test rig consists of the following parts: a certified test gas; a MFC (Vögtlin red-y smart series); an adsorber; a custom built gas wash bottle which can mount a pH electrode; a pH meter with electrode and a gas analyser for monitoring H_2S content.

The test gas bottle is equipped with a pressure regulator ensuring a stable pressure of 2.4 *bar* at the outlet. A flexible metallic gas hose is used to connect the test gas bottle with the MFC. All elements following the MFC are made of PTFE or glass to avoid undesired reactions. The adsorber is a glass made cylinder with 150 *mm* length and an inner diameter of 17 *mm*. The adsorber is sealed with lab stoppers made of PTFE on both sides. This allows mounting different sorbents without major reconstruction. In order to achieve a uniform gas distribution, a layer of inert material is placed on top of the sorbent (see blue pellets in Figure 3.19). The custom made gas wash bottle is suitable for taking up a pH electrode.

To prevent a possible falsification of measurements, the gas wash bottle was filled with deionized H_2O. In order to maximize the solubility of the gaseous HCl in the deionized H_2O, the gas wash bottle is equipped with a frit. The pH electrode which is mounted in the gas wash bottle is connected with a pH meter. The pH value in the aqueous phase was measured every 30 seconds with a Mettler Toledo Seven2Go^{TM} pH meter (accuracy 0.002%). While performing test runs with H_2S and HCl, the H_2S concentration in the gas stream at the gas wash bottle outlet was continuously measured with an ABB AO 2000 gas analyser (accuracy 0.05 *ppmv*). The control of the MFC and the recording of process data was achieved with the aid of LabVIEW software and hardware. During the test phase of this carefully developed system, comparative measurements using gas chromatography were performed. The experiments showed a very good agreement down to a pH value of 3. Here, the deviations from the gas chromatography measurements were below 5%. At a pH value around 2, however, the deviations became more significant, which is also the reason for the chosen termination criterion. The concept of this measuring system and the calculation method were adapted from the work of Micoli et al.

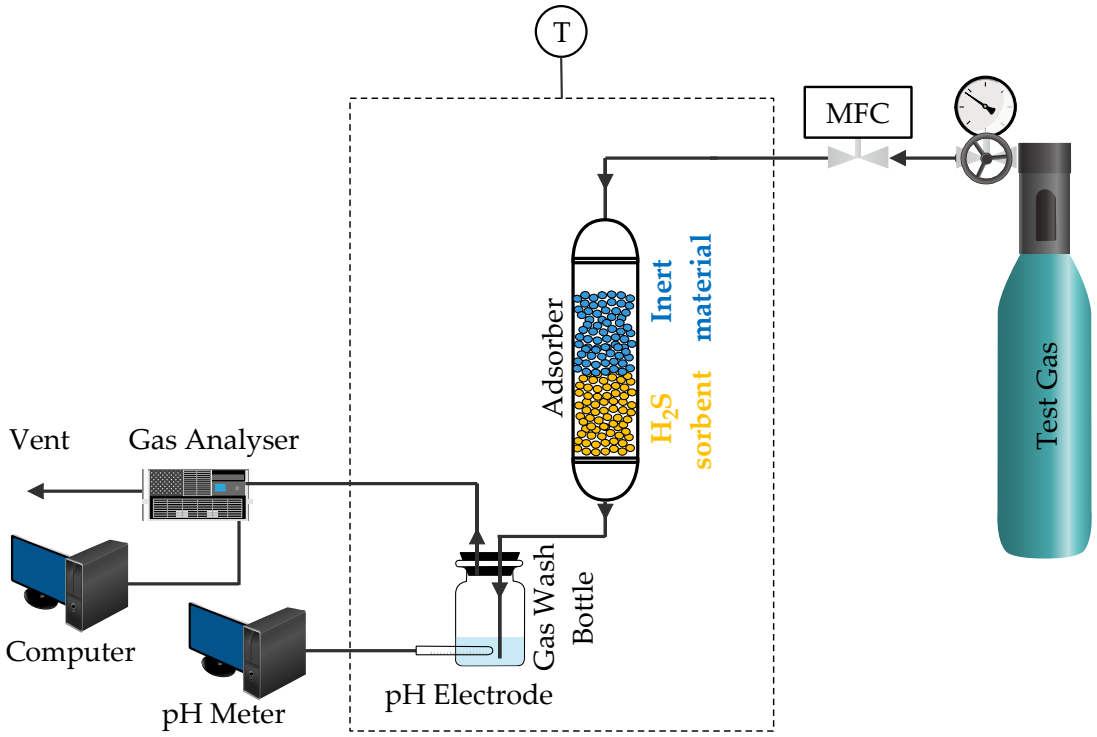

Figure 3.19: Flow chart of adsorption test rig consisting of a: a certified test gas; a MFC; an adsorber; a gas wash bottle which can mount a pH electrode; a pH meter and a gas analyser.

[278]. The fact that the measurements by gas chromatography are complex and no in situ measurements are possible led to the development of the measuring system described here.

Variant types of the test runs were carried out using the sorbents listed in Table 3.14. The test gas mixtures were passed through the glass made adsorber and the gas wash bottle while monitoring the pH value of the deionized H_2O in the gas wash bottle in time steps of 30 seconds. These test runs were carried out to investigate the parameters $GHSV$, particle size and HCl inlet concentration on the HCl adsorption capacity of the sorbents. A typical test run was carried out according to the following procedure: the pH meter including the pH electrode was calibrated; a measured quantity of sorbents was loaded into the adsorber to achieve a desired space velocity; 150 *ml* of deionized H_2O were filled into the gas wash bottle with the installed pH electrode. After connecting all pipes, all seals were checked by passing N_2 through the apparatus. Following the activation of the data logging, the test gas mixture was fed into the adsorber. The pH value was measured continuously and the value was recorded every 30 seconds. The test run was stopped after the pH value dropped below 3. By using the certified test gas with 100 or 1000 *ppmv* HCl in N_2 and the given gas volume flow, it was possible to calculate the total amount of HCl that entered the adsorber. The amount of HCl that passed the adsorber at certain measuring points of the test run was calculated based on pH value shift. The use of a frit causes small gas bubbles to flow through the H_2O in the gas wash bottle. Due to the small gas bubbles, the mass transfer is favored. To calculate the amount

of HCl, it was assumed that all remaining HCl in the gas phase dissolved in the H_2O of the gas wash bottle. Preliminary tests with different amounts of H_2O and depth of the bubbling point allowed to optimise the operating conditions. The pH value measured at a given time allowed to determine the amount of HCl dissolved in H_2O until that time, that corresponds to the amount not adsorbed by the material. The HCl concentration c_{HCl} in moles per liter is calculated according to Equation 3.1. From these data, by a derivative procedure, the HCl concentration in the effluent was obtained as a function of time. In this way the breakthrough curve was obtained [278].

$$pH = -log[H^+] = -log[c_{HCl}] \Rightarrow c_{HCl} = 10^{-pH} \tag{3.1}$$

The test runs involving H_2S followed almost the same procedure. After leaving the gas wash bottle, the gas was passed through the H_2S gas analyser. After completion of the test run, all parts were disassembled, cleaned and dried. To minimize differences and eliminate measurement errors, all measurements were done by double identification. It was always possible to achieve a good reproducibility. The Cl_{cap} value of the sorbent samples was calculated using Equation 2.47 (see Section 2.6.7).

Effect of GHSV on HCl adsorption performance

Test runs were conducted at $GHSV$s of 8000 h^{-1} and 16000 h^{-1} respectively. The other parameters for those test runs were kept constant. The experimental test runs were carried out with 1000 *ppmv* HCl in N_2 at a reaction temperature of 20 °C and with pellets of size 3 to 4 *mm*.

Figure 3.20 shows the results of the test runs performed at space velocity of 8000 h^{-1} (left) and 16000 h^{-1} (right). The x-axis scaling between the left and right figures varies to better represent the results. The black horizontal dashed lines at a HCl outlet concentration of 10 *ppmv* mark the HCl limit of the SOFC. Loading the reactor with the activated alumina samples at $GHSV$ of 8000 h^{-1} resulted in breakthrough times of 64 and 59 minutes respectively. The best performance, namely the HCl adsorption capacity of 24.48 *mg/g* and a breakthrough time of 82 minutes, was achieved with the impregnated activated carbon. The results achieved by increasing the $GHSV$ up to 16000 h^{-1} are demonstrated in Figure 3.20 on the right side. For the impregnated activated carbon, the HCl adsorption capacity decreased from 24.48 to 14.62 *mg/g*. On the other hand, using the sorbents based on activated alumina led to HCl uptakes of 15.90 respectively 8.84 *mg/g*.

Comparing the results leads to the following conclusion: Doubling the space velocity from 8000 h^{-1} to 16000 h^{-1} had a significant impact on the capture capacity Cl_{cap}. This Cl_{cap} decrease is a result of the shortened contact time between gas and sorbent, and is in line with the literature [241]. The capture capacity of sorbents depends on the gas solid contact time in the reactor which decreases at higher $GHSV$s. Furthermore, it can be concluded that the activated

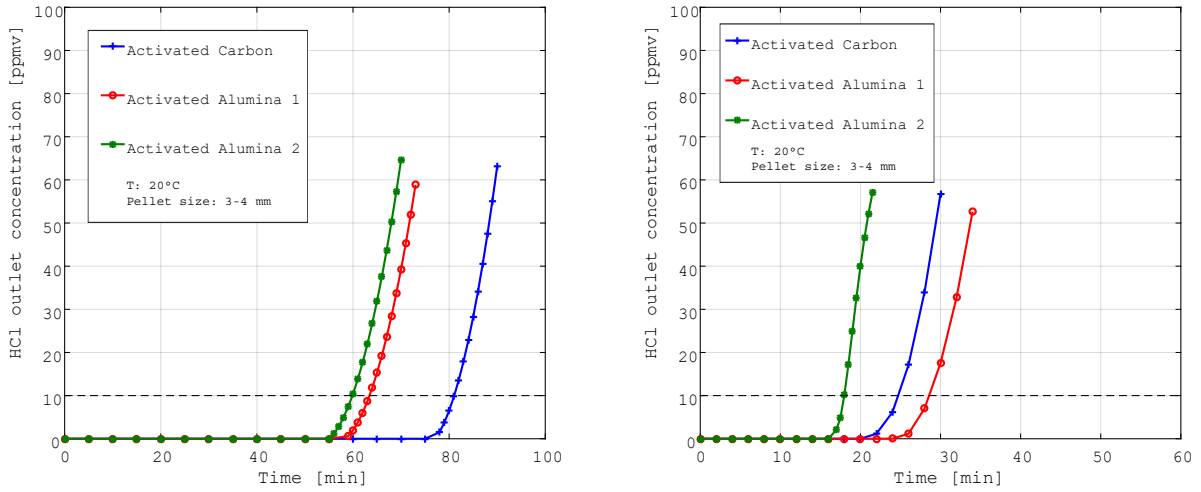

(a) *GHSV*s of 8000 h^{-1} **(b)** *GHSV*s of 16000 h^{-1}

Figure 3.20: HCl adsorption performance of different sorbents. Reaction temperature 20 °C; HCl inlet concentration 1000 *ppmv*; pellet size 3-4 *mm*.

alumina 1 took up most HCl until breakthrough at space velocity of 16000 h^{-1} while the impregnated activated carbon sample had the best capture capacity at 8000 h^{-1}. The numbers in Table 3.15 represent the amount of HCl in *mg/g* that had been adsorbed by the sorbent until the HCl outlet concentration reached 10 *ppmv*. Additionally, a significant decrease of Cl_{cap} on activated carbon sample and activated alumina 2 sample by doubling the *GHSV* can be seen. On the other hand, there is just a minor difference in Cl_{cap} between *GHSV* 8000 h^{-1} and 16000 h^{-1} for the activated alumina 1 sample.

Table 3.15: Cl_{cap} values in *mg/g* and *BT* values in *min* for experiments operated at GHSVs 8000 and 16000 h^{-1}; pellet size 3-4 *mm*; temperature 20 °C; HCl inlet concentration 1000 *ppmv*.

Sorbent	Activated carbon		Activated alumina 1		Activated alumina 2	
	Cl_{cap} [*mg/g*]	*BT* [*min*]	Cl_{cap} [*mg/g*]	*BT* [*min*]	Cl_{cap} [*mg/g*]	*BT* [*min*]
GHSV 8000 h^{-1}	24.48	82	15.64	64	13.85	59
GHSV 16000 h^{-1}	14.62	25	15.90	28	8.84	18

Effect of sorbent particle size on HCl adsorption performance

Besides *GHSV* and inlet concentration, the sorbent pellet size is one of the parameters with an influence on adsorption performance. In the adsorption tower design it is a limiting factor since apart from the tower height, the pellet size is decisive for the pressure drop [202]. On the other hand, finely ground pellets provide shorter diffusion paths, and this results in a larger mass transfer. Adsorbents have a more or less regular, interspersed with pores structure in which the

pores are interconnected. According to 2.6.5 these pores are divided into micropores (<2 *nm*), mesopores (2-50 *nm*) and macropores (>50 *nm*). The actual adsorptive effect and, thus, the active surface are largely based on the micropores. The adsorptive is transported through the macro and mesopores. They can be considered as accesses to the actual active surface [201].

The sample preparation was carried out the following way. Mortar and pestle were used to crush the pellets. After that a column of sieves was used to get a fraction of sorbent particles into the size between 500 and 1000 μm. This particle fraction was loaded into the reactor. In order to compare the results among each other, the tests were performed at $GHSV$s of 8000 h^{-1} and 16000 h^{-1}. Figure 3.21 presents the results for the particles at different $GHSV$s and have to be compared with Figure 3.20 (particle size 3-4 *mm*). It should be noted that the scaling of the x-axis varies.

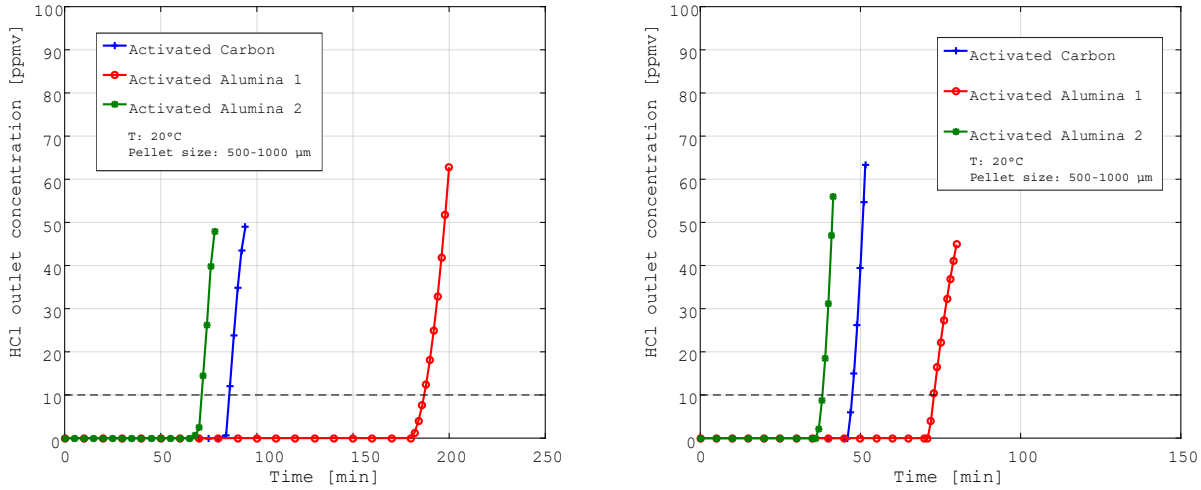

(a) $GHSV$s of 8000 h^{-1} **(b)** $GHSV$s of 16000 h^{-1}

Figure 3.21: HCl adsorption performance of different sorbents. Reaction temperature 20 °C; HCl inlet concentration 1000 *ppmv*; particle size 500-1000 μm.

Comparing Figures 3.20 and 3.21 (left side) resulted in the following conclusions: Crushing the 3 *mm* impregnated activated carbon pellets into particles in the size of 500 to 1000 μm had no major influence on the adsorption performance for the experiments performed at a GHSV of 8000 h^{-1}. The breakthrough time for both experiments was around 80 minutes. In numbers (compare Tables 3.15 and 3.16), the HCl uptake increased from 24.48 *mg/g* to 24.82 *mg/g*. Comparing the results of the activated alumina 2 sample, led to a similar conclusion. There was only a light influence on Cl_{cap} and breakthrough time. However, the performance of the activated alumina I sample increased by crushing the pellets into particles. In numbers, Cl_{cap} increased from 15.64 *mg/g* to 34.51 *mg/g* for the experiments performed at $GHSV$ 8000 h^{-1} and from 15.90 *mg/g* up to 31.71 *mg/g* at space velocity 16000 h^{-1}. Therefore, it can be concluded that the sorbents are not completely loaded at the selected termination criterion (pH value 3). All samples almost doubled their Cl_{cap} uptake at $GHSV$ 16000 h^{-1}.

All investigated sorbents were originally pellets. These were crushed and the fraction between

Table 3.16: Cl_{cap} values in *mg/g* and *BT* values in *min* for experiments operated at *GHSV*s 8000 and 16000 h^{-1}; particle size 500-1000 μm; temperature 20 °C; HCl inlet concentration 1000 *ppmv*.

Sorbent	Activated carbon		Activated alumina 1		Activated alumina 2	
	Cl_{cap} [*mg/g*]	*BT* [*min*]	Cl_{cap} [*mg/g*]	*BT* [*min*]	Cl_{cap} [*mg/g*]	*BT* [*min*]
GHSV 8000 h^{-1}	24.82	83	34.51	182	13.77	69
GHSV 16000 h^{-1}	22.70	48	31.71	74	15.22	41

500 and 1000 μm was used for the experiments. Technically, crushing the pellets increases the surface which should have a positive impact as with smaller particles, the diffusion paths are shorter. Due to the longer contact time between the gas phase and the sorbent, this effect should also be monitored at *GHSV* of 8000 h^{-1} in order to compare pellets and particles. In the case of activated carbon and activated alumina 2, however, at a GHSV of 8000 h^{-1} there is no positive effect of smaller particles on the adsorption performance. When the *GHSV* is doubled up to 16000 h^{-1}, however, both adsorbents show a positive effect due to the smaller particles.

The following conclusions are derived: According to the literature [279], pore volume and surface area increase with particle size reduction. Pore size distribution of small pores (<10 *nm*) changes among varying particle size. Pore volume proportion of small pores (<10 *nm*) increases and pore volume proportion of big pores (>10 *nm*) decreases with decreasing particle size. Decreasing particle size by crushing sample introduces new connectivity for closed pores to the particle surface. By performing experiments multiple times with consistent results, a measurement error can be excluded. Pore volume, surface area and the difference in pore size distribution has to be determined for further investigations in future experiments.

Effect of HCl concentration on adsorption performance

The experiments were performed at a temperature of 20 °C and a *GHSV* of 16000 h^{-1} with pellets in the size of 3-4 *mm*. Figure 3.22 shows the performance of the three different sorbents while using a HCl concentration of 100 *ppmv* in the feed gas, balanced with N_2. Figure 3.20 (right side), shows the performance of the same sorbents at an HCl inlet concentration of 1000 *ppmv*.

The contemplation of the x-axis demonstrates the major influence of the HCl inlet concentration. It can be easily identified that the test run duration increased 6-8 times before reaching the breakthrough concentration, an HCl value of 10 *ppmv*. The corresponding numbers are given in Table 3.17. Those numbers have to to be compared with the results for the test performed at a GHSV of 16000 h^{-1} in Table 3.15. Comparing the sorbent uptake capacity Cl_{cap} shows that using a higher HCl inlet concentration led to a 10 % higher sorbent uptake. This can be explained by the concentration gradient. One of the driving forces of adsorptive separation is the concentration of the feed. In other words, the higher the dilution the lower the driving

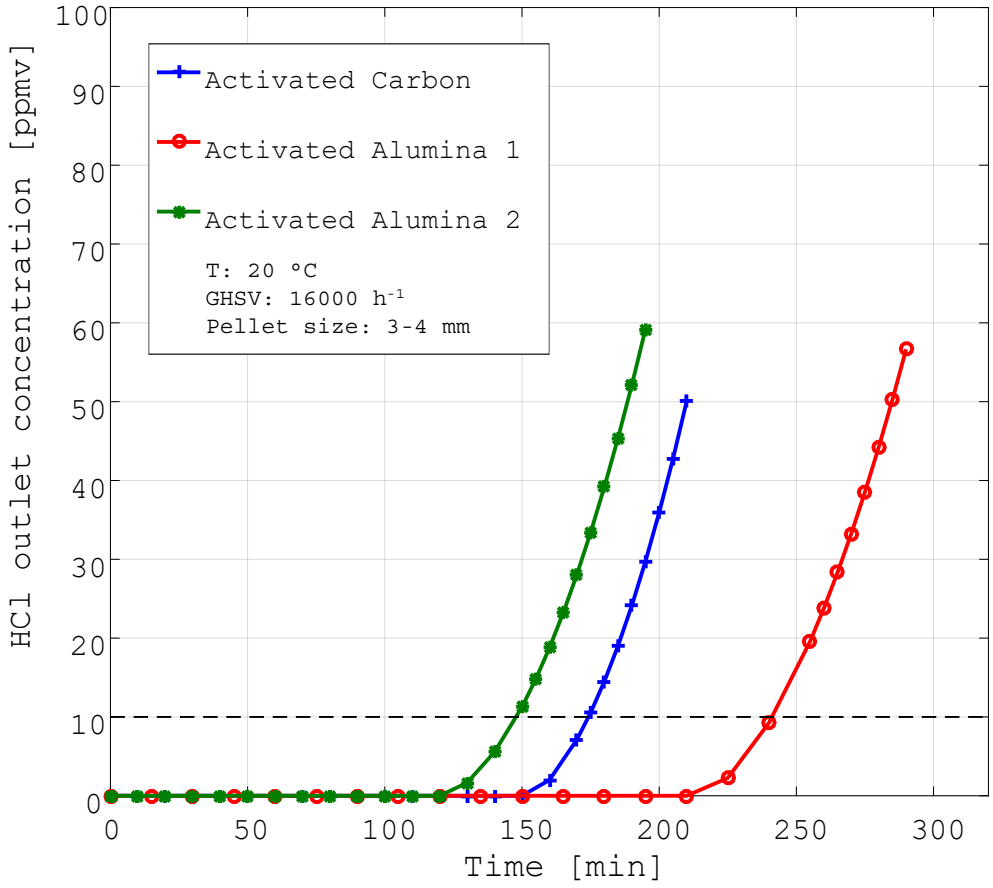

Figure 3.22: HCl adsorption performance of different sorbents. Reaction temperature 20 °C; HCl inlet concentration 100 *ppmv*; *GHSV* 16000 h^{-1}; pellet size 3-4 *mm*.

force and the higher the increase in technical effort [201, 202]. This means particularly that the extent of sorbent utilization was improved by the HCl content of the test gas.

Table 3.17: Cl_{cap} values in *mg/g* and *BT* values in *min* for experiments operated at HCl inlet concentration 100 *ppmv*; *GHSV* 16000 h^{-1}; particle size 3-4 *mm*; temperature 20 °C.

Sorbent	Activated carbon		Activated alumina 1		Activated alumina 2	
	Cl_{cap} [*mg/g*]	*BT* [*min*]	Cl_{cap} [*mg/g*]	*BT* [*min*]	Cl_{cap} [*mg/g*]	*BT* [*min*]
GHSV 16000 h^{-1}	11.47	174	13.77	239	8.25	147

However, the increased time until reaching the breakthrough criteria could be explained as follows: Less pollutant molecules (e.g. HCl) in the gas feed mean less saturation of free adsorbent sites on the solid. In other words, a minor feed concentration increases the duration until saturation of the sorbent is reached. The sum of the conducted experiments in this work led to the conclusion that decreasing the *GHSV* at lower HCl inlet concentration will result in very long test runs with similar HCl uptake.

Simultaneous separation of HCl and H_2S

As described in Section 2.3, H_2S and HCl are pollutants for a SOFC CCHP system. The concentration of components is listed in Table 2.2. The negative impact is not limited to SOFCs and reformers. Pipes and plant components are also affected. Apart from the static capacitance effect, the steric effect and the kinetic effect, the equilibrium effect is one of the four mechanisms the selectivity of adsorption is essentially based on. Since all thermodynamic systems strive to minimum of free energy, the component with higher energy of bonding is adsorbed preferably. In adsorption, measurement of breakthrough curves is preferred over adsorption of multicomponent mixtures. In particular, this provides information on kinetics and dilution effects [202].

The activated carbon is impregnated with K_2CO_3, which allows a simultaneous adsorption of HCl and H_2S [34]. In addition to the K_2CO_3 impregnated activated carbon, no other adsorbent investigated in this work was able to simultaneously separate H_2S and HCl. The reaction of K_2CO_3 with HCl leads to potassium chloride (KCl) which has a bond dissociation energy of -436 *kJ/mol* (Equation 3.2). On the other hand, the reaction between K_2CO_3 and H_2S leads to potassium sulfide (K_2S) which has a bond dissociation energy of -380.7 *kJ/mol* (Equation 3.3).

$$K_2CO_3 + 2HCl \rightharpoonup 2KCl + CO_2 + H_2O \tag{3.2}$$

$$K_2CO_3 + H_2S \rightharpoonup K_2S + CO_2 + H_2O \tag{3.3}$$

Figure 3.23 shows the performance of the activated carbon while using a feed gas consisting of 100 *ppmv* HCl and 200 *ppmv* H_2S balanced with N_2, at 20 °C and at GHSV 8000 h^{-1} (left) and 16000 h^{-1} (right), respectively. The dashed red and blue lines at 2 and 10 *ppmv* concentration mark the maximum inlet concentration of H_2S and HCl for the SOFC, respectively. A comparison leads to the following conclusion: The measured H_2S output concentrations seen in Figure 3.23 increase immediately after starting the experiment. By the end of the experiment, after 6 or 4 hours, the concentration in both experiments increases to about 180 *ppmv*. Exceeding of the 2 *ppmv*, which is the tolerance limit for the SOFC, happens 5 (at $GHSV$=8000 h^{-1}) and 4 (at $GHSV$=16000 h^{-1}) minutes after the start of the test runs. By doubling the $GHSV$, the HCl breakthrough time had been halved from 5.2 to 2.6 hours. The results for the HCl and H_2S uptake until breakthrough (2 *ppmv* for H_2S and 10 *ppmv* for HCl) are given in Table 3.18. The low values for S_{cap} can be explained as follows: The maximum outlet concentration of 2 *ppmv* H_2S was chosen as calculation limit. This results from the entry limit for H_2S in SOFCs defined in Section 2.3.2. These boundary conditions lead to a breakthrough within a few minutes, which results in low S_{cap} values.

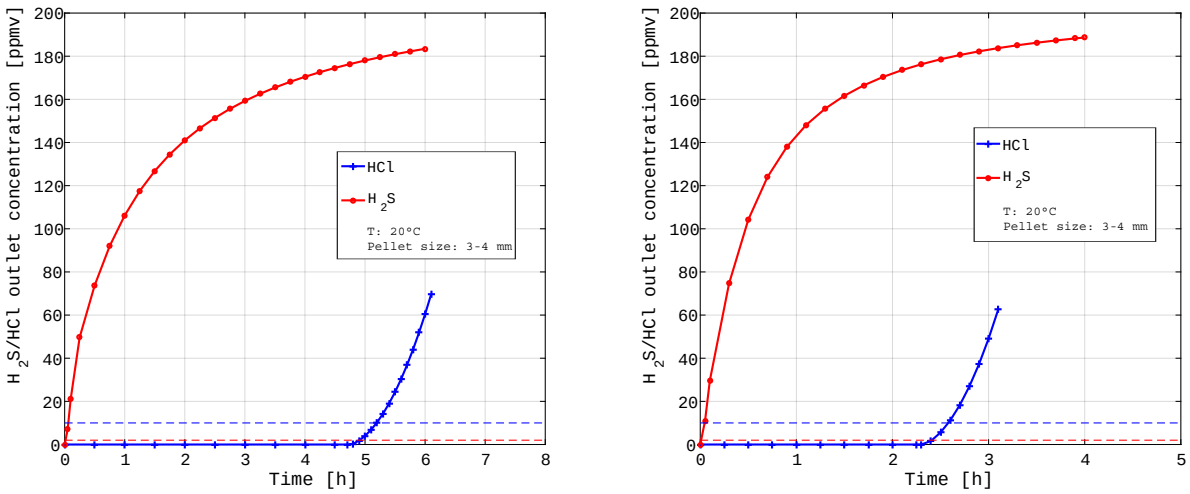

(a) $GHSV$s of 8000 h^{-1} **(b)** $GHSV$s of 16000 h^{-1}

Figure 3.23: HCl-H_2S adsorption at reaction temperature 20 °C; HCl inlet concentration 100 *ppmv*; H_2S inlet concentration 200 *ppmv*; pellet size 3-4 *mm*.

Table 3.18: Values for Cl_{cap}, S_{cap} in *mg/g* and associated BT vales in h for experiments operated at reaction temperature 20 °C; HCl inlet concentration 100 *ppmv*; H_2S inlet concentration 200 *ppmv*; pellet size 3-4 *mm*.

Sorbent	Activated carbon	
	S_{cap} / Cl_{cap} [*mg/g*]	BT [h]
S_{cap} at GHSV 8000 h^{-1}	$7.19 \cdot 10^{-5}$	0.08
Cl_{cap} at GHSV 8000 h^{-1}	20.56	5.20
S_{cap} at GHSV 16000 h^{-1}	$6.51 \cdot 10^{-5}$	0.06
Cl_{cap} at GHSV 16000 h^{-1}	11.34	2.60

Summary

In summary, the following statements can be made for this test series. Three different adsorbents were tested for their ability to separate HCl from a gas stream. A K_2CO_3 impregnated activated carbon and two sorbents based on activated aluminuma were used. Increasing the $GHSV$ from 8000 h^{-1} to 16000 h^{-1} resulted in a limited breakthrough time for all sorbents. For activated alumina 1 and 2, the breakthrough times were reduced by over 50% by doubling the $GHSV$ (from 63 to 28 minutes for activated alumina 1 and from 60 to 17 minutes for activated alumina 2). In the case of activated carbon, the breakthrough time reduced from 81 to 24 minutes (see Table 3.15).

The study of the influence of particle size on the adsorption performance did not provide consistent results. At a $GHSV$ of 16000 h^{-1}, an increase of Cl_{cap} was measured for all crushed adsorbents (particle size 500-1000 μm). With $GHSV$ 8000 h^{-1}, crushing of the pellets only had a positive effect on Cl_{cap} of the activated aluminuma 1 sorbent (see Tables 3.15 and 3.16).

Comparing the sorbent uptake capacity at HCl inlet concentrations of 100 and 1000 $ppmv$ Cl_{cap} shows that a higher HCl inlet concentration led, to a 10 % higher sorbent uptake (see Tables 3.15 and 3.17). This results from the increased concentration gradient and coincides with the literature [201, 202]. By decreasing the HCl inlet concentration, the BT values increased from 25 to 174 minutes for activated carbon, from 28 to 239 minutes for the activated alumina 1, and from 18 to 147 minutes for activated alumina 2.

By using K_2CO_3 impregnated activated carbon, simultaneous separation of HCl and H_2S was achieved. This is an advantage of impregnated activated carbon. Several substances of the biogas, which are harmful to the SOFC, can be separated. However, the S_{cap} values are very low (see Table 3.18). The reason for this is the 2 $ppmv$ limit for H_2S, which had already been exceeded after 4 or 5 minutes (see Figure 3.23).

3.1.5 Selection of adsorbents for scale-up

The adsorbents investigated in this work were selected based on their separation properties. The physical and chemical properties of the different types of adsorbents have already been described in section 2.6.5. The experiments carried out in Section 3.1 served to classify the individual sorbents with regard to their suitability for use in the biogas-fueled SOFC CCHP plant. In the experiments carried out the following observations were made:

- The ZnO sorbent shows a good desulfurization performance at elevated temperatures (100-200°C). At room temperature, however, no satisfactory results were achieved. In addition, there was a deterioration in the separation effect with increasing $GHSV$ and H_2S inlet concentration. Due to the modest performance and the requirement to perform the biogas cleaning at room temperature, no further tests were carried out with ZnO.

- MnO-doped zeolite was used only in the test series with NH_3 (Section 3.1.3). In the reference case (Test 1 - 200 *ppmv* H_2S in N_2) good results were obtained. A full breakthrough occurred after 28.2 *h* and a S_{cap} of 67.51 *mg/g* was calculated. However, in Tests 2-5, performance decreased for both the breakthrough time and the S_{cap}. For this reason, no further tests were carried out with the MnO doped zeolite.
- The CuO-doped zeolite showed an average performance compared with CuO-MnO sorbent and impregnated activated carbon. In the presence of NH_3 in the gas, the values for breakthrough time and S_{cap} were behind those of the CuO-MnO sorbent and the impregnated activated carbon. In the investigation of the influence of gas composition and moisture, the breakthrough time and S_{cap} values were ahead of those of the impregnated activated carbon.
- Impregnated activated carbon was characterized by several positive properties. Despite moderate breakthrough times and S_{cap} levels, K_2CO_3 impregnated activated carbon is a versatile adsorbent for biogas purification. This is confirmed by the tolerance to moisture (see Section 3.1.2) and the tolerance to NH_3 (see Section 3.1.3). In addition, K_2CO_3 impregnated activated carbon makes it possible to simultaneously separate several acidic components such as HCl and H_2S from biogas.
- CuO-MnO sorbent is characterized by comparatively high S_{cap} values and breakthrough times. However, the experiments performed showed sensitivity to moisture in the gas.
- In addition to the impregnated activated carbon, another two sorbents were tested for the separation of HCl. These activated aluminas both showed promising results in terms of separation performance and breakthrough time. The results obtained from the experiments were not used for the scale-up. The experiments were performed with 1000 *ppmv* HCl in N_2. The boundary conditions of the scale up were determined after these tests to 100 *ppmv* HCl.

Based on these results, which are described with numbers in Sections 3.1.1-3.1.4, the CuO-MnO sorbent and the K_2CO_3 impregnated activated carbon were selected for the scale-up calculation. Due to their properties, these sorbents are suitable for use in the biogas operated SOFC CCHP plant. As already described, K_2CO_3 impregnated activated carbon has the ability to separate H_2S and HCl from the biogas. In contrast, the selected CuO-MnO sorbent can only separate H_2S. For a complete scale-up, the CuO-MnO sorbent would have to be supported by activated aluminum 1 for the removal of HCl. The existing experimental data does not cover the scale-up scenario, therefore, this calculation is not performed.

Finally, the economic components should be considered, even if specific product prices are not available. Specific prices could not be determined because manufacturers only calculate bids on the basis of industrial purchase quantities. In the literature, however, there are indications that sorbents based on metal oxides are 3-8 times more expensive than (impregnated) activated carbons [34, 280].

3.2 Steam reforming

As described in Section 2.7, SR is the most suitable option for upgrading biogas and use it in a SOFC. By controlling the S/C ratio, possible carbon deposits can be counteracted and the SOFC can be protected from damage. The theoretical fundamentals of this procedure have already been explained in Sections 2.3.1 and 2.7. After the separation of the pollutants (H_2S and HCl), the biogas is ready for the next process step, which is SR.

The production of pure H_2 and synthesis gas by steam conversion of CH_4, the main component of biogas, is an important and established industrial process. Supported Ni catalysts are commonly used in this reaction and their activity and deactivation patterns have been widely studied [281]. However, at low O/C ratios optimal for overall energy efficiency, Ni catalysts deactivate because of carbon deposition. Carbonaceous depositions are produced by the Boudouard reaction (see 2.10) and the CH_4 decomposition reaction (see Equation 2.11). Carbon covered surfaces or bulk carbides no longer catalyze the reforming reaction because active Ni sites are blocked [282]. SR of CH_4 is an endothermic reaction, hence it is operated at high temperatures of 700–900°C. In this reaction Rostrup-Nielsen [124] observed three kinds of carbon species:

- Whiskerlike carbon formed on the catalyst surfaces at greater than 450°C;
- Encapsulated hydrocarbons formed by polymerization at less than 500°C;
- pyrolytic carbon formed by cracking of hydrocarbons at above 600°C.

Whisker carbon occurs at low S/C ratio and at high temperatures. This formation is typical for SR (also in the internal reforming of CH_4 at the anode). Whisker carbon causes a mechanical destruction of the catalyst particles which can not be reversed. The formation arises as follows:

- Adsorbed hydrocarbon or carbon monoxide dissociates and forms elemental carbon;
- The carbon is dissolved in the Ni;
- The carbon diffuses through the Ni and deposits on the back side between Ni and carrier material;
- The Ni particle changes shape leaving small Ni fragments in the whisker;
- Upon reaching the pore wall, the catalyst particle is destroyed by the strong action of the whisker [124, 244].

It was found that the whisker formation is also related to the size of the Ni particles at the anode. Larger Ni particles are more likely to be saturated with whisker formation than small Ni particles. In order to avoid the formation of carbon deposits as far as possible, care must be taken during SR that sufficient water vapor is present in relation to the higher hydrocarbons. Whether one is in the carbon-depositing range can be determined by thermodynamic equilibrium calculations. Depending on the temperature and pressure, the equilibria and the associated products, i.e. a possible carbon deposition, can be recorded in a carbon-hydrogen-oxygen

(CHO) diagram (see Figure 2.6). If the concentration of the gas is above the associated limit line, one lies in the carbon-separating region [124].

The direct electrochemical conversion of CH_4, the main component of biogas, in a SOFC is an additional option, although it is not feasible at present (see Section 2.1.4). Internal SR is an attractive option offering a significant cost reduction and higher system efficiencies for a biogas SOFC CCHP system. Complete internal reforming can lead to carbon formation in the anode chamber and to large temperature gradients in the stack caused by a strong cooling effect of the very fast reforming reaction in the fuel inlet area. Solid carbon formation on the anode reduces mass transport of gas reactants to the TPB and deactivates catalytic activity of Ni contained in the anode. The rate of carbon formation and deposition is strongly dependent on temperature. At higher temperatures (and low O_2 partial pressure), the carbon formation rate is controlled by the cracking reaction. By increasing the O_2 content (adding H_2O, CO or CO_2 to the gas), the temperature dependence of deposit formation is inverted and the rate of coke formation increases with decreasing temperature [103].

The experiments were carried out using a Ni-based catalyst from Clariant. The used ReforMax 100 [247] is a catalyst that is used for pre-reforming. A pre-reformer is an adiabatic fixed-bed reactor upstream of the primary (steam) reformer. It allows greater flexibility in the choice of feedstock and an increased lifetime of the SR catalyst. Furthermore, it allows operation at lower S/C ratios. ReforMax 100 is a pre-reforming catalyst designed to handle the entire range of hydrocarbon feedstocks, from natural gas up to and including LPGs and naphthas [247]. The pre-reforming catalyst converts higher hydrocarbons that are present in the gas feedstock into a mixture of CH_4, CO_2, CO, and H_2. Moreover, the pre-reforming catalyst can adsorb any slip of sulfur from the desulfurisation section. Because the pre-reforming catalyst is more expensive than the steam methane reforming catalyst, reliable upstream desulfurisation is recommendable [283]. Due to the adsorption in the SOFC CCHP system, which reduces the H_2S content to less than 2 *ppmv* to prevent damage to the anode, there is no risk of sulfur poisoning of the reformer.

For a reforming catalyst, a high Ni surface area is essential due to the temperature of operation in adiabatic reactors with moderate reactor size. The catalyst crush strength, thermal shock resistance and pressure drop are less important than in other applications. This allows the use of catalyst pellets of moderate size to be used in reforming reactors. The operating temperature is reported to be in the range of approximately 400–600 °C and the operating pressure is recommended to be between atmospheric and 6.0 *MPa*. The optimum S/C ratio is approximately 1.5–3.0 and the *GHSV* is approximately 1000–3000 h^{-1} [283].

The catalysts consists of 56 wt% NiO and is shipped in form of pellets sized 4.7 *mm* x 4.7 *mm* [247]. The catalyst features the following [283]:

- Excellent reforming activities and stability, especially high activity at low temperature;
- Suitability for pre-reforming under high space velocity;
- Excellent reducibility; able to be reduced in pre-reformer;

Figure 3.24: SR test rig including reactor, gas control system, tube furnace for preheating and gas analyzer.

- Stability for long service life ;
- Suitability for a wide range of feedstock.

Reforming experiments were carried out at atmospheric pressure in a fixed-bed reactor shown in Figure 3.24. The associated flow chart is shown in Figure 3.25. The used reforming reactor had the inlet port at the bottom and the outlet port on the top side. All elements of the reactor (e.g. valves, pipes) were made of stainless steel type 1.4841. This type of steel is used in fields where excellent scale resistance with high heat resistance is of advantage. The heating of the reforming reactor was realized by means of two separate electrical heating tapes on the outside of the reactor. This has the advantage that heat losses are compensated and the reactor can be heated up to 900 °C. Programmable PID elements controlled and monitored the set temperatures. Ten type K thermocouples were placed over the reactor height at fixed positions to monitor the temperature profile within the reactor. A total inner reactor volume of 1.76 dm^3 was realized by a reactor height of 500 *mm* and an inner diameter of 67 *mm*. The catalyst was placed within layers of inert material (see Figure 3.25) on the top and bottom. The inert material ensured a homogenous plug flow profile of the gas flow. The inert materials were alumina based inert spheres with an Al_2O_3 mass amount of >99 %.

The input gas mixture, a synthetic biogas consisting of CH_4, CO_2, was generated with a gas mixing rig with adjustable volume fractions. For rinsing and for activating the catalyst, it was also possible to feed the system with forming gas (5 vol% H_2 in N_2). The gas flows were controlled by calibrated high-precision thermal MFCs (Vögtlin red-y smart series) with maximum gas flow ranges of 10 *slpm*. The H_2O content of the gas flow was controlled by a temperature-regulated water reservoir filled with deionized water. Due to the solubility of CO_2 in H_2O, CO_2 was bypassed. This is also the reason, or the technical limitation, that the system

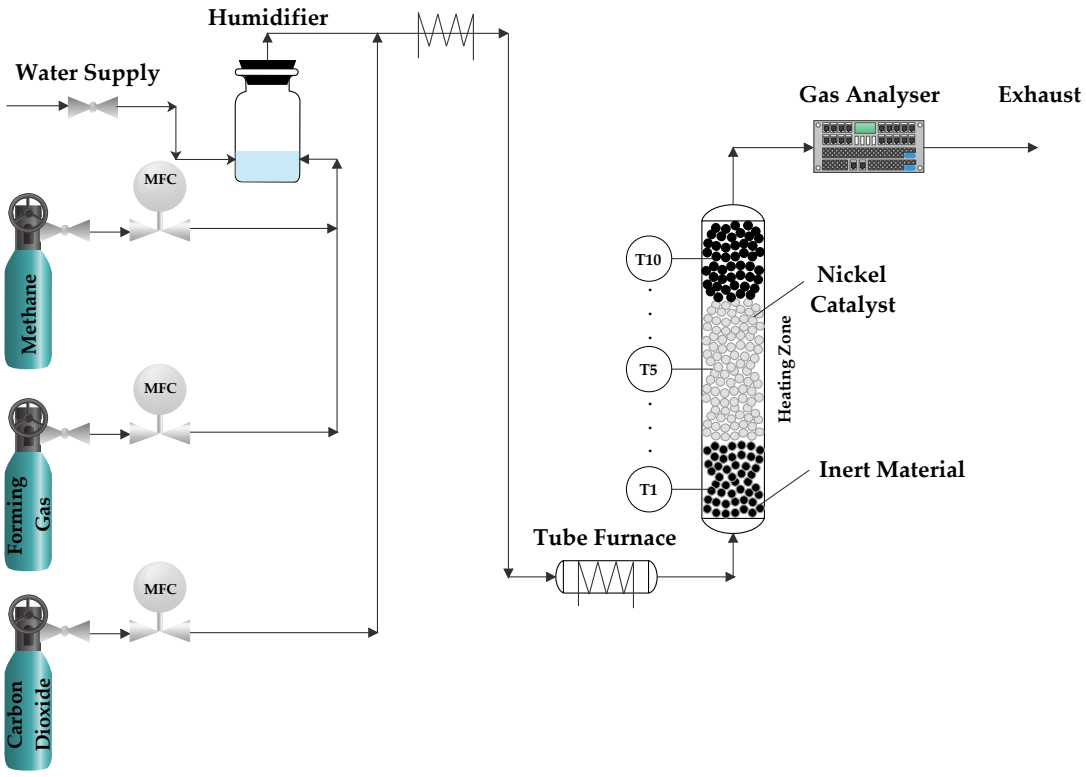

Figure 3.25: Flow chart of SR test rig.

was tested at S/C ratios up to 2 and no higher. Electrical wirings heated all pipes and valves to avoid formation of condensed water within the system. For measuring the components of the syngas, an ABB Advanced Optima gas analyser was used. The gases CH_4, CO, CO_2 and H_2 were continuously analysed and recorded. Before entering the gas analyser, the syngas was dried and cleaned from impurities by using temperature-controlled washing bottles filled with deionized water.

The catalyst was tested at S/C ratios 1.5 and 2 and at space velocities of 1000 h^{-1} and 1500 h^{-1}. According to the literature [284], it is possible to limit carbon deposition thermodynamically by adding excess steam or CO_2. Carbon formation becomes thermodynamically unfavored when the H_2O to CH_4 ratio is greater than 1 and no carbon deposition was observed for S/C ratios higher than 1.5-1.6 on Ni/YSZ in SOFCs. As mentioned in Section 2.7, this applies to the same extent to the catalyst. The fact that the CH_4 will be converted into H_2 in the SR for the most part, the SOFC receives less CH_4 in the anode chamber, which is a protection against carbon deposits. The experiments were carried out in a temperature range from 400 to 600 °C. To pre-evaluate the key parameters, it was necessary to determine a range of parameters in a virtual reforming reactor in HSC Chemistry. The following parameters were chosen: CH_4:CO_2 = 60:40 and S/C = 1.5. The reactor can be described as isothermal and is based on a Gibbs reactor by minimising the Gibbs enthalpy $\Delta_R G$. Therefore, it was possible to draw an equilibrium curve for different S/C-ratios at different temperatures.

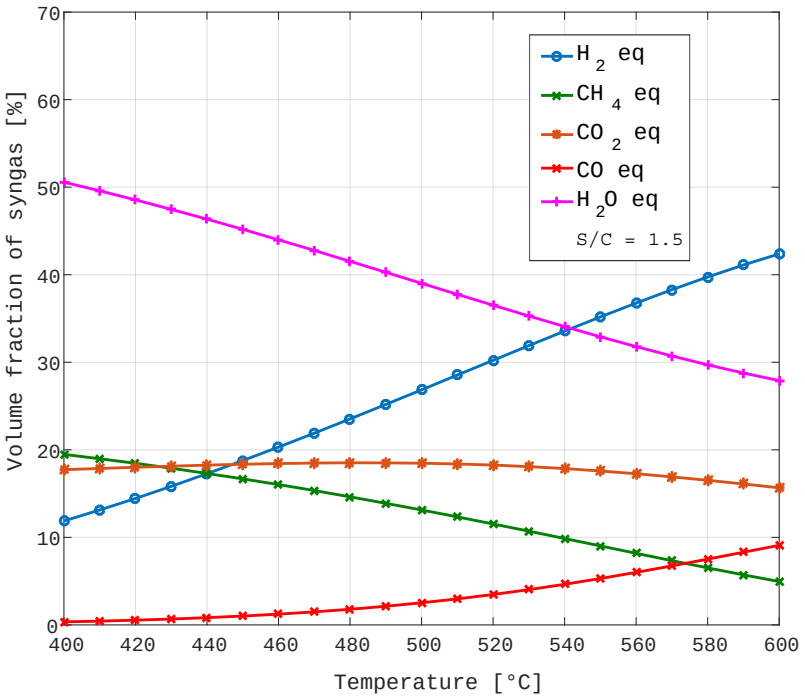

Figure 3.26: Syngas equilibrium composition between 400 and 600 °C; ambient pressure; CH_4:CO_2 = 60:40; S/C=1.5.

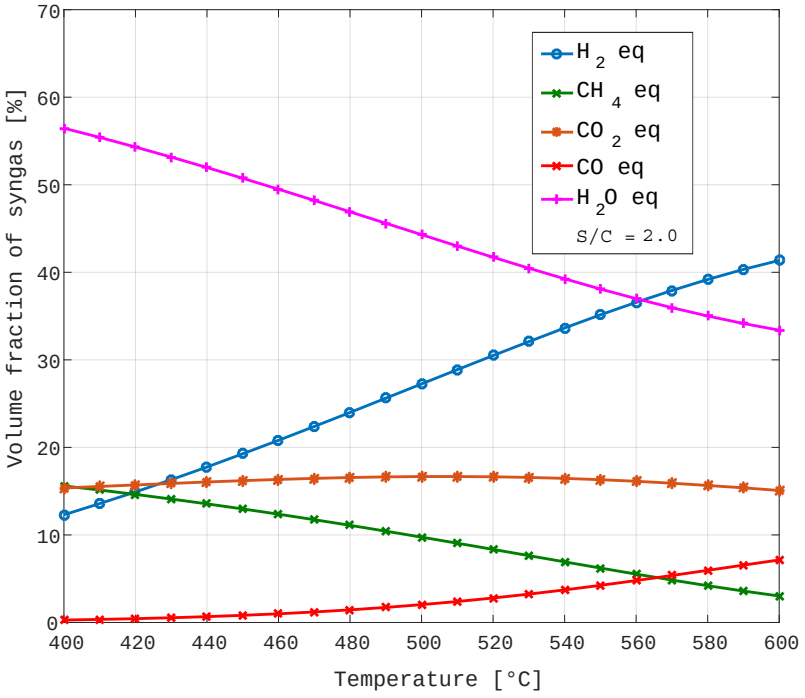

Figure 3.27: Syngas equilibrium composition between 400 and 600 °C; ambient pressure; CH_4:CO_2 = 60:40; S/C=2.

The calculated equilibrium composition at S/C = 1.5 is shown in Figure 3.26. Similarly, the calculated equilibrium composition at S/C = 2 is shown in Figure 3.27. The calculated equilibria still contain the proportion of H_2O. In order to be able to compare the data with the results from the experiments, the values have to be related to dry syngas.

The test rig was supported by a synthetic biogas consisting of 60 vol% CH_4 and 40 vol% CO_2. In addition, a forming gas (5 vol% H_2 in N_2) was used for the activation and heat up of the catalyst. The activation or heat up was performed according to the manual [285]. The flowrate of the forming gas was set at 150 *slpm* while heating up the catalyst is set at 100 °C with 50 °C per *h*. Further heating up to 130 °C is achieved with a heating rate of 15 °C per *h*. After reaching 130 °C, the temperature is being kept steady for 1 h. The heating rate can now be increased again to 50 °C/*h* until the desired operating temperature is reached. The activation was only performed once because the catalyst was never been changed.

3.2.1 Test series at S/C = 1.5 [5]

In this test series the deviation of the experimental results from the simulated equilibrium calculations at an S/C ratio of 1.5 and a *GHSV* of 1000 hh^{-1} in the temperature range between 400 and 600 °C at ambient pressure was investigated. The results are shown in Figure 3.28 and the corresponding numbers are given in Table 3.19.

The solid lines represent the simulated equilibrium composition at the respective temperatures. The dashed lines represent a fit based on the measured compositions at 400, 500 and 600 °C (average temperature from the ten temperature sensors, see Figure 3.25). The results of CO and CO_2 show only a slight deviation from the simulated values. At 600 °C, the measured amount of H_2 is about 4% lower, CO_2 is about 3% higher, CH_4 is about 4% higher and CO is about 1.5% lower compared to the calculated equilibrium values. At 400 °C, only the measured amount of H_2 is about 2.7% lower compared to the calculated equilibrium. The fact that the value for CH_4 is above and the value for H_2 is below the equilibrium composition at 600 °C indicates that CH_4 has not fully reacted. A possible cause of these deviations could be the temperature distribution. Cooler zones in the reactor could account for the deviation from the simulated values.

Table 3.19: Results of the simulation and the experiment; S/C = 1.5; *GHSV* = 1000 h^{-1}.

Temperature [°C]	Volume fraction eq. [vol%]				Volume fraction exp. [vol%]			
	H_2	CO_2	CH_4	CO	H_2	CO_2	CH_4	CO
400	24.02	35.87	39.41	0.70	21.24	35.91	39.75	0.65
500	44.03	30.29	21.53	4.14	38.99	31.52	23.28	3.77
600	58.79	21.72	6.87	12.61	52.27	24.46	10.60	10.54

[5] Segments of Section 3.2.1 have already been published in Journal of Electrochemical Energy Conversion and Storage [286].

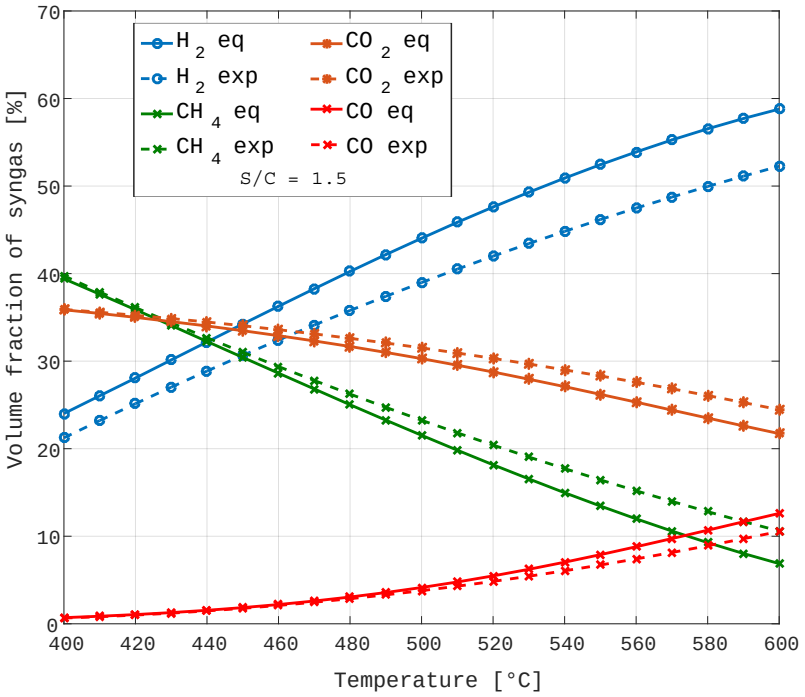

Figure 3.28: Facing the experimental results and the simulated equilibria; S/C = 1.5; $GHSV$ = 1000 h^{-1}; temperature range 400 – 600 °C.

The next test runs were performed at a S/C ratio of 1.5, a $GHSV$ of 1500 h^{-1} and at temperatures 400, 500 and 600 °C. A comparison between those results and the results gained at a $GHSV$ of 1000 h^{-1} at a temperature of 600 °C are given in Figure 3.29. By increasing the $GHSV$ from 1000 up to 1500 h^{-1}, the H_2 content in the produced syngas dropped from 52 down to 48 vol% at a reaction temperature of 600 °C. At the same time, the CH_4 fraction in the syngas increased from 7 to 11 vol%. This deviation of the results from the calculated equilibrium concentration can be explained with Figure 3.30. Due to the ten thermocouples, which are arranged over the height of the reactor, it is possible to plot a temperature profile over the reactor height. Figure 3.30 shows the temperature profile for the experiment performed at $GHSV$ 1500 hh^{-1}, temperature 600 °C and S/C of 1.5.

The temperature at the reactor inlet is at about 570 °C. With increasing reactor height, the temperature rises up to the reactor outlet where a temperature of about 630 °C prevails. SR is an endothermic process step, i.e. the reaction requires energy to drain. At the reactor inlet, the gas stream consists of CH_4, CO_2 and water vapor and gets into contact with the catalyst which is required to carry out the SR. Due to the prompt reaction, the reactor temperature drops and the PID control is unable to compensate for this with additional heating power. Additionally, the observation that the temperature towards the reactor exit is above 600 °C and the measured concentration deviates from the calculated equilibrium reaction may indicate that the $GHSV$ is too high. The contact time of the gas with the catalyst may not be sufficient to reach the possible calculated equilibrium concentration. However, due to the fact that there is only a

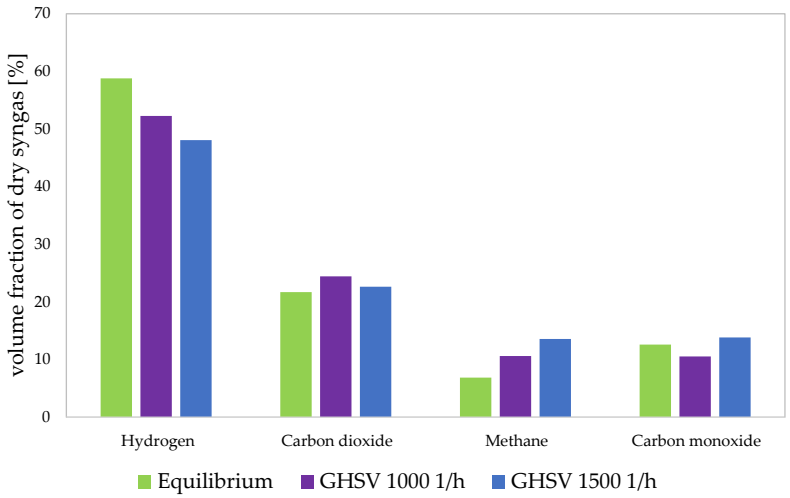

Figure 3.29: Comparison between test runs (S/C=1.5; $GHSV$ = 1000 and 1500 h^{-1}; T = 600 °C).

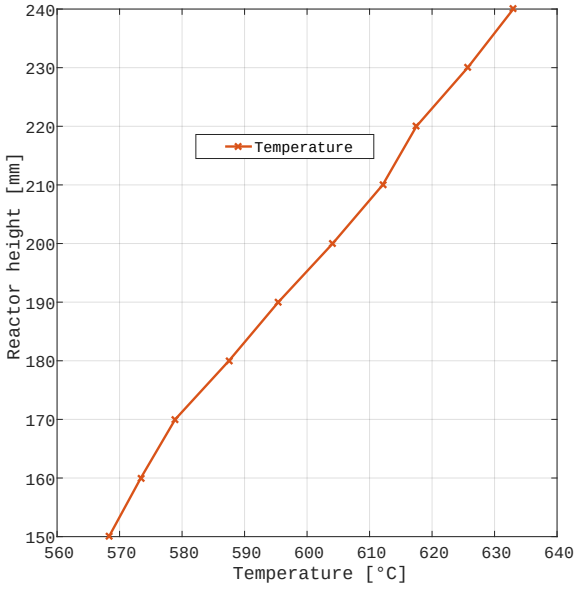

Figure 3.30: Temperature distribution (average T1-T10) in the reactor at 600 °C; $GHSV$ = 1500 h^{-1} and S/C=1.5.

slight deviation of the measured from the calculated values at 400 °C, the deviation at 600 °C can be attributed to the lack of heat output.

3.2.2 Test series at S/C = 2 [6]

These tests were carried out analogously to the tests at S/C = 1.5. Only the amount of H_2O was increased. The results are shown in Figure 3.31 and the corresponding numbers are given in Table 3.20. The solid lines represent the simulated equilibrium composition at the respective temperatures. The dashed lines represent a fit based on the measured compositions at 400, 500 and 600 °C (average temperature from the ten temperature sensors, see Figure 3.25). At a reaction temperature of 400 °C and a $GHSV$ of 1000 h^{-1}, there was again a slight deviation of the measured values from the calculated equilibrium composition. At 400 °C, the measured amount of H_2 is about 3% lower compared to the calculated equilibrium value. The results of CO, CO_2 and CH_4 show almost no deviation from the simulated values. As the temperature increases, however, the measured values deviate from the simulated values. At 600 °C, the measured amount of H_2 is about 8% lower, CO_2 is about 3% higher, CH_4 is about 4% higher and CO is about 1.5% lower compared to the calculated equilibrium values.

Table 3.20: Results of the simulation and the experiment; S/C = 2; $GHSV$ = 1000 h^{-1}.

Temperature [°C]	Volume fraction eq. [vol%]				Volume fraction exp. [vol%]			
	H_2	CO_2	CH_4	CO	H_2	CO_2	CH_4	CO
400	28.45	35.28	35.83	0.64	25.52	35.56	39.74	0.64
500	48.92	29.92	17.50	3.66	39.51	31.06	22.81	4.16
600	62.10	22.64	4.54	10.72	54.43	25.38	8.83	9.23

By increasing the $GHSV$ from 1000 up to 1500 h^{-1}, the H_2 content in the produced syngas dropped from 54 down to 50 vol% at a reaction temperature of 600 °C. At the same time, the CH_4 content increased from 9 to 12 vol%. The comparison of the experiments at a $GHSV$ of 1000 and 1500 hh^{-1} is shown in Figure 3.32. The interpretation of these results leads to the following conclusion: As the temperature rises and the $GHSV$ increases, the deviation of the H_2 content at the output increases. Analogous to Section 3.2.1, the deviation (between calculation and experiment) from the temperature over the reactor height can be described here. An academic solution would be a modification of the reactor with several heating zones which are controlled separately by means of PID controls. However, this is not feasible for an industrial-scale plant. Nevertheless, the steam reformer subsystem is fully functional, ready for coupling with the adsorber and SOFC or for determining the catalyst performance for future projects.

[6] Segments of Section 3.2.2 have already been published in Journal of Electrochemical Energy Conversion and Storage [286].

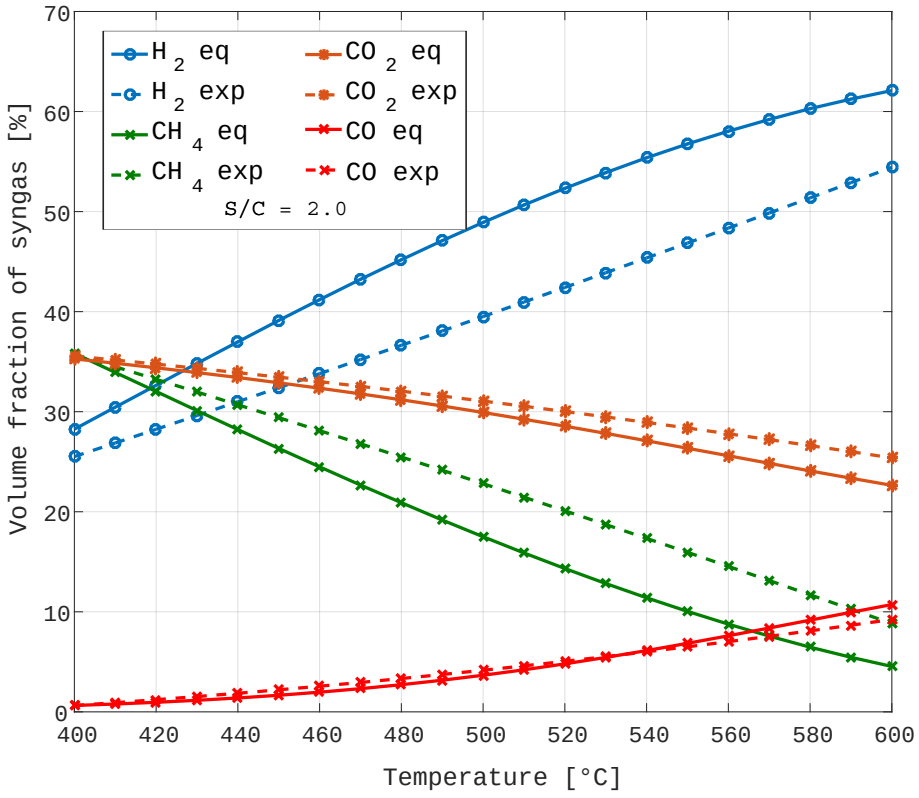

Figure 3.31: Facing the experimental results and the simulated equilibria; S/C = 2; $GHSV$ = 1000 h^{-1}; temperature range 400 – 600 °C.

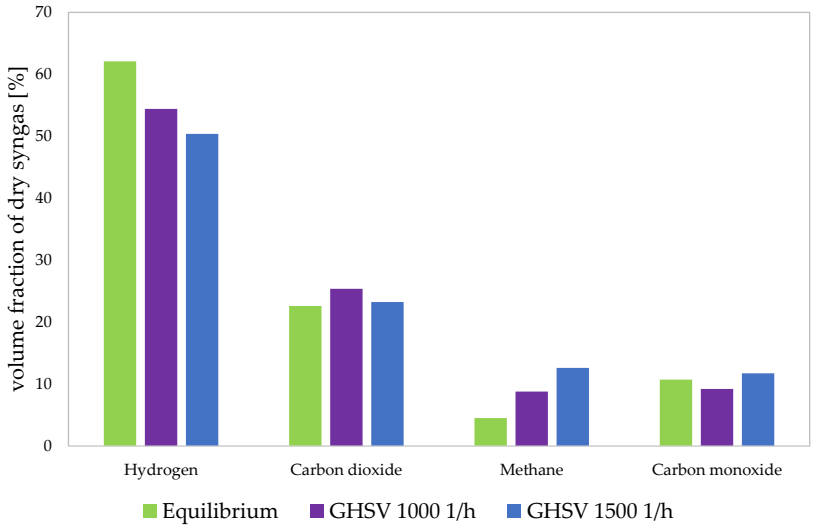

Figure 3.32: Comparison between test runs (S/C=2; $GHSV$ = 1000 and 1500 h^{-1}; T = 600 °C).

3.3 10 cell SOFC stack

The SOFC stacks and the associated housing used in this study were provided by the IKTS. It is a planar 10 cell stack of the MK 351 design. The electrolyte supported cells have an active area of 127 cm^2 (110 x 115 mm^2). Details about this type of stack have already been discussed in Section 2.2. The focus is on the commissioning of the stack within a test rig, (which has been rebuilt for this purpose), in order to observe parameters, such as the heating process, and to investigate the behavior under load. For this purpose, the SOFC stacks are put into operation and measured at pre-defined operating conditions. A flow chart of the entire FC test rig is shown in Figure 3.33.

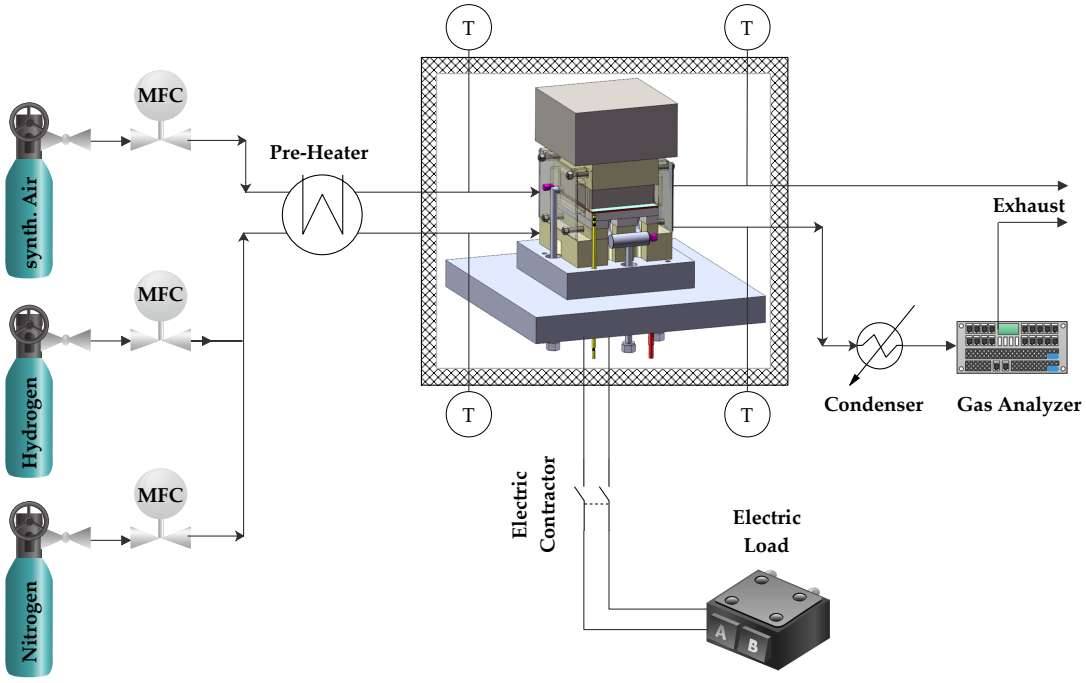

Figure 3.33: Flow chart of SOFC test rig.

Due to an existing Carbolite top-hat furnace at the Institute of Thermal Engineering (IWT), which had be used in these experiments, some changes had to be made to integrate the stack. The Carbolite top-hat furnace is shown in Figure 3.34. Commonly, IKTS supplies an integration to the stacks, which enables safe SOFC operation. The concept of the IKTS integration provides the media preheating, on both, the anode and cathode side, by means of heating coils in the oven. Due to the small amount of space available in the top-hat furnace, this concept had to be modified in coordination with IKTS. The reason was a possible short circuit of the passive heating coils for the gas preheating with the electric heating coils of the furnace.

This problem was solved by means of a second oven for preheating of the fuel gas. For gas

Figure 3.34: Left: top-hat furnace front view; Right: interior view with heating coils.

preheating a slit tube oven existing was used. The slit tube oven (see Figure 3.33) was positioned next to the top-hat furnace and the remaining distance of the media supply pipes between slit tube oven and top-hat furnace were insulated. Further components are, an ABB Advance Optima 2000 gas analyser for analysing the gases before and after the cell, and an electrical load connected by an electric contractor.

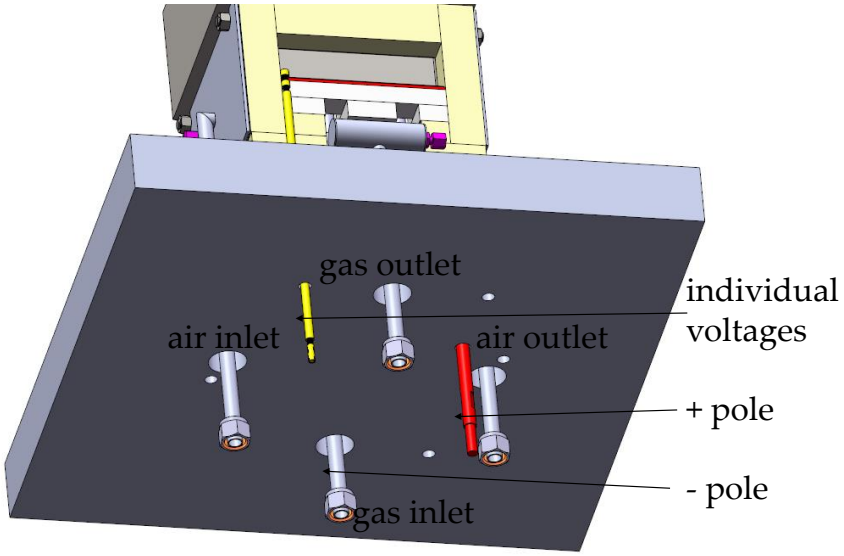

Figure 3.35: Bottom of the integration [287].

The gas supply was ensured by means of an MFC-controlled gas control system. Calibrated high-precision thermal MFCs (Vögtlin red-y smart series) were used for gas dosing. The MFCs are controlled by means of a B&R programmable logic controller. The next step was to start customizing the integration. First, the bottom plate of the oven was adapted to the hole pattern of integration. The air inlet and outlet, gas inlet and outlet, as well as an opening for the positive pole connection and an opening for the connections of the individual voltages had to be drilled. The negative pole was fixed to the grounding and connected to the gas pipes.

In addition, there are several smaller holes for the installation of the thermocouples. Six type N thermocouples were used to determine the gas and air inlet and outlet temperatures, the temperature inside the furnace housing as well as the temperature underneath the bottom plate of the stack. Figure 35 shows the bottom of the integration with the connectors for air inlet/outlet, gas inlet/outlet, the poles and the connector for the individual voltages.

The further set-up of the integration was carried out according to the assembly manual provided by IKTS [287]. One problem occurred with the platinum loops for measuring the single cell voltages. Broken eyelets were responsible for the fact that a tapping of the individual voltage was not possible. Due to the interconnection of the single cells, it was possible to measure the total voltage of the stack. A repair on site was not possible with the existing technical equipment. For stack 2, a different attachment method was chosen for the eyelets. With the revised eyelets, it was possible to measure the individual voltages. Figure 3.36 shows the platinum eyelets of the two stacks. In stack 1 (top), there were several broken eyelets due to wire breakage. In stack 2 (bottom), the eyelets were modified and the platinum measuring wires were attached directly from IKTS.

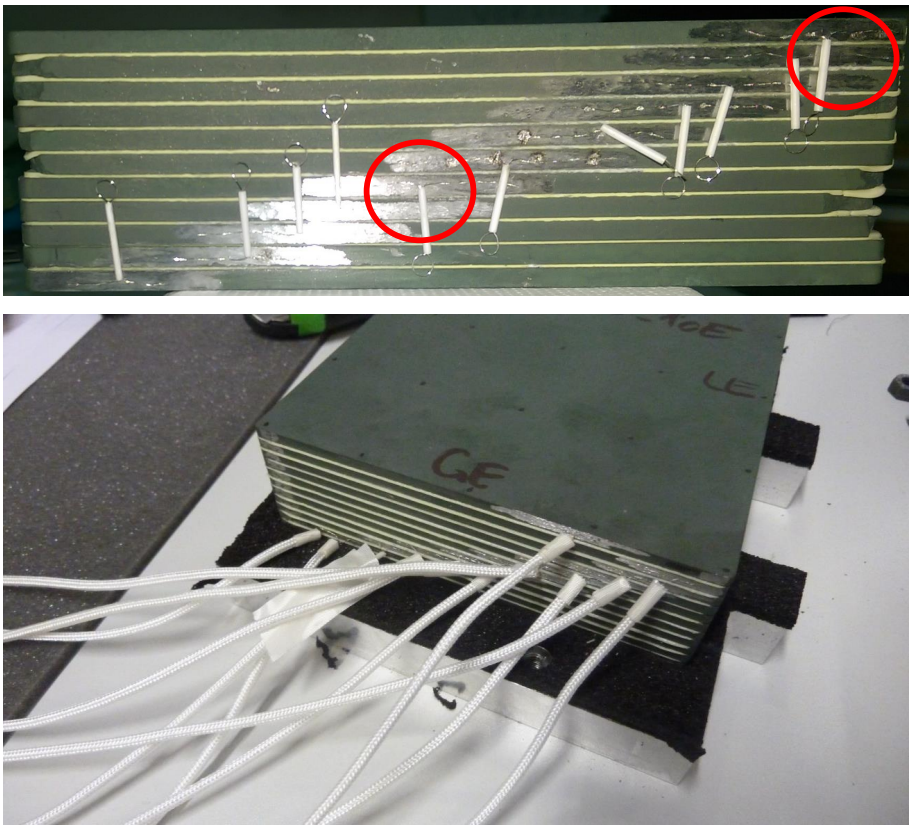

Figure 3.36: Top:defective loops of stack 1 marked in red; Bottom: modified loops of stack 2.

Figure 3.37 shows the built-in integration in the furnace. To test the seal, the stack was purged with H_2 at room temperature. For this purpose, a leakage test was applied to the sealing points, which makes gas escaping through leaks visible through bubble formation. At the same time, the stack was checked for leaks at the sealing points by means of a portable hydrogen warning

device. No leakage was found, confirming a correct and functional installation of the stack.

Figure 3.37: Integration with mounted stack.

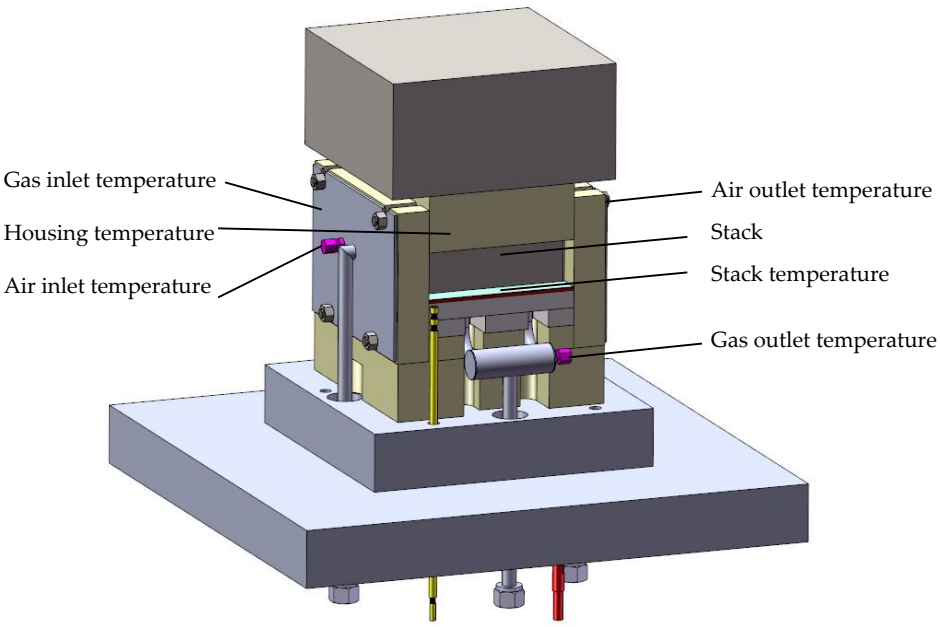

Figure 3.38: Measuring points on the stack [287].

3.3.1 Stack 1

After successful installation of the stack, the test according to IKTS standard was started. According to the protocol, the maximum heat-up ramp is 4 *K/min* and the total voltage of the cell must not fall below 0.68 *V* in any case. If an undervoltage occurs, the control switches into an emergency program and starts lowering the current with 0.5 *A/s*. During heating with the fixed ramp, the stack is supplied with 10 *slpm* forming gas (5% H_2 in N_2) on the anode side. On the cathode side, the stack is purged with 30 *slpm* process air. The supply of forming gas was ensured by means of bundles of 12 bottles (50 litre per bottle) from the gas storage. The process air was ensured by means of the compressed air available in the laboratory. To ensure particle-free air, 2 filters were connected in series at the pick-up point. After reaching operating temperature, the stack was operated for several hours in OCV mode. The operating temperature of the stack was measured at the bottom of the stack (see Figure 3.38). At a stable operating temperature of 820 °C, the test was started.

According to the test protocol, 3 different pre-defined operating conditions must be approached with the stack. The pre-defined operating condition points are denoted by $\eta_{FU} = 60$, $\eta_{FU} = 75$ and $\eta_{FU} = 80$, where FU stands for fuel utilization (see Table 3.21). Fuel utilization is defined as the ratio of converted fuel gas flow at the outlet to the supplied fuel gas flow at the inlet. In FCs, all the fuel in the cell is never converted. Normally, fuel utilization ranges between 80% and 90%. The exhaust gas from the SOFC is then recycled or externally combusted. Conversion of some fuel behind the SOFC has several reasons. With increasing fuel utilization, the O_2 partial pressure at the anode increases. This causes a lowering of the cell voltage. Complete fuel utilization would raise the O_2 partial pressure to an extent so high that the voltage would go to zero. Furthermore, the anode contains Ni as catalyst. High O_2 partial pressure at the anode increases the risk of NiO formation. Thus, the anode surface would be oxidized at this point, and thus, no longer active. This means that this point of power generation is no longer available until the oxidized spot is reduced again by means of sufficiently high hydrogen concentration. In order to achieve the situation of complete depletion of hydrogen at the anode in practice, the residence time of the fuel gas must be very high. This results in lower power per cell area. To ensure that the fuel utilization in SOFC cells is still high, a cascading can be performed in the SOFC stack. The individual stacks are interconnected differently. This results in different levels of voltage that can be tapped and results in a higher performance than at only one operating point in which one taps the voltage. The stack is supplied with a volume flow of anode fresh gas (40% H_2 in N_2) and a defined volume flow of air on the cathode side. A load change (up to 1 *A/min*) is initiated and the voltage of the stack begins to drop. An overview of the pre-defined operating condition points and the measured parameters can be found in Table 3.21. The voltage over current characteristics as well as the power over current characteristics are shown in the following graphs. The required pre-defined operating condition points are marked with black dots at the secondary vertical axis in Figures 3.39, 3.40 and 3.41 which have to be achieved at a load of 35 *A*.

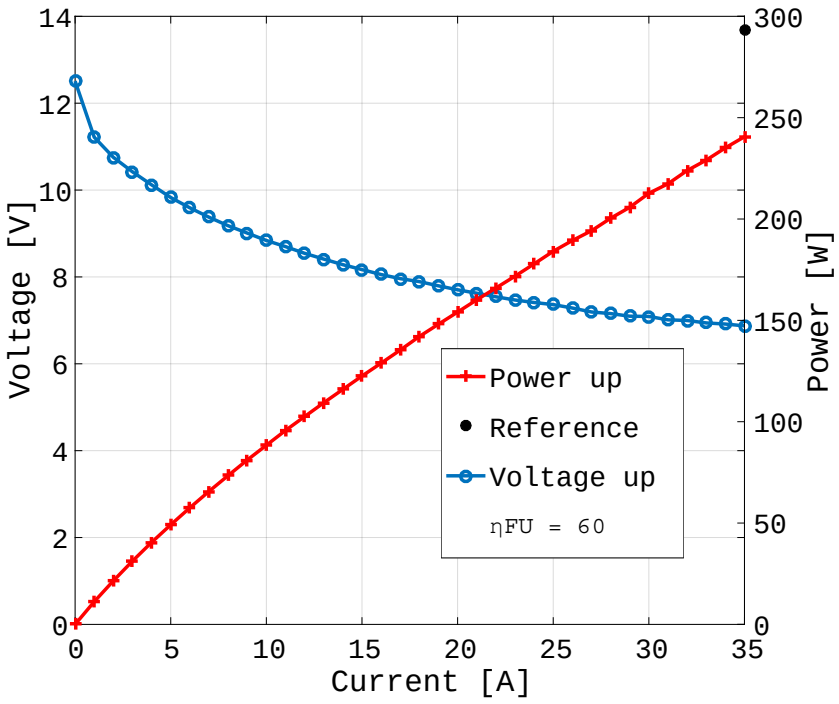

Figure 3.39: Measurement results stack 1 for the reference point $\eta_{FU} = 60$.

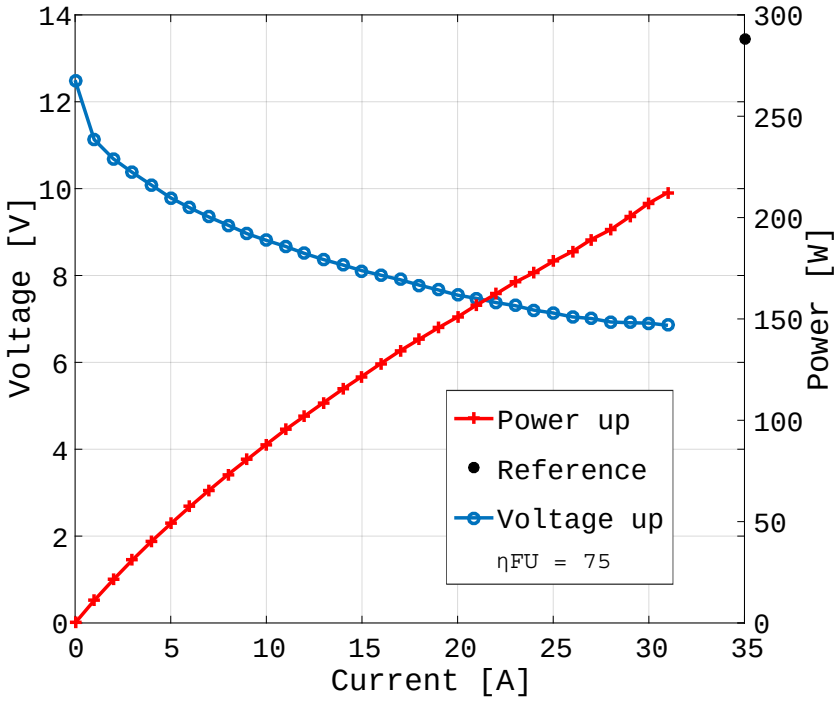

Figure 3.40: Measurement results stack 1 for the reference point $\eta_{FU} = 75$.

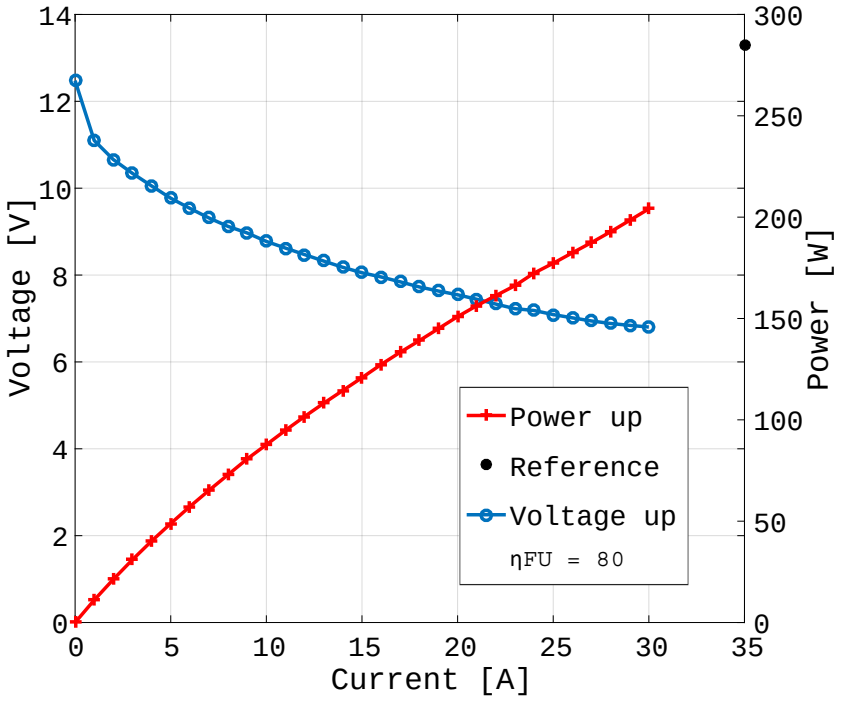

Figure 3.41: Measurement results stack 1 for the reference point η_{FU} = 80.

Table 3.21: Reference points stack 1 including measured values.

	$\eta_{FU} = 60$	$\eta_{FU} = 75$	$\eta_{FU} = 80$
Volume flow gas (40% H_2 in N_2) [*slpm*]	10.1	8.2	7.7
Volume flow air [*slpm*]	60	60	60
Reference temperature stack [°C]	830	830	830
Measured temperature stack [°C]	824	821	821
Measured temperature gas inlet [°C]	671	702	707
Measured temperature gas outlet [°C]	837	846	837
Measured temperature air inlet [°C]	662	661	717
Measured temperature air outlet [°C]	821	820	811
Measured power at 35 A [W]	240	-	-
Reference power at 35 A [W]	293	288	287

Figure 3.39 shows the results of the measurements for the reference point η_{FU} = 60. Although it was possible to increase the load to 35 A, the required power of 293 W was not achieved. Only a power of 240 W was measured at a load of 35 A. Figure 3.40 and 3.41 show an even clearer deviation from the reference points. When checking the reference point η_{FU} = 75 in Figure 3.40, the measurement had to be stopped at a load of 31 A in order to prevent falling below the critical minimum voltage. Similarly, the measurement at the reference point η_{FU} = 80, in which the load at 30 A already led to an underrun of the minimum voltage. These 3 experiments were conducted over a period of several days and there was no evidence of leakage at the seals. In addition to staying in the OCV mode, the stack has been loaded several times to check the functionality. The basics of these IV characteristic curves were described in Section 2.1.6. A comparison of the Figures 3.39, 3.40 and 3.41 with Figure 2.4 clearly shows the activation polarization. Starting from 12.4 V, the voltage (blue graph) drops sharply at the beginning, this represents the activation polarization.

The performances assigned to the reference points were not reached in the experiments. With the specialists of IKTS on site it was possible to perform a comprehensive troubleshooting. Then the stack was cooled down and the conversion work on the preheater started. It quickly turned out that the temperature of the anode fresh gas was too low. At the inlet gas temperatures of 671, 702 and 707 °C were measured (see Table 3.21). According to IKTS, the temperature should be at least 730 °C. The reduced gas inlet temperature results from the external slit tube oven. The existing top-hat furnace at the IWT is too small to accommodate the integrated heating coils offered by IKTS. To counteract this problem the heating cycle was optimized in the control of the furnace. Furthermore, an optimization in the sealing of the top-hat furnace was performed. The point, where the top-hat furnace closes and stays in contact with the bottom plate, was lined with new sealing material.

3.3.2 Stack 2

In addition to the new sealing of the top-hat furnace, the main task prior to commissioning of stack 2 was to improve the preheater. In order to ensure a higher gas inlet temperature, the distance between the oven and the preheater was shortened. In addition, the gas pipes between preheater and top-hat furnace were insulated. After completion of the test rig optimization, the test procedure was carried out in the same way as described for stack 1 (see Section 3.3.1).

An overview of the results is given in Table 3.22. In comparison with Table 3.21, it can be seen that the load increased to 35 A at all 3 reference points. This is due to the increased gas inlet temperature which could be increased by 30-60 °C. Due to the optimization acceptable results were achieved, the deviation of the measured values was less than 5% of the reference values. The required pre-defined operating conditions points are marked with black dots at the secondary vertical axis in Figures 3.42, 3.43 and 3.44 which have to be achieved at a load of 35 A.

Table 3.22: Reference points stack 2 including measured values.

	$\eta_{FU} = 60$	$\eta_{FU} = 75$	$\eta_{FU} = 80$
Volume flow gas (40% H_2 in N_2) [*slpm*]	10.1	8.2	7.7
Volume flow air [*slpm*]	60	60	60
Reference temperature stack [°C]	830	830	830
Measured temperature stack [°C]	828	826	829
Measured temperature gas inlet [°C]	735	746	730
Measured temperature gas outlet [°C]	839	853	843
Measured temperature air inlet [°C]	684	690	687
Measured temperature air outlet [°C]	898	889	892
Measured power at 35 A [W]	293	288	285
Reference power at 35 A [W]	278	276	278

According to the test protocol provided by IKTS, a power of 293 W is required at the reference point η_{FU} = 60. With the described optimizations, the power was increased from 240 to 278 W. The results of this measurement are shown in Figure 3.42.

In the experiments with stack 1 at reference point η_{FU} = 75, the load could only be increased to 31 A. At this point, the stack already reached the minimum voltage due to the boundary conditions (gas inlet temperature, furnace seal), which precluded an increase on the load to 35 A. Due to the optimizations it was possible to measure stack 2 under a load of 35 A. The reference power according to the reference report is 288 W. In the test run, a power of 276 W was achieved. The measurement results are shown in Figure 3.43.

Also, the reference point with η_{FU} = 80, which was not reached with stack 1 since the minimum cell voltage was already underranged at a load of 30 A, was successfully controlled after the optimizations. A power of 278 W was achieved under a load of 35 A. In the test report, the reference point is given as 285 W. As with the stack 2 tests, this minor deviation is in the range of measurement uncertainty and is less than 5% from the reference value. The results are shown in Figure 3.44. In summary, stack 2 was successfully put into operation. The measured IV characteristics correspond to the expectations of the theory (see Figure 2.4). The required pre-defined operating conditions were achieved. Further minimization of the delta between reference and measurement power can be achieved with a larger top-hat furnace. As a result, the heating coils are integrated in the SOFC hotbox as intended by IKTS. By eliminating the pre-heating (slit-tube oven) and the associated necessary insulation between pre-heater and SOFC hotbox, the system is reduced by one source of error. However, the stack test rig subsystem is fully functional, ready for coupling with the adsorber and SR or for measuring stacks for future projects. The niche market for biogas operated SOFC CCHPs offers a variety of applications. Examples are facilities for computer centers, office complexes or hospitals.

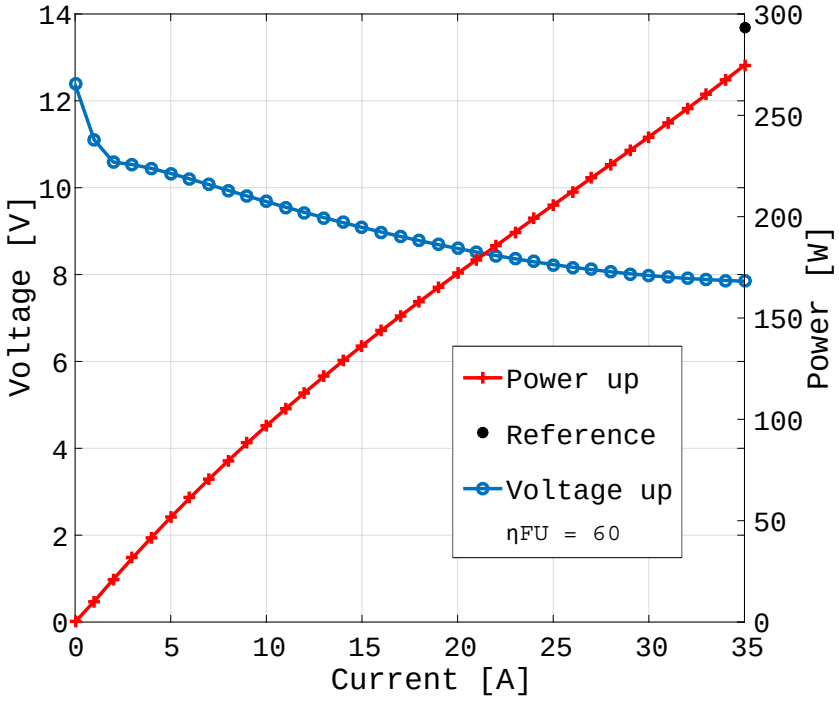

Figure 3.42: Measurement results stack 2 for the reference point η_{FU} = 60.

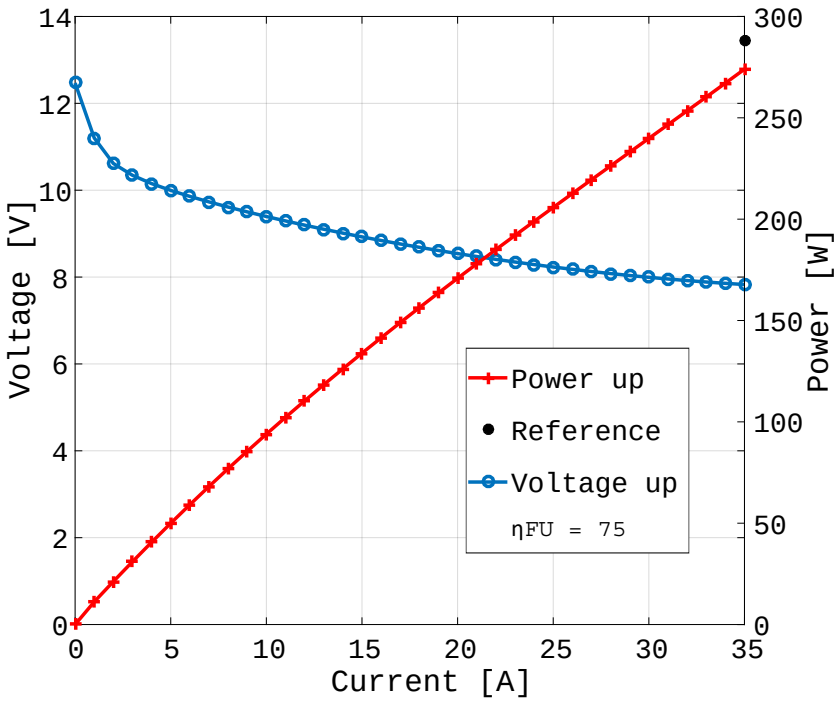

Figure 3.43: Measurement results stack 2 for the reference point η_{FU} = 75.

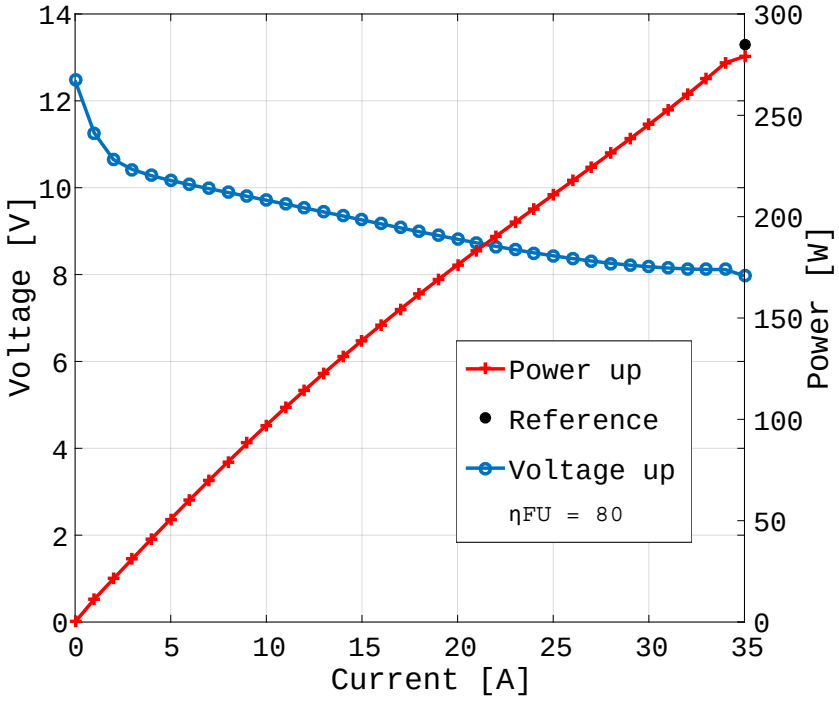

Figure 3.44: Measurement results stack 2 for the reference point η_{FU} = 80.

The direct conversion of chemical into electrical energy results in high efficiencies, since lossy conversion steps are not necessary. Finally, it can be stated that the SOFC stack was successfully set up and put into operation.

3.4 Summary

At the end of this Chapter, the research questions be repeated and the corresponding answers will be provided. More detailed answers to these questions can be found in Chapter 3 as well as in the conclusion in Chapter 5. Based on the research questions provided in the Section "Motivation and Purpose of the Work" (Section 1.4) the following answers were found by means of experimental test runs and literature research.

- How is the operation of H_2S and HCl removal influenced by different parameters like temperature, $GHSV$, pollutant inlet concentration and biogas composition?

  Temperature has a negative effect on adsorption capability. The adsorption capability increases if the adsorption temperature decreases. Furthermore, the gas flow rate has to increase in case that the $GHSV$ increases. Therefore, the amount of time that it takes for a compound to move from the gas stream to the surface of the adsorbent decreases.

A lower inlet concentration results in a lower mass-transfer flux from the gas to the adsorbent. On the other hand, a higher inlet concentration yields enhanced driving force along the pores, thus resulting in higher adsorption capacity.

The experiments carried out during the course of this work revealed that the NH_3 that is present in the biogas has a negative effect on the H_2S adsorption capacity. A minor influence was observed for K_2CO_3 impregnated activated carbon. A major negative impact on H_2S adsorption capacity in the presence of NH3 could be seen in all other examined sorbents.

- Is a successful commissioning of the subsystems (gas purification, steam reforming and 10-cell stack) possible?

  All subsystems were successfully set up and put into operation. For the separation of H_2S and HCl an adsorption test rig was set up. CuO-MnO sorbent, CuO-doped zeolite, MnO-doped zeolite, K_2CO_3 impregnated activated carbon, ZnO and two sorbents based on Al_2O_3 were investigated. A SR test bench was used for investigating a Ni catalyst at different temperatures, $GHSV$s and S/C ratios. Finally, the construction and commissioning of the SOFC test rig was performed successfully. Measuring of the IV characteristic curves resulted in the expected results, which are determined by reference points.

4 Scale-Up

Within this chapter, a basic design of an adsorption unit is presented. All used boundary conditions related to the adsorber have been presented and discussed in the previous chapters. Hence, this chapter is intended to provide an answer to research question 5 "What is the service interval of this biogas upgrade approach?", (cf. page 7) in the light of a real application.

Based on the LUB method and the experimental results presented in Sections 2.6.8 and 3.1, two different scale-up scenarios will now be considered. These scenarios result from the findings about the separation properties of the different adsorbents. According to Section 3.1.5, the CuO-MnO sorbent and the K_2CO_3 impregnated activated carbon were selected for the scale-up calculation. The investigated CuO-MnO sorbent showed exceptional values for both S_{cap} and BT. However, to remove HCl, an additional sorbent is needed because CuO-MnO sorbent can only separate H_2S. The aluminum oxide 1 investigated in Section 3.1.4 is suitable for this purpose. However, the experimental data of activated alumina 1 does not cover the scale-up requirement profile. This is the reason why scale-up for this sorbent is not performed. K_2CO_3 impregnated activated carbon has the ability to separate H_2S and HCl from the biogas. In addition, (impgregnated) activated carbon is 3-8 times cheaper than sorbents based on metal oxides [34, 280]. For this reason and due to the possibility to separate two pollutants at the same time, a scale-up for the K_2CO_3 impregnated activated carbon is carried out. The boundary conditions for these scale-ups have been determined in consultation with AVL. The adsorber unit should be designed for a service life of 6 months. The reaction temperature is 20 °C, the $GHSV$ is fixed at 8000 h^{-1}. As biogas, a dry gas with the following composition was determined: 200 *ppmv* H_2S, 100 *ppmv* HCl, 40 vol% CO_2 and balance CH_4. The conditions are summarized in Table 4.1.

4.1 Scale-up for CuO-MnO sorbent

The objective is to use the available experimental data to perform a scale-up corresponding to the real application (see Table 4.1).The starting point for this calculation is Figure 4.1 which was determined experimentally in Section 3.1.3. Figure 4.1 shows Test 1 from Figure 3.17. The

Table 4.1: Boundary conditions for scale-up.

Requirement	Value
Service life [h]	4260 = 6 months
Temperature [$°C$]	20
GHSV [h^{-1}]	8000
H_2S concentration [$ppmv$]	200
HCl concentration [$ppmv$]	100
CO_2 concentration [$vol\%$]	40
CH_4 concentration [$vol\%$]	59.97

blue horizontal dashed line at a H_2S outlet concentration of 2 $ppmv$ marks the H_2S limit of the SOFC. The test gas consists of 200 $ppmv$ H_2S in N_2 flowing at $GHSV$ = 8000 h^{-1} and a temperature of 20 °C through the CuO-MnO sorbent filled reactor. These experimental data were used as a starting point for the scale-up since they correspond to the required boundary conditions and because the breakthrough curve was measured up to a ratio of $c_i/c_{i,0}$ = 0.8. Only a small part of the breakthrough curve was extrapolated. Other test runs were stopped earlier and more of the breakthrough curve would have had to be extrapolated. In order to keep the deviation low, the most comprehensive data set was chosen for the scale-up.

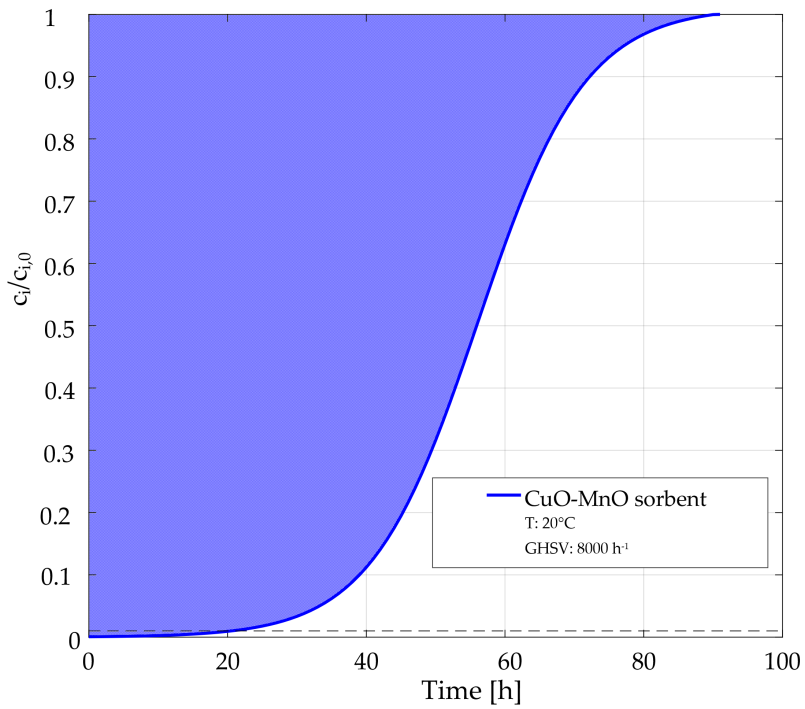

Figure 4.1: Breakthrough curve for CuO-MnO sorbent. $GHSV$ = 8000 h^{-1}; Temperature 20 °C; H_2S inlet concentration 200 $ppmv$.

First, the solute feed rate F_A is calculated according to Equation 4.1. The variables used are v,

superficial velocity, $c_{i,0}$, inlet concentration and M, molar mass H_2S. Per square centimeter of bed cross section, the solute feed rate is:

$$F_A = v * c_{i,0} * M \;=\; 39.79 * 10^{-4}\ g/(cm^2 * s) \tag{4.1}$$

The total solute adsorbed is the area above the graph (blue colored) multiplied by F_A. For the investigated bed, the area is calculated according to Equation 4.2.

$$\int_0^t (1 - \frac{c_i}{c_{i,0}}) * dt \;=\; 54.67\ h \tag{4.2}$$

This area corresponds to the ideal time that would be required to adsorb the same amount if the breakthrough curve were a vertical line. Next $q_{i,sat}$, the adsorbate at equilibrium (saturation), is calculated according to Equation 4.3.

$$q_{i,sat} = \frac{F_A * t}{\rho_b * L} \;=\; 152.15\ mg/g \tag{4.3}$$

At the break point, where $c_i/c_{i,o}$ = 0.01 and t_b = 20 h the amount of solute adsorbed is calculated according to Equation 4.4 and 4.5.

$$\int_0^{t_b} (1 - \frac{c_i}{c_{i,0}}) * dt \;=\; 19.9\ h \tag{4.4}$$

$$q_{i,b} = \frac{F_A * t}{\rho_b * L} \;=\; 55.37\ mg/g \tag{4.5}$$

By dividing $q_{i,b}$ by $q_{i,sat}$, according to Equation 4.6, the fraction of reactor bed used is obtained.

$$\frac{q_{i,b}}{q_{i,sat}} \;=\; 0.36 \tag{4.6}$$

The LUB is calculated according to Equation 4.7.

$$LUB = (1 - \frac{q_{i,b}}{q_{i,sat}}) * L \;=\; 1.39\ cm \tag{4.7}$$

For a lifetime of 6 months, solving of Equation 4.8 can find the following length for the adsorber.

$$t_b = \frac{(L - LUB) * \rho_b * q_{i,sat}}{F_A} \tag{4.8}$$

A service life of 6 months at a temperature of 20 °C and a $GHSV$ of 8000 h^{-1} results in an adsorber length of 175 cm. This corresponds to an utilization of the adsorber bed of 99.2%. In addition, the diameter of the adsorber must be adapted to the new volume flow. According to the scale-up procedure, the $GHSV$ remains at 8000 h^{-1}. The volume flow of 2 m^3/h results in a column diameter of 13 cm. While combining this diameter with the chosen length of the adsorber of 175 cm leads to a specific volume, combining it with the density of the adsorber results in a mass of 148 kg.

Until this step, the calculation was performed based on 200 ppmv H_2S in N_2. In Section 3.1.2 the influence of different biogas components on the H_2S separation was investigated. To complete the scale-up, the adsorber must be adapted to the influence of the changed gas composition. According to the requirement profile for the scale-up (see Table 4.1), a biogas consisting of 40 vol% CO_2 and 59.98 vol% CH_4 should serve as the basis for calculation. For this purpose, the results of Section 3.1.2 are discussed. Instead of the required 59.97 vol% CH_4, 59.98 vol% CH_4 was used as the basis for calculation. The reason for this lies in the synthetic biogas with which the experiments with the CuO-MnO sorbent were carried out. The absence of 100 $ppmv$ HCl in this gas mixture increased the CH_4 content minimally. An impact on the results is negligible. The right side of Figure 3.9 shows that the shape of the breakthrough curve remains the same, but the breakthrough time is reduced. In terms of numbers, a BT of 27.2 h was measured for gas mix 1 (200 $ppmv$ H_2S in N_2). With gas mix 4 (200 $ppmv$ H_2S, 40 vol% CO_2 and 59.98 vol% CH_4) a BT of 24.2 h was measured. However, the ratio of $q_{i,b}/q_{i,sat}$ remains unchanged, meaning that a new height and a new mass of adsorbent can be easily calculated. For the required boundary conditions, an adsorber for H_2S separation results in the following dimensions: Length 235 cm, mass of adsorbent 198 kg.

An adsorber with 235 cm length and 198 kg weight describes an acceptable compromise between transport, assembly and handling for a lifetime of 6 motnhs. Based on the requirement profile of AVL, the adsorber is designed for dry biogas. The CuO-MnO sorbent is severely weakened in its effect on H_2S separation by the presence of moisture. If no dry biogas is used, the adsorber would increase massively while the service life remains constant. In this case, a recommendation for an upstream dehumidification stage is given.

Increasing the operating temperature of the adsorber would be noticeable by the effect described in Sections 2.6.3 and 3.1.1. The efficiency of sulfur removal is kinetically favoured at higher temperatures, while its equilibrium is restricted to lower temperatures. The operating temperature influences both the diffusion rate and the thermodynamic equilibrium. In general, the equilibrium load decreases with increasing temperature. Increasing the $GHSV$ would also have a negative impact. Increasing the $GHSV$ results in steeper breakthrough curves and decreasing breakthrough times. This is due to the residence time of the solute in the column, which is not long enough for adsorption equilibrium to be reached at high flow rate. A detailed description can be found in Sections 2.6.3 and 3.1.1.

4.2 Scale-up for impregnated activated carbon

The calculation of the LUB for K_2CO_3 impregnated activated carbon is analogous to the calculation in Section 4.1. The basis for the scale-up is the data from Section 3.1.4. These experimental data are from a test run performed at a temperature of 20 °C and a $GHSV$ of 8000 h^{-1}. The gas mixture used was 200 *ppmv* H_2S and 100 *ppmv* HCl in N_2. With the exception of gas composition, these conditions meet the requirements profile of AVL for the SOFC CCHP system (see Table 4.1). The described deviation of the gas composition is taken into account in the scale-up calculation. After a calculation based on H_2S in N_2, the negative influence of CH_4 and CO_2, which was determined experimentally in Section 3.1.2, is taken care of in the calculation.

Figure 4.2 represents the starting point of the scale-up procedure. This is an adapted form of Figure 3.23 left side. The breakthrough curve for H_2S was measured up to a ratio of $c_i/c_{i,o}$ = 0.9, and only the last part was extrapolated. The dashed horizontal lines mark the limits of the SOFC with respect to H_2S and HCl. The dashed blue line at 10 *ppmv* represents the limit of the HCl concentration, the dashed red line at 2 *ppmv* that of the H_2S concentration.

As described in Section 3.1.4, the K_2CO_3 impregnated activated carbon allows a simultaneous adsorption of HCl and H_2S. While the reaction of K_2CO_3 with HCl leads to KCl which has a bond dissociation energy of -436 *kJ/mol* (Equation 3.2), the reaction between K_2CO_3 and H_2S leads to K_2S which has a bond dissociation energy of -380.7 *kJ/mol* (Equation 3.3). Since all thermodynamic systems strive to a minimum of free energy, the component with a higher energy of bonding is adsorbed preferably. HCl is the preferred adsorbed material. The calculation is based on the adsorption of H_2S, thus the separation of HCl, the primary adsorbed component, is ensured.

The solute feed rate F_A is calculated according to Equation 4.9. Per square centimeter of bed cross section, the solute feed rate is:

$$F_A = v * c_{i,0} * M \;=\; 39.79 * 10^{-4}\ g/(cm^2 * s) \tag{4.9}$$

The total solute adsorbed is the area above the graph (red colored) multiplied by F_A. For the investigated bed, the area is calculated according to Equation 4.10.

$$\int_0^t (1 - \frac{c_i}{c_{i,0}}) * dt \;=\; 2.14\ h \tag{4.10}$$

Next $q_{i,sat}$, the adsorbate at equilibrium (saturation), is calculated according to Equation 4.11.

$$q_{i,sat} = \frac{F_A * t}{\rho_b * L} \;=\; 6.78\ mg/g \tag{4.11}$$

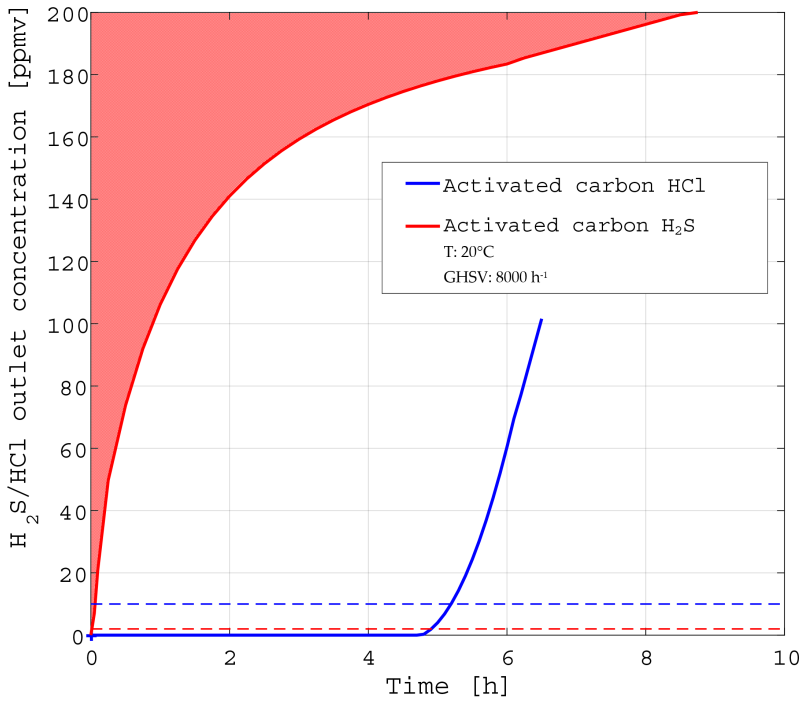

Figure 4.2: Breakthrough curve for impregnated activated carbon. $GHSV$ = 8000 h^{-1}; Temperature 20 °C; H_2S inlet concentration 200 *ppmv*; HCl inlet concentration 100 *ppmv*.

At the break point, where $c_i/c_{i,o}$ = 0.01 and t_b = 0.03 h the amount of solute adsorbed is calculated according to Equation 4.12 and 4.13.

$$\int_0^{t_b} (1 - \frac{c_i}{c_{i,0}}) * dt \; = \; 0.029 \; h \tag{4.12}$$

$$q_{i,b} = \frac{F_A * t}{\rho_b * L} \; = \; 0.094 \; mg/g \tag{4.13}$$

The fraction of reactor bed used is obtained according to Equation 4.14:

$$\frac{q_i, b}{q_{i,sat}} \; = \; 0.014 \tag{4.14}$$

The LUB is calculated according to Equation 4.15.

$$LUB = (1 - \frac{q_{i,b}}{q_{i,sat}}) * L \; = \; 2.17 \; cm \tag{4.15}$$

For a lifetime of 1 month, solving of Equation 4.16 can find the following length for the adsorber.

$$t_b = \frac{(L - LUB) * \rho_b * q_{i,sat}}{F_A} \tag{4.16}$$

A service life of 1 month already results in an adsorber length of 927 *cm*. This order of magnitude is economically inefficient for the use in the SOFC CCHP system. For comparison, the scale-up was additionally performed for an adsorber without considering the influence of HCl. For this purpose, experimental results from Section 3.1.3 were used. Specifically, these are the experimental results of Test 1 from Figure 3.16. With an operating temperature of 20 °C and a $GHSV$ of 8000 h^{-1}, the boundary conditions comply with the specifications in Table 4.1. Test 1 was performed with a test gas consisting of 200 *ppmv* H_2S in N_2. Nevertheless, in this case a length of 685 *cm* results for a service life of 1 month. The reason for this lies in the rapid exceeding of the 2 *ppmv* H_2S limit. Considering the Figures 3.23 and 3.16, which provided the data for the scale-up calculations, confirms this. In both figures, exceeding the H_2S outlet concentration above 2 *ppmv* is already visible after a few minutes.

Despite all the benefits of K_2CO_3 impregnated activated carbon like NH_3 tolerance, moisture insensitivity and simultaneous removal of H_2S and HCl, this is unacceptable from an economic point of view. Under the same boundary conditions (T = 20 °C; $GHSV$ = 8000 h^{-1}), a 175 *cm* long column packed with CuO-MnO sorbent is capable of desulfurizing the gas stream for a period of 6 months (see Section 4.1). In addition to the costs, the biogas-powered SOFC CCHP plant should remain compact in size in order to be both, competitive and flexible. For the reasons mentioned above, the recommendation is to desulfurize the biogas for use in a SOFC CCHP plant with CuO-MnO sorbent. In this case, additional pollutants present in the biogas, such as HCl and NH_3, must to be removed by means of further adsorbers.

The research question introduced at the beginning of the Chapter has been answered. With the available data, a scale-up was possible for both selected adsorbents. However, an applicable solution is only provided by the CuO-MnO sorbent. Under the required boundary conditions, the scale-up leads to an CuO-MnO based adsorber with a length of 235 *cm* and a mass of 198 *kg* for a service life of 6 months . For the separation of HCl, the activated aluminua 1 which was examined in Section 3.1.4 is suitable. However, to perform a scale-up for the required boundary conditions insufficient experimental data were available.

In addition, a scale-up was carried out with the K_2CO_3 impregnated activated carbon. Despite the benefits of K_2CO_3 impregnated activated carbon, an application for the SOFC CCHP system described in this thesis is not recommended. The rapid exceeding of the limit of 2 *ppmv* H_2S necessary for the SOFC results in the scale-up in an adsorber of impracticable size. An application under the required boundary conditions (see Table 4.1) would already lead to an adsorber length of 927 *cm* with a service life of 1 month.

5 Conclusion and Outlook

5.1 Conclusion

Operating SOFCs with biogas as fuel is a challenging and interdisciplinary field of research. This thesis is aimed to provide answers to several research questions stated in the introduction of this work. This chapter provides possible answers and is, thus, structured according to the initially arisen research questions which are the following:

- What are the limits of SOFCs with respect to H_2S and HCl load in the feed gas? What is the cause of carbon deposits and how can they be prevented? How much does the concentration of H_2S and HCl in biogases vary?

- Which gas upgrading operation is suitable for the specific requirements of a small scale (7 kW_{el}) SOFC CCHP system?

- How is the operation of H_2S and HCl removal influenced by different parameters like temperature, $GHSV$, pollutant inlet concentration and biogas composition?

- Is a successful commissioning of the subsystems (gas purification, steam reforming and 10-cell stack) possible?

- What is the service interval of this biogas upgrade approach?

What are the limits of SOFCs with respect to H_2S and HCl load in the feed gas? What is the cause of carbon deposits and how can they be prevented? How much does the concentration of H_2S and HCl in biogases vary?
Based on the literature, a H_2S limit in the feed gas of 2 *ppmv* is necessary for SOFCs to prevent degradation of the cell. H_2S is being adsorbed on the Ni active sites preventing H_2 and CO oxidation as well as CH_4 reforming. An SOFC operating at 800 °C with H_2 in N_2 showed a dramatic drop in cell current of 16.67% within minutes after the addition of 50 *ppmv* H_2S.

Furthermore, another study investigated long-term durability of a cell with Ni/YSZ anode at 800 °C and the syngas feed containing 2 *ppmv* H_2S. No noticeable power loss was shown through impedance spectra. Based on the literature reviewed, the concentration of H_2S in biogas varies greatly. The sources used here describe values between 50 and 6800 *ppmv*.

The limits concerning HCl of SOFCs specified in the literature scatter. A power loss of 17% is reported for a SOFC operated at 800 °C by the addition of 20 *ppmv* HCl. Another source reports the operation of a SOFC at 850 °C and the addition of 9 *ppmv* HCl with no measurable power loss. The concentration of HCl in biogas is much lower than that of H_2S. It varies from 0.1 to 25 *ppmv*, depending on the source of biogas. Based on available data, a limit of 10 *ppmv* HCl was chosen for this thesis.

The carbon deposits occurring at the SOFC anode are due to the Ni component of the anode. Ni is an excellent catalyst for carbon deposition reactions such as CH_4 cracking, reduction of CO and disproportionation of CO. Factors which increase the thermodynamic favourability of carbon deposition include lower temperatures, higher carbon:oxygen ratios and low oxygen fluxes. Formation of solid carbon is favoured thermodynamically in a large proportion of the potential operating space of SOFCs. In the literature, the use of an external reformer is recommended to supply syngas derived from the SR of CH_4. The syngas consists of CO_2, CO, H_2, vapor and residual CH_4. However, for typical biogas, the content of CO_2 is insufficient to conduct the reforming process safely. For those cases, steam is added to prevent carbon deposition. In order to avoid the formation of carbon deposits in the reformer, an S/C ratio >2.2 must be selected.

Which gas upgrading operation is suitable for the specific requirements of a small scale (7 kW_{el}) SOFC CCHP system?
Basically, process engineering offers a variety of basic operations to remove impurities from gases. Suitable technologies for gas purification can be divided into absorption, adsorption and membrane purification. However, especially for small systems such as the 7 kW_{el} system discussed in this thesis, there are major differences between the factors economy, complexity and flexibility. In terms of flexibility, adsorption opens up a variety of possibilities. If the system is supplied with a different fuel, the adsorbers can easily be adapted to any new pollutants in the biogas. Compared to the other basic operations, adsorption is advantageous due to equipment compactness, low energy requirement, low capital investment cost and, finally, due to its safety and simplicity of operation. These advantages show why this technology is the best choice for small plants.

How is the operation of H_2S and HCl removal influenced by different parameters like temperature, GHSV, pollutant inlet concentration and biogas composition?
The variety of different experiments performed as part of this thesis with adsorbents helps to answer this question. The influence of the temperature was investigated at 20, 100 and 200 °C for CuO-MnO sorbent and ZnO sorbent. The temperature dependency of the ZnO sorbent separation performance was more pronounced than that of CuO-MnO sorbent. This coincides

with the results published in literature. Temperature has a negative effect on adsorption capability, and adsorption capability decreases when adsorption temperature increases. In general, the equilibrium load decreases with increasing temperature.

$GHSV$ and performance have an inverse relationship: as the $GHSV$ increases, the performance of the adsorber decreases. Increasing the flow rate results in steeper breakthrough curves and decreasing breakthrough times. This is because of the residence time of the solute in the column, which is not long enough for adsorption equilibrium to be reached at high flow rate. So at high flow rate the adsorbate solution leaves the column before equilibrium is achieved. Furthermore, a fixed saturation capacity of bed based on the same driving force gives rise to a shorter time for saturation at higher flow rate. In this work, experiments were carried out at $GHSV$s of 4000, 8000 and 12000 h^{-1}. Depending on the sorbent used, there was a more or less pronounced influence of the $GHSV$ on the adsorption performance.

An increase in the H_2S input concentration from 200 to 1000 *ppmv* with a constant adsorber size resulted in an increased concentration at the adsorber outlet. For larger feed concentration, steeper breakthrough curves are found, because of the lower mass-transfer flux from the bulk solution to the particle surface due to the weaker driving force. In addition, at high concentration, the isotherm gradient is lower, yielding a higher driving force along the pores. Thus the equilibrium is attained faster for values of higher adsorbate concentration.

In the performed experiments, different influences of biogas on the adsorption were investigated. It started with measurements that examined a comparison between H_2S in N_2 and H_2S in a synthetic biogas of CH_4 and CO_2. The investigated sorbents (impregnated activated carbon, CuO-doped zeolite and CuO-MnO sorbent) showed strong influences of the gas composition on the adsorption behavior of H_2S. For example, the time to reach an outlet concentration of 2 *ppmv* decreased from 39 to 12 minutes for the activated carbon investigated by changing the carrier gas N_2 to CH_4 and CO_2. For the CuO-MnO sorbent, the time to reach the 2 *ppmv* at the reactor outlet was reduced from 10 to 7.5 *h*. The boundary conditions of the experiments were of course the same. The different magnitude of the results of minutes for activated carbon, and hours for CuO-MnO sorbent, should be highlighted here again. However, the experiments carried out also revealed the biggest weak point of the CuO-MnO sorbent compared to the activated carbon, the humidity. A relative humidity of 20% in the feed gas showed no appreciable effect on the performance of the activated carbon. The CuO-MnO sorbent shows no significant difference up to an exit concentration of 2 *ppmv*, but if the breakthrough times are compared for a value of 20 *ppmv* at the outlet, the breakthrough time is reduced from 27 to 12 *h*. Another advantage of activated carbon is its ability to simultaneously separate H_2S and HCl.

The investigations in this work revealed that the NH_3 present in the biogas has a negative effect on the H_2S adsorption capacity of CuO-MnO sorbent, CuO-doped zeolite and MnO-doped zeolite. In case of the impregnated activated carbon, only a small, negligible influence of NH_3 on the H_2S separation in the feed gas was detected. For the CuO-MnO sorbent, a reduction of the breakthrough time from 90 to 60 *h* was measured by adding 270 *ppmv* NH_3.

Increasing the NH_3 concentration to 2700 *ppmv* even reduced the breakthrough time to 32 *h*. Microscopic studies of CuO-MnO sorbent showed surface changes. In addition to cracks on the surface, further destruction was spotted. The reason for this remains unclear, even the literature provides almost no explanation. There is evidence that Cu forms a complex with NH_3. The exact formula of these compounds is being debated. Changing the oxidation state of Cu is associated with loss of adsorptive properties. At this point, a recommendation for future work should be pronounced to investigate these causes in detail. NH_3 massively reduces S_{cap} in 3 of the 4 adsorbents tested, only impregnated activated carbon was excluded from this problem.

Is a successful commissioning of the subsystems (gas purification, steam reforming and 10-cell stack) possible?
All subsystems were successfully set up and put into operation. The most extensive part was the work with the adsorption test rig. For the separation of H_2S, CuO-MnO sorbent, CuO-doped zeolite, MnO-doped zeolite, K_2CO_3 impregnated activated carbon and ZnO were used. For the separation of HCl, in addition to the activated carbon already used for H_2S, two sorbents based on Al_2O_3 were successfully used. The removal of NH_3 was accomplished with an activated aluminium based sorbent. Due to the amount of Ni in the selected alloy, there were interactions with the H_2S in the test gas, which were detected by sulfur imbalances on the performed adsorption experiments. For this reason, a glass reactor was subsequently installed in which no interactions with H_2S were found. With increasing project duration and experience, the test bench was rebuilt several times. In addition to a series connection of adsorbers, a wash bottle and a heating thermostat were installed. In the experiments, which were carried out with HCl, a special wash bottle with frit and pH electrode was used. All experiments were reproducible.

The second major work package was the construction and commissioning of the SOFC test rig. Two 10 cell stacks were installed by means of a special integration in the hood furnace existing in the laboratory. After installation of 2nd stack, the measurements of the IV characteristic curves were performed for different load cases. The expected results, which are determined by reference points, were achieved. With an H_2 content of 40% by volume in N_2 and an operating temperature of 830 °C, the stack should reach a power of 285 *W* under a load of 35 *A* according to the reference point. With stack 2, a power of 278 *W* was measured under the given conditions.

The completion of the commissioning of the subsystems was the test series with the steam reforming test bench. A Ni catalyst was investigated at different temperatures, *GHSV*s and S/C ratios. Using the HSC Chemistry software, equilibrium compositions were calculated at the temperatures and S/C ratios to be tested. The test rig was supported by a synthetic biogas consisting of 60 vol% CH_4 and 40 vol% CO_2. At an S/C ratio of 1.5, a *GHSV* of 1000 h^{-1} and a temperature of 600 °C an H_2 fraction of 58.79 vol% was calculated. The measured proportion of H_2 in the experiment was 52.27 vol%. The measurements carried out at 400 °C showed only a difference of 2.8 vol% between calculated and measured H_2 content.

What is the service interval of this biogas upgrade approach?
The service life of the adsorbers are calculated using the LUB method. The LUB method is a scale-up method which works with the data from the laboratory-scale experiments. Due to the flow rate, the diameter of the adsorber is fixed, the length is varied. The length of the adsorber is crucial for the lifetime. In the scale-up the adsorbers were designed for a service life of 6 months. The scale-up calculation showed that only the CuO-MnO sorbent meets the requirements. Despite all the benefits of impregnated activated carbon (NH_3 tolerance, moisture insensitivity, simultaneous removal of H_2S and HCl), it is unacceptable for the SOFC CCHP system from an economic point of view.

The calculated length of about 2.35 *m* for a CuO-MnO filled adsorber describes an acceptable compromise between transport, assembly, handling and service life (6 months). Based on the existing data and the requirement profile on the part of AVL, the adsorbers were designed for dry biogas. However, the recommended and selected CuO-MnO sorbent is severely weakened in its efficiency on H_2S separation by the presence of moisture. If, contrary to expectations, no dry biogas is used, the adsorber would increase massively. In this case, a recommendation for an upstream dehumidification stage is given. This is unavoidable for reasons of economy alone.

5.2 Outlook

A sustainable operation combined with a high efficiency is absolutely necessary for modern power plants in order to reduce or even avoid problems caused by increased CO_2 emissions and by shortages of fossil fuels. This thesis was part of the project SOFCool, where the combination of a biogas operated SOFC with an AC was considered to achieve efficiencies above 50% and total efficiencies above 90%. This project reflects the high interest of electrochemical systems based on SOFCs to operate as the core of future energy systems with renewable fuels. Renewable fuels like biogas have a wide potential in terms of availability and diffusion over the territory. The fuels considered are not only of interest because of their carbon neutrality, but also for certain peculiarities. For example, biogas coming from a sewage plant represents a by-product of a dedicated process of waste-water treatment. Such plants have already a large diffusion over the territory with an existing mature technology. Another example are the already existing biogas production facilities as used in the agricultural sector. Here, an already well-developed technology is working in the background as well. Therefore, a substantial biogas potential ready to be exploited already subsists and, therefore, a large market potential for such SOFC CCHP systems.

For instance, the SOFC CCHP technology is especially attractive for buildings and hospitals where a seasonal (summer/winter) or spatial (surgery room/patient room) distribution for heating and cooling is desired. SOFC technology offers highly efficient power generation even

at small scale, higher power to heat ratios and the opportunity to operate on biogas and fluctuating composition.

SOFC, AC, Adsorber and SR are the key elements of the biogas fuelled SOFC CCHP system described in this thesis. In the course of carrying out this work, the subsystems SOFC, adsorber and SR have already been successfully tested. The AC system was extensively and successfully investigated by Mr. Johannes Albert. The results of this examination can be found in his thesis. The next step is the commissioning of the entire system by AVL. An extension of the potential fuel portfolio would be a promising step in terms of fuel flexibility. Applications with synthetic diesel, natural gas or highly contaminated biogas (keyword: siloxanes) form a solid foundation in terms of flexibility. Especially for small plants $<30\ kW_{el}$, the fuel treatment by means of adsorption offers a technically mature as well as adaptable solution. In addition, this has a positive impact on the investment costs, which are lower compared to more expensive and technically complex solutions such as absorbers. Different pollutants sometimes require different sorbents to achieve the purities required by the SOFC in terms of gas quality. The investigation of the interactions between the pollutants and the sorbents certainly warrants further research as the gas complexity of impurities increases. The use of microscopic methods to investigate possible changes on the surface of the adsorbents should be a focus in further experiments. From the current state of knowledge, some changes on the surface are not describable (interaction between CuO-MnO sorbent and MnO doped zeolite with NH_3). However, an understanding of these mechanisms would be desirable. With knowledge of various interactions sorbents can be specifically excluded, or attempts can be made to counteract these interactions. It should be noted at this point that further promising scale-up methods, such as Wheeler-Jonas, exist and can be applied to future projects. Furthermore, computer-aided methods should be considered for future projects. The combination of experimentally obtained data with the extensive database stored in the program provides numerous possibilities.

Bibliography

[1] F. Ramadhani, M. Hussain, H. Mokhlis, et al. Optimization strategies for Solid Oxide Fuel Cell (SOFC) application: A literature survey. *Renewable and Sustainable Energy Reviews*, **76** (2017): 460–484.

[2] V. Palomba, M. Prestipino, and A. Galvagno. Tri-generation for industrial applications: Development of a simulation model for a gasification-SOFC based system. *International Journal of Hydrogen Energy*, **42** (46) (2017): 27866–27883.

[3] R. Roshandel, F. Golzar, and M. Astaneh. Technical, economic and environmental optimization of combined heat and power systems based on solid oxide fuel cell for a greenhouse case study. *Energy Conversion and Management*, **164** (2018): 144–156.

[4] R. Jing, M. Wang, W. Wang, et al. Economic and environmental multi-optimal design and dispatch of solid oxide fuel cell based CCHP system. *Energy Conversion and Management*, **154** (2017): 365–379.

[5] A. Baghernejad, M. Yaghoubi, and K. Jafarpur. Exergoeconomic comparison of three novel trigeneration systems using SOFC, biomass and solar energies. *Applied Thermal Engineering*, **104** (2016): 534–555.

[6] K. Comakli. Economic and environmental comparison of natural gas fired conventional and condensing combi boilers. *Journal of the Energy Institute*, **81** (4) (2008): 242–246.

[7] D. Y. Goswami and F. Kreith. Energy conversion. 2nd Ed. CRC Press, 2017, 1193.

[8] V. Nian, Z. Ma, and H. Li. A Comparative Cost Assessment of Energy Production from Central Heating Plant or Combined Heat and Power Plant. *Energy Procedia*, **104** (2016): 556–561.

[9] P. A. Breeze. Power generation technologies. 2nd Ed. Elsevier Ltd., 2014, 396.

[10] R. Beith. Small and micro combined heat and power (CHP) systems : advanced design, performance, materials and applications. Woodhead Publishing, 2011, 553.

[11] U. Çakir, K. Çomakli, and F. Yüksel. The role of cogeneration systems in sustainability of energy. *Energy Conversion and Management*, **63** (2012): 196–202.

[12] M. Noussan, M. Jarre, R. Roberto, et al. Combined vs separate heat and power production – Primary energy comparison in high renewable share contexts. *Applied Energy*, **213** (2018): 1–10.

[13] D. W. Wu and R. Z. Wang. Combined cooling, heating and power: A review. *Progress in Energy and Combustion Science*, **32** (5-6) (2006): 459–495.

[14] M. Ebrahimi and A. Keshavarz. Combined Cooling, Heating and Power Decision-Making, Design and Optimization. Elsevier, 2014, 218.

[15] L. F. Drbal, P. G. Boston, and K. L. Westra. Power Plant Engineering. 1st. Springer US, 1996, 768.

[16] M. Anderl, J. Burgstaller, M. Gössl, et al. *Climate Protection Report*. Tech. rep. Vienna, 2017, 168.

[17] NOAA National Centers for Environmental Information. *State of the Climate: Global Climate Report for Annual 2017*. Tech. rep. Asheville, NC, 2018.

[18] C. Schluckner. "Carbon Formation and Effective Removal Strategies in High Temperature Solid Oxide Fuel Cell Anodes Fueled with Diesel Reformates." PhD Thesis. Graz University of Technology, 2017, 183.

[19] V. Subotić. "Detection of Carbon Depositions and Development of Novel Regeneration Approaches for Solid Oxide Fuel Cells." PhD Thesis. Graz University of Technology, 2017, 164.

[20] S. C. Singhal. Solid Oxide Fuel Cells: Status, Challenges and Opportunities. *Advances in Science and Technology*, **45** (2006): 1837–1846.

[21] S. Hardman, A. Chandan, and R. Steinberger-Wilckens. Fuel cell added value for early market applications. *Journal of Power Sources*, **287** (2015): 297–306.

[22] O. Z. Sharaf and M. F. Orhan. An overview of fuel cell technology: Fundamentals and applications. *Renewable and Sustainable Energy Reviews*, **32** (2014): 810–853.

[23] C. Bao, Y. Wang, D. Feng, et al. Macroscopic modeling of solid oxide fuel cell (SOFC) and model-based control of SOFC and gas turbine hybrid system. *Progress in Energy and Combustion Science*, **66** (2018): 83–140.

[24] J. Lewis. Stationary fuel cells – Insights into commercialisation. *International Journal of Hydrogen Energy*, **39** (36) (2014): 21896–21901.

[25] S. P. S. Badwal, S. Giddey, C. Munnings, et al. Progress in high temperature solid oxide fuel cells. *J. Austceram. SOC.* **50** (1) (2014): 23–37.

[26] T. Elmer, M. Worall, S. Wu, et al. Emission and economic performance assessment of a solid oxide fuel cell micro-combined heat and power system in a domestic building. *Applied Thermal Engineering*, **90** (2015): 1082–1089.

[27] B. Dziurdzia, Z. Magonski, and H. Jankowski. Commercialisation of Solid Oxide Fuel Cells - opportunities and forecasts. *IOP Conference Series: Materials Science and Engineering*, **104** (1) (2016): 012–20.

[28] A. Chitsaz, J. Hosseinpour, and M. Assadi. Effect of recycling on the thermodynamic and thermoeconomic performances of SOFC based on trigeneration systems; A comparative study. *Energy*, **124** (2017): 613–624.

[29] M. Błesznowski, J. Jewulski, and A. Zieleniak. Determination of H2S and HCl concentration limits in the fuel for anode supported SOFC operation. *Open Chemistry*, **11** (6) (2013): 960–967.

[30] A. Hagen. Sulfur Poisoning of the Water Gas Shift Reaction on Anode Supported Solid Oxide Fuel Cells. *Journal of the Electrochemical Society*, **160** (2) (2012): F111–F118.

[31] A. Hauch, A. Hagen, J. Hjelm, et al. Sulfur Poisoning of SOFC Anodes: Effect of Overpotential on Long-Term Degradation. *Journal of the Electrochemical Society*, **161** (6) (2014): F734–F743.

[32] Z. Ud Din and Z. Zainal. The fate of SOFC anodes under biomass producer gas contaminants. *Renewable and Sustainable Energy Reviews*, **72** (2017): 1050–1066.

[33] J. Trembly, R. Gemmen, and D. Bayless. The effect of coal syngas containing HCl on the performance of solid oxide fuel cells: Investigations into the effect of operational temperature and HCl concentration. *Journal of Power Sources*, **169** (2) (2007): 347–354.

[34] A. Petersson. "Biogas cleaning." In: *The Biogas Handbook*. Ed. by A. Wellinger, J. Murphy, and D. Baxter. Cambridge: Elsevier, 2013, 329–341.

[35] S. C. Singhal and K. Kendall. High-temperature solid oxide fuel cells : fundamentals, design, and applicatons. Ed. by S. Singhal and K. Kendall. Oxford, UK: Elsevier Advanced Technology, 2003, 405.

[36] M. Cimenti and J. Hill. Direct Utilization of Liquid Fuels in SOFC for Portable Applications: Challenges for the Selection of Alternative Anodes. *Energies*, **2** (2) (2009): 377–410.

[37] R. O'Hayre, S. Cha, W. Colella, et al. Fuel Cell Fundamentals. 3rd. Hoboken, NJ: John Wiley & Sons, Ltd, 2016, 600.

[38] Y. Chen, W. C. Jung, Y. Kuru, et al. Chemical, Electronic and Nanostructure Dynamics on Thin-Film Surfaces at High Temperatures. *ECS Transactions*, **35** (1) (2011): 2409–2416.

[39] M. Lo Faro, V. Antonucci, P. Antonucci, et al. Fuel flexibility: A key challenge for SOFC technology. *Fuel*, **102** (2012): 554–559.

[40] S. Vasileiadis and Z. Ziaka-Vasileiadou. Biomass reforming process for integrated solid oxide-fuel cell power generation. *Chemical Engineering Science*, **59** (22-23) (2004): 4853–4859.

[41] D. S. Cameron. Fuel Cells Science and Technology 2008. *Platinum Metals Review*, **53** (3) (2009): 147–154.

[42] C. Kunusch, P. Puleston, and M. Mayosky. "PEM Fuel Cell Systems." In: *Sliding-Mode Control of PEM Fuel Cell*. London: Springer, London, 2012. Chap. PEM Fuel C, 13–33.

[43] H. Yokokawa, N. Sakai, T. Horita, et al. Electrolytes for Solid-Oxide Fuel Cells. *MRS Bulletin*, **30** (08) (2005): 591–595.

[44] C.-Y. Yuh, A. Franco, L. Chen, et al. Electrolyte Management in Liquid Electrolyte Fuel Cells. *ECS Transactions*, **65** (1) (2015): 75–86.

[45] V. Antonucci, L. Branchini, G. Brunaccini, et al. Thermal integration of a SOFC power generator and a Na–NiCl2 battery for CHP domestic application. *Applied Energy*, **185** (2017): 1256–1267.

[46] A. Galvagno, M. Prestipino, G. Zafarana, et al. Analysis of an Integrated Agro-waste Gasification and 120 kW SOFC CHP System: Modeling and Experimental Investigation. *Energy Procedia*, **101** (2016): 528–535.

[47] E. Naimaster and A. Sleiti. Potential of SOFC CHP systems for energy-efficient commercial buildings. *Energy and Buildings*, **61** (2013): 153–160.

[48] T. Hatae, N. Kakuda, T. Taniyama, et al. Low temperature preparation and performance of Ni/YSZ anode with a multi-layered structure for SOFC. *Journal of Power Sources*, **135** (1-2) (2004): 25–28.

[49] R. Maric, K. Furusaki, D. Nishijima, et al. "Thin Film Low Temperature Solid Oxide Fuel Cell (LTSOFC) by Reactive Spray Deposition Technology (RSDT)." In: *ECS Transactions*. Vol. 35. 1. The Electrochemical Society, 2011, 473–481.

[50] X.-V. Nguyen, C.-T. Chang, G.-B. Jung, et al. Study of sealants for SOFC. *International Journal of Hydrogen Energy*, **41** (46) (2016): 21812–21819.

[51] B. Karmakar. "Glass and glass-ceramics for solid oxide fuel cell (SOFC) sealants." In: *Functional Glasses and Glass-Ceramics*. Oxford: Elsevier, 2017. Chap. Glass and, 281–293.

[52] K. Kendall. High-Temperature Solid Oxide Fuel Cells for the 21st Century: Fundamentals, Design and Applications: 2nd. London: Elsevier, 2016, 508.

[53] M. Irshad, K. Siraj, R. Raza, et al. A Brief Description of High Temperature Solid Oxide Fuel Cell's Operation, Materials, Design, Fabrication Technologies and Performance. *Applied Sciences*, **6** (3) (2016): 75.

[54] J. W. Fergus. Solid oxide fuel cells : materials properties and performance. Boca Raton, FL: CRC Press, 2009, 295.

[55] D. Stolten and B. Emonts. Fuel cells science and engineering : materials, systems, processes and technology. Weinheim: Wiley-VCH, 2012, 1268.

[56] B. Timurkutluk, C. Timurkutluk, M. D. Mat, et al. Development of high-performance anode supported solid oxide fuel cell. *International Journal of Energy Research*, **36** (15) (2012): 1383–1387.

[57] K. Huang and S. C. Singhal. Cathode-supported tubular solid oxide fuel cell technology: A critical review. *Journal of Power Sources*, **237** (2013): 84–97.

[58] S. Lee, M. Bevilacqua, P. Fornasiero, et al. Solid oxide fuel cell cathodes prepared by infiltration of LaNi0.6Fe0.4O3 and La0.91Sr0.09Ni0.6Fe0.4O3 in porous yttria-stabilized zirconia. *Journal of Power Sources*, **193** (2) (2009): 747–753.

[59] S. Islam and J. M. Hill. "Anode Material Development." In: *Solid Oxide Fuel Cells: From Materials to System Modeling*. Ed. by The Royal Society of Chemistry. London: RSC Publishing, 2013. Chap. Chapter 4, 88–105.

[60] D. Roehrens, F. Han, M. Haydn, et al. Advances beyond traditional SOFC cell designs. *International Journal of Hydrogen Energy*, **40** (35) (2015): 11538–11542.

[61] S. Badwal, R. Deller, K. Foger, et al. Interaction between chromia forming alloy interconnects and air electrode of solid oxide fuel cells. *Solid State Ionics*, **99** (3-4) (1997): 297–310.

[62] M. Turco, A. Ausiello, and L. Micoli. "Fuel Cells Operating and Structural Features of MCFCs and SOFCs." In: *Treatment of Biogas for Feeding High Temperature Fuel Cells*. Switzerland: Springer, Cham, 2016, 31–76.

[63] EG&G Technical Services. Fuel cell handbook. 7th. Springfield, U.S. Department of Energy, 2004, 427.

[64] C. W. Tanner, K. Fung, and A. V. Virkar. The Effect of Porous Composite Electrode Structure on Solid Oxide Fuel Cell Performance. *Journal of The Electrochemical Society*, **144** (1) (1997): 21.

[65] N. Q. Minh. Ceramic Fuel Cells. *Journal of the American Ceramic Society*, **76** (3) (1993): 563–588.

[66] B. C. H. Steele and R. M. Dell. Materials for High-Temperature Fuel Cells [and Discussion]. *Philosophical Transactions of the Royal Society A: Mathematical, Physical and Engineering Sciences*, **354** (1712) (1996): 1695–1710.

[67] S. Presto, P. Kumar, S. Varma, et al. Electrical conductivity of NiMo–based double perovskites under SOFC anodic conditions. *International Journal of Hydrogen Energy*, **43** (9) (2018): 4528–4533.

[68] J. W. Kim, K. Bae, H. J. Kim, et al. Three-dimensional thermal stress analysis of the re-oxidized Ni-YSZ anode functional layer in solid oxide fuel cells. *Journal of Alloys and Compounds* (2018).

[69] E. S. Hecht, G. K. Gupta, H. Zhu, et al. Methane reforming kinetics within a Ni–YSZ SOFC anode support. *Applied Catalysis A: General*, **295** (1) (2005): 40–51.

[70] P. Holtappels, L. G. J. D. Haart, U. Stimming, et al. Reaction of CO/CO2 gas mixtures on Ni–YSZ cermet electrodes. *Journal of Applied Electrochemistry*, **29** (5) (1999): 561–568.

[71] T. Takeguchi, Y. Kani, T. Yano, et al. Study on steam reforming of CH4 and C2 hydrocarbons and carbon deposition on Ni-YSZ cermets. *Journal of Power Sources*, **112** (2) (2002): 588–595.

[72] R. Peters, E. Riensche, and P. Cremer. Pre-reforming of natural gas in solid oxide fuel-cell systems. *Journal of Power Sources*, **86** (1-2) (2000): 432–441.

[73] J. Sehested, J. A. Gelten, I. N. Remediakis, et al. Sintering of nickel steam-reforming catalysts: effects of temperature and steam and hydrogen pressures. *Journal of Catalysis*, **223** (2) (2004): 432–443.

[74] A. Nakajo, F. Mueller, J. Brouwer, et al. Mechanical reliability and durability of SOFC stacks. Part I : Modelling of the effect of operating conditions and design alternatives on the reliability. *International Journal of Hydrogen Energy*, **37** (11) (2012): 9249–9268.

[75] M. Backhaus-Ricoult. SOFC – A playground for solid state chemistry. *Solid State Sciences*, **10** (6) (2008): 670–688.

[76] D. Ding, X. Li, S. Y. Lai, et al. Enhancing SOFC cathode performance by surface modification through infiltration. *Energy & Environmental Science*, **7** (2) (2014): 552.

[77] J.-C. Grenier, J.-M. Bassat, and F. Mauvy. "Novel cathodes for solid oxide fuel cells." In: *Functional Materials for Sustainable Energy Applications*. Ed. by J. Kilner, S. J. Skinner, C. Irvine, et al. Cambridge: Elsevier, 2012, 402–444.

[78] Z. Yang, M. Guo, N. Wang, et al. A short review of cathode poisoning and corrosion in solid oxide fuel cell. *International Journal of Hydrogen Energy*, **42** (39) (2017): 24948–24959.

[79] K.-C. Lee, M.-B. Choi, D.-K. Lim, et al. Effect of humidification on the performance of intermediate-temperature proton conducting ceramic fuel cells with ceramic composite cathodes. *Journal of Power Sources*, **232** (2013): 224–233.

[80] B. Hu, M. K. Mahapatra, M. Keane, et al. Effect of CO2 on the stability of strontium doped lanthanum manganite cathode. *Journal of Power Sources*, **268** (2014): 404–413.

[81] Z. Zhao, L. Liu, X. Zhang, et al. High and low temperature behaviors of Lao.6 Sro.4 Coo.2 Feo.8 O3-δ cathode operating under CO2/H2O-containing atmosphere. *International Journal of Hydrogen Energy*, **38** (35) (2013): 15361–15370.

[82] M. Perz, E. Bucher, C. Gspan, et al. Long-term degradation of Lao.6Sro.4Coo.2Feo.8O3-δIT-SOFC cathodes due to silicon poisoning. *Solid State Ionics*, **288** (2016): 22–27.

[83] J. A. Schuler, C. Gehrig, Z. Wuillemin, et al. Air side contamination in Solid Oxide Fuel Cell stack testing. *Journal of Power Sources*, **196** (17) (2011): 7225–7231.

[84] J. M. Porras-Vazquez, R. I. Smith, and P. R. Slater. Investigation into the effect of Si doping on the cell symmetry and performance of Sr1-yCayFeO3-δ SOFC cathode materials. *Journal of Solid State Chemistry*, **213** (2014): 132–137.

[85] T. Kawada and H. Yokokawa. Materials and Characterization of Solid Oxide Fuel Cell. *Key Engineering Materials*, **125-126** (1997): 187–248.

[86] R. Wang, Z. Sun, Y. Lu, et al. Chromium Poisoning of Cathodes in Solid Oxide Fuel Cells and its Mitigation Employing CuMn 1.8 O 4 Spinel Coatings on Interconnects. *ECS Transactions*, **78** (1) (2017): 1665–1674.

[87] S. Megel, M. Kusnezoff, N. Trofimenko, et al. "High Efficiency CFY-Stack for High Power Applications." In: *ECS Transactions*. Vol. 35. 1. The Electrochemical Society, 2011, 269–277.

[88] S. Megel, C. Dosch, S. Rothe, et al. CFY-Stacks for Use in Stationary SOFC and SOEC Applications. *ECS Transactions*, **57** (1) (2013): 89–98.

[89] J. B. Goodenough and Y.-H. Huang. Alternative anode materials for solid oxide fuel cells. *Journal of Power Sources*, **173** (1) (2007): 1–10.

[90] V. Subotic, C. Schluckner, H. Schroettner, et al. Analysis of possibilities for carbon removal from porous anode of solid oxide fuel cells after different failure modes. *Journal of Power Sources*, **302** (2016): 378–386.

[91] W. Y. Lee, J. Hanna, and A. F. Ghoniem. On the Predictions of Carbon Deposition on the Nickel Anode of a SOFC and Its Impact on Open-Circuit Conditions. *Journal of the Electrochemical Society*, **160** (2) (2012): F94–F105.

[92] P. Kaparaju and J. Rintala. "Generation of heat and power from biogas for stationary applications: boilers, gas engines and turbines, combined heat and power (CHP) plants and fuel cells." In: *The Biogas Handbook*. Ed. by A. Wellinger, J. Murphy, and D. Baxter. Cambridge: Elsevier, 2013, 404–427.

[93] S. Rasi, A. Veijanen, and J. Rintala. Trace compounds of biogas from different biogas production plants. *Energy*, **32** (8) (2007): 1375–1380.

[94] M. Turco, A. Ausiello, and L. Micoli. "The Use of Biogas in MCFCs and SOFCs Technology: Adsorption Processes and Adsorbent Materials for Removal of Noxious Compounds." In: *Treatment of Biogas for Feeding High Temperature Fuel Cells*. Switzerland: Springer, Cham, 2016, 95–130.

[95] A. Hagen, J. F. Rasmussen, and K. Thydén. Durability of solid oxide fuel cells using sulfur containing fuels. *Journal of Power Sources*, **196** (17) (2011): 7271–7276.

[96] J. Rostrup-Nielsen, J. Hansen, S. Helveg, et al. Sites for catalysis and electrochemistry in solid oxide fuel cell (SOFC) anode. *Applied Physics A*, **85** (4) (2006): 427–430.

[97] M. Turco, A. Ausiello, and L. Micoli. "The Effect of Biogas Impurities on SOFC." In: *Treatment of Biogas for Feeding High Temperature Fuel Cells*. Switzerland: Springer, Cham, 2016, 137–149.

[98] J. Bao, G. N. Krishnan, P. Jayaweera, et al. Effect of various coal contaminants on the performance of solid oxide fuel cells: Part I. Accelerated testing. *Journal of Power Sources*, **193** (2) (2009): 607–616.

[99] M. Argyle and C. Bartholomew. Heterogeneous Catalyst Deactivation and Regeneration: A Review. *Catalysts*, **5** (1) (2015): 145–269.

[100] M. C. Bradford and M. A. Vannice. Catalytic reforming of methane with carbon dioxide over nickel catalysts I. Catalyst characterization and activity. *Applied Catalysis A: General*, **142** (1) (1996): 73–96.

[101] P. Menon. Coke on catalysts-harmful, harmless, invisible and beneficial types. *Journal of Molecular Catalysis*, **59** (2) (1990): 207–220.

[102] P. Boldrin, E. Ruiz-Trejo, J. Mermelstein, et al. Strategies for Carbon and Sulfur Tolerant Solid Oxide Fuel Cell Materials, Incorporating Lessons from Heterogeneous Catalysis. *Chemical Reviews*, **116** (22) (2016): 13633–13684.

[103] E. Ivers-Tiffée, H. Timmermann, A. Leonide, et al. "Methane reforming kinetics, carbon deposition, and redox durability of Ni/8 yttria-stabilized zirconia (YSZ) anodes." In: *Handbook of Fuel Cells*. Ed. by W. Vielstich, A. Lamm, and H. A. Gasteiger. Chichester, UK: John Wiley & Sons, Ltd, 2010, 3826.

[104] K. Sasaki and Y. Teraoka. Equilibria in Fuel Cell Gases. *Journal of The Electrochemical Society*, **150** (7) (2003): A885.

[105] Y. Lin, Z. Zhan, J. Liu, et al. Direct operation of solid oxide fuel cells with methane fuel. *Solid State Ionics*, **176** (23-24) (2005): 1827–1835.

[106] J. Liu and S. A. Barnett. Operation of anode-supported solid oxide fuel cells on methane and natural gas. *Solid State Ionics*, **158** (1-2) (2003): 11–16.

[107] T. Chen, W. G. Wang, H. Miao, et al. Evaluation of carbon deposition behavior on the nickel/yttrium-stabilized zirconia anode-supported fuel cell fueled with simulated syngas. *Journal of Power Sources*, **196** (5) (2011): 2461–2468.

[108] P. Vernoux, M. Guillodo, J. Fouletier, et al. Alternative anode material for gradual methane reforming in solid oxide fuel cells. *Solid State Ionics*, **135** (1-4) (2000): 425–431.

[109] A. Gunji, C. Wen, J. Otomo, et al. Carbon deposition behaviour on Ni–ScSZ anodes for internal reforming solid oxide fuel cells. *Journal of Power Sources*, **131** (1-2) (2004): 285–288.

[110] C. Schluckner, V. Subotic, V. Lawlor, et al. Carbon Deposition Simulation in Porous SOFC Anodes: A Detailed Numerical Analysis of Major Carbon Precursors. *Journal of Fuel Cell Science and Technology*, **12** (5) (2015): 051007.

[111] G. Brus, R. Nowak, J. S. Szmyd, et al. An experimental and theoretical approach for the carbon deposition problem during steam reforming of model biogas. *Journal of Theoretical and Applied Mechanics*, **53** (2) (2015): 273.

[112] M. Liu, G. Wei, J. Luo, et al. Use of Metal Sulfides as Anode Catalysts in H2S-Air SOFCs. *Journal of The Electrochemical Society*, **150** (8) (2003): A1025.

[113] M. Riegraf, G. Schiller, R. Costa, et al. Elementary Kinetic Numerical Simulation of Ni/YSZ SOFC Anode Performance Considering Sulfur Poisoning. *Journal of the Electrochemical Society*, **162** (1) (2014): F65–F75.

[114] K. Haga, S. Adachi, Y. Shiratori, et al. Poisoning of SOFC anodes by various fuel impurities. *Solid State Ionics*, **179** (27-32) (2008): 1427–1431.

[115] J. F. Rasmussen and A. Hagen. The effect of H2S on the performance of Ni–YSZ anodes in solid oxide fuel cells. *Journal of Power Sources*, **191** (2) (2009): 534–541.

[116] D. Papurello, A. Lanzini, S. Fiorilli, et al. Sulfur poisoning in Ni-anode solid oxide fuel cells (SOFCs): Deactivation in single cells and a stack. *Chemical Engineering Journal*, **283** (2016): 1224–1233.

[117] D. G. Ivey, E. Brightman, and N. Brandon. Structural modifications to nickel cermet anodes in fuel cell environments. *Journal of Power Sources*, **195** (19) (2010): 6301–6311.

[118] K. Sasaki, K. Haga, T. Yoshizumi, et al. Chemical durability of Solid Oxide Fuel Cells: Influence of impurities on long-term performance. *Journal of Power Sources*, **196** (22) (2011): 9130–9140.

[119] S. Zha, Z. Cheng, and M. Liu. Sulfur Poisoning and Regeneration of Ni-Based Anodes in Solid Oxide Fuel Cells. *Journal of The Electrochemical Society*, **154** (2) (2007): B201.

[120] T. S. Li, M. Xu, C. Gao, et al. Investigation into the effects of sulfur on syngas reforming inside a solid oxide fuel cell. *Journal of Power Sources*, **258** (2014): 1–4.

[121] J. G. McCarty and H. Wise. Thermodynamics of sulfur chemisorption on metals. III. Iron and cobalt. *The Journal of Chemical Physics*, **76** (2) (1982): 1162–1167.

[122] E. Brightman, D. Ivey, D. Brett, et al. The effect of current density on H2S-poisoning of nickel-based solid oxide fuel cell anodes. *Journal of Power Sources*, **196** (17) (2011): 7182–7187.

[123] T. R. Smith, A. Wood, and V. I. Birss. Effect of hydrogen sulfide on the direct internal reforming of methane in solid oxide fuel cells. *Applied Catalysis A: General*, **354** (1-2) (2009): 1–7.

[124] J. R. Rostrup-Nielsen. "Catalytic Steam Reforming." In: *Catalysis*. Berlin, Heidelberg: Springer Berlin Heidelberg, 1984, 1–117.

[125] N. Vivet, S. Chupin, E. Estrade, et al. 3D Microstructural characterization of a solid oxide fuel cell anode reconstructed by focused ion beam tomography. *Journal of Power Sources*, **196** (18) (2011): 7541–7549.

[126] H. Madi, A. Lanzini, D. Papurello, et al. Solid oxide fuel cell anode degradation by the effect of hydrogen chloride in stack and single cell environments. *Journal of Power Sources*, **326** (2016): 349–356.

[127] K. Haga, Y. Shiratori, K. Ito, et al. Chlorine Poisoning of SOFC Ni-Cermet Anodes. *Journal of The Electrochemical Society*, **155** (12) (2008): B1233.

[128] O. Marina, L. Pederson, E. Thomsen, et al. Reversible poisoning of nickel/zirconia solid oxide fuel cell anodes by hydrogen chloride in coal gas. *Journal of Power Sources*, **195** (20) (2010): 7033–7037.

[129] C. Xu, M. Gong, J. W. Zondlo, et al. The effect of HCl in syngas on Ni–YSZ anode-supported solid oxide fuel cells. *Journal of Power Sources*, **195** (8) (2010): 2149–2158.

[130] P. V. Aravind, J. P. Ouweltjes, N. Woudstra, et al. Impact of Biomass-Derived Contaminants on SOFCs with Ni/Gadolinia-Doped Ceria Anodes. *Electrochemical and Solid-State Letters*, **11** (2) (2008): B24–B28.

[131] K. Hauptmeier, M. Penkuhn, and G. Tsatsaronis. Economic assessment of a solid oxide fuel cell system for biogas utilization in sewage plants. *Energy*, **117** (2016): 361–368.

[132] D. Andriani, A. Wresta, T. D. Atmaja, et al. A Review on Optimization Production and Upgrading Biogas Through CO2 Removal Using Various Techniques. *Applied Biochemistry and Biotechnology*, **172** (4) (2014): 1909–1928.

[133] B. K. Adhikari, A. Trémier, J. Martinez, et al. Home and community composting for on-site treatment of urban organic waste: perspective for Europe and Canada. *Waste Management & Research*, **28** (11) (2010): 1039–1053.

[134] N. Scarlat, J.-F. Dallemand, and F. Fahl. Biogas: developments and perspectives in Europe. *Renewable Energy*, **in Press** (2018).

[135] A.-A. S. M. Magomnang and E. P. Villanueva. "Removal of Hydrogen Sulfide from Biogas using Dry Desulfurization Systems." In: *International Conference on Agricultural, Environmental and Biological Sciences*. Phuket: International Conference on Agricultural, Environmental and Biological Sciences, 2014, 65–68.

[136] I. Ullah Khan, M. Hafiz Dzarfan Othman, H. Hashim, et al. Biogas as a renewable energy fuel – A review of biogas upgrading, utilisation and storage. *Energy Conversion and Management*, **150** (2017): 277–294.

[137] D. Deublein and A. Steinhauser. "Utilization of Biogas for the Generation of Electric Power and Heat." In: *Biogas from Waste and Renewable Resources*. Ed. by D. Deublein and A. Steinhauser. Weinheim, Germany: Wiley-VCH Verlag GmbH & Co. KGaA, 2008, 361–388.

[138] K. Starr, G. Villalba, and X. Gabarrell. Upgraded biogas from municipal solid waste for natural gas substitution and CO2 reduction – A case study of Austria, Italy, and Spain. *Waste Management*, **38** (2015): 105–116.

[139] M. Beil and W. Beyrich. "Biogas upgrading to biomethane." In: *The Biogas Handbook*. Ed. by A. Wellinger, J. Murphy, and D. Baxter. Cambridge: Elsevier, 2013, 342–377.

[140] D. Deublein and A. Steinhauser. "Biogas for Feeding into the Natural Gas Network." In: *Biogas from Waste and Renewable Resources*. Ed. by D. Deublein and A. Steinhauser. Weinheim, Germany: Wiley-VCH Verlag GmbH & Co. KGaA, 2008, 389–395.

[141] A. Trendewicz and R. Braun. Techno-economic analysis of solid oxide fuel cell-based combined heat and power systems for biogas utilization at wastewater treatment facilities. *Journal of Power Sources*, **233** (2013): 380–393.

[142] M. Hauth, M. Seidl, C. Sallai, et al. Development of a SOFC CCHP system towards flexible production of electricity, heat and cooling power for transport applications. *ECS Transactions*, **78** (1) (2017): 155–170.

[143] D. Deublein and A. Steinhauser. "Biology." In: *Biogas from Waste and Renewable Resources*. Ed. by D. Deublein and A. Steinhauser. Weinheim, Germany: Wiley-VCH Verlag GmbH & Co. KGaA, 2008, 93–128.

[144] J. D. Murphy and Thanasit Thamsiriroj. "Fundamental science and engineering of the anaerobic digestion process for biogas production." In: *The Biogas Handbook*. Ed. by A. Wellinger, J. Murphy, and D. Baxter. Cambridge: Elsevier, 2013, 104–130.

[145] E. K. Yiridoe, R. Gordon, and B. B. Brown. Nonmarket cobenefits and economic feasibility of on-farm biogas energy production. *Energy Policy*, **37** (3) (2009): 1170–1179.

[146] T. Amon, B. Amon, V. Kryvoruchko, et al. Methane production through anaerobic digestion of various energy crops grown in sustainable crop rotations. *Bioresource Technology*, **98** (17) (2007): 3204–3212.

[147] E. Ryckebosch, M. Drouillon, and H. Vervaeren. Techniques for transformation of biogas to biomethane. *Biomass and Bioenergy*, **35** (5) (2011): 1633–1645.

[148] D. Deublein and A. Steinhauser. "Biochemical Reaction." In: *Biogas from Waste and Renewable Resources*. Ed. by D. Deublein and A. Steinhauser. Weinheim, Germany: Wiley-VCH Verlag GmbH & Co. KGaA, 2008, 87–91.

[149] G. J. Tortora, B. R. Funke, and C. L. Case. Microbiology : an introduction. 12th ed. Pearson, 2014.

[150] R. Braun. "Anaerobic digestion: a multi-faceted process for energy, environmental management and rural development." In: *Improvement of Crop Plants for Industrial End Uses*. Dordrecht: Springer Netherlands, 2007, 335–416.

[151] M. Herout, J. Malaťák, L. Kučera, et al. Biogas composition depending on the type of plant biomass used. *Research in Agricultural Engineering*, **57** (4) (2011): 137–143.

[152] A. Ideris, E. Croiset, M. Pritzker, et al. Direct-methane solid oxide fuel cell (SOFC) with Ni-SDC anode-supported cell. *International Journal of Hydrogen Energy*, **42** (36) (2017): 23118–23129.

[153] X.-F. Ye, J. Zhou, S. Wang, et al. Research of carbon deposition formation and judgment in Cu-CeO2-ScSZ anodes for direct ethanol solid oxide fuel cells. *International Journal of Hydrogen Energy*, **37** (1) (2012): 505–510.

[154] J. Rostrup-Nielsen. Production of synthesis gas. *Catalysis Today*, **18** (4) (1993): 305–324.

[155] S. Sui, G. Xiu, S. Sui, et al. "Fuels and fuel processing in SOFC applications." In: *High-Temperature Solid Oxide Fuel Cells for the 21st Century*. Elsevier, 2016, 461–495.

[156] T. Trabold, J. Lylak, M. Walluk, et al. Measurement and analysis of carbon formation during diesel reforming for solid oxide fuel cells. *International Journal of Hydrogen Energy*, **37** (6) (2012): 5190–5201.

[157] A. T. Ashcroft, A. K. Cheetham, M. L. H. Green, et al. Partial oxidation of methane to synthesis gas using carbon dioxide. *Nature*, **352** (6332) (1991): 225–226.

[158] L. Navadol, R. Shivanahalli, S. Wattana, et al. "Effects of H2S, CO2, and O2 on Catalytic Methane Steam Reforming over Ni Catalyst on CeO2 and Al2O3 Supports." In: *Sustainable Energy and Environment*. Hua Hin, Thailand: Sustainable Energy and Environment (SEE), 2004, 129–133.

[159] R. Sitthikhankaew, D. Chadwick, S. Assabumrungrat, et al. Effects of humidity, O2, and CO2 on H2S adsorption onto upgraded and KOH impregnated activated carbons. *Fuel Processing Technology*, **124** (2014): 249–257.

[160] C.-C. Huang, C.-H. Chen, and S.-M. Chu. Effect of moisture on H2S adsorption by copper impregnated activated carbon. *Journal of Hazardous Materials*, **136** (3) (2006): 866–873.

[161] N. Murgi, G. Lorenzo, O. Corigliano, et al. Influence of Anodic Gas Mixture Composition on Solid Oxide Fuel Cell Performance: Part 2. *International Journal of Heat and Technology*, **34** (2) (2016): 309–314.

[162] I. D. Kellogg, U. O. Koylu, V. Petrovsky, et al. Effectiveness of anode in a solid oxide fuel cell with hydrogen/oxygen mixed gases. *International Journal of Hydrogen Energy*, **34** (12) (2009): 5138–5143.

[163] M. Pihlatie. "Stability of Ni-YSZ composites for solid oxide fuel cells during reduction and re-oxidation." PhD Thesis. Aalto University School of Science and Technology, 2010, 99.

[164] V. Subotic, B. Stoeckl, C. Schluckner, et al. Development of Cell-Protecting Methods for Carbon-Removal from Porous Ni-YSZ Anodes and Regeneration of the Cell Performance. *ECS Transactions*, **78** (1) (2017): 2441–2449.

[165] F. Watanabe, I. Kaburaki, N. Shimoda, et al. Influence of nitrogen impurity for steam methane reforming over noble metal catalysts. *Fuel Processing Technology*, **152** (2016): 15–21.

[166] G. Tchobanoglous, H. D. Stensel, R. Tsuchihashi, et al. Wastewater engineering : treatment and resource recovery. 5th. New York: McGraw Hil, 2013, 2048.

[167] P. N. L. Lens, A. Visser, A. J. H. Janssen, et al. Biotechnological Treatment of Sulfate-Rich Wastewaters. *Critical Reviews in Environmental Science and Technology*, **28** (1) (1998): 41–88.

[168] D. G. Cirne, F. P. van der Zee, M. Fernandez-Polanco, et al. Control of sulphide during anaerobic treatment of S-containing wastewaters by adding limited amounts of oxygen or nitrate. *Reviews in Environmental Science and Bio/Technology*, **7** (2) (2008): 93–105.

[169] A. Afif, N. Radenahmad, Q. Cheok, et al. Ammonia-fed fuel cells: a comprehensive review. *Renewable and Sustainable Energy Reviews*, **60** (2016): 822–835.

[170] G. Cinti, G. Discepoli, E. Sisani, et al. SOFC operating with ammonia: Stack test and system analysis. *International Journal of Hydrogen Energy*, **41** (31) (2016): 13583–13590.

[171] N. Maffei, L. Pelletier, J. Charland, et al. An intermediate temperature direct ammonia fuel cell using a proton conducting electrolyte. *Journal of Power Sources*, **140** (2) (2005): 264–267.

[172] N. Maffei, L. Pelletier, and A. McFarlan. A high performance direct ammonia fuel cell using a mixed ionic and electronic conducting anode. *Journal of Power Sources*, **175** (1) (2008): 221–225.

[173] B. Drosg, R. Braun, G. Bochmann, et al. "Analysis and characterisation of biogas feedstocks." In: *The Biogas Handbook*. Ed. by A. Wellinger, J. Murphy, and D. Baxter. Cambridge: Elsevier, 2013, 52–84.

[174] W. Ho and J. W. Bozzelli. Validation of a mechanism for use in modeling CH_2Cl_2 and/or CH_3Cl combustion and pyrolysis. *Symposium (International) on Combustion*, **24** (1) (1992): 743–748.

[175] K. W. Reeping, J. A. Bohn, and R. A. Walker. Chlorine-induced degradation in SOFCs operating with biogas. *Sustainable Energy & Fuels*, **1** (6) (2017): 1320–1328.

[176] K. W. Reeping, J. D. Kirtley, J. M. Bohn, et al. Chlorine-Induced Degradation in Solid Oxide Fuel Cells Identified by Operando Optical Methods. *The Journal of Physical Chemistry C*, **121** (5) (2017): 2588–2596.

[177] H. K. Jun, S. Y. Jung, T. J. Lee, et al. The effect of HCl and H_2O on the H_2S removing capacities of Zn-Ti-based desulfurization sorbents promoted by cobalt and nickel oxide. *Korean Journal of Chemical Engineering*, **21** (2) (2004): 425–429.

[178] A. Veksha, A. Giannis, W.-D. Oh, et al. Catalytic activities and resistance to HCl poisoning of Ni-based catalysts during steam reforming of naphthalene. *Applied Catalysis A: General*, **557** (2018): 25–38.

[179] R. Dewil, L. Appels, and J. Baeyens. Energy use of biogas hampered by the presence of siloxanes. *Energy Conversion and Management*, **47** (13-14) (2006): 1711–1722.

[180] P. Tower. New Technology for Removal of Siloxanes in Digester Gas Results in Lower Maintenance Costs and Air Quality Benefits in Power Generation Equipment. *Proceedings of the Water Environment Federation*, **2003** (9) (2003): 440–447.

[181] T. Montanari, E. Finocchio, I. Bozzano, et al. Purification of landfill biogases from siloxanes by adsorption: A study of silica and 13X zeolite adsorbents on hexamethylcyclotrisiloxane separation. *Chemical Engineering Journal*, **165** (3) (2010): 859–863.

[182] M. Turco, A. Ausiello, and L. Micoli. "The Effects of Siloxanes on High-Temperature Fuel Cells." In: *Treatment of Biogas for Feeding High Temperature Fuel Cells*. Ed. by M. Turco, A. Ausiello, and L. Micoli. New York: Spriger, 2016, 151–166.

[183] A. D. Wiheeb, I. K. Shamsudin, M. A. Ahmad, et al. Present technologies for hydrogen sulfide removal from gaseous mixtures. *Reviews in Chemical Engineering*, **29** (6) (2013): 449–470.

[184] Laura Bailon Allegue and J. Hinge. *Biogas upgrading Evaluation of methods for H2S removal*. Tech. rep. December. Danish Technological Institute, 2014, 1–31.

[185] X. Y. Chen, H. Vinh-Thang, A. A. Ramirez, et al. Membrane gas separation technologies for biogas upgrading. *RSC Advances*, **5** (31) (2015): 24399–24448.

[186] P. Cozma, W. Wukovits, I. Mămăligă, et al. Modeling and simulation of high pressure water scrubbing technology applied for biogas upgrading. *Clean Technologies and Environmental Policy*, **17** (2) (2015): 373–391.

[187] Y. T. Shah. Chemical energy from natural and synthetic gas. 1st. Boca Raton, FL: CRC Press, 2017, 688.

[188] S. Kurella, M. Balla, P. K. Bhukya, et al. Scrubbing of HCl Gas from Synthesis Gas in a Multistage Dual-Flow Sieve Plate Wet Scrubber by Alkaline Solution. *Journal of Chemical Engineering & Process Technology*, **06** (05) (2015).

[189] I. Angelidaki, L. Treu, P. Tsapekos, et al. Biogas upgrading and utilization: Current status and perspectives. *Biotechnology Advances*, **36** (2) (2018): 452–466.

[190] A. Makaruk, M. Miltner, and M. Harasek. Membrane biogas upgrading processes for the production of natural gas substitute. *Separation and Purification Technology*, **74** (1) (2010): 83–92.

[191] M. Harasimowicz, P. Orluk, G. Zakrzewska-Trznadel, et al. Application of polyimide membranes for biogas purification and enrichment. *Journal of Hazardous Materials*, **144** (3) (2007): 698–702.

[192] S. M. S. Niknejad, H. Savoji, M. Pourafshari Chenar, et al. Separation of H2S from CH4 by polymeric membranes at different H2S concentrations. *International Journal of Environmental Science and Technology*, **14** (2) (2017): 375–384.

[193] F. Bauer, C. Hulteberg, T. Persson, et al. *Biogas upgrading - Review of commercial technologies*. Tech. rep. 2013, 82.

[194] R. Augelletti, M. Conti, and M. C. Annesini. Pressure swing adsorption for biogas upgrading. A new process configuration for the separation of biomethane and carbon dioxide. *Journal of Cleaner Production*, **140** (2017): 1390–1398.

[195] C. Peng, J. Luo, A. R. Sanger, et al. Sulfur-Tolerant Anode Catalyst for Solid Oxide Fuel Cells Operating on H2S-Containing Syngas. *Chemistry of Materials*, **22** (3) (2010): 1032–1037.

[196] S. Sengodan, R. Lan, J. Humphreys, et al. Advances in reforming and partial oxidation of hydrocarbons for hydrogen production and fuel cell applications. *Renewable and Sustainable Energy Reviews*, **82** (2018): 761–780.

[197] K. H. Hofstad, O. A. Rokstad, and A. Holmen. Partial oxidation of methane over platinum metal gauze. *Catalysis Letters*, **36** (1-2) (1996): 25–30.

[198] Y. Boucouvalas, Z. Zhang, and X. E. Verykios. Partial oxidation of methane to synthesis gas via the direct reaction scheme over Ru/TiO2 catalyst. *Catalysis Letters*, **40** (3-4) (1996): 189–195.

[199] S. H. Clarke, A. L. Dicks, K. Pointon, et al. Catalytic aspects of the steam reforming of hydrocarbons in internal reforming fuel cells. *Catalysis Today*, **38** (4) (1997): 411–423.

[200] B. D. Crittenden and W. J. Thomas. Adsorption technology and design. 1st. Butterworth-Heinemann, 1998, 271.

[201] D. Bathen and J. Ciprian. "Adsorption." In: *Fluidverfahrenstechnik*. Ed. by R. Goedecke. 1st. Weinheim, Germany: Wiley-VCH Verlag GmbH & Co. KGaA, 2006, 303–380.

[202] K. Sattler and H. J. Feindt. "Adsorption." In: *Thermal Separation Processes*. 1st. Weinheim, Germany: Wiley-VCH Verlag GmbH, 1995, 281–316.

[203] A. Dabrowski. Adsorption — from theory to practice. *Advances in Colloid and Interface Science*, **93** (1-3) (2001): 135–224.

[204] B. L. Karger, L. R. Snyder, and C. Horváth. An introduction to separation science. Wiley, 1973, 586.

[205] R. T. Yang. Gas separation by adsorption processes. London: World Scientific, 1997, 352.

[206] A. W. Adamson and A. P. Gast. Physical chemistry of surfaces. 6th. Hoboken, NJ: Wiley-Interscience, 1997, 784.

[207] A. Mersmann, M. Kind, and J. Stichlmair. "Adsorption, Chromatography, Ion Exchange." In: *Thermal Separation Technology*. 1st. Berlin, Heidelberg: Springer Berlin Heidelberg, 2011, 483–560.

[208] M. W. Johns. "The simulation of gold adsorption by carbon using a film diffusion model." PhD thesis. University of the Witwatersrand, 1987, 120.

[209] R. H. Perry and D. W. Green. Perry's Chemical Engineers' Handbook. 8th. McGraw-Hill, 2008, 2640.

[210] B. Babu and S. Gupta. Modeling And Simulation Of Fixed Bed Adsorption Column: Effect Of Velocity Variation. *i-manager's Journal on Future Engineering and Technology*, **1** (1) (2005): 60–66.

[211] R. W. Rousseau. Handbook of separation process technology. J. Wiley, 1987, 1010.

[212] A. Pfennig and H. Martin. "Verfahrenstechnische Grundlagen zu Stoffaustausch und Wärmeübertragung." In: *Fluidverfahrenstechnik*. Ed. by R. Goedecke. 1st. Weinheim, Germany: Wiley-VCH Verlag GmbH & Co. KGaA, 2006, 187–301.

[213] A. Schönbucher. Thermische Verfahrenstechnik : Grundlagen und Berechnungsmethoden für Ausrüstungen und Prozesse. 1st. Berlin: Springer Berlin Heidelberg, 2002, 1049.

[214] M. Binns. Molecular sieve dryers for ethanol production. *Biofuels International Magazine*, **9** (3) (2015): 36–40.

[215] D. M. Ruthven. Principles of adsorption and adsorption processes. 1st. New York: Wiley, 1984, 433.

[216] A. Bagreev and T. J. Bandosz. A Role of Sodium Hydroxide in the Process of Hydrogen Sulfide Adsorption/Oxidation on Caustic-Impregnated Activated Carbons. *Industrial & Engineering Chemistry Research*, **41** (4) (2002): 672–679.

[217] J. Przepiorski and A. Oya. K2CO3-loaded Deodorizing Activated Carbon Fibre Against H2S Gas: Factors Influencing the Deodorizing Efficiency and the Regeneration Method. *Journal of Materials Science Letters*, **17** (8) (1998): 679–682.

[218] M. C. Castrillon, K. O. Moura, C. A. Alves, et al. CO2 and H2S Removal from CH4 - Rich Streams by Adsorption on Activated Carbons Modified with K2CO3, NaOH, or Fe2O3. *Energy & Fuels*, **30** (11) (2016): 9596–9604.

[219] J.-H. Tsai, F.-T. Jeng, and H.-L. Chiang. Removal of H2S from Exhaust Gas by Use of Alkaline Activated Carbon. *Adsorption*, **7** (4) (2001): 357–366.

[220] M. Husmann, C. Hochenauer, X. Meng, et al. Evaluation of Sorbents for High Temperature In Situ Desulfurization of Biomass-Derived Syngas. *Energy & Fuels*, **28** (4) (2014): 2523–2534.

[221] W. Elseviers and H. Verelst. Transition metal oxides for hot gas desulphurisation. *Fuel*, **78** (5) (1999): 601–612.

[222] C. Weinlaender, R. Neubauer, M. Hauth, et al. Removing H2S from Biogas Using Sorbents for Solid Oxide Fuel Cell Applications. *Chemie Ingenieur Technik*, **89** (9) (2017): 1247–1254.

[223] L. D. Gasper-Galvin, A. T. Atimtay, and R. P. Gupta. Zeolite-supported metal oxide sorbents for hot-gas desulfurization. *Industrial and Engineering Chemistry Research*, **37** (10) (1998): 4157–4166.

[224] W. Xie, L. Chang, D. Wang, et al. Removal of sulfur at high temperatures using iron-based sorbents supported on fine coal ash. *Fuel*, **89** (4) (2010): 868–873.

[225] H. Zhao, D. Zhang, F. Wang, et al. Modification of ferrite–manganese oxide sorbent by doping with cerium oxide. *Process Safety and Environmental Protection*, **86** (6) (2008): 448–454.

[226] T. Ko, H. Chu, L. Chaung, et al. High temperature removal of hydrogen sulfide using an N-150 sorbent. *Journal of Hazardous Materials*, **114** (1-3) (2004): 145–152.

[227] N.-K. Park, D.-H. Lee, J.-D. Lee, et al. Effects of reduction of metal oxide sorbents on reactivity and physical properties during hot gas desulphurization in IGCC. *Fuel*, **84** (17) (2005): 2158–2164.

[228] R. B. Slimane and J. Abbasian. Regenerable mixed metal oxide sorbents for coal gas desulfurization at moderate temperatures. *Advances in Environmental Research*, **4** (2) (2000): 147–162.

[229] W. Mojtahedi and J. Abbasian. H2S Removal from Coal Gas at Elevated Temperature and Pressure in Fluidized Bed with Zinc Titanate Sorbents. 1. Cyclic Tests. *Energy & Fuels*, **9** (3) (1995): 429–434.

[230] H. K. Jun, S. Y. Jung, T. J. Lee, et al. The effect of HCl and H2O on the H2S removing capacities of Zn-Ti-based desulfurization sorbents promoted by cobalt and nickel oxide. *Korean Journal of Chemical Engineering*, **21** (2) (2004): 425–429.

[231] M. D. Dolan, A. Y. Ilyushechkin, K. G. McLennan, et al. Sulfur removal from coal-derived syngas: thermodynamic considerations and review. *Asia-Pacific Journal of Chemical Engineering*, **7** (1) (2012): 1–13.

[232] J. Abbasian and R. Slimane. A Regenerable Copper-Based Sorbent for H2S Removal from Coal Gases (1998).

[233] L. Alonso, J. Palacios, E. Garcı-a, et al. Characterization of Mn and Cu oxides as regenerable sorbents for hot coal gas desulfurization. *Fuel Processing Technology*, **62** (1) (2000): 31–44.

[234] H.-J. Bart and U. von Gemmingen. "Adsorption." In: *Ullmann's Encyclopedia of Industrial Chemistry*. Weinheim, Germany: Wiley-VCH Verlag GmbH & Co. KGaA, 2005, 38.

[235] David T. Lundie, Alastair R. McInroy, Robert Marshall, et al. Improved Description of the Surface Acidity of η-Alumina (2005).

[236] A. R. McInroy, D. T. Lundie, J. M. Winfield, et al. The interaction of alumina with HCl: An infrared spectroscopy, temperature-programmed desorption and inelastic neutron scattering study. *Catalysis Today*, **114** (4) (2006): 403–411.

[237] P. V. Broadhurst. *Removal of chloride compounds*. Tech. rep. Technical Report: Johnson Matthey Catalysts, 2003.

[238] H. Werner and P. Rosmus. Theoretical dipole moment functions of the HF, HCl, and HBr molecules. *The Journal of Chemical Physics*, **73** (5) (1980): 2319–2328.

[239] J. D. Seader and E. J. Henley. Separation process principles. 3rd. Hoboken NJ: Wiley, 2010, 756.

[240] D. Bathen and J. Ciprian. "Adsorption." In: *Fluidverfahrenstechnik*. Weinheim, Germany: Wiley-VCH Verlag GmbH & Co. KGaA, 303–380.

[241] K. Kim, S. K. Jeon, C. Vo, et al. Removal of Hydrogen Sulfide from a Steam-Hydrogasifier Product Gas by Zinc Oxide Sorbent. *Industrial & Engineering Chemistry Research*, **46** (18) (2007): 5848–5854.

[242] I. Novochinskii, S. Chunshan, M. Xiaoliang, et al. Low-Temperature H2S Removal from Steam-Containing Gas Mixtures with ZnO for Fuel Cell Application. 1. ZnO Particles and Extrudates. *Energy Fuels*, **18** (2) (2004): 576–583.

[243] R. G. Harrison, P. Todd, S. R. Rudge, et al. Bioseparations science and engineering. Oxford: Oxford University Press, 2015, 576.

[244] G. Ertl, H. Knözinger, and J. Weitkamp. Handbook of heterogeneous catalysis. 2nd. Wiley-VCH, 2008, 2497.

[245] K. Huang. Fuel utilization and fuel sensitivity of solid oxide fuel cells. *Journal of Power Sources*, **196** (5) (2011): 2763–2767.

[246] A. L. Dicks. Hydrogen generation from natural gas for the fuel cell systems of tomorrow. *Journal of Power Sources*, **61** (1-2) (1996): 113–124.

[247] Clariant. *Material Safety Data Sheet Clariant Reformax 100*. Tech. rep. Clariant, 2012, 33.

[248] K. Ahmed and K. Föger. Fuel Processing for High-Temperature High-Efficiency Fuel Cells. *Industrial & Engineering Chemistry Research*, **49** (16) (2010): 7239–7256.

[249] J. R. Anderson and M. Boudart. Catalysis : Science and Technology. Springer Berlin Heidelberg, 1984, 281.

[250] J. Oudar and H. Wise. Deactivation and poisoning of catalysts. M. Dekker, 1985, 327.

[251] L. Li and D. L. King. H2S removal with ZnO during fuel processing for PEM fuel cell applications. *Catalysis Today*, **116** (4) (2006): 537–541.

[252] H. Atakül, J. Wakker, A. W. Gerritsen, et al. Removal of H2S from fuel gases at high temperatures using MnO/γ-Al2O3. *Fuel*, **74** (2) (1995): 187–191.

[253] J. Wang, L. Wang, H. Fan, et al. Highly porous copper oxide sorbent for H2S capture at ambient temperature. *Fuel*, **209** (2017): 329–338.

[254] M. Ozekmekci, G. Salkic, and M. F. Fellah. Use of zeolites for the removal of H2S: A mini-review. *Fuel Processing Technology*, **139** (2015): 49–60.

[255] S. Janke and M. Pearson. Alumina adsorbents effectively remove HCl from reformer H/sub 2/ gas streams. *Oil Gas J.; (United States)*, **84:19** (1986).

[256] D. Saha and S. Deng. Characteristics of Ammonia Adsorption on Activated Alumina. *Journal of Chemical & Engineering Data*, **55** (12) (2010): 5587–5593.

[257] C. Weinlaender, R. Neubauer, and C. Hochenauer. Low-temperature H2S removal for solid oxide fuel cell application with metal oxide adsorbents. *Adsorption Science & Technology*, **35** (1-2) (2016): 120–136.

[258] Clariant International Ltd. *Actisorb S2 Material Safety Data Sheet*. Tech. rep. Muttenz: Clariant International Ltd, 2006, 8.

[259] Clariant International Ltd. *Clariant GS 6 Material Saftedy Data Sheet*. Tech. rep. Muttenz: Clariant International Ltd, 2008, 7.

[260] A. L. Kohl and R. Nielsen. Gas purification. Gulf Pub, 1997, 1395.

[261] H. Sun Choo, L. C. Lau, A. Mohamed, et al. Hydrogen sulfide adsorption by alkaline impregnated coconut shell activated carbon. *Journal of Engineering Science and Technology*, **8** (2013): 741–753.

[262] Y. Xiao, S. Wang, D. Wu, et al. Experimental and simulation study of hydrogen sulfide adsorption on impregnated activated carbon under anaerobic conditions. *Journal of Hazardous Materials*, **153** (3) (2008): 1193–1200.

[263] I. Isik-Gulsac. Investigation of impregnated activated carbon properties used in hydrogen sulfide fine removal. *Brazilian Journal of Chemical Engineering*, **33** (2016): 1021–1030.

[264] Donau Carbon GmbH. *Desorex K43a Material Safety Data Sheet*. Tech. rep. Frankfurt am Main: Donau Carbon GmbH, 2011, 6.

[265] Clariant International Ltd. *Clariant GS 23 Material Safety Data Sheet*. Tech. rep. Muttenz: Clariant International Ltd, 2009, 6.

[266] P. S. Bárcia, L. Bastin, E. J. Hurtado, et al. Single and Multicomponent Sorption of CO 2 , CH 4 and N 2 in a Microporous Metal-Organic Framework. *Separation Science and Technology*, **43** (13) (2008): 3494–3521.

[267] J. Yang, J. Li, W. Wang, et al. Adsorption of CO 2 , CH 4 , and N 2 on 8-, 10-, and 12-Membered Ring Hydrophobic Microporous High-Silica Zeolites: DDR, Silicalite-1, and Beta. *Industrial & Engineering Chemistry Research*, **52** (50) (2013): 17856–17864.

[268] B. Steuten, C. Pasel, M. Luckas, et al. Adsorptive Entfernung von Schwefelverbindungen aus Erdgas. *Chemie Ingenieur Technik*, **85** (3) (2013): 333–343.

[269] H. L. Chiang, J. H. Tsai, C. L. Tsai, et al. Adsorption Characteristics of Alkaline Activated Carbon Exemplified by Water Vapor, H2S, and CH3SH Gas. *Separation Science and Technology*, **35** (6) (2007): 903–918.

[270] F. Yazdanbakhsh, J. A. Sawada, M. Alizadehgiashi, et al. Effect of Moisture on High Temperature H2S Adsorption by Copper-Exchanged Engelhard Titanosilicate-2. *Journal of Nanoscience and Nanotechnology*, **17** (5) (2017): 3409–3414.

[271] M. M. Tomadakis, H. H. Heck, M. E. Jubran, et al. Pressure-Swing Adsorption Separation of H2 S from CO2 with Molecular Sieves 4A, 5A, and 13X. *Separation Science and Technology*, **46** (3) (2011): 428–433.

[272] C. Weinlaender, R. Neubauer, M. Hauth, et al. Investigation of NH3 Influence on Adsorptive H2S Removal from Biogas for Solid Oxide Fuel Cell Application. *Chemie Ingenieur Technik*, **90** (7) (2018): 937–946.

[273] E. Satomi, H. Iwai, S. Suzuki, et al. Development of Ammonia-Fueled SOFC. *ECS Transactions*, **78** (1) (2017): 2537–2540.

[274] M. Ni, M. K. H. Leung, and D. Y. C. Leung. Ammonia-fed solid oxide fuel cells for power generation-A review. *International Journal of Energy Research*, **33** (11) (2009): 943–959.

[275] P. Lodewyckx. Adsorption of chemical warfare agents. *Interface Science and Technology*, **7** (2006): 475–528.

[276] J. Rossin, E. Petersen, D. Tevault, et al. Effects of environmental weathering on the properties of ASC-whetlerite. *Carbon*, **29** (2) (1991): 197–205.

[277] C. Weinlaender, R. Neubauer, M. Hauth, et al. Adsorptive hydrogen chloride and combined hydrogen chloride–hydrogen sulphide removal from biogas for solid oxide fuel cell application. *Adsorption Science & Technology*, **36** (5-6) (2018): 1215–1232.

[278] L. Micoli, G. Bagnasco, and M. Turco. HCl removal from biogas for feeding MCFCs: Adsorption on microporous materials. *International Journal of Hydrogen Energy*, **38** (1) (2013): 447–452.

[279] J. Zou and R. Rezaee. Effect of particle size on high-pressure methane adsorption of coal. *Petroleum Research*, **1** (1) (2016): 53–58.

[280] M. Turco, A. Ausiello, and L. Micoli. Treatment of biogas for feeding high temperature fuel cells : removal of harmful compounds by adsorption processes.

[281] C. Bernardo, I. Alstrup, and J. Rostrup-Nielsen. Carbon deposition and methane steam reforming on silica-supported Ni-Cu catalysts. *Journal of Catalysis*, **96** (2) (1985): 517–534.

[282] J. Guo, C. Xie, K. Lee, et al. Improving the Carbon Resistance of Ni-Based Steam Reforming Catalyst by Alloying with Rh: A Computational Study Coupled with Reforming Experiments and EXAFS Characterization. *ACS Catalysis*, **1** (6) (2011): 574–582.

[283] M. Bertau, H. Offermanns, L. Plass, et al. Methanol: The Basic Chemical and Energy Feedstock of the Future Asinger's Vision Today. Berlin-Heidelberg: Springer, 2014, 677.

[284] H. Madi, S. Diethelm, J. Van herle, et al. Effect of Steam-to-Carbon Ratio on Degradation of Ni-YSZ Anode Supported Cells. *ECS Transactions*, **57** (1) (2013): 1517–1525.

[285] Clariant. *Reformax 100 Instructions*. Tech. rep. Clariant, 2012, 14.

[286] C. Weinländer, J. Albert, C. Gaber, et al. Investigation of subsystems for combination into a SOFC based CCHP system. *Journal of Electrochemical Energy Conversion and Storage*, **16** (2) (2018): 12.

[287] Fraunhofer IKTS. *Assembly documentation*. Tech. rep. Dresden: Fraunhofer IKTS, 2016, 24.